CRANFIELD UNIVERSITY

DANIEL A. LEWIS

THE EFFECT OF IONISING RADIATION ON THE EXPLOSIVES: TATB, HMX AND PETN

CENTRE FOR DEFENCE CHEMISTRY

PhD
Academic Year: 2019–2020

Supervisors: Professor J. Akhavan, Professor M. Cook, Dr I. Wilson, Dr C. Stennett

June 2019

CRANFIELD UNIVERSITY

CENTRE FOR DEFENCE CHEMISTRY

PhD

Academic Year: 2019–2020

DANIEL A. LEWIS

The effect of ionising radiation on the explosives: TATB, HMX and PETN

Supervisors: Professor J. Akhavan, Professor M. Cook, Dr I. Wilson, Dr C. Stennett

June 2019

This thesis is submitted in partial fulfilment of the requirements for the degree of PhD.

Abstract

The effect ionizing radiation, specifically gamma, has on three of the most well known explosive materials; HMX, PETN and TATB, has been studied experimentally and computationally. Samples of these explosives that had been irradiated in vacuum to a total dose (equivalent to water) of 200 kGy by an average incident energy of 1.25 MeV, showed changes to their explosive and physical properties to varying degrees, with sensitivity to impact being most notably changed for PETN and HMX.

Changes to the thermal properties of HMX and TATB, alongside the detection of long lived radicals for TATB and PETN, suggests alterations to each material's chemistry. Changes were only detectable in solid state analytical methods, indicating that alterations to these materials are isolated within this state. Through comparison with other data, these changes appear to be highly dependant on the gaseous environment in which they are irradiated, with vacuum having the most significant effect.

The widely reported greening of TATB under the influence of gamma (and ultraviolet and x-Ray) irradiation was found to be reversible upon re-crystallisation, with the process also appearing to remove the long lived radical that had existed in the material for over eight years. Radical concentration appears to correlate with total absorbed dose along with the level of green within the material. Computational investigation attributes the discolouration of TATB to the cationic radical derivative of TATB, which is stabilised by de-localised pi-bonding resonance of the constitutive aromatic ring, it is also suggested that this is the source of the radical signal observed in ESR analysis.

Further computational investigation suggests that purported decomposition products of TATB such as the mono-furazan, mono-nitroso and phenoxyl radical are not the source of the discolouration and are also not thermodynamically favourable, unless the mono-furazan or phenoxyl derivatives are in a cationic form. Thermodynamic evaluation of potential decomposition pathways for PETN and HMX yield a selection of energetically favourable products, however the significant majority are, like TATB, in the cationic radical form.

Simulated ESR spectra for purported HMX decomposition products did not agree with those observed in literature, attributed to their short lived nature. However a measured long lived radical in TATB is attributed to the cationic radical form of TATB, the purported source of the discolouration. A long lived radical in PETN was also measured and assigned to the cation derivative of PETN by comparison with computational predictions.

Keywords

Green TATB; HMX; TATB; PETN, Irradiation; Explosives

Contents

List of Figures

List of Tables

List of Abbreviations

AMU	Atomic mass unit
AWE	Atomic Weapons Establishment
BET	Braunauer-Emmett-Teller
CEP	Chloroethylphosphate
CIS	Configuration interaction singlets
CISD	Configuration interaction singlets and doublets
CW	Continuous wave
DSC	Differential scanning calorimetry
DPA	Diphenylamine
DFT	Density functional theory
ESR	Electron spin resonance
EDC	Explosive division composition
FoI	Figure of insensitivity
GC	Gas chromatography
GIAO	Gauge independent atomic orbital
HF	Hartree-Fock
HMX	High melting explosive
HPLC	High performance liquid chromatography
IR	Infrared
LANL	Los Alamos National Laboratory
LEP	Life extension programme

MS	Mass spectroscopy
NEQ	Net explosive quantity
NMR	Nuclear magnetic resonance
NTO	Nitrotriazolone
ONIOM	Own N-layered integrated molecular orbital and molecular mechanics
ORNL	Oak Ridge National Laboratory
PBC	Periodic boundary conditions]
PBX	Polymer bonded explosive
PCM	Polarized continuum model
PETN	Pentaerythritoltetranitrate
RDX	Research development explosive
RMS	Route mean squared
STAB	Stearyl-trimethyl-ammonium-bromide
TATB	Triaminotrinitrobenzene
TD-DFT	Time dependant density functional theory
TD-HF	Time dependant Hartree-Fock
TMS	Tetramethylsilane
TNB	Trinitrobenzene
TNT	Trinitrotoluene
UV-VIS	Ultraviolet - visible
XPS	x-ray photoelectron spectrometer

Acknowledgements

I would like to thank my supervisors, Professor Jackie Akhavan, Doctors Ian Wilson, Nathan Flood, Christopher Stennett and James Padfield, who have provided me with their continued advice, guidance and support during this project. I would also like to thank fellow AWE employee Professor Malcolm Cook for his invaluable input into this project, particularly the computational and ESR aspects of this study.

Recognition must also be given to AWE Plc. who have permitted me the time and the resource to enable me to complete this research project, in particular the use of their extensive computational facilities. Further thanks must go to Dr. David Duncan, for his continued support in transferring packages of data across AWE networks.

I must also recognise my parents, who's support and guidance throughout my life, particularly with proof reading large documents, has played no small part in my current or future success.

Finally, I would like thank my wife Sarah, who has always loved and supported me through my endeavours, with this project spanning the past six years, being no exception.

Chapter 1

Introduction

In order to assure, assess and ultimately predict the safe working life of energetic materials, the quantification and physical understanding of potential effects that arise from external stimuli present in the surrounding environment, must be well understood. Energetic materials are employed in numerous and varied applications, often resulting in exposure to a wide array of differing environments. In all of these applications, life assessment of these materials focuses on predicting and understanding any physicochemical processes which may occur through life, and may potentially alter the three main characteristics of an explosive's suitability; performance, safety and mechanical properties.

1.1 Relevance

In cases where energetic materials are utilised within nuclear or space applications, additional processes that would not typically be considered need to be assessed as to their potential to affect the material, due to the exposure to radiation. Of the potential types of radiation that energetic materials may experience through their life, those that are highly penetrating, such as gamma radiation, are of particular interest. This is due principally to the relative ease of which an energetic material could become exposed to such radiation, despite shielding, housing or other materials being employed within a device, which of-

fer little protection. In contrast, the effect from radiations such as ultraviolet and visible light (UV-Vis) light, as well as some x-rays, will be significantly reduced if not nullified by such surrounding materials and shielding. There is one main exception to this and that is in the case of an explosive material being intimately and directly mixed with a radionuclide, most likely for the generation of a so called "dirty bomb". These two extreme cases offer significantly different scenarios. Explosives utilised for nuclear weapon applications will typically be well characterised, of high power and will be comparatively much safer; they will likely experience long-term low level exposure to well characterised radiations. In contrast, explosives utilised within "dirty bombs" are more likely to be inherently poorly characterised, of comparatively low power and of high sensitiveness; they will typically be exposed to high levels of radiation, for short periods of time [1].

The research presented within this thesis focuses on the former scenario, the effect that long term low-levels of highly penetrating gamma radiation has on well characterised, military grade explosive materials. This topic of research has been active since the advent of nuclear weapons in the mid 1940s, but is becoming increasingly relevant due to enhanced service life requirements and associated life extension programmes (LEP). These programmes typically feature more traditional thermally accelerated ageing experiments, where the rate of chemical degradation is artificially increased through temperature. This process yields materials with an equivalent age significantly greater than the material's actual age. This, in turn, allows characterisation and subsequent mathematical relationships that are a function of both time and temperature to be derived, allowing properties of the material to be predicted at and beyond a required service life.

An analogous process can be used to assess the effect of radiation on these materials, where increased dose rates (relative to a service environment) are utilised to achieve the required total dose over significantly shorter time scales. This approach, alongside thermally accelerated ageing, has its drawbacks. In the case of increased temperature, chem-

ical reactions which may be dormant at service temperatures may be accessed, giving an unrepresentative kinetic description of the processes which may occur. For significantly increased dose rates, a similar effect is likely through the generation of increased concentrations of excited and/or radical species, allowing for recombination reactions which may not occur in service.

Nuclear weapon life assessment programmes need to consider the effect that both thermally and radiologically driven processes (as well as other physical factors where appropriate e.g. humidity) have on energetic materials. The best way to address the shortcomings of both thermally and radiologically accelerated ageing is to be able to mathematically describe all the processes as a function of time, temperature and radiation environment, often described as an explicit predictive model. This approach acknowledges that accelerated ageing is not representative of a service environment, but data gathered from the characterisation of such accelerated aged materials provides model validation, alongside data from surveillance programmes which enhances confidence in model predictions. This approach also allows the consideration of synergistic effects, for example, the generation of daughter products through radiological means, which may then catalyse a thermally driven process, previously thought not to occur.

The research presented within this thesis aims to understand and describe the interactions and subsequent effect radiation has on explosive materials so that it may be incorporated within such a model. This is achieved through a combination of literature review, to identify purported decomposition products and pathways, experimental analysis of bulk materials, to validate end time daughter products and their associated effects on the material, and the development of an in-situ gamma irradiative Electron Spin Resonance (ESR) technique, to identify early time radical generation. This is complemented by computational modelling which is used to predict daughter product speciation through thermodynamic analysis and the generation of associated characteristic electronic spectra.

1.2 Selected materials

Due to time and resource restrictions, a select few materials have been studied in specific radiological environments. However, it is envisioned that the research presented within may be used as a framework for other materials to be irradiated and analysed in a similar fashion.

Pure bulk explosive powders were selected over mixtures/composites, due to the added complexity of multi-material interactions, although some relevant Polymer Bonded Explosives (PBX) materials were irradiated as part of a parallel study allowing for some comparison. The three materials selected for this research were HMX (1,3,5,7-Tetranitro-1,3,5,7-tetrazoctane), TATB (1,3,5-Triamino-2,4,6-trinitrobenzene) and PETN (Pentaerythritol tetranitrate) as shown in Figure 1.1. These pure bulk explosive materials were selected due to their acknowledged use within nuclear applications [2]. HMX - based secondary explosive compositions typically provide comparatively higher performance at an increased sensitiveness over TATB; which is one of the most commonly known insensitive secondary explosives. PETN is comparatively more sensitive than both TATB and HMX, but is less powerful than HMX. For this reason it is typically used in detonator applications and was used in the bridgewire detonators within the first atomic bombs [3].

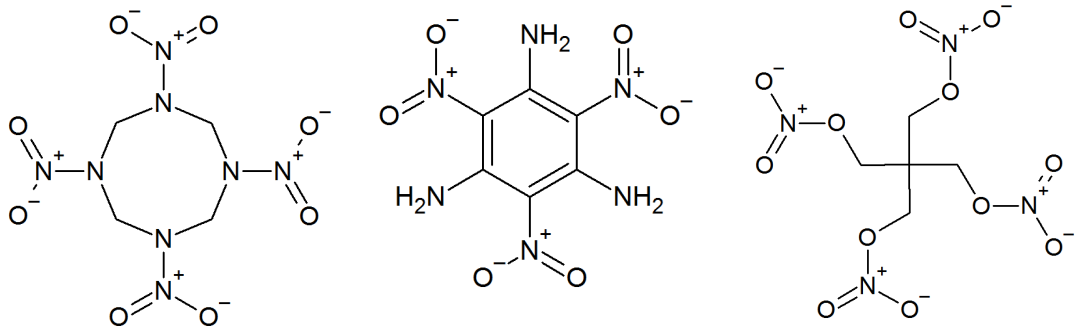

(a) HMX (b) TATB (c) PETN

Figure 1.1: Selected explosive materials

All three materials were sourced from AWE plc. The HMX supplied for this work was from batch MC/3/806 and of the beta polymorph [4, 5, 6, 7], which is the highest density variant at 1.90 g cm^{-3}, offering the greatest explosive power per unit volume and improved shock propagation [8]. The material is known to be very pure and has been milled from HMX type A to HMX type B, resulting in a very fine powder with a poly-modal particle size ranging from sub-micron to approximately 100 microns. The PETN supplied for this research was certified as Explosive Division Composition (EDC) 40 of the alpha polymorph which has been re-crystallised to provide 0.5 mm sized particles [9, 10]. The TATB supplied was in powder form, from batch number AD/6/12, and of the type B variety, although some materials used were also of the type C variety, which has a much finer particle size.

Chapter 2

Radiation and its interaction with matter

Radiation is abundant in nature, as unstable stable states of matter decay through de-excitation; this is often achieved by the expulsion of energy and/or matter. Depending on the magnitude of the ejected energy and/or matter, the corresponding energy can be classed either as ionising (where electrons can be ejected from a subjected material), or non-ionising (where electrons can be promoted into higher energy levels within the electronic structure of their binding atom).

This research focusses on gamma radiation which is purely electromagnetic in nature (i.e. no mass), of high frequency and low wavelength. Gamma radiation photons are of very high energy, especially when compared to other species of electromagnetic radiation such as visible and UV light. Typical gamma energies range from thousands of electron volts to tens of million, which is classified as ionising. Gamma-rays and x-rays have historically been defined by their energies, with gamma-rays being at the higher end of the spectrum. However, with the advent of more powerful x-ray generators that can produce emissions of order 25 MeV, this distinction is no longer applicable.

A more accurate distinction comes from the source of the energy, whereas gamma-rays are produced from transitions/relaxations within the nucleus of an atom, x-rays are generated through transitions/relaxations of electrons external to the nucleus. Regardless of the source, it is the magnitude of the energy emitted that determines the subsequent interaction, alongside the ionisation potential of the absorbing medium, which is typically of the order of single electron volts, for organic matter. The three main interactions of electromagnetic radiation applicable to the range of energies potentially emitted as gamma radiation with increasing energy are; the Photoelectric Effect, Compton Scattering and Pair Production.

2.1 Photoelectric effect

The Photoelectric effect, as shown in Figure 2.1, is achieved when electromagnetic radiation greater than the order of single electron volts is incident on matter; like all radiolytic interactions, it is highly material dependant. The phenomenon describes the absorption of incident electromagnetic energy by an electron that is greater than that of the energy binding the charged particle to the atom, often referred to as the work function of the material. The absorption causes ejection of the electron, and ionisation of the parent molecule/atom results. Any excess energy from the incident photon is transferred to the kinetic energy of the ejected electron. Following this initial interaction, a local electron may relax to replace the lost inner electron through florescence.

The majority of gamma-rays are orders of magnitude greater in energy than that required to cause photoelectron ejection. Resultantly gamma-rays do not themselves typically interact via the Photoelectric effect, rather they interact through higher energy processes.

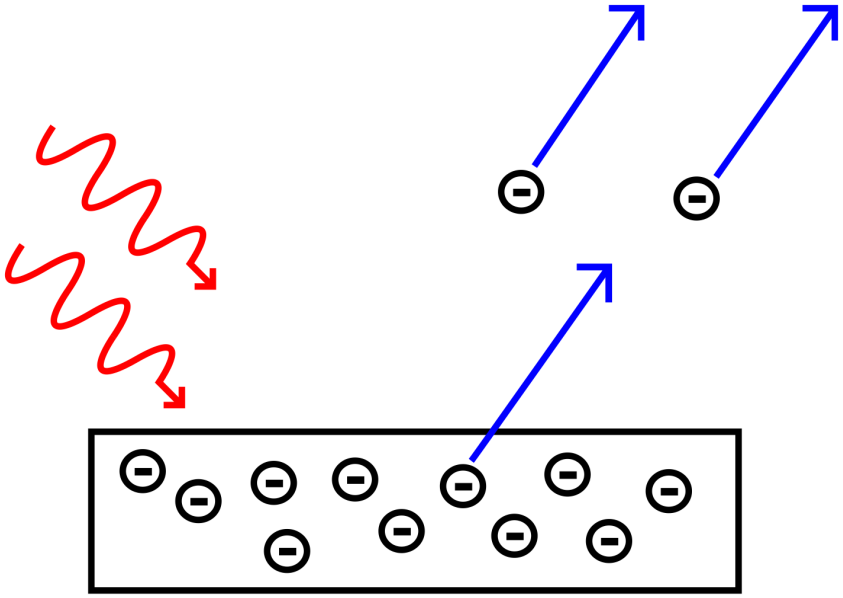

Figure 2.1: Photoelectric effect [11]

2.2 Compton scattering

Compton scattering, as shown in Figure 2.2, is a more energetic process than the Photoelectric effect. The process involves the inelastic interaction between an incident photon and an electron, which is typically treated as free (i.e. unbound) due to the several orders of magnitude difference between the incident photon and electron binding energies. The interaction causes the scattering of both the electron and the incident photon where a quantity of the incident photon energy is transferred to an electron in the form of kinetic energy. This results in a net loss of energy for the photon and the ejection of the electron from the parent atom, i.e. ionisation. According to the Planck-Einstein relationship [12] this change in photon energy corresponds to a new wavelength.

The most significant difference between Compton scattering and the Photoelectric effect is that the incident photon is not absorbed, rather it is scattered as the name suggests. The net result of both interactions is that the parent molecule/atom becomes ionised.

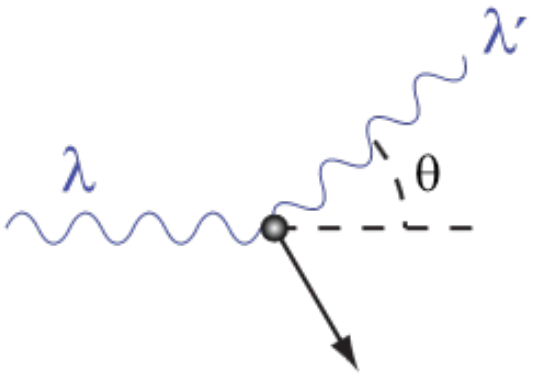

Figure 2.2: Compton scattering [13]

Interpretation of the Compton equation [12] shows that an angular distribution of energies will be transferred to electrons within a subjected medium as well as to any scattered photons. It also suggests that several subsequent interactions are possible between a scattered photon and other bound electrons of which lower energy interactions could result in a lower energy process such as the Photoelectric effect, or potentially a non-ionisation process, such as photo-isomerisation.

2.3 Pair production

Pair production, as shown in Figure 2.3, details the interaction of high energy photons with an atomic nucleus creating an electron and its antiparticle, a positron. The creation of such matter and anti-matter, is possible only when incident quanta has an energy greater than that of the combined rest mass energies of the electron and positron pair, 1.022 MeV.

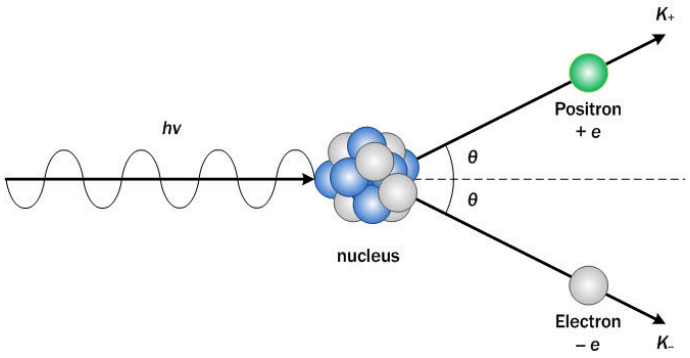

Figure 2.3: Pair production [14]

Any excess of this energy manifests itself as kinetic energy, equally shared between the electron and positron. The probability of a pair production reaction is proportional to the proton number (z) of the subjected nucleus squared, hence low z material are significantly less affected by this interaction. Electrons and positrons can under go a reverse reaction called annihilation where two back-to-back photons of 0.511 MeV are created, which may go on to interact with the exposed media via Compton scattering and follow through to other lower energy processes. Pair production reactions are therefore possible in nuclear weapon environments due to the use of high z materials, however the two most commonly used fissile materials; uranium-235 and plutonium-239 [2], do not have gamma emissions of sufficient energy.

2.4 Probability of interaction and linear mass attenuation coefficient

The probability for each of the forementioned reactions occurring is directly related to the incident energy of the electromagnetic radiation as well as the atomic structure of the exposed media. An example of the relative probabilities for each reaction, as a function of incident energy and the atomic number of the absorber, is shown in Figure 2.4. This highlights that the vast majority of any interaction between organic matter such as explosives

and gamma radiation will be through Compton scattering, because the atomic number for the elements in an explosive composition at typically low, i.e. hydrogen (1), carbon (12), nitrogen (14) and oxygen (16), ignoring isotopes.

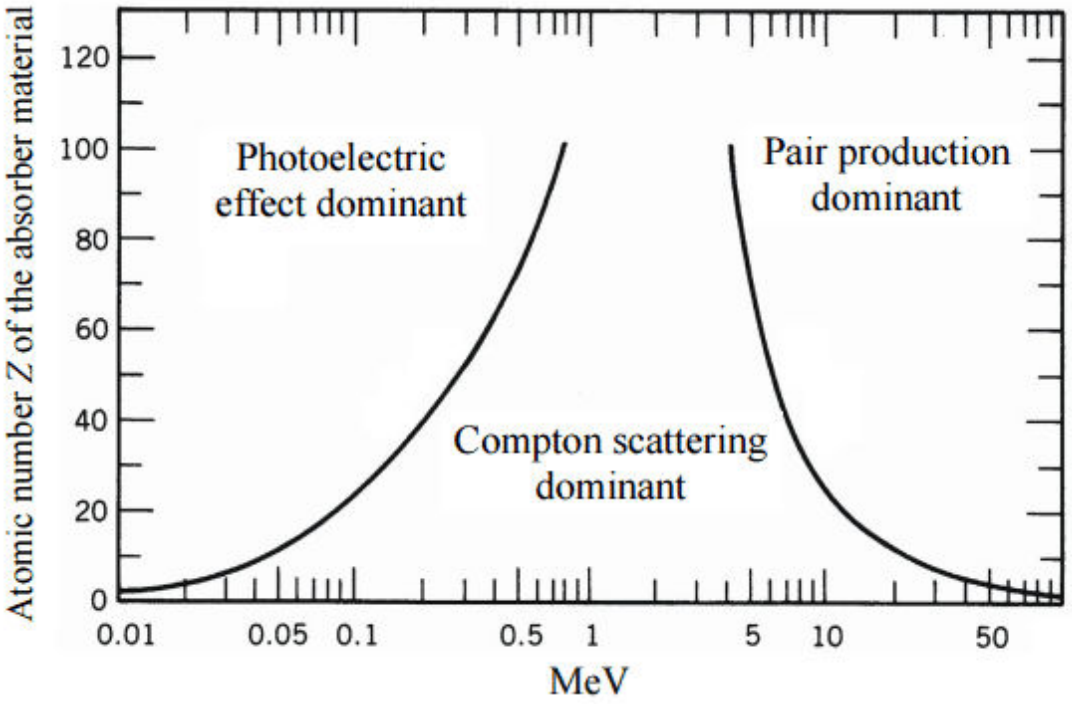

Figure 2.4: Energy dependence of interaction [15]

This relationship informs of the relative probabilities for each type of nuclear reaction to occur when electromagnetic radiation interacts with a medium; it does not inform on the probability of that interaction actually occurring within the medium.

The linear attenuation coefficient, μ, offers a solution. It describes the proportion of incident energy that is lost (through both scattering and absorption interactions) for a specific material; the coefficient also varies as a function of incident energy. The linear mass attenuation coefficient μ/ρ is a close relative, that also varies as a function of incident energy, but takes into account the density, ρ, of the subjected material. This is very important as without the consideration of density, most explosives would appear to have near identical absorption properties, as described by just the linear attenuation coefficient, due

to their similar atomic constituents (namely Carbon, Nitrogen, Oxygen and Hydrogen).

The linear mass attenuation coefficient is often used within the Beer-Lambert Law, as shown in Equation 2.1, to assess how much radiation may penetrate a material of a certain thickness and is often used in shielding calculations.

$$I = I_0 e^{-\mu/\rho l} \tag{2.1}$$

Where I is the intensity of photons from a collimated uniform beam of known flux denoted by I_0, μ is the mass attenuation coefficient and l is the reference thickness.

In addition, a further derivative of the linear mass attenuation coefficient is the linear mass-energy attenuation coefficient μ_{en}/ρ, which rather than describing the total interactions for a material and incident radiation, describes only those that interact through absorption mechanisms. This is a very useful and powerful parameter as it can be used to ascertain, with the Beer-Lamber law, how many quanta of radiation will be absorbed and therefore how many molecules will become ionised, as a function of thickness and incident energy.

The linear mass and mass-energy attenuation coefficients are derived from the relative probabilities of the forementioned interactions of radiation and matter occurring for a given incident energy and atomic make-up of the material. An example functional form of how the linear mass and mass-energy coefficients vary as a function of incident energy, is shown for hydrogen in Figure 2.5. It can be seen that interactions with radiation up to 0.01 MeV will be dominated by the photo electric effect, interactions between 10 keV and 1 MeV will be dominated by Compton scattering and interactions greater that 1 MeV begin to involve pair production, which dominated beyond 10 MeV. The diagram also highlights the difference between the mass and mass-energy attenuation functions. Due to the low z of hydrogen, pair production is not favourable and this is why both attenua-

tion coefficients decrease rapidly after 1 MeV, as shown in Figure 2.4.

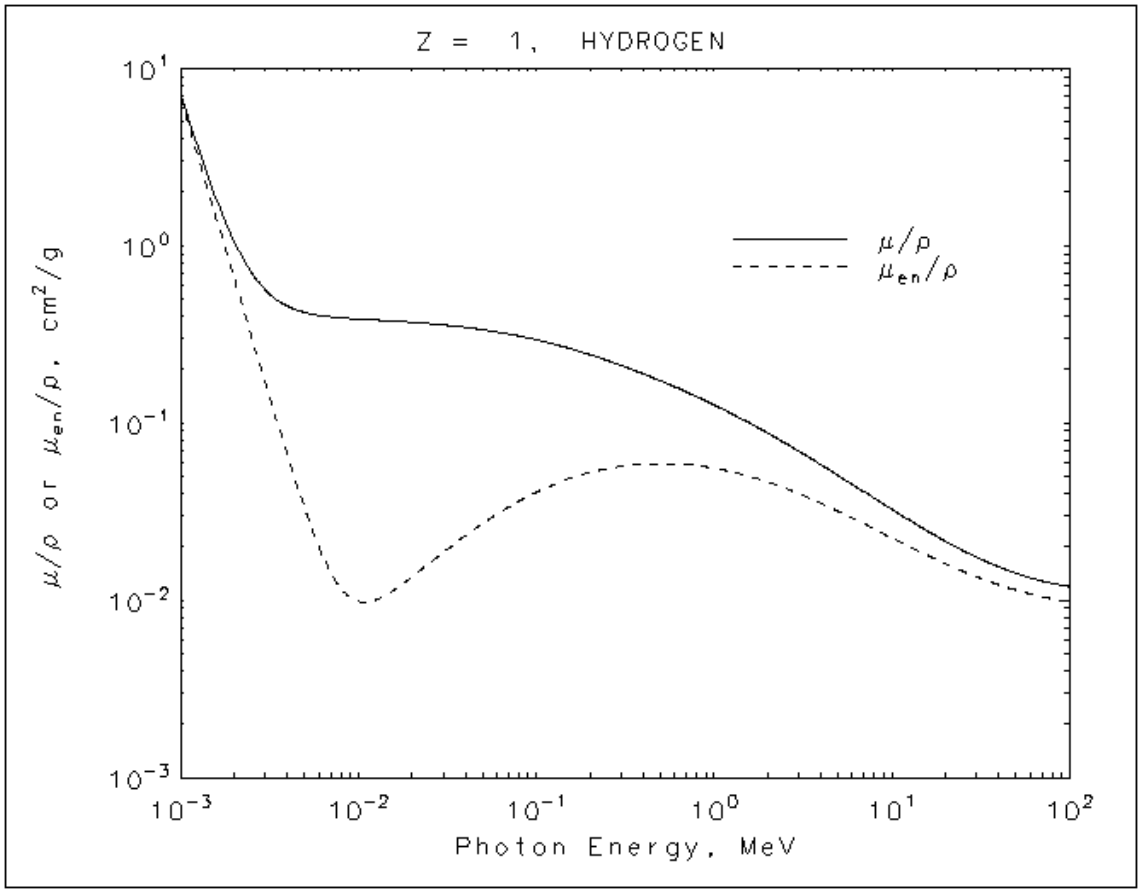

Figure 2.5: Mass and mass energy attenuation coefficient function of hydrogen [16]

The attainment of the mass and mass-energy attenuation coefficients as a function of incident energy has a further advantage for supporting experimental work as it is required in order to calculate the actual number of interactions that will occur from an exposure, rather than having values equivalent to a reference standard, such as water. It is also key in being able to relate any historical and future irradiative experiments, often undertaken using different sources, incident energies, dose rates and total doses, to the target radiological environment of a nuclear weapon. This is a key point, as without it, irradiations undertaken in radiological environments that differ from a nuclear weapon would be hard to relate, the determination for the mass and mass-energy attenuation coefficients as a function of energy is therefore highly desirable.

2.4.1 Theoretical determination of μ/ρ and μ_{en}/ρ

The theoretical determination of both the mass and mass-energy attenuation coefficients is actually reasonably simple and is based upon the published x-ray mass attenuation coefficients by the US National Institute of Standards and Technology (NIST) [17].

The published data consists of tables of data that detail the mass and mass-energy coefficients as a function of incident energy for atoms with atomic numbers ranging from z=1 (hydrogen) to z=92 (uranium). The data combines the various probabilities of an interaction occurring via one of the forementioned interactions (as well as some more specific reactions beyond the scope of this work) for each atom. If the molecular structure of a medium is known, then these tables can be utilised to calculate the required attenuation coefficients by simply summing the corresponding atomic attenuation coefficient, multiplied by its relative abundance within the molecule, i.e. in accordance with Equation 2.2.

$$\frac{\mu}{\rho} = \sum_i w_i (\frac{\mu}{\rho})_i \tag{2.2}$$

Where w_i is the weight fraction of the ith atomic constituent.

The linear mass and linear mass-energy coefficients can therefore be derived for a material of interest. This is achieved by iteratively calculating the mass and mass-energy calculations between 0.001 MeV and 20 MeV (the range in the tables); linear interpolation is used for calculations of values between explicit energies. The linear attenuation and linear-energy coefficients can then be calculated by multiplying the mass and mass-energy attenuation coefficients by the material density, as shown in Figure 2.6.

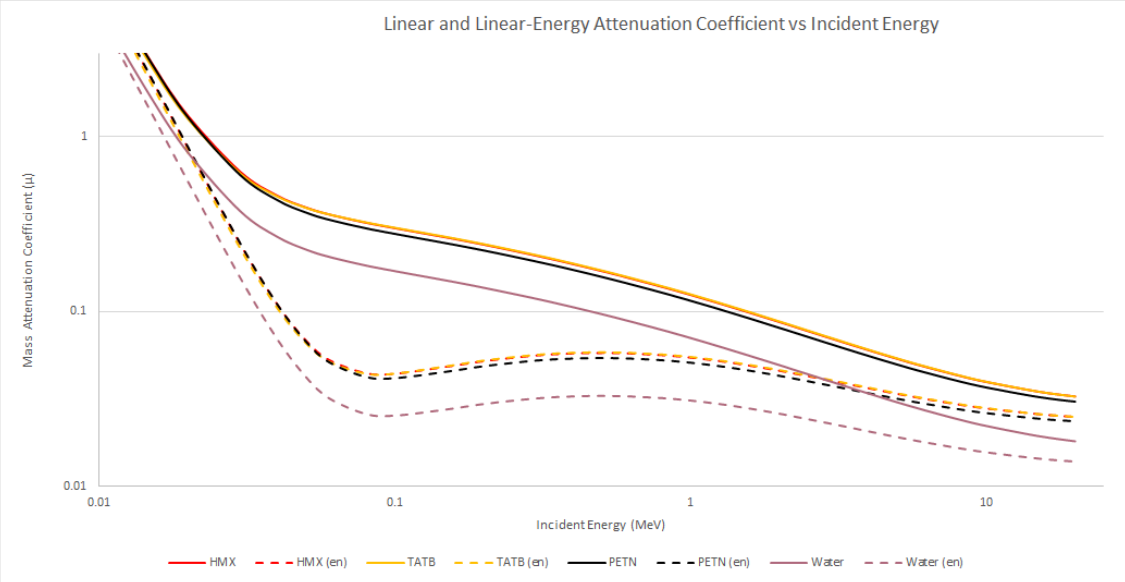

Figure 2.6: Linear and linear energy attenuations vs. energy for materials of interest

2.5 Likely physical effects of gamma radiation of explosives

From consideration of the physical effects of gamma radiation on organic explosive materials, it can be seen that the applicable reactions for gamma interactions are the Photoelectric effect, and most likely Compton scattering, both of which will cause ionisation and hence free radical formation. Pair production is deemed not relevant due to the comparatively low energy of the incident energy, and low proton number of the materials in question. The rate of ionic free radical formation will be proportional to the flux of incident radiation as well as the material properties (as described by the linear mass-energy attenuation coefficients). Generated free radical species are likely to be short lived intermediate states, with some being longer lived through mechanisms such as molecular resonance, mostly applicable for aromatic species, such as TATB [18].

Daughter product speciation resultant from ionisation is likely to follow various relax-

ation pathways as such radical species seek to relax to ground energy states. It is likely in cases where radicals are longer lived that relaxation will follow fewer, more specific pathways to daughter products, as the initial ionisation of a parent molecule will have time to relax to the most energetically favourable ground state radical, regardless of which electron is initially ejected from the molecule.

In molecules where radicals are very short lived, daughter product speciation may potentially be effected by the location of the ejected electron as molecular reactions may occur prior to the radical relaxing to a ground state. The probability of radical-radical coupling reactions will be more favourable for longer lived radicals that have been generated in high radiation flux environments, when compared to service levels, producing a comparatively higher density of radicals per unit time.

In order to assess the effect of radiation on these materials in a useful time frame, an increased level of gamma radiation flux will have to be utilised in order to accelerate the effect, compared to a typical environment experienced by these materials in a nuclear weapon application. This can be achieved one of two ways: exposure of these materials to a significantly increased mass of plutonium or uranium, relative to a nuclear weapon environment; or the exposure of these materials to other, more active gamma emitting source(s). Where other radiolytic sources are utilised, not only will the activity differ, but so will the incident energy. Emission spectra for plutonium and uranium, are towards the lower end of the energy spectra for gamma radiation, therefore utilisation of other sources is likely to result in a exposure to more energetic gamma quanta.

This presents a contradictory issue to using a more active source in that, as shown by the linear mass and mass-energy attenuation coefficient functions, the more energetic quanta are less likely to be absorbed, reducing the number of interactions, therefore a trade off is required. However, this point emphasises the usefulness of knowing the linear mass

and mass-energy attenuation coefficients as a function of incident energy, in that the number of interactions for varying incident energies can actually be equated/approximated, rather than being made equivalent to an arbitrary material such as water. Knowing this functional form also has significant advantages when evaluating pieces of literature which contains a significantly varied selection of different radiolytic environments and materials and allows trials to be undertaken using other radionuclides over large quantities of plutonium and uranium, which is somewhat hard to come by.

Having considered the process of which gamma radiation will interact with matter, it is necessary to undertake a comprehensive literature review to assess previous works that consider how such radiation interacts with energetic matter.

Chapter 3

Prior Art

Despite the comparatively niche research topic, there have been numerous studies covering the effect(s) that radiation exposure has on energetic materials. Perhaps unsurprisingly, the significant majority of published works correspond in time with the advent of nuclear weapons, when energetic materials were first being intimately placed alongside selected radionuclides. Consideration has been given in the published literature to a significantly varied selection of energetic materials and all major forms of radiation, including Alpha, Beta (Positive and Negative), Gamma, x-ray, neutron, electron as well as UV-Vis light. The aforementioned works detailed within this review focus on the energetic materials HMX, TATB, PETN as well as any close relatives, and their exposure to Gamma (and some x-ray) radiations. Even within this confined scope, a significantly varied selection of radiation environments exists, with materials being exposed to gamma radiations of energies and dose rates that vary by orders of magnitude. This variation presents difficulty in comparing results, however, the forementioned understanding of interactions of gamma radiation with matter and the associated mass-energy coefficient, help.

3.1 Previous studies on the irradiation of explosive materials

One of the first published works studying the effect of direct gamma radiation exposure to energetic materials, was a preliminary investigation between Los Alamos Scientific Laboratory, (now known as Los Alamos National Laboratory LANL)and Oak Ridge National Laboratory (ORNL) of the United States of America [19]. The study looked at exposing various explosives to a total (assumed gamma) dose of 86 kGy over ten days, although some neutron radiation was also present due to the use of activated Uranium as the radionuclide. The explosives selected for the study consisted of Tetryl, TNT, RDX and composition B [1]. Although the selected materials are not the same as those considered in this thesis, their interaction with gamma radiation is believed to be analogous as both aromatic compositions are similar to TATB and the RDX is an analogous nitroamine to HMX. The report did not find any evidence of a significant change in either physical appearance, gas evolution or melt temperature, indicating that the explosive materials had not been notably influenced by exposure to the radiation. A second study was reportedly [19] commissioned in parallel by Aberdeen Proving Ground, where a selection of various explosive formulations and mixtures, including TNT and Tetryl, were exposed to approximately 400 Gy of 1 MeV γ-rays. Findings were similar, in that no increase in sensitivity or change in thermal properties were recorded post irradiation. However, both studies were limited and were by no means comprehensive, likely due to the availability of analytical techniques as well as materials at the time.

Continuation of the research was reported in 1955 in conjunction with Picatinny Arsenal [20], where a technical report was commissioned despite the limited findings of the previous studies. This work focused on a similar selection of explosive materials, again including TNT, Tetryl and RDX, but also included PETN. However, irradiations were

[1] Composition B is mixture a 59.5 % RDX 39.5 % TNT and 1 % paraffin wax

achieved by neutron activated gold rods rather than Uranium fuel slugs. This change of radionuclide generated a significantly different incident gamma energy (410 keV), as well as emission of Beta (960 keV) radiation from the modified gold rods. Further complications arise from the comparatively short half life of the gold rods of 2.69 days, implying that the activity of the radiation environment would have changed significantly during the exposure, which lasted 90 days, resulting in a total dose of 2 MGy. This significantly non-linear activity would have likely affected results due to the differing levels of radical concentration through time. Specimens were held in bespoke glass ampoules which were deemed sufficient in blocking emitted Beta particles, allowing any material changes to be attributed to gamma radiation only; however, this was not confirmed. The ampoules were monitored during the irradiations for gas evolution whilst being held in vacuum to test stability. Conclusions were limited in the report, however the published gas evolution results for the various explosives provides an interesting insight into comparative radiation resistance. The amount of gas evolved for TNT and Tetryl was significantly lower than that of the nitroamine RDX and the nitro-ester PETN, possibly due to the purported radiation resistance of aromatic based compounds, due to resonance; this suggests that TATB could also be comparatively resistant. A notable difference was also observed between TNT and Tetryl as shown in Figure 3.1, suggesting that radiation resistance due to resonance through aromaticity is likely to be material specific, and in the case of Tetryl, likely to be attributed to the nitroamine group and its distance from the aromatic ring in Tetryl.

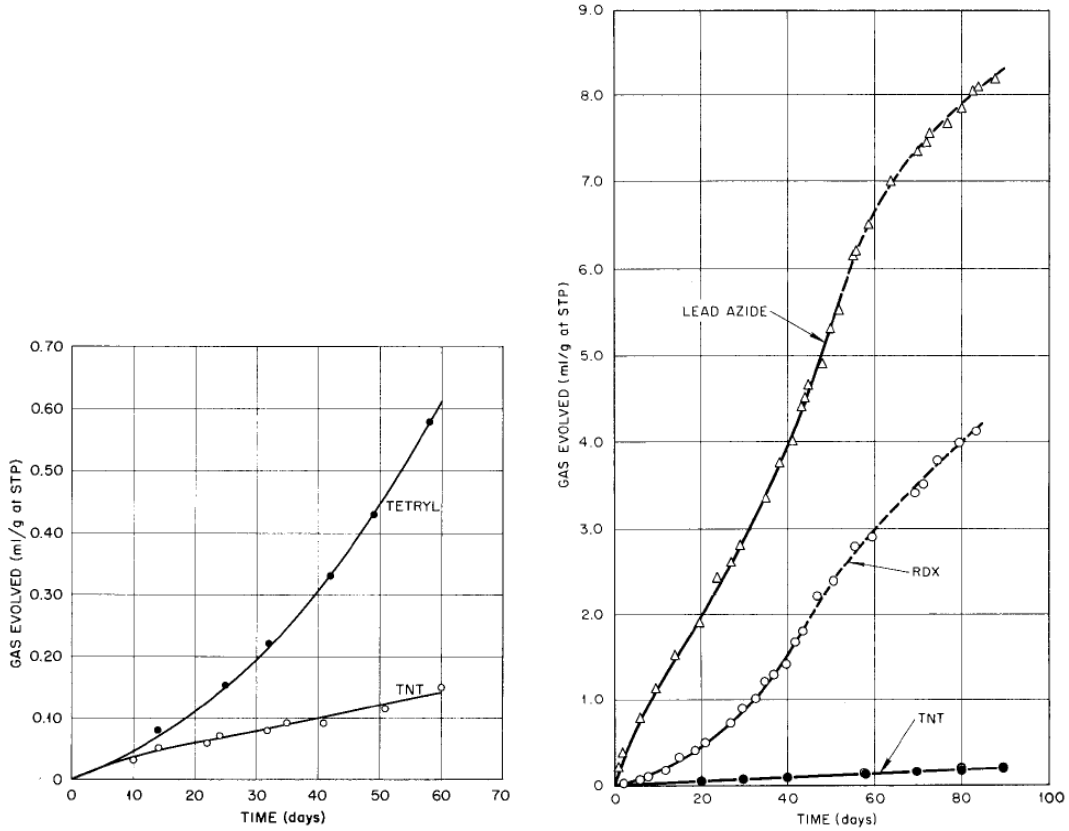

Figure 3.1: Gas evolution of RDX, TNT and Tetryl, reproduced from [20]

Changes in thermal properties were also measured for all materials with PETN showing the most significant difference of a 3.8°C decrease in melting point temperature that the researchers attributed to a radiolytic decomposition product, however this was not isolated or confirmed. It was also noted that the TNT samples changed colour after irradiation, darkening from their standard light yellow to a shade of brown; a similar change was also confirmed for Tetryl but appeared to be less dramatic. Again suggested radiolytic daughter products were not isolated or confirmed. A publication by Kaufman followed [21] which summarised the results found from the joint work and evaluated a general statement that *"the lower limit of γ-radiation dose at which decomposition could be detected under the conditions employed was $10^6 r$"* (approximately 10 kGy), and is most likely referring to the data from Lead Azide which released significant amounts of gas. In his review, Kaufman comments on the colour change exhibited by some of the energetic compounds used within the study with TNT being specifically mentioned, suggesting an

alteration to the molecule causing a change in the material's chromophore; however, no mechanism or daughter product is suggested.

Work continued at Picatinny Arsenal where a report was issued in April 1962 in conjunction with Brookhaven National Laboratory, which considered the effects of gamma radiation from a cobalt-60 source on five polymer bonded explosive formulations [22]. The reported work was not the first undertaken under this collaboration, as a preliminary study is referenced that considered the effect of gamma radiation on the Polymer Bonded Explosive (PBX) PBX9404[2]. Irradiations were carried out at rates of either 0.45 or 2 kGy hr^{-1}, up to a maximum total dose of 3.5 MGy; some irradiations were undertaken continuously whereas others were carried out incrementally, making comparisons of results difficult. Beyond the preliminary study, five HMX based formulations including PBX9404 were selected for the irradiation, each with differing polymeric binder systems. It is likely that these materials were investigated due to their potential use in nuclear weapons that were being developed at the time, although this is not confirmed in either report. If this assumption is accurate, then the selected radiation environment was significantly different than that expected within a weapon (i.e. dose rate, total dose and incident energy). The results focused on the physical changes on the materials as well as the effect on detonation velocity and on plate acceleration (further adding to the assumption of nuclear weapon use), however no identification of potential radiolytic daughter products through analytical techniques was attempted. Irradiating samples of PBX9404 resulted in embrittlement, with the irradiated material containing cracks and chips with a strong odour of NO_2 also being reported, however this is particularly subjective with no positive identification on the gas formed.

Later that year, Urizar et al (Los Alamos National Laboratory (LANL)) published his work on the irradiation of raw explosive materials [25]. This paper exposed TNT, Tetryl,

[2]PBX9404 - 94 % HMX, 2.9 % Nitrocellulose, 3 % tris-β chloroethylphosphate (CEF)) 0.1 % diphenylamine (DPA) [23, 24]

NC, RDX, HMX and PETN as well as four mixtures (PBX9404, PBX9010[3], PBX9407[4] and Composition-B) formulations to neutron and gamma radiations from enriched Uranium slugs within a power reactor. The irradiations consisted of a combination of a very high neutron flux coupled with gamma radiation, meaning that noted changes could not be solely attributed to either the interaction of gamma or neutrons. This is a significant draw back of the work in terms of its applicability to the effect of just gamma radiation, but it does further suggest that it was focused on nuclear weapons research. Irradiations were undertaken at two doses with dosimetry yielding approximate total gamma doses of 45 kGy and 2 MGy. Initial physical results were negligible for the lower dose sample, however significant differences were found for the higher dose, with TNT being notably discoloured from yellow to brown (in agreement with work undertaken in the previous decade [20]). The NC containing PBX9404 was also noted to have changed colour from blue to yellow, which was attributed to reactions of the stabiliser. Although no chemical analysis was undertaken to confirm, this was not reported in Mapes work [22], so could be due to the neutron radiation or the substantially different Gamma environment. Results were highly qualitative with reductions in density observed and gaseous products formed. Results offered little in terms of chemical identification of degradation products formed. The raw explosive materials showed little change at the lowest level of irradiation. HMX, PETN and NC showed significant susceptibility to gamma radiation when compared to that of TNT and Tetryl, again suggesting aromatic structures are much more resistant.

A couple of years later, Berberet [27] undertook a study on the irradiation of a selection of aromatic and heterocyclic explosive compounds including TNT, Tetryl, TNB, RDX and HMX under cobalt-60 to a maximum total dose of approximately 20 MGy. It was generally noted that the radiation stability of the aromatic compounds were “significantly greater” than the heterocyclic, a point which is in agreement with previous studies [20, 25]. Berberet acknowledged in his work that “of order” 99% of energy associ-

[3]PBX9010 - 90 % RDX, 10 % Kel-F Elastomer [24]
[4]PBX9407 - 94 % RDX and 6 % Exon 461 [26]

ated with an incident electromagnetic radiation is absorbed through electron perturbation methodologies, i.e. ionisation of atomic and molecular structures through Photoelectric or Compton phenomenon. His studies also considered the effect of fast nuclear electrons on the materials, i.e. the effect due to ejected electrons from a previous Compton interaction. The experimental set-up for Berberet's irradiations was different to previous works, with samples pressed into pellets and irradiated in ampoules which were sealed under Helium. It is thought that the specimens were placed under Helium due to the gas's known inert properties, however this inert characteristic is chemical in nature only and not physical. As such, a noble gas can be ionized under gamma radiation to form free radicals, thus potentially causing side reactions within the samples being irradiated.

The irradiation environment utilised for this work consisted of eight stainless steel canned cobalt-60 rods which, alongside the sample itself, were contained underwater. Two configurations were available with irradiations within the central tube yielding a dose rate of 90 kGy hr^{-1}, whilst irradiations undertaken in the outer tubes obtained a dose rate equivalent to 23 kGy hr^{-1}. Samples were irradiated to a variety of doses, ranging from approximately 200 kGy to 20 MGy, with analysis being undertaken in the form of weight loss and dimensional changes as a function of total dose and rate. The axial deformation of the heterocyclic compounds differed significantly with RDX crumbling at low doses, and HMX changing significantly; where the RDX measurements were successful, i.e. did not crumble, they exhibited a similar response to that shown by HMX at the same doses. Dimensional data from the HMX experiments is reproduced below in Figure 3.2, which specifically highlights the effect of dose rate, with the lower yielding the greatest observable effect. The axial dimension, however, remained significantly less effected for the aromatic compounds, with the cause again most likely due to the resonance induced stability of potential aromatic centred formed free radicals.

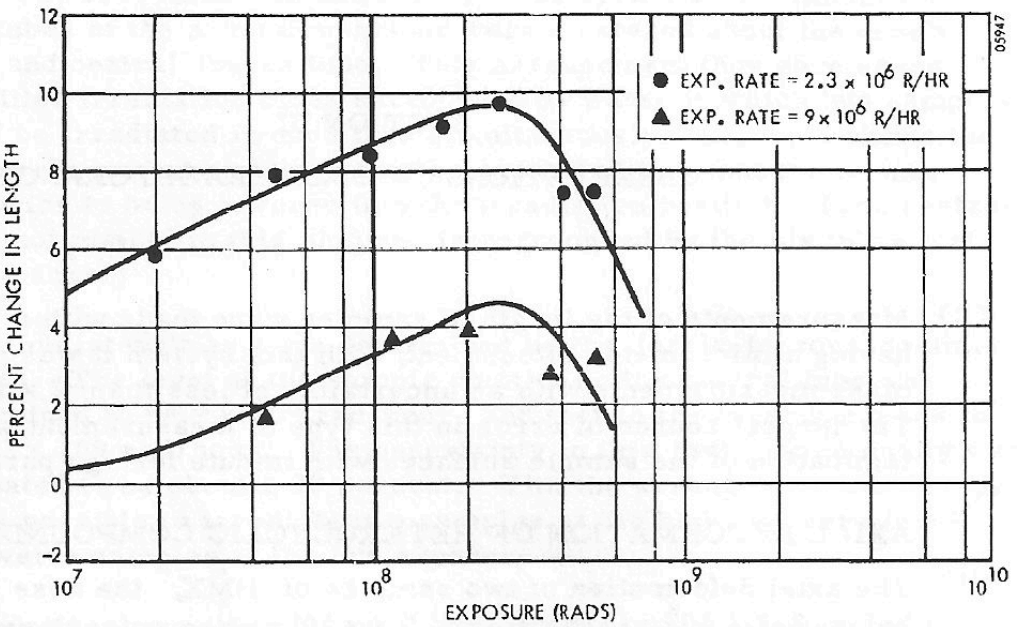

Figure 3.2: Axial dimension change of HMX exposed to cobalt-60, reproduced from [27]

The effect on the masses of the selected materials was also investigated, with the greatest effect being measured for the heterocyclic compound HMX. Unfortunately, measurements were not possible for RDX (with the exception of a couple at very low dose), due to prior noted loss of physical integrity for the pressed irradiated samples. It is noted that the successful low dose measurements of mass loss for RDX were in close agreement with HMX. The resultant mass loss as a function of total dose and rate have been reproduced from [27] below in Figure 3.3.

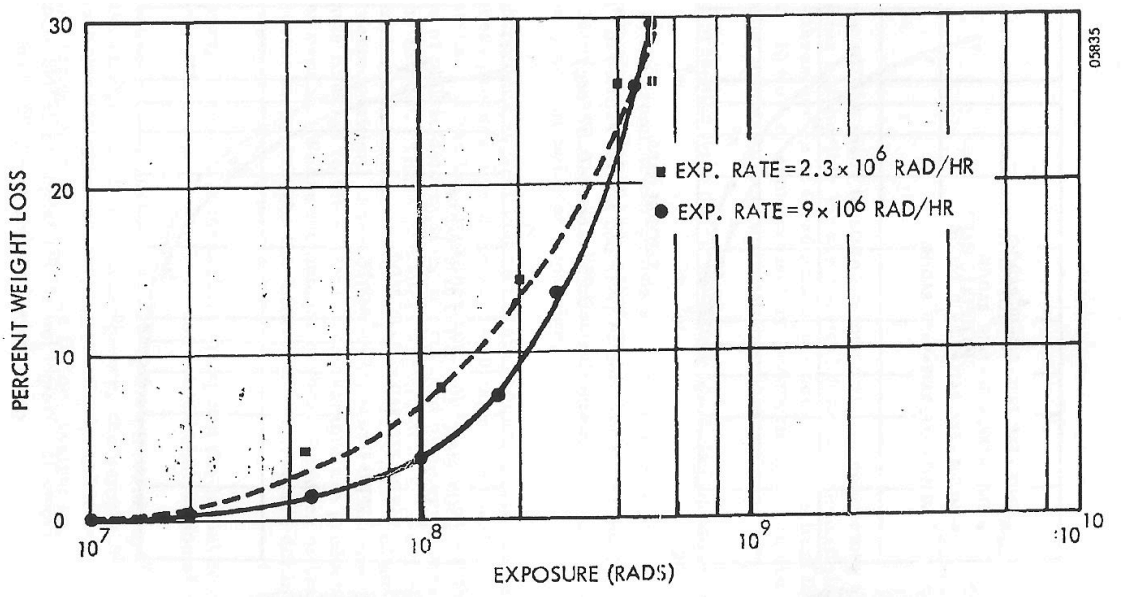

Figure 3.3: Mass loss of HMX exposed to cobalt-60, reproduced from [27]

The mass loss data for HMX shows a strong dependency on total dose but not on exposure rate, leading the author to suggest that the potential gaseous products formed within the material are done so at a rate which is lower than that of diffusion through the sample. Contrarily, within the experimental error there is an observable difference between the two dose rates, again with the lower yielding a greater difference. The report makes limited conclusions as to the mechanisms involved which cause the reported observables in both dimensional change and mass loss. The similarity in chemical make-up and observable results between HMX and RDX (albeit at low doses only) suggests a similar mechanism is responsible between the materials. One of the hypotheses made is that evolved gaseous species create areas of stress within the materials, causing a plastic deformation and hence the observed increase in dimension. The theoretical hypothesis continues with fissures which are created by this process, relieving built up pressures within the material causing contraction after certain total doses. The hypothesis is supported by the gathered experimental data for the heterocyclic compounds, however the data for some of the aromatic materials refutes this theory.

A second hypothesis is also presented where incident radiation causes a change in the crystal's polymorphic phase, which could potentially explain the contraction seen for some of the aromatic samples being irradiated. The author acknowledges that the theory is "very hypothetical" and has not taken into consideration other effects, such as radiation induced heating, yielding thermal expansion. However, the data shown from HMX would counter this suggestion as the lower dose causes a greater increase in dimension. Unfortunately, as the paper does not delve into any temperature measurements, coupled with the fact that samples were irradiated in different locations and that materials were potentially submerged during the irradiation which offers a large heat transfer, it makes explicit conclusions hard to draw. No additional information is available within the report, despite the high values of dose which were achieved. Hazard and performance analysis would have been highly desirable, however it is likely, as with most similar experimentation, that irradiated material was scarce, limiting additional testing.

The effect of gamma radiation on the surface activity of HMX in the gamma polymorphic phase was investigated by Castorina, et al in January 1968 [28]. The work describes measurements of surface area via Braunauer-Emmett-Teller (BET) methods and surface activity measurements by adsorption of Carbon-14 labelled stearyl-trimethyl-ammonium-bromide (STAB). Samples of HMX were irradiated in vacuum (one of the first examples), as well as under vapours of nitrous oxide, nitrogen dioxide and water, with all irradiations undertaken in a water bath closely monitored at 20°C $\pm$ 1°C. The surface activity of the samples of HMX which were irradiated increased when compared to a control sample and correlated with total dose. The phenomena is attributed to strong polar daughter groups/products of HMX being formed which purportedly increased the chemical bonding between the surface of HMX and the adjacent STAB molecules, however consideration that the surface of the HMX has become charged through ionisation is not made. An assumption is made within the work that, as the control HMX specimens are apparently non-porous to Nitrogen and Argon gas, interactions between HMX and the much larger

(when compared to the gases) STAB molecules are confined to the surface. However, if other mechanisms are to be considered, (such as the creation of gaseous fissures within the HMX crystals, as reported by Berberet [27]), it is possible that this would also increase the measured adsorption of STAB. Contrary to this argument, however, is that the measured surface areas of the irradiated HMX samples appeared to decrease with a difference of 22% being noted for the 640 kGy irradiated material.

A chemical analysis of head-space gases was also undertaken via mass spectroscopy (MS) from a selection of evacuate ampoules which contained HMX; these were irradiated to an equivalent total dose of 160 kGy at a rate of 10 kGy hr^{-1}. Samples were taken at three days post irradiation, with successive sampling undertaken at 4, 6, 10, 24 and 26 days to investigate whether off-gassing continued after irradiation; data has been reproduced in Figure 3.4 below.

Gaseous products	cm^3(gas) STP $\times$ 10^3/g HMX with post-irradiation time (days)						
	Control	3 days	4 days	6 days	10 days	24 days	36 days
H_2	0.004	4.3	5.0	5.9	6.0	4.0	3.3
CO		25.7	28.6	30.0	30.0	32.9	27.1
N_2	0.017	365.7	375.7	407.1	407.1	442.9	358.6
NO	0.023	91.4	88.6	111.4	111.4	121.4	111.4
N_2O		60.0	60.0	72.0	72.9	75.7	72.9
CO_2	0.051	35.7	38.6	47.1	47.1	61.4	55.7
Mass 52		0.6	0.6	0.7	0.8	0.8	0.7
Total	0.096	583.4	597.0	675.3	675.4	739.1	629.7

Figure 3.4: Gaseous products of HMX irradiated by cobalt-60 under vacuum to 160 kGy hr^{-1}, reproduced from [28]

The volumes and types of gas produced for irradiated HMX begin to identify potential degradation mechanisms with significant quantities of nitrogen gas being measured. In addition, various oxides of nitrogen and carbon are also recorded albeit at significantly reduced concentrations; very small quantities of hydrogen are also measured. There does not seem to be a significant change from successive measurements taken at increasing time intervals after irradiation, indicating that the production of gases does not appear to

be hindered by diffusion through the material. Water was also attempted to be measured under the same conditions, however due to the difficulty in quantification, measurements were omitted from results. In addition to the raw data presented in 3.4 at 160 kGy, a graph displaying the total amounts of gas formed at varying total doses is presented and reproduced in Figure 3.5. The graph shows that whilst other gases appear to be created as a linear function of total dose, nitrogen and carbon dioxide potentially could have a more complex relationship, assuming no atmospheric leakage occurs as the containers degrade.

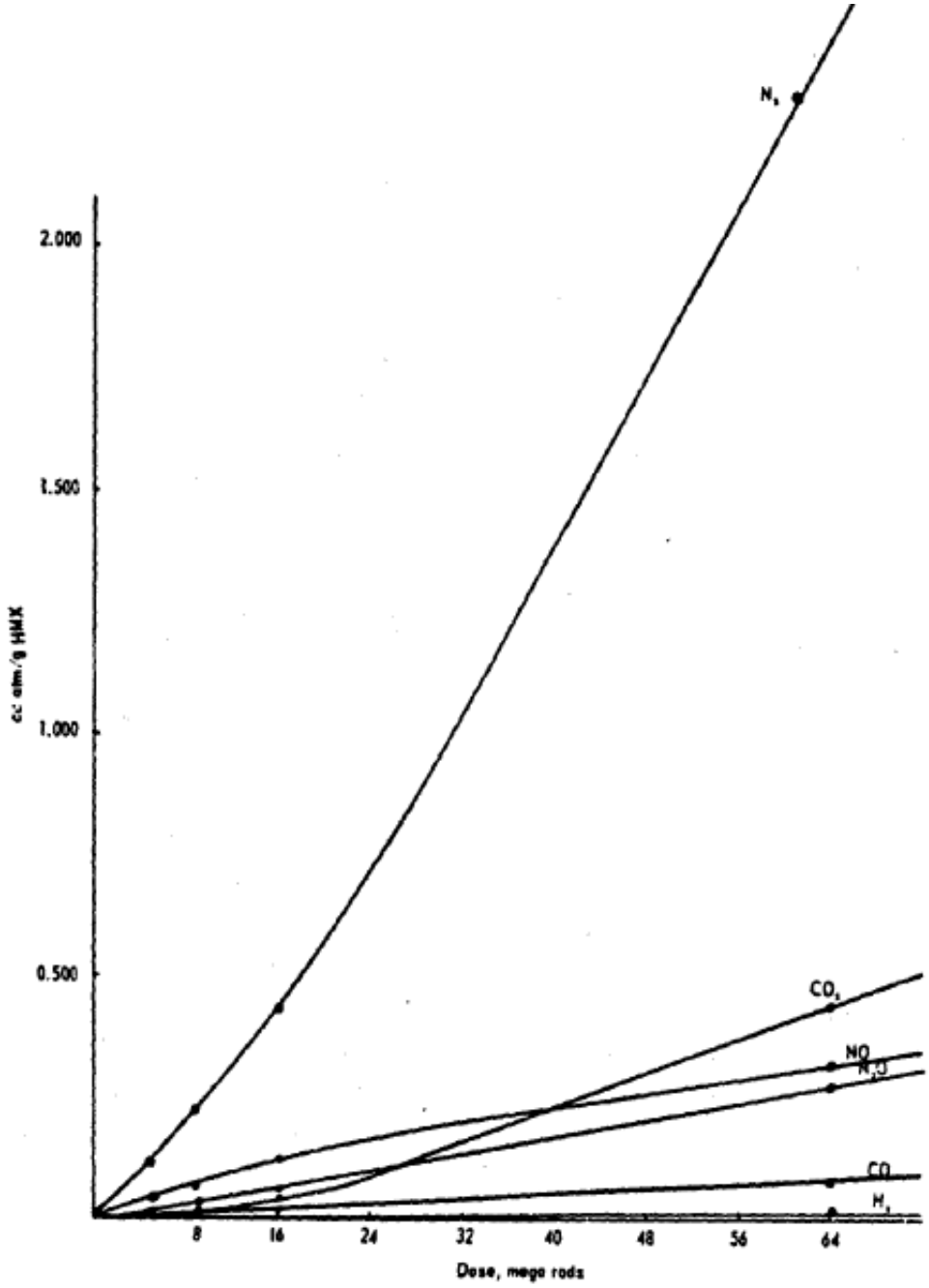

Figure 3.5: Gaseous products of HMX irradiated by cobalt-60 under vacuum as a function of total dose, reproduced from [28]

The research went further to consider the effects of radiation on HMX contained within various gaseous mixtures. This was undertaken to try and explain the lack of an effect from gamma radiation on the surface activity of HMX at low doses of 10 kGy. It was postulated that the observed increase of surface activity may be partially or solely attributed

to the presence of gases created from irradiation of HMX. Initial measurements of control samples of HMX in the presence of H_2O, NO and NO_2 did show a marked increase in surface activity, with no difference being measured once the mixtures were irradiated to 10 kGy. It was observed that mixtures of H_2O and HMX yielded the same gaseous degradation products under radiation as evacuated specimens, but in significantly greater concentrations. This is not unexpected as water was detected as a degradation product of HMX irradiated under vacuum, therefore the available water would increase with dose as would secondary reaction products, which suggests that the presence of water significantly enhances radiolytic decomposition of HMX.

The irradiation of water is known to produce numerous radical, ionic and oxidative species as shown by Byungjin et al [29]. It is therefore not surprising that, in Castorina's work [28], all detected gaseous daughter products were affected by the presence of water. This signifies one of two possibilities: 1) the random formation of numerous daughter products derived from irradiated water, may cause a variety of secondary reactions yielding an increase of all detectable gases; 2) one of the daughter products of water is rate determining, which causes the HMX molecule to undergo degradation yielding the recorded gaseous products. A third option potentially exists where the degradation of HMX in vacuum proceeds through a different mechanism when compared to HMX in the presence of H_2O. Unfortunately, as there are very few repeats and significant variability within the experimental data set, it is difficult to provide conclusions. However, the atmosphere in which materials are irradiated appear to be significant.

In December 1973, Louis Avrami et al, of Picatinny Arsenal, published one of his first pieces of work which is often cited in proceeding works [30]. His work considered several energetic material that were irradiated using cobalt-60 and focused upon quantifying the direct effect of the radiation primarily on the thermal stability, purity, sensitivity and explosive performance of the materials. Selected samples were irradiated to doses of almost

10 MGy, at a dose rate of approximately 8.8 kGy hr^{-1}. Samples selected for irradiation were prepared as both pressed pellets and loose powders, which were irradiated within quartz vials that were closed using glass wool and were subsequently placed within aluminium containment vessels to shield the cobalt-60 source from any potential damage resulting from an explosive event. The materials are assumed to be irradiated under atmospheric conditions due to the sealing method, however it is not confirmed within the work. This also does not provide any gaseous containment for daughter products which was shown by Castorina to be an important consideration, however this may have been deliberate. Numerous explosives were used in the study, of which HMX, PETN and TATB feature as well as other related materials. The general and overarching conclusion, which has been cited in several successive works, is an order of explosives in terms of their ability to withstand the effects of gamma radiation, as shown below.

$$\text{TACOT} \geq \text{TATB} \geq \text{DATB} \geq \text{HMX} \geq \text{Tetryl} \geq \text{TNB} \geq \text{TNT} \geq \text{RDX} \geq \text{PETN} \geq \text{NGu} \geq \text{BaN}_6$$

The ordering of these explosives is surprising upon consideration of the forementioned mechanisms, specifically aromatic resonance, with HMX purportedly offering more resistance to radiation than Tetryl, Trinitrobenzene (TNB) and Trinitrotoluene (TNT), a finding that does not agree with that of Urizar [25]. Consideration of the non aromatic species show a correlation of increasing resistance with increasing density, (acknowledging the exception of Barium azide, thought to be due to its highly stressed ionic molecular arrangement). This correlation is contrary to that which is expected as such high energy gamma rays (1.17 and 1.33 MeV) should be indiscriminate in their ionisation location and, as shown by the mass-energy coefficient, higher density should correlate to a greater absorbed total dose, i.e. more decomposition reactions.

The dimensional change in the materials was recorded as a function of total dose which allows for a comparison to the work undertaken by Berberet [27]. Unfortunately, as with

the majority of literature available, direct comparisons are difficult as experimental conditions are often dissimilar. The reported dimensional change in Avrami's work is approximately 1.2% for HMX which compares poorly to the 8% from Berberet. Avrami quotes a dose rate for these experiments (assumed equivalent to water) of around 7 kGy hr^{-1} to his total dose of 1.14 MGy, which compares poorly to Berberet's 23 kGy hr^{-1} but well to total dose of 1 MGy. The difference in total dose can be considered negligible, however the dose rate cannot. Furthermore, consideration of Berberet's work, which showed for HMX that an increase in dose rate tended to reduce any change in dimension, signifies a contradiction of the findings between the works. The differences between the respective experimental set-ups are too significant to make meaningful critical comparisons, for instance sample size, pressing conditions and irradiative environments. A very similar situation arises upon consideration of mass loss data between Avrami and Berberet, with 1% and 7% being recorded respectively. Similar deviations between dimension change and mass loss can be observed between both authors for a selection of other materials such as TNT and DATB, suggesting that it is not material specific, but more likely experimental set-up differences.

Results from varying total doses on the vacuum stability of TATB, HMX and PETN were notable with some recorded spontaneous deflagrations, mass loss was also significant, especially for PETN at the higher total doses. Changes in thermal properties of HMX and PETN were notable, specifically a large reduction in the onset temperature of the first endotherm and changes to melt temperatures and profiles. This could be due to a phase change, but the report does not comment. Values tend to fluctuate at various total doses which may perhaps be attributed to the rather high heating rate of 20°C per minute. Despite this, the main exothermic peaks for HMX and TATB appear to be sharp and clean with no evidence of daughter/secondary products until approximately 9 MGy irradiations, where HMX showed a notable change in phase transition and exothermic behaviour. The thermal behaviour of PETN appears to be much more susceptible to radiation as shown

in the comparative thermograms that have been reproduced below in Figures 3.6, 3.7 and 3.8 respectively.

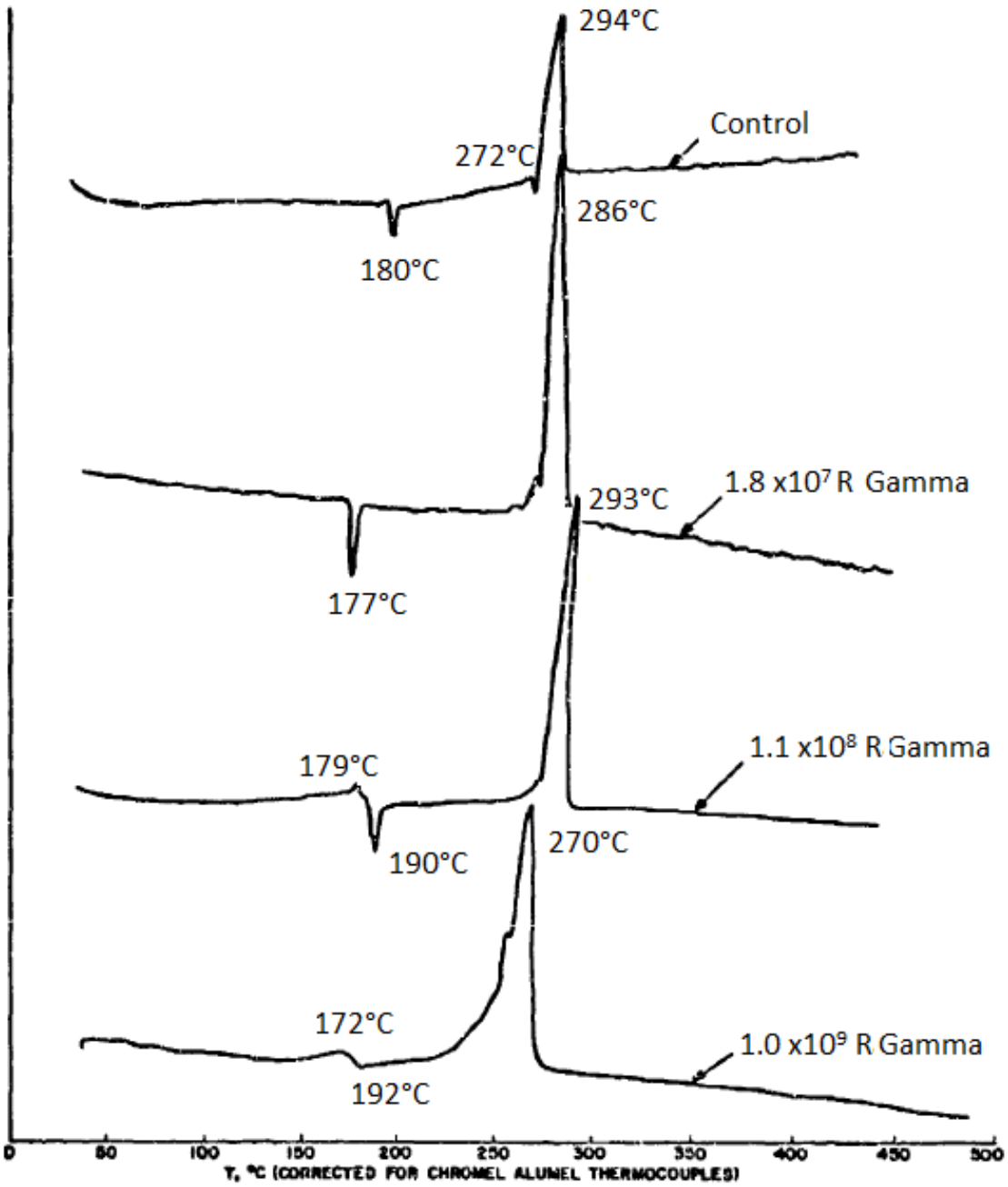

Figure 3.6: Thermograms of HMX, reproduced from [30]

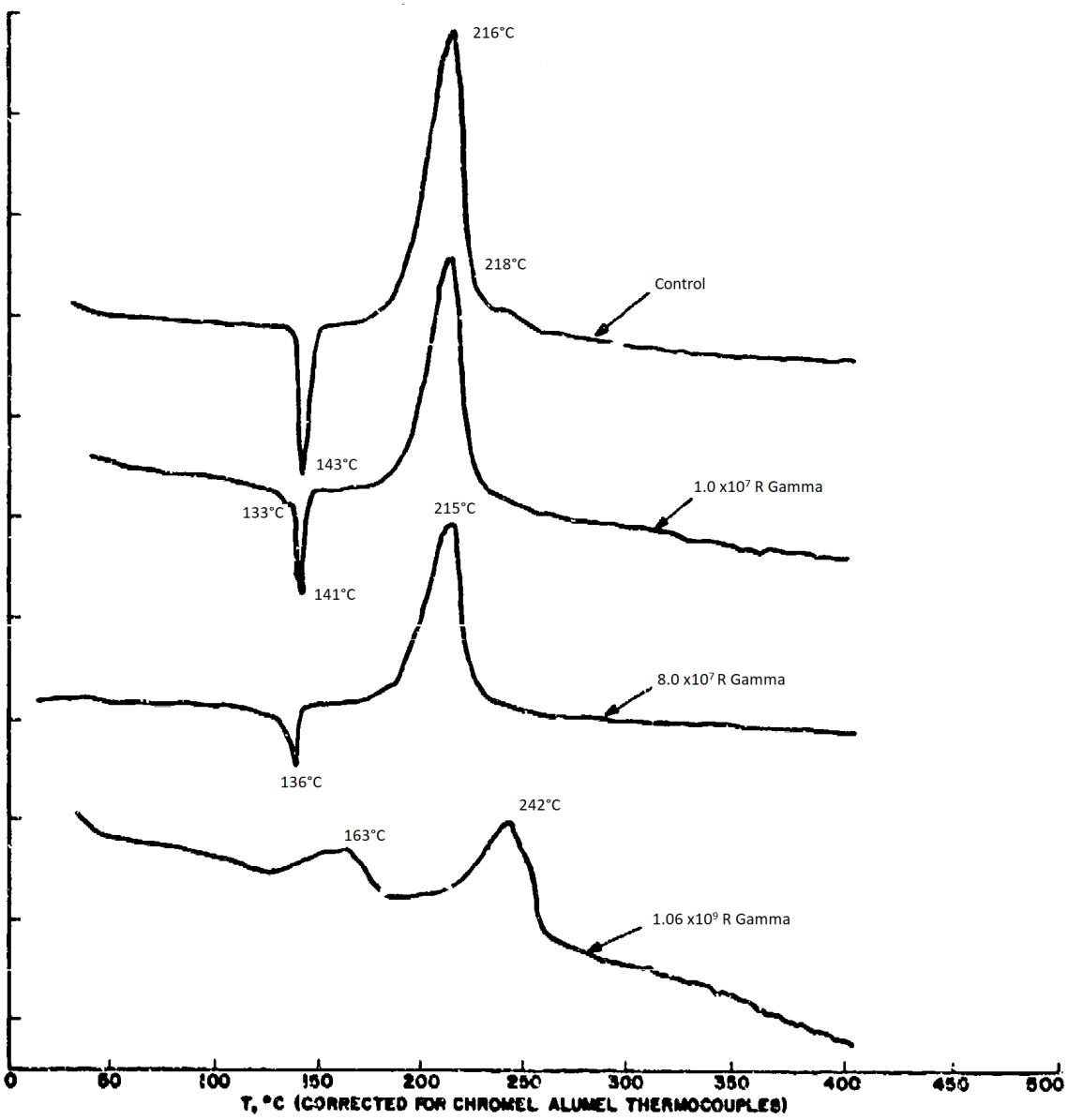

Figure 3.7: Thermograms of PETN, reproduced from [30]

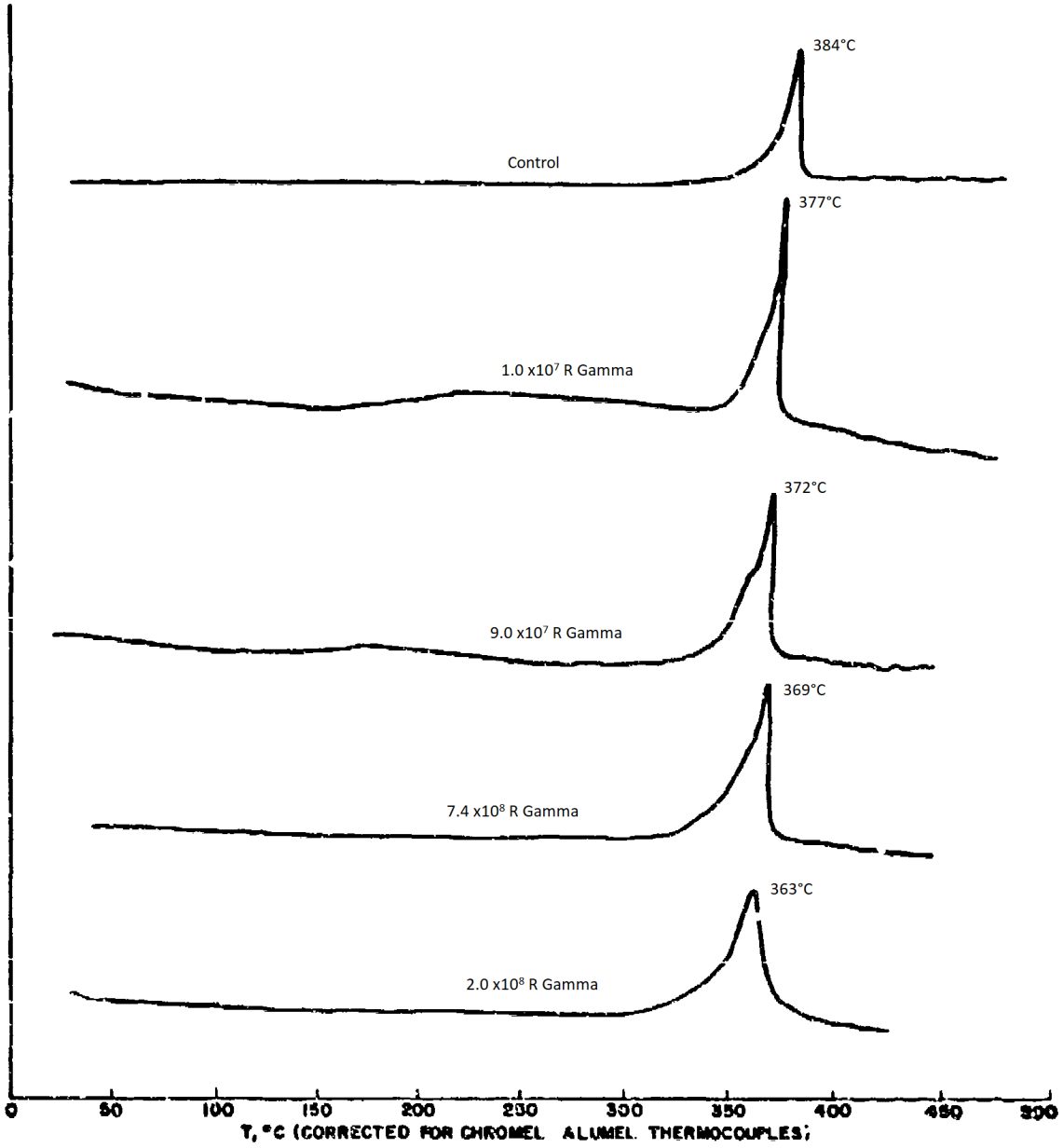

Figure 3.8: Thermograms of TATB, reproduced from [30]

Impact sensitivity appeared to be significantly effected by exposure to gamma radiation. In particular, HMX with values of impact (US Fall Hammer) reduced from a control height of 14.04 to 11.04 inches for the 114 kGy dose; this reduced further to 8.96 for 1 MGy. These are significant differences in impact sensitivity, however as shown by the thermograms, no daughter products or significant deviations are detectable. A possibility may be that the gamma radiation is causing a phase change within the HMX crystals to a

more impact sensitive variant such as alpha. This could potentially explain the difference in the initial endotherm. However, with limited repeats and such a high temperature ramp rate, it is difficult to draw solid conclusions. A further potential cause may be the evolution of gases causing fissures within the crystals which would not show up on thermograms, but could explain the increased impact sensitiveness, however this is not commented upon within the work.

Avrami continued his work in conjunction with Henry [31] as to the effect of low level gamma radiation from cobalt-60. The total dose was obtained at a rate of 2 Gy hr^{-1} (significantly lower than his previous work) over a maximum exposure of 150 Days; this equates to approximately 7 kGy. These low level long duration exposures were designed to mimic several of those undertaken by Piantanida and Piazzia [32] which showed negligible changes to the materials even after long term ageing, post irradiation. Avrami selected RDX, HMX, mixtures of the two at 9:1, 1:1 and 1:9 ratios respectively, and composition B for his second study. Samples appeared to be sealed using a different mechanism when compared to Avrami's earlier work as ampoules were equipped with hand-tightened end caps. In keeping with his previous work and that of Piantanida and Piazzia, samples were irradiated under ambient i.e. non-evacuated conditions, with it being noted in the report that high humidity was prevalent at the time. Results obtained by Avrami were in agreement with those of Piantanida and Piazzia, with the general conclusions that *"long term low-level gamma irradiation had no significant effect on the thermal stability thermal and impact sensitivities of RDX, HMX, selected mixtures and Comp B"*. Despite this statement, there were observable differences in the thermal properties of some materials and a possible difference in the impact sensitivities, albeit within experimental error. The endotherms, which can be attributed to delta polymorphic phase change and the crystalline melt prior to decomposition, for the HMX samples appear to increase in onset and peak temperatures as did the main decomposition exotherm by values between 5 to 15 degrees, indicating a potential effect; such effects were not seen in samples exposed to

the lowest dose.

It is noted within Avrami's work, through private communication with E.D. Loughran, that he had detected a small exotherm that was observed prior to the endotherm attributed to the HMX β to δ polymorphic change. It is acknowledged that a similar exotherm was detected by Urizar [25] during his gamma and neutron irradiations of RDX and HMX. A general conclusion hypothesised that this exotherm could potentially be the decomposition of a HMX derived daughter product or the potential escape of trapped gas evolved from decomposition. In keeping with his previous work, Avrami ran the DTA experiments at a rate of 20°C/min, which is very fast compared to modern standards of 2°C/min [33] for such a test, and may be responsible for some of the differences in various data sets.

In 1980 Avrami published a review on radiation effects of Explosive, Propellant and Pyrotechnic materials [34]. The review holds a quote which summarises the general findings to date regarding the exposure of such materials to gamma radiation; *"Steady-state γ-radiation of any expl[osive] has not been known to initiate a detonation. The effect of such irradiation appears to result in slow decomposition with a deterioration in the functional properties of the expl[osive], or more generally energetic materials"*.

The effect of gamma radiation on the shock initiation sensitivity of single PETN crystals was investigated by J.J. Dick at Los Alamos National Laboratory in mid-1982 [35]. The crystals of PETN were subjected to total doses up to 10 kGy from a cobalt-60 source, a marked reduction compared to the majority of previous studies. The sensitivity to gamma irradiation was measured by differences in run to detonation distances with 10 kGy reportedly shortening baseline values by up to 40%. A threshold of 6 kGy was determined to be the maximum dose PETN crystals can receive before detectable changes in shock sensitisation occurs. This is orders of magnitude lower in terms of total dose compared to previous works, where measurable effects had been attributed to gamma exposure.

Optical microscopy was undertaken resulting in the observation of fissures, purportedly formed through gaseous molecule generation, within the crystal of order 10 μm suggested from decomposition of the PETN which is in agreement with [27]. Unfortunately, no additional testing was carried out on the irradiated material such as thermal, hazard or chemical characterisation, which may have further indicated an effect. It is noted in the work that the irradiated crystal remained perfectly translucent and there was a notable yellowing of which Miles et al [36] theorised NO_2 radicals were the cause. It is observed in the work that the yellowing reduced over a period of days, signifying that the radicals had decayed. Once the yellowing had subsided, the run to detonation values remained unchanged, signifying that the presence of radicals was not the cause and that the effect was permanent.

Miles and DeVries undertook a study considering free radical generation in RDX and HMX by both mechanical and irradiative methods [36]. Generation of free radicals through the application of mechanical stress was unsuccessful, however radicals were generated and confirmed by electron spin resonance (ESR) for samples exposed to gamma irradiation, undertaken in sub-ambient conditions in an effort to freeze in the radicals allowing time for detection. The source used in this work was Caesium, most likely the 137 AMU isotope, up to a total dose of 100 kGy, however dose rate was not detailed. Explosive samples were contained within sealed quartz tubes which were evacuated prior to irradiations; likely selected for ease of subsequent analysis in the ESR, spectra were successfully generated for HMX and RDX. Although there is no attempt to try and model the spectra using computational methods, the almost identical spectra observed in the RDX and HMX samples were attributed to NO_2 radicals, from comparison with literature. Due to the similarity in spectra, it was concluded that there existed a common dominant radical between the two materials upon gamma irradiation, this is not surprising considering the similarities in chemical structure, and the gamma energy emitted (assumed to be 660 keV). Work was undertaken on the effect of annealing on concentrations of radicals

for irradiated materials. Samples which were irradiated at sub-ambient conditions were transferred quickly and measured within the ESR, samples were then warmed to room temperature with subsequent measurements undertaken. It was noted that the HMX radical was more stable than that of the RDX, however radicals generated were reactive even at low temperatures in the presence of binders.

One of the most pertinent points made in this paper is the reported significant increase in sensitivity of both the gamma irradiated RDX and HMX. The statement, which often gets reproduced in later works of *"we encountered frequent accidents wherein irradiated HMX and RDX crystalline powders spontaneously exploded"*, indicates a significant change in the material's behaviour. Such accidents were typically observed when sub-ambient samples of HMX were taken from liquid nitrogen dewars and allowed to warm, resultantly the sudden activity of radicals upon warming was initially attributed as the root cause. In addition to these "accidents" the authors undertook some sensitivity testing of irradiated HMX samples and found a *"marked increase in the sensitivity of HMX to impact when irradiated in vacuum"*. Only impact testing was undertaken, no additional information into the effects of gamma radiation on other hazard properties, such as temperature of ignition or spark sensitivity, are available from this work. The initial investigation was limited in its conclusion, suggesting it was the sudden activity of the radicals that caused the explosions, however later work [37] which focused on the change in impact sensitivity of gamma irradiated HMX, suggested that it was more likely due to physical defects within the material and not the concentration and sudden annealing of the NO_2 radicals. The reported change in impact sensitiveness is much more apparent from Miles' work when compared to that of Avrami, where HMX showed a only a slight change in impact sensitiveness at an equivalent total dose of 130 kGy, further signifying that incident energy, dose rates and gaseous environment must have a significant impact. Miles and DeVries also acknowledge in their initial work that the detected NO_2 radical was not likely to be the initially generated, but chain terminating radical due to the in-

evitable period of increased temperature when exchanging samples from their radiation source and ESR equipment.

Miles and DeVries's second work focused on increased sensitivity and studied irradiated HMX powder at both ambient and sub-ambient conditions. Samples were reportedly irradiated to 75 kGy, i.e. 75% of that undertaken in their previous work, and were reportedly irradiated under vacuum and ambient atmospheric conditions. The sub-ambient vacuum irradiated samples suffered the same notable increased sensitiveness, with some spontaneously exploding. However, for samples which were not evacuated but still irradiated at sub-ambient conditions, i.e. with atmospheric gases present, the marked increase in sensitiveness was not apparent, as show in Figure 3.9, where F is the explosion frequency. There is a noted *"modest increase in sensitivity for HMX irradiated at room temperature"* whilst in the presence of atmospheric gases, however results are close to a baseline measurement, especially when considering the scatter. Miles and DeVries' conclusions are limited and although they identify a possible link between increased sensitiveness and vacuum irradiations potentially due to a lack of Oxygen and subsequent peroxy radicals, they acknowledge that they did not undertake irradiations at room temperature in vacuum to confirm this finding to rule out the effect of low temperature.

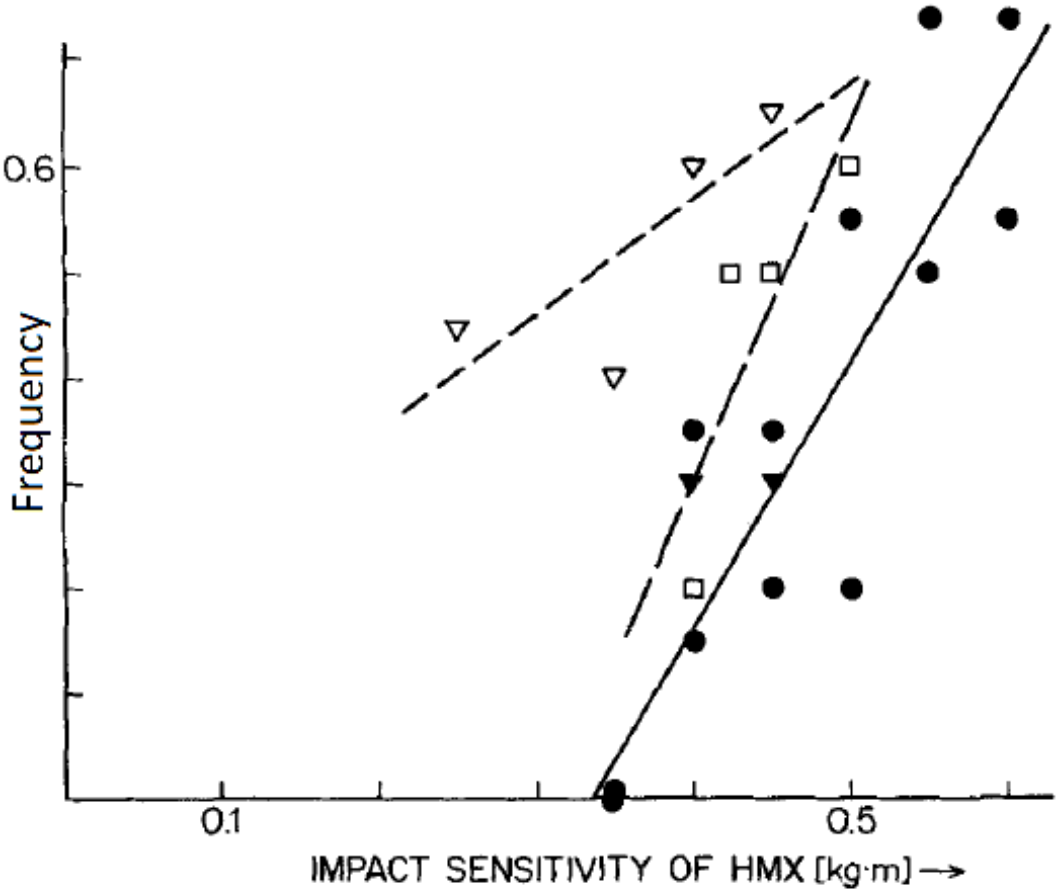

● As received HMX; ❑ Room temperature atmosphere pressure irradiation; ▽ Vacuum liquid nitrogen irradiation; ▼ Atmosphere pressure liquid nitrogen irradiation.

Figure 3.9: Impact sensitivity at room temperature, reproduced from [37]

In order to test the theory from their previous work that the spontaneous detonations and increase in sensitiveness was due to the accumulation of free radical species, the sensitivity to impact was measured for sub-ambient vacuum irradiated HMX, which was stored for a period of weeks then subsequently annealed at 50°C in warm water for several hours to remove all radical species. Specimens were analysed using ESR to confirm that all radical species had been removed. Impact testing was carried out and data compared against a suitable baseline of HMX samples irradiated under vacuum and sub ambient conditions. A comparison of the data obtained, as shown in Figure 3.10, shows a negligible difference

between the materials.

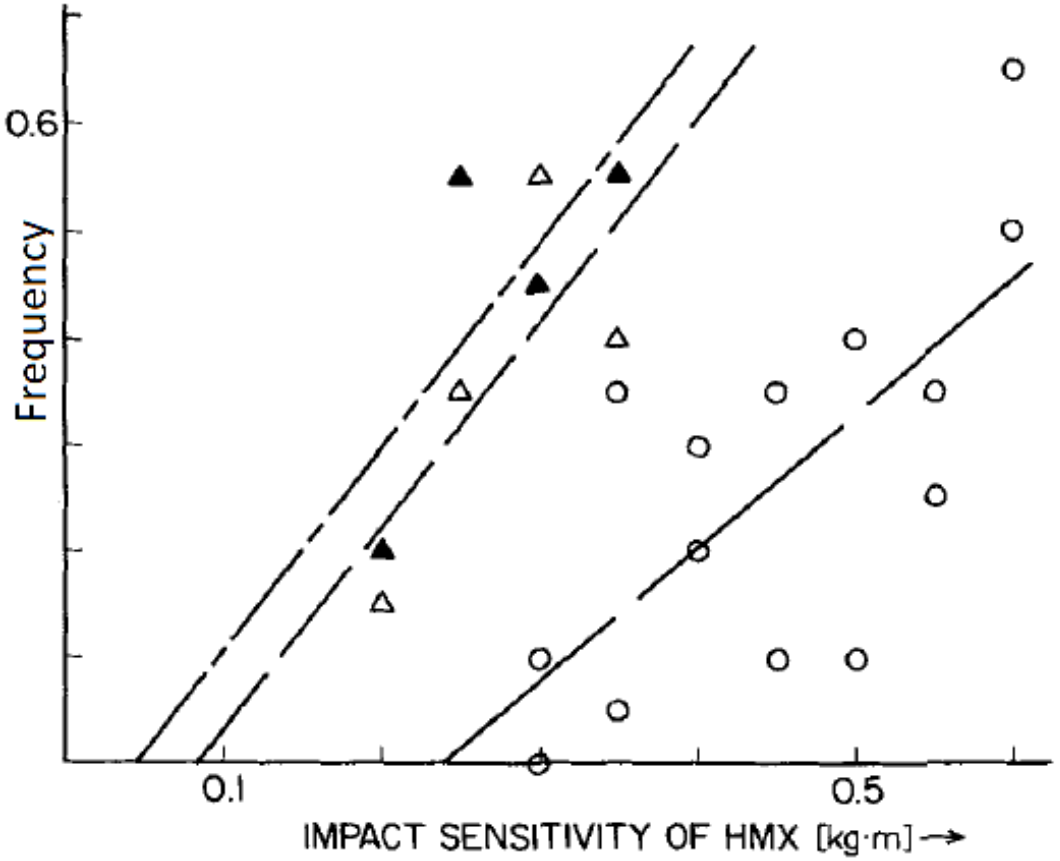

○ As received HMX; △ Vacuum liquid nitrogen irradiation impacted with frozen-in γ-radicals; ▲ Vacuum liquid nitrogen irratiation impacted with γ-radicals removed by annealing.

Figure 3.10: Impact sensitiveness at Sub-Ambient Conditions [37]

This result essentially signifies that the alteration to hazard properties of HMX under these conditions cannot be attributed, as previously thought, to an accumulation of radicals, but to a fundamental and apparently permanent change to the material. Despite this conclusive work, it is unfortunate that Miles et al did not investigate this effect at room temperature to determine whether this change in sensitiveness is isolated to sub-ambient conditions alone. Additional analysis techniques would have been especially useful on irradiated materials, such as microscopy to confirm if gaseous fissures had been generated which may be the cause of the increased sensitiveness, or other chemical characterisation

in an effort to identify potential daughter products.

Miles and DeVries furthered their research into the effects of gamma radiation on explosive materials by investigating the effects of such radiations on PETN [38]. Contrary to their previous work, samples of PETN were irradiated only to 20 kGy, however in keeping with previous work, samples were irradiated under vacuum and in sub-ambient conditions. ESR spectra were obtained for PETN which suggested, as with RDX and HMX, the presence of the long lived and likely chain terminating NO_2 radical. However, a significant difference in spectra was noted for samples of PETN immediately after irradiations, with spectra decaying to those observed for HMX and RDX after a matter of hours. The initial spectra were attributed to a short lived unstable radical which formed before the chain terminating NO_2 radical.

The radiation sensitivity of Nitrotriazolone (NTO) was investigated by Beard et al in 1989 [39], but also considered the explosives TATB, RDX and HMX. Although the work mainly focuses on the effects of x-ray and UV sources, the results are still relevant. The work concluded that the radiation sensitivity of the explosives in order of most sensitive proceeds as RDX; HMX; NTO; TATB, with the response of RDX and HMX being noted as very similar, again most likely due to their analogous chemistry. The work does not offer any analysis of the gamma radiation sensitivity of the materials, which is disappointing considering its title. However, the work does suggest decomposition products, which is more than some previous studies. Consideration of the most likely mechanism, non-ionic photo-dissociation, suggests a rearrangement and the paper informs of three possible degradation products including a nitroso-based derivative as potential candidates for NTO daughter products.

The sensitivity of RDX to x-ray radiation, including hypothesised decomposition reaction pathways, was presented by Beard in 1991 [40]. In his work, RDX was exposed to

x-rays with resultant photoelectrons being analysed using an x-ray photoelectron spectrometer (XPS) resulting in the potential identification of daughter products formed at both room temperature and -50°C. The rate employed was significantly greater than previous research at approximately 300 kGy hr^{-1}. Temperature rises were detected within the irradiated material with a 12°C increase being measured for the maximum eleven hour irradiation equivalent to 3.3 MGy. It was reported that thermally unstable and volatile products were formed at low temperature irradiations, with residual gases being analysed by the warming of degradation products from -50°C to room temperature. The identification of a nitrite ester intermediary was hypothesised (sub-ambient only) along with nitroso and triazine derivatives.

One of the major differences between x-ray and gamma rays is their ability to penetrate materials prior to interaction; any x-ray damage deposited into the materials would likely be confined to the surface. This fact is also valid when measurement of daughter product XPS spectra was undertaken, this technique is constrained to the surface of exposed materials for identical reasons. Beard acknowledges this and notes that the technique is limited to approximately the first 5 nanometres (nm) of a sample. Samples of claimed high purity were ground and spread as a thin film onto an adhesive tape prior to exposure and subsequent analysis. Exposures were undertaken in the presence of atmosphere, implying that interactions of free radicals with atmospheric bodies such as Oxygen were likely, this too is acknowledged in that the Nitrogen chemistries of the decomposition were the focus. Unfortunately as shown by Miles [36, 37, 38] the presence of atmosphere significantly alters the resultant products being formed and most likely the degradation pathway.

The percentage loss of nitrogen (NO_2), was measured as a function of total dose at both room and sub-ambient temperatures. This shows that at room temperature over 90% of the nitrogen has been lost at total doses of approximately 3 MGy. This result, however, is in disagreement with previous research which considered gamma radiation [21, 30, 35, 36]

at similar total doses, where the materials were still very much energetic and therefore nitrogen containing. It is most likely that this discrepancy is due to the difference in the penetrating ability of x-rays vs. gamma rays. Beard's work does imply that gaseous decomposition products are expected (and for gamma more likely within the crystal vs the surface, due to this more penetrating ability), giving theories of internal fissures and/or cracking of HMX and RDX pellets exposed to gamma radiation, more weight.

Beard does comment on the overall effect of radiation dose on the physical and explosive properties of relevant materials and makes comparisons to Avrami's work in 1973 [30], but rather than suggest that it is the generation of gaseous products which causes the physical integrity to fall for RDX, he suggests it is the loss of NO_2 from the bulk material and resultant loss of hydrogen bonding which causes the change. This argument is questionable due to the previous point regarding the explosive properties of such materials; if the material were 80% depleted of Nitrogen, the explosive properties would be significantly hindered, which is not apparent. Beard also attributes Avrami's measured increases in impact sensitivity to the presence of hypothesised daughter products, rather than gaseous fissures. This is a valid argument, however the presence of daughter products if in a high enough concentration to sensitise, should have altered the thermographs from Avrami's DTA experiments, acknowledging the high heating rate.

Residual gas analysis of RDX irradiated at -50°C was undertaken by allowing the sample to warm to room temperature and analysing gases through mass spectrometry. Results signified typical gases evolution for these products of water, and oxides of carbon and nitrogen. It was noted that the presence of NO_2 and HONO (Nitrous acid) was absent from the measurements. Unfortunately, gas analysis of samples irradiated at room temperature were not undertaken so these results can only be assumed to be valid in sub-ambient conditions.

Based on the XPS and gas analysis data, Beard hypothesised a selection of routes to which RDX, and by association HMX, may undergo radiolytic degradation. This is reproduced in Figure 3.11. The initial and most likely rate determining step is the scission of the N-N bond. Subsequent reactions are then hypothesised based upon the XPS and mass spectrometry as well as evidence available in the literature, mostly derived from combustion of RDX which is a notably different mechanism. This basis for such a hypothesis is questionable as no NO_2 gas was detected in the mass spectrometry. Furthermore, the hypothesised presence of nitrous oxide was not detected using the gas analysis. The sampling of these gases, if generated on the surface only, will be difficult. In the case of gamma radiation, if these degradation pathways are valid, gases may become trapped inside crystals and be easier to sample (assuming a low rate of diffusion). The presence of the nitrite ester was only confirmed at sub-ambient conditions which was attributed to the low bond energy and suggested thermolysis to an oxidised ring oxygen. Results indicating the presence of a nitroso compound are discredited by the loss of corresponding XPS signals upon warming to room temperature, with the acknowledgement from Beard that nitroso-derivatives are known to be stable at room temperature.

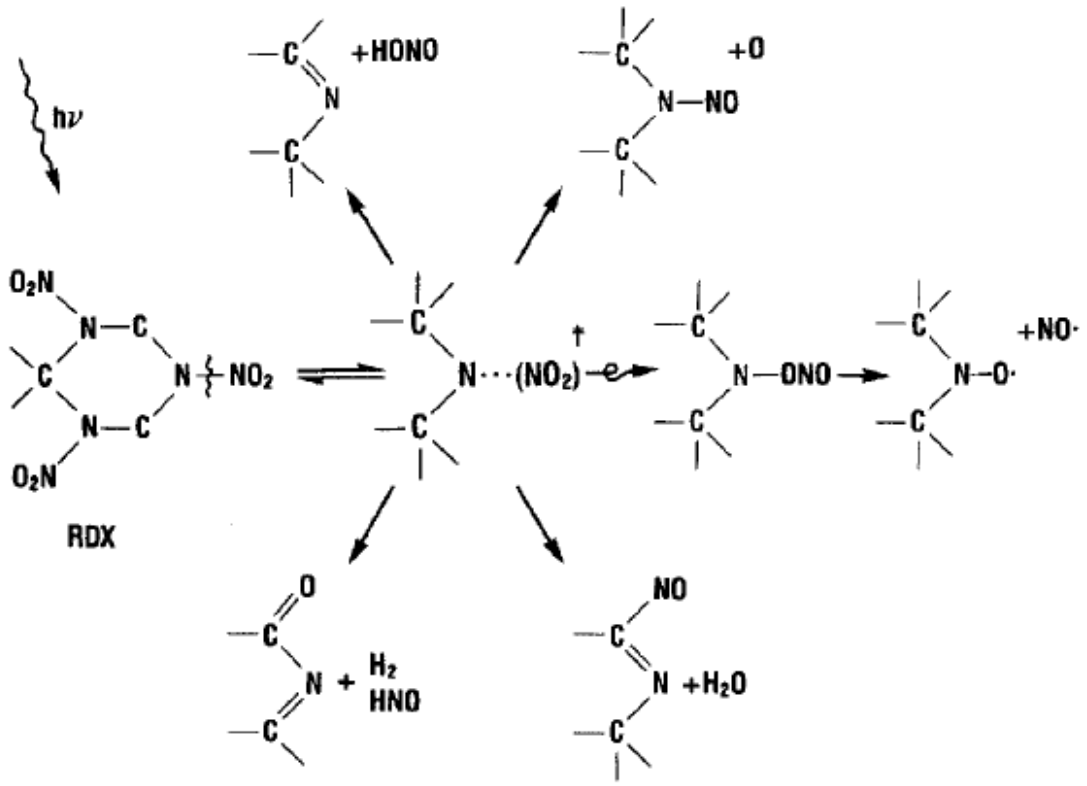

Figure 3.11: Proposed degradation pathways of RDX, reproduced from [40]

The degradation mechanisms presented are very hypothetical with no understanding of radical pathways presented. The suggested products are also non-ionic suggesting that the exposure to x-rays simply causes excitation of electrons and not expulsion (unless they are re-captured, which is unlikely with x-rays). In the case of ionising radiation, particularly gamma, it is known that per interaction only one radical and one ion are formed [41]. Based upon this theory, it is likely that most of the above products will be invalid or ionic.

C. Skidmore et al, published a summary paper on the ageing of PBX9502[5] [42]. The paper summarises effects of natural ageing out to approximately two decades worth of service in undisclosed nuclear weapons systems, as well as the effect of radiation on a TATB and fluoropolymer based PBX. Skidmore comments on previous research which

[5]PBX9502 - 95 % TATB, 5 % KelF-800 fluoropolymer[42, 43]

shows the darkening/greening of TATB when exposed to electromagnetic radiations of wavelength lower than 450 nm, and references works which have isolated decomposition products from other stimuli, such as impact and shock. Skidmore comments on the work undertaken by Britt et al [44], who showed the stability of detected free radicals in TATB from UV exposure can exceed over two years, and associates the detected spectra to a simple hydrogen adduct of TATB, although this was later disputed [45]. The work also comments on the instability of free radicals observed within the cyclonitamine RDX, which decay rapidly at temperatures above approximately -60°C.

Skidmore et al also reported irradiations of TATB materials by gamma rays and proton beams. Proton beam irradiations were undertaken on pressed pellets of TATB, whereas gamma irradiations were undertaken on powders which were subsequently pressed. Total doses of 90 and 700 kGy were obtained for TATB materials exposed to gamma rays at a rate of approximately 600 Gy hr^{-1}, noted to be equivalent to "thousands of years of stockpile life". Samples analysed by Scanning Electron Microscopy, infrared (IR) and mass spectrometry yielded null results when compared to baseline; most likely due to concentrations of daughter products and the sensitivity of the selected tests. It would have been valuable to have undertaken SEM analysis of pellets which were pressed prior to irradiations to evaluate the presence of gaseous fissures as reported in previous research [27, 35]. Slight changes to thermograms were observed, and results from thin layer chromatography suggested that a furazan derivative could be responsible.

The investigation into the effect of radiation on TATB was continued by Manaa et al [46] who aimed to demonstrate experimentally along with supporting computational modelling methods, that a mono-nitroso derivative of TATB resulted from UV exposure rather than the purported furazan from Skidmore. Manaa also suggested that this daughter product was the cause of the much reported greening of the insensitive explosive when exposed to electromagnetic radiation. The UV-Vis spectra was calculated semi-empirically along-

side the purported decomposition products, i.e. the mono-nitroso, mono-furazan and a di-furazan derivative, in an effort to identify which compound contained the chromaphore responsible for the widely reported green TATB. Manaa reports a calculated absorption around 600 nm for the mono-nitroso derivative but does not provide a spectra. No further comment is made as to the UV-Vis properties of the derivative, however it is possible that these absorptions are responsible for the greening of the material, as absorptions at 600 nm correspond to orange light which intensifies the reflection of blue light from the material [47]; this could mix with the reflected yellow light of TATB, making it appear green. It is also noted that Manaa employed semi-empirical computational methods which are significantly less accurate than techniques such as time-dependent density function theory (TD-DFT) [48], calling into question the accuracy of the results.

Computational vibrational analysis of the mono-nitroso molecule was undertaken and a resultant IR spectra provided, but there is no equivalent for the mono or di-furazan products presented. Manaa does however acknowledge that experimental determination of the IR spectra would be significantly difficult due to concentration effects and questions if experimental comparison is achievable. Manaa does not detail the computational methods employed other than to say that the UV-Vis spectra were obtained semi-empirically; it is also assumed that all calculations are undertaken in the gas phase, limiting the applicability of findings when comparing to the solid phase. Manaa also describes a synthetic procedure for the production of the mono-nitroso derivative of TATB and details a selection of tandem MS experiments that suggests the molecule is the purported decomposition product of TATB by comparison of baseline, synthesised and irradiated materials.

A few years later, Padfield undertook a scoping study [49] into the effects of gamma radiation from a cobalt-60 source on a selection of materials, including TATB. Materials were irradiated to a total dose of between 10 and 100 Gy at 275 Gy hr^{-1} under vacuum and atmospheric gases at 30°C. Samples were analysed by differential scanning calorimetry

(DSC), gel permeation chromatography where appropriate, and head space gas was analysed using gas chromatography mass spectrometry (GC-MS). In addition to these tests, in support of safety concerns, an impact (rotter) test based on the Langlie statistic was undertaken to obtain a Figure of insensitivity (FoI). No significant differences in the FoI were measured for any material with the exception of a TATB containing equivalent to PBX9502, which was recorded to have a slight reduction in FoI at 80, compared to the baseline value of 100. However, as noted in the work, due to the limited amount of material and resultant number of firings on the rotter the confidence of this change is small.

Results for the irradiated samples of greater than 90 % HMX based PBX were negligible when compared to baseline, with the exception of thermal results from DSC testing, where samples irradiated under both atmosphere and vacuum showed an earlier onset and peak temperatures for decompositions. Considering previous works, it is also surprising that, for a formulation mainly consisting of HMX, no increase in sensitiveness was observed when irradiated under vacuum [36, 37, 38, 25, 27, 31, 30]. However it is thought that the vacuum was lost during these irradiations. This indicates a significant radiation resistance of the materials, most likely due to the aromatic plasticiser and stabiliser present. Unfortunately, data from the GC-MS head space analysis was unsuccessful. Padfield's work was very much a qualitative study on bulk materials properties with no attempt to identify chemical degradation mechanisms and associated products, which may be formed in small enough quantities to have a negligible effect on the material immediately, but could manifest themselves under natural ageing.

As a continuation of Padfield's work, one of the most recent pieces was undertaken by one of his students, Connors, in 2014 [43] who investigated the effect of gamma radiation on TATB, a selection of fluoropolymers and a related insensitive polymer bonded explosive. The work, alongside Padfield, is particularly relevant as it was carried out at the same institution as the current research, which has allowed for quick adoption of experimen-

tal work. Connors undertook chemical analysis of the pre and post irradiated specimens but was heavily experimentally based and offered no theoretical degradation mechanisms or computational modelling. Despite this, and in disagreement with the work undertaken by Manaa [46], *"A mono-furazan derivative of TATB"* was suggested as a possible degradation product, which was attributed to a measured increase in explosives impact sensitiveness. As with Padfield's work, head space analysis of irradiated samples were, for the most part, unsuccessful despite some further development. The determination of the mono-furazan contaminant was achieved using High Performance Liquid Chromatography (HPLC) negative electrospray Mass spectrometry with the identification of a peak in the chromatogram that was not present in baseline non irradiated material. This peak, of which area correlated to total dose, corresponded to a mass loss of 18 atomic mass units (AMU), allowing Connors to conclude that water has been eliminated from TATB yielding the mono-furazan derivative. Despite the synthesis of the mono-nitroso being available in Manaa's earlier work, no attempt was made to isolate the suspected impurity or confirm it with analytical sample comparison.

The work undertaken by Connors and his supervisor Padfield confirmed the previously reported observation that TATB, when exposed to gamma radiation, changed colour from yellow to green. This reported change was observed throughout irradiated pellets of pressed TATB, indicating the penetrative power of gamma radiation to these materials; especially when one considers the numerous reports of TATB turning green just on the surface, when exposed to UV-Vis radiation [50]. Padfield, in conjunction Williams of Sam Houston State University [51], attempted to quantitatively correlate the colour change within the irradiated TATB pellets to the total absorbed dose (equivalent to water), with the resulting correlation being shown in Figure 3.12.

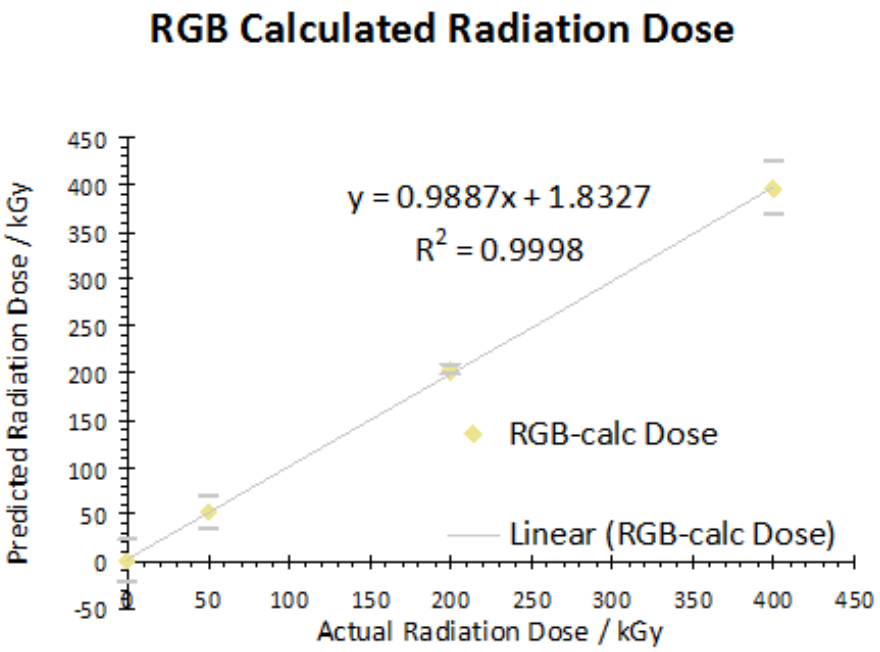

Figure 3.12: TATB discolouration as a function of absorbed dose to water [51]

Using a UV-Vis spectrometer, the exact reflectance spectra of the individual pressed TATB samples was measured at various dose levels as shown in Figure 3.13. The previous work by Manaa [46] suggested an absorption (i.e. lower reflectance) at approximately 600 nm. Whilst this cannot be seen explicitly, the data presented by Padfield does suggest a general increased absorption in orange/red wavelengths greater than 600 nm, which would cause a material to appear green/blue. Manaa's conclusions were limited and no UV-Vis spectra was presented in his work for comparison. Furthermore the equivalent spectra for the mono-furazan is not presented for an equivalent comparison. What can be drawn from both the HPLC and UV-Vis spectra is that the concentration of the degradation product appears, perhaps unsurprisingly, to correlate with total dose. No work was undertaken to assess the effect of dose rate in a similar manner.

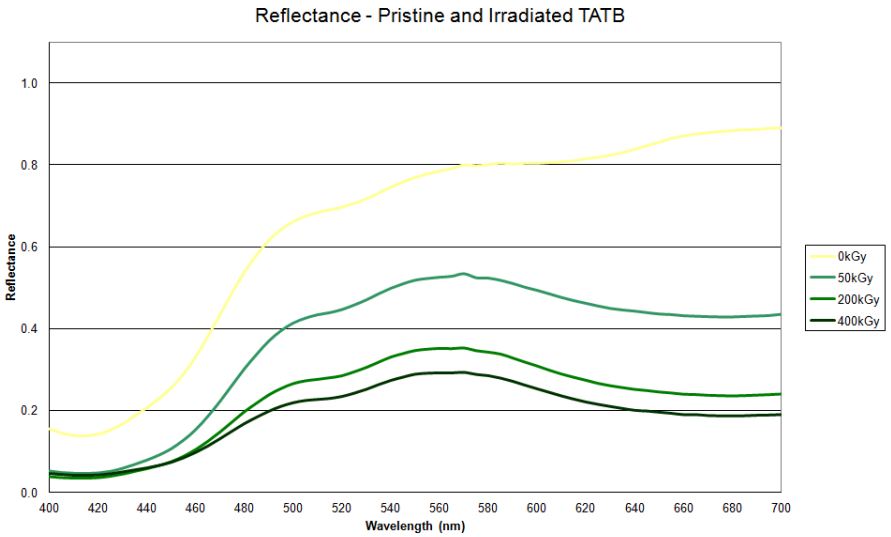

Figure 3.13: TATB reflectance as a function of absorbed dose to water [51]

Investigating the effect of radiation on TATB using computational chemistry techniques, Ying et al [52] claimed to identify the free radical formed by photolysis of TATB in August 2014. In his work, Ying also refutes the findings of Britt [44] in that the concluded H-adduct of TATB is not the formed radical of TATB resultant from irradiation. The work correctly identifies that quantum chemical calculations need to be of suitable complexity in order to provide accurate predictions and details a selection of calculations undertaken at the time dependent Density Functional Theory (TD-DFT) level of theory utilising the B3YLP and 6-311++g(d,p) functional and basis set. Whilst the computational calculations appear sound, Ying only considers ground, first singlet and triplet excited states of TATB and a selection of daughter products; thus this work is only applicable to low energy non-ionising processes i.e. photolysis through molecular rearrangement, due to the promotion of bonding orbitals into anti-bonding states. The conclusion was that a phenoxyl radical derivative of TATB was the thermodynamically most favoured radical due to photolysis. Ying complemented his work with some UV irradiations of some TATB material and showed a growth of an absorption between 600 and 750 nm, which he corresponded to a calculated UV spectra (specifically an absorption at 611 nm) of the purported phenoxyl radical. This is quite a tentative conclusion as there is a fair difference between the

predicted and measured absorption, with the shape of the predicted spectra enhanced by Gaussian fitting; nevertheless the absorption is in the correct region in terms of wavelength to impart the greening seen in TATB. As with other computational chemistry calculations of this nature, they are undertaken in the gas phase and there is no mention in Ying's work that considerations or approximations to the solid state have been made.

Taking a different approach, Tian, et al. [53] hypothesised, supported with some limited visual evidence, that the green colour of TATB was not caused by the presence of a daughter product, but rather due to crystalline structure changes resultant from disrupted hydrogen bonding. The evidence presented in the paper is very limited and an ESR spectra of what is assumed to be UV irradiated TATB is presented alongside a baseline sample. The typical simple spectra of the irradiated and baseline TATB only differ in magnitude, with Tian concluding that the spectra supports his theory of disruptions in crystalline structure causing a simple radical to be formed. This is unlikely to be the cause as crystalline disruptions do not cause paramagnetic species to be formed. Tian's assessment that the colour change is due to alterations in the crystalline structure is flawed as changes to the colour of a material require alterations to a colour centre and not just the structure. An example of this is the gamma irradiation of Topaz, where the gamma radiation induces a change in the colour of the material, but only when aluminium is present as its ionic form is responsible for the change. Tian also does not comment on the published thesis of Connors or Skidmore, who provided significant evidence of a chemical species being generated upon irradiation.

3.1.1 Brief summary

Literature in this field is very hard to compare as the vast majority of studies vary in incident energy, total dose, dose rate, selected material and environment. These differences are likely to have an impact for different reasons, i.e. a higher dose rate will increase the

likelihood of radical-radical reactions due to their short lived nature.

HMX and PETN appear to be comparatively sensitive to gamma radiation under certain conditions, sometimes yielding spontaneous detonations [36, 37, 38]. It is unclear as to the underlying mechanism to this sensitisation, however its identification is a key objective of this research. A key area of investigation will be to irradiate HMX in vacuum at room temperature to complete Miles' work [36, 37, 38], and confirm his hypothesis that it is not the temperature, but the gaseous environment that causes the increased sensitisation. Equivalent irradiations should also be undertaken on PETN followed by a suite of analytical techniques to identify possible daughter products that may have formed.

TATB appears to be comparatively resistant to radiation, although increases in sensitiveness to impact is reported alongside HMX and PETN. However, unlike the nitro-ester and heterocyclic nitroamine, TATB presents a significant colour change upon irradiation. The aromatic nature of the molecule is likely the source of the explosive's resistance to radiation, a mechanism which will allow for molecular rearrangement and likely daughter product speciation. Computations generation of UV-Vis spectra using more complex levels of theory than that presented by Manaa for both purported species could be undertaken to provide additional evidence, as should synthesis of marker compounds allowing potential confirmation by HPLC-MS of the findings of Connors.

Various literatures [27, 35] have suggested that explosive crystalline materials may undergo changes and/or defects within the crystal structures, which may be the cause of increased sensitivity and, in the case of TATB, colour changes. Optical and Scanning Electron microscopies could be undertaken on baseline and irradiated materials to investigate if this is a potential cause.

There have been numerous studies on detection and characterisation of radical species

formed from UV, x-ray and gamma-ray sources for HMX, PETN and TATB; however all of these studies involve the detection of late time, chain-terminating and in some cases long-lived radicals. This is principally due to the very short life span of such species and the time taken between irradiation and subsequent analysis by ESR techniques, despite some efforts utilising sub-ambient irradiations. The ability to undertake in-situ ESR analysis of irradiated samples would prove to be highly advantageous in identifying early time radical generation, however this will take significant development work.

With the exception of Manaa's work [46], there has been little use of computational methods to aid the prediction of potential daughter product speciation from gamma irradiation, rather they have, for example Ying's [52] work, been used to calculate the mechanisms and resultant speciation of non-ionising processes, such as photolysis. As shown in these works, computational chemistry can be utilised to calculate thermodynamically favourable routes for chemical decompositions and importantly in the case of mechanisms which start with ionisations, initial starting points for the calculations must be taken from the optimised ground states of the ionised and radical parent TATB, PETN or HMX molecules, which will be, by definition in the doublet state. Furthermore, consideration as to both the charge and spin state needs to be made for all daughter products and fragments suspected to be resultant from ionisation as charge must be conserved throughout any purported mechanism. As long as these considerations are made, such methods can be employed as a means of elucidating the formation of potential daughter products resultant from irradiation. In addition to thermodynamics, the electronic structure characteristics such as UV-Vis and IR spectra, as well as Nuclear Magnetic Resonance (NMR) and, for radical products ESR spectra, can also be generated. This can be compared to experimental data, providing increased understanding and evidence.

3.2 Computational methods

Modelling methodologies can be categorised into regimes according to the length and time-scales over which they are applied. At the smallest of length and time-scales, quantum chemistry calculations are utilised which are often used to determine electronic structures of atoms and molecules in ground and excited states, with transitions often happening on the femtosecond time-scale [54]. A many-bodied atomistic/molecular problem is considered to be the next hierarchical level in terms of length and time-scales, with modelling strategies such as molecular dynamics being utilised. At this level, interactions between bodies are often treated using classical Newtonian physics and force potentials that are either calculated explicitly from quantum chemistry calculations or approximated by force fields calculated by molecular mechanics.

At larger length and time-scales, models begin to operate on a micro-structural/meso-scale level, where a model is discretised into elements of length, area or volume depending on the number of dimensions. A suitable time step is selected to solve numerous differential equations over a selected time period using explicit or implicit integration techniques. Modelling at this level is not relevant for this study as degradation resultant from ionisation is expected to be concentrated at the molecular and atomic scale. A final modelling methodology which is often used and can span all length and time-scales is deterministic modelling [54]. Such models are derived from known relationships and often rely on mathematical functions which can be solved either explicitly or numerically.

Quantum chemistry modelling is clearly a very applicable technique due to its ability to calculate predicted ground and excited electronic states as well as corresponding thermodynamics for parent and daughter molecules, especially when considering that the main interaction of gamma radiation with matter is with the electronic structure of the irradiated material. It is acknowledged that recent work [53] suggests that the greening of TATB is a result of crystalline deformation, and that molecular dynamics simulations could be used

to explore this phenomenon. However, due to the number of bodies required to be simulated within a crystal, individual molecules would need to be treated with semi-empirical quantum mechanics or force field methods due to the significant computational cost; this would cause a considerable reduction in the fidelity of the electronic structures of individual molecules within the system.

It is known that imperfections within a material's crystal structure, such as point-defects, grain boundaries or dislocations sites, affects the sensitiveness of explosive materials [55]. Observations within the literature detail increased sensitiveness, particularly to impact, for explosive materials that are exposed to gamma radiation [43, 51, 30, 36, 37]. It is therefore quite possible that the observed increase in sensitiveness is due to the generation of such crystalline defects. The use of methods such as molecule dynamics could elucidate the as to a potential formation of such defects.

Meso-scale modelling is quite applicable in order to assess the global affect that radiation has on a composite material, such as a PBX, where, as shown by the linear mass attenuation coefficients, differing rates of absorption may be calculated for each constituent. It is foreseen that such a model would be complemented by Ab Initio calculations which can be used to calculate rates of reaction and hence rates of formation of daughter products, based on the calculated number of interactions resultant from the radiation field. Whilst the generation of such a meso-scale model is interesting and would be based upon deterministic modelling methods, it is beyond the scope of this work.

Upon consideration of the applicability and the strengths and weaknesses of the available computational methods, it was decided that modelling efforts would focus on Ab Initio methods that can be used to directly predict the affect of gamma radiation on individual energetic molecules through predictions of ground, elevated and radical states. Such calculations will provide electronic and nuclear structure information in addition to

thermodynamic and spectral characteristics. It is acknowledged that this will omit the ability to determine the effects of radiation on the crystalline structures of the selected materials, but it is envisioned that once the effect of radiation has been determined on a individual molecule basis at this high level of fidelity, results may be incorporated into a larger simulation, perhaps utilising a molecular dynamics strategy, within future work.

Ab Initio modelling methods contain a significant number of sub-methods, often referred to as "different levels of theory", usually trading accuracy for computational demand. In order to select the correct level of theory, a review of the available methods and their associated advantages and disadvantages is required.

3.2.1 Quantum chemistry methods

Quantum chemistry simulations typically focus on atomistic and molecular length scales, where electronic and physical properties can be calculated by application of quantum mechanics to describe fundamental interactions of electrons and nuclei within a system. The foundation to this method is that each individual component can be represented as a wave and as a particle, according to wave particle duality [54]. Each component may be described according to its wavefunction $\psi(r,t)$, a probabilistic description of a particle's location within an area of space. A measurable observable, such as energy, may be calculated from a particle's wavefunction by the use of operators and Schrödinger's equation.

A unique operator is required for each observable, with the Hamiltonian H the corresponding operator for energy. Schrödinger's equation is considered solved when a wavefunction is operated upon and equates to the product of the observable and the wavefunction. Only for very simple models such as the hydrogen atom, can Schrödinger's equation be solved. For multi-bodied systems, approximation methods must be used [48]. Two main methodologies are suitable for such approximations, these are variational and per-

turbation methods, with one of the first successful models being the variational Hartree-Fock method.

Hartree-Fock

The Hartree-Fock method calculates an approximation to the wave function of an atom, or system of atoms, and applies it to Schrödinger's equation in order to test the solution, by calculation of the total energy of the system. Approximations to the wave function are made in the stationary state where the affect of Coulombic forces through electron-electron interactions (often referred to as electron correlation [48]) are not calculated explicitly; rather the average field of the system is used to account for this affect. It is for this reason that the Hartree-Fock methods were originally called self-consistent field methods, as the calculated solution to Schrödinger's equation needed to be self-consistent with the assumed initial mean electronic field [54, 48, 56].

This approximation of Columbic interactions is the key drawback of the Hartree-Fock method, as is the method's very poor rate of computational convergence for solutions, yielding significant resource requirements for relatively simple calculations. The method is also only capable of calculations based upon the ground state of an atom or system, signifying that transition, and more importantly excited state calculations, are not valid for this method, limiting the usefulness of this method.

Post-Hartree-Fock

The issue of explicit Colombic interactions within the Hartree-Fock method were overcome using a selection of techniques collectively called post-Hartree-Fock methods. Each of these techniques utilises different treatments of electron-electron quantum interactions with the main three being Møller-Plesset Perturbation theory, Configuration Interaction

and Coupled Cluster.

Møller-Plesset Perturbation Theory

Møller-Plesset Perturbation theory addresses the short-comings of the Hartree-Fock method by explicitly calculating the affects of electron correlation by Rayleigh-Schrödinger Perturbation Theory, where the Hamiltonian operator H is broken down into an unperturbed H_o and perturbed operator V. It is this perturbation which describes the electron correlation within a system; where λ is a parameter which can vary between zero and unity, describing how close the overall Hamiltonian is to the true solution.

The method can be used to calculate a variety of differing orders of electron correlation correction, with the summation of the zeroth and first order-corrections corresponding to the Hartree-Fock energy. It is therefore necessary to correct to at least the second level (MP2) of Møller-Plesset perturbation theory [54, 48, 56, 57] in order to obtain any increase in computational accuracy when compared to Hartree-Fock methods. Additional levels of correction i.e. MP3 and MP4 offer increased accuracy due to the calculation and incorporation of energies from triple and quadruple excitements; these calculations come with a significantly higher computational cost.

Configuration Interaction

One of the most idealistic approaches to address the lack of electron correlation within Hartree-Fock calculations is to include explicit excited states within the calculation of the system. This is achieved by the representation of the wave function as a linear combination of ground and excited state wave functions called configuration state functions [48, 56, 58, 54]. Unfortunately such methods are incredibly computationally intensive and are hence limited to very idealistic systems, ruling this method out for this study. Reduced accuracy configuration interaction methods are also available and offer an at-

tractive mid-ground when it comes to a trade off of accuracy and computational resource time. These methods, such as CID (Configuration Interaction Doubles substitutions only) and CISD (Configuration Interaction Single and Doubles substitutions only) essentially limit the number of excitations that are included in the wave function. CID calculations place a limit on double excitations only, whereas CISD calculations also include single excitations [56, 58, 48, 54].

Coupled Cluster

This technique again accounts for electron correlation and is typically more accurate than Configuration Interaction and Møller-Plesset Perturbation methods; with a comparable resource requirement to the former [59]. Much like Configuration Interaction treatment, excitations are limited to single, double, triplet and/or quartets, utilising a similar naming convention, i.e. a coupled cluster calculation involving single, double and triplet substitutions would be named CCSD(T), with parenthesis an indication of the triplet excitations being treated by perturbation theory. While offering some of the most accurate results available, the computational requirement is massive and therefore limited to simple systems and is therefore not applicable to this study.

Density Function Theory

The calculations considered so far (referred to either Hartree-Fock or post Hartree-Fock methods) are based upon calculating the wavefunction for each individual electron within a system; Density Function Theory (DFT) does not. The theory is based upon the knowledge that the total spatially dependant electron density is related to the total electronic energy of the system. As a result, DFT by itself, is significantly less accurate than the other forementioned methods, unless only the simplest of systems, i.e. a Hydrogen atom, is considered.

The incorporation of mathematical descriptions (often called functionals) for electron exchange and correlation, addresses this shortfall, whist maintaining computational efficiency. Some of the most accurate and up-to-date functional descriptions of electron correlation and exchange are found in Metta-GGA (Generalised Gradient Approximation) functionals which contain the second derivative of electron density in addition to the actual density and the first derivative of the corresponding electron-exchange potential, as found in standard GGA functionals [48, 56, 60].

Taking these approximations further are hybrid functionals, where a proportion of the electron exchange energy is calculated explicitly using Hartree-Fock methods, providing some of the most accurate computational calculations available today with only a moderate increase in computational demand over standard DFT. The Minnesota hybrid functionals are examples of these cutting edge approximations, with the M06-HF functional offering 100 % of the electron exchange energy being calculated using the Hartree-Fock method. These are known to provide some of the most accurate data in computational chemistry [61] with only a comparatively moderate computational cost which lends the method to semi-complex systems, such as those being considered within this study.

3.2.2 Basis-sets

Computational chemistry calculations of all types require a mathematical formalisation to describe the molecular orbitals being studied. This is typically achieved using basis sets where mathematical functions (usually Gaussian) are used to describe molecular and atomic orbitals. Basis sets vary from simplistic to complex, and can describe different physical phenomena, i.e. the inclusion of polarisation and diffuse effects. Numerous basis sets exist [48, 59] and the selection must be driven by a trade off between accuracy, computational efficiency and suitability. Numerous DFT calculations are reported in the

literature using Pople basis sets such as 6-31 and 6-311++(d,p), as two common examples. These basis sets are considered to be reasonably accurate, with the latter being a split valance triple zeta basis set with polarisation and diffuse descriptions for all elements [59].

Despite their complexity, Pople basis sets use a fixed number of functionals per orbital. This was addressed by Thom Dunning who formalised his correlation consistent basis sets, which are considered state of the art [48, 59, 56]. Designed to converge to an infinitely complex basis (aka complete basis set limit), these basis sets use extrapolation techniques to calculate the number of functionals required to give results where the addition of more would not increase the accuracy of the calculation.

Like the Pople basis sets, various different flavours of the correlation consistent basis sets exist, where additional physics, such as diffuse (necessary for describing ions) and polarisation functionals (necessary for hydrogen bonding), can be added along with more functionals for valence orbitals. It is noted that the triple zeta basis set offers significant advantages over double in terms of accuracy. However, increasing numbers of functionals for the valence electrons above three (i.e. triple) yields diminishing returns at significantly increased computational cost [48, 56, 59].

3.2.3 Methods to approximate solid state

Computational chemistry calculations are normally undertaken on single molecules in the gas phase where influence from surrounding molecules are not considered. Inferring results from gas phase calculations for molecules that are in reality liquid or solid in nature is a significant approximation and can cause considerable discrepancies between computational and measured results. An example of this is often seen in optimised geometries, where different crystalline polymorphs, such as the boat configuration of the alpha polymorph of the HMX molecule, may be calculated in the gas phase, rather than

the chair configuration of the beta polymorph of the HMX molecule, that may be present in the solid [62]. These alternative molecular geometries can give significantly different electronic structures, which in turn may yield inaccurate thermodynamic and spectral properties.

This does call into question the appropriateness of using data generated from calculations based upon structures optimised within the gas state, when in real life, the selected molecules exist in the solid phase. The ideal solution is clearly the generation of an optimised structure derived from the interactions bourn from explicit simulation of every molecule within a typical unit cell of the solid, i.e. utilising such quantum chemistry calculations within a molecular dynamics simulation. As elucidated to earlier this is prohibitively computationally expensive and beyond what is currently possible and why most molecular dynamic simulations require a reduced mathematical treatment for each molecule. However, as with most computational modelling methods, approximations can be used in order to improve accuracy of a simulation at a palatable computational cost, compared to that of the perfect explicit solution.

In the case of increasing the applicability of the gas phase computational chemistry calculations mentioned so far, a few options exist, namely the ONIOM, periodic boundary conditions (PBC) and implicit solvent methods. The first, ONIOM (short for our Own N-layered Integrated molecular Orbital and Molecular mechanics) [63, 48] utilises a combination of quantum chemical and molecular mechanics calculations, where molecule(s) of interest are treated with a higher level of theory i.e. quantum chemical methods such as DFT or HF, and surrounding bodies are treated with a lower level, i.e. molecular mechanics. Whilst this approximation does close the gap between gas and solid phase calculations, there is still a significant computational penalty associated with such a treatment. This increased computational cost often results in the reduction in the complexity of the quantum chemistry treatment of the problem, either with a reduced level of theory

or a smaller basis set.

The second option is to utilise periodic boundary conditions, where molecules within the unit cell of the crystal structure in question are used. These periodic boundary conditions are effectively reflective and allow the approximation of the interactions of an infinite number of adjacent unit cells on the individual molecular geometries being considered. Whilst this method is perhaps the closest approximation to the solid state, again it has a significant computational cost. This expense is not due to the method itself, but rather the requirement to simulate the numerous molecules within a unit cell. As a result, due to computational limitations, the level of theory and basis sets used is often significantly reduced for all but the most simple of molecules.

The third option is to employ an implicit solvent method such as the Polarised continuum model (PCM) [48, 64], where the influence of surrounding molecules is treated implicitly rather than explicitly. Such an option is only applicable when the influence from surrounding bodies may be considered as an isotropic continuum. Originally developed to increase the appropriateness of simulations of molecules within the liquid phase, the methodology can be applied to the solid. One of the most attractive properties of this method is the comparatively low additional computational cost over the previous two methods, permitting high levels of theory and complex basis sets to be used.

3.3 Experimental methods

As with the experimental investigations undertaken in the literature, new irradiations and subsequent analysis of materials that would support this study is subject to the availability and suitability of available facilities and methods. This is particularly relevant to the irradiation of high explosives for two main reasons; firstly the provision of a facility in which

explosives may be irradiated safely and legally is very difficult and only a few facilities in the world offer such an opportunity and secondly, the inability to transport irradiated explosives to other facilities for analysis as they are considered insulted. Resultantly, experimental investigations are limited to those available at Cranfield University's Shrivenham campus, which has a comprehensive analytical capability and a facility called the J.J. Thomson facility where the exposure of high explosives to gamma radiation is possible.

3.3.1 J.J. Thomson facility and cobalt-60

The JJ-Thomson cobalt-60 irradiation facility at the Shrivenham Campus, which is co-located at the Defence Academy of the United Kingdom shown in Figure 3.14, was used throughout this project to expose the selected materials to known doses of gamma radiation. The facility houses an irradiation cell that contains an array of cobalt-60 rods within a cylindrical aluminium vessel which, due to the close proximity of the individual rods, may be treated as a single point source that is capable (at the time of writing) of dose rates up to a 1 kGy per hour, equivalent to water.

Figure 3.14: JJ-Thomson irradiation facility

Cobalt-60 is a synthetic isotope of cobalt and is not found naturally. The radionuclide is produced by the neutron activation of cobalt-59, with the resultant isotope decaying via beta(-) and gamma radiation to nickel-60 over a comparatively short half-life of approximately 5.3 years. The decay, as shown in Figure 3.15, results in an almost equal distribution of two gamma quanta with energies of 1.17 MeV and 1.33 MeV; due to this equal distribution, the gamma energy of cobalt-60 is often quoted as 1.25 MeV [43]. Beta(-) emission consists of an electron and an anti-electron neutrino, which may cause concern that such particles generated from the cobalt-60 source may interact with exposed materials. However, these concerns are unfounded as the emitted electron interacts very readily with matter and hence has a very large probability of being captured by the aluminium containment can, whereas the anti-electron neutrino almost doesn't interact with matter implying that it will be released from the can, but it is very unlikely to interact with exposed material [12]. For these reasons, the Cobalt-60 source within the JJ-Thomson facility can essentially be treated as a pure point source of gamma radiation.

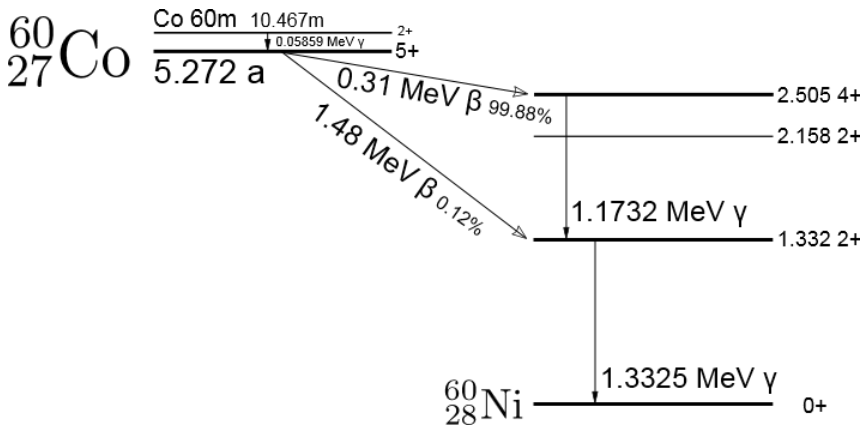

Figure 3.15: Cobalt-60 decay Scheme [65]

The decay of radioisotopes by disintegration cannot be slowed, stopped or accelerated, the rate is fixed and is described by the material's half life and an exponential decay law. Cobalt-60 is no exception, and therefore the activity of the source within the JJ-Thomson is also fixed at a given time. Resultantly the only pragmatic way to control the exposure is to increase or decrease the distance between the sample and the source, as radiation flux approximately (i.e. not considering interactions with air) obeys the inverse square law where an increase of 10 times the distance would yield a 100 times reduction. In order to control the distance and hence the radiation environment, samples need to be secured appropriately using a repeatable and safe method. Such a method has already been designed and developed for use with explosive materials within the facility.

Sample containment

Connors and Padfield [43, 66, 51, 49] both utilised the JJ-Thomson facility for their experiments which considered the effect of radiation on various explosive and inert materials. Padfield initially designed an explosives containment unit that would safely house small quantities of energetic materials (0.75g NEQ), that if initiated accidentally would pose no danger to the radiation source. Within the explosive containment unit itself, samples were

held inside typical analytical glassware sealed with a polymer septum that often degraded under long durations of radiation exposure, causing gaseous leaks.

Connors took this design and refined it, opting for bespoke glass ampoules, as shown in Figure 3.16, that were individually flame sealed, offering more durability than the polymer septum seals used by Padfield permitting a much stronger and more permanent vacuum to be placed within the ampoule. This design also benefited from a "fine glass break tube" which permitted gas sampling of the head space by analytical means.

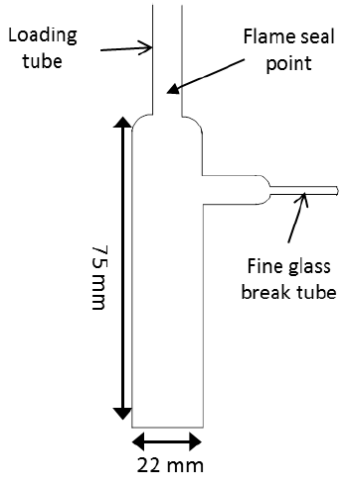

Figure 3.16: Glass ampoule (taken from [43])

The design of the explosive containment units remained mostly unchanged from Padfield's and featured a dual ammunition box construction, Figure 3.17, with a heater plate within the inner container, Figure 3.18, allowing the temperature of any irradiations to be controlled by a control box unit connected to a thermocouple within the inner container. As with Padfield's design, space between the ammunition boxes was again filled with vermiculite, used as a blast mitigant, to reduce the effect in the event of an accidental ignition. However, during his design work, Connors also took the opportunity to up-rate the explosive containment units by undertaking some live trials which proved that if five grams of explosive material were spontaneously detonated, both inner and outer ammunition con-

tainers become distorted, but remained intact and contained the explosion without rupture.

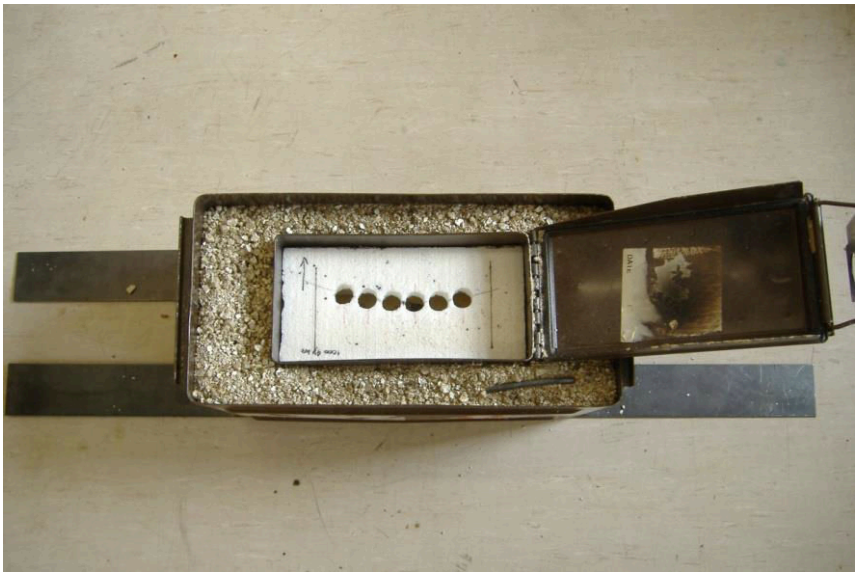

Figure 3.17: Full containment unit (taken from [43])

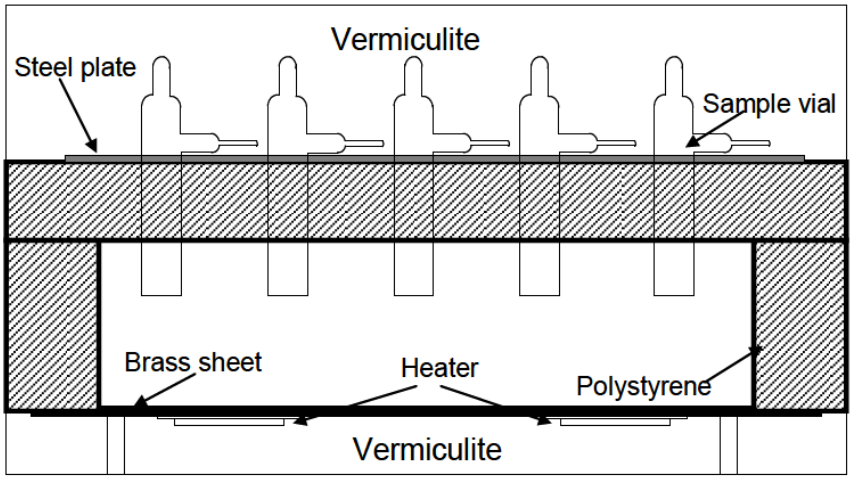

Figure 3.18: Schematic of inner containment unit (taken from [43])

Of primary concern when irradiating explosive samples within the JJ-Thomson facility is an incident which would cause either dispersion of the radionuclide or the failure of the retraction mechanism used to bring the cobalt-60 rods into and out of the aluminium retaining can; this is the mechanism that shields the source which negates the significant majority of radiation within the cell. Whilst a dispersion incident is highly improbable

and mitigated by the use of gram quantities of explosives, the impingement of the can resultant from the deformation of the outer ammunition container was seen as a much more likely outcome. Connors foresaw this, and took measurements of the maximum deformation of the outer explosive container during his live trials. He reasoned that by limiting the maximum quantity of explosives per box to 4 grams within the JJ-Thomson facility (i.e. one less than what was undertaken in the live trial) the deformation of the outer ammunition can within the JJ-Thomson facility would be less than the live trial. Therefore, by applying a minimum distant requirement of 5 cm between the source can and the outer side of ammunition box greater than that seen in the deformation of box from the live trial of 1 cm, the risk to the source would be acceptably small. As the dose rate within the JJ-Thomson facility is controlled by distance alone, this effectively limits the maximum possible dose rate which an explosive sample can experience.

3.3.2 Analytical methods

Differential scanning calorimetry (DSC)

DSC is a standard thermal analysis tool that enables the direct heating of both a sample and a known reference in order to accurately determine the thermal properties of the sample, including onset and peak temperatures of thermal transitions. Changes in a material's chemical structure and chemistry often have a significant effect on a material's thermal properties, and as such DSC offers an excellent tool for identifying potential changes in an material, induced through radiation.

High performance liquid chromatography (HPLC)

HPLC is a wet chemistry analytical method that separates different molecular species contained within a liquid phase. This is achieved by passing the solution through a col-

umn which is packed with a medium designed to interact with the constituent molecules at differing extents, depending on each molecule's chemistry. The methodology lends itself very well to the separation of organic substances and is often used to detect trace explosives for forensic applications. This ability of the technique to separate out trace quantities of molecular species is very useful for the analysis of daughter products potentially induced by radiation that if generated, are likely to be in low concentration. The analysis of separated molecular species is then achieved by a detector(s), for which both UV-Vis and MS are available.

The UV-Vis light detector provides evidence as to the number of species within an elute, and can therefore be used qualitatively to ascertain if a daughter product has formed as a result of radiation, assuming the species have been separated. The detector may also provide electronic structure data that may be used as evidence alongside the TD-DFT analysis undertaken computationally.

The MS detector allows the determination of molecular masses of species eluted from the HPLC column. This is achieved by the ionisation of the molecules in question and the subsequent application of an electric field used to accelerate the ions towards a magnetic field that affects the trajectory of each molecule according to its mass and charge. The method of ionisation is very important with hard ionisation causing fragmentation of the eluted molecules, which requires significant analysis effort to hypothesise what the initial molecule was. Soft ionization, such as positive and negative electrospray, uses a high voltage electric field to cause droplets of ions to move towards the mass spectrometer. Negative and positive electrospray does not usually cause fragmentation, and therefore permits identification of a molecule much more easily. However, the ionisation process itself is complex, with positive mode requiring a reduced pH to encourage protonation and resultant ion formation, whereas the negative electrospray methodology utilises a much higher pH to cause de-protonation.

Gas chromatography - mass spectrometry (GC-MS)

GC-MS is an analogous technique to LC-MS, where typically gas samples are separated using specialised gas chromatography columns which can then be eluted into a mass spectrometer for analysis. The method is typically used to separate volatile, gaseous components either by direct injection of a gaseous specimen or by the injection of a specimen dissolved in a solvent, which is subsequently vaporised, usually by a hot filament. Unfortunately HMX, TATB and PETN are not suitable for direct liquid injection, as they are either too unstable (HMX and PETN) or too insoluble (TATB) for the method to work. The method is however more suitable for analysing head space gasses, such as those present within irradiation ampoules.

Nuclear magnetic resonance (NMR) spectroscopy

NMR is a spectroscopy technique used to fingerprint chemical compounds according to local magnetic fields resultant from unpaired nuclear spin. Typically, as with electrons, proton spins pair up in an opposing (anti-parallel) direction, in order to minimise the net angular momentum of the spin system of that atom, hence producing a lower and more favourable energy state. The same occurs for neutrons, however despite protons and neutrons aligning against themselves in an anti-parallel manner, protons and neutrons align their spins together in a parallel direction due to the quark structure of each nucleon.

The result is a net spin of zero for atoms with an even number of protons and neutrons, but more importantly a non zero value for atoms with an uneven number of these nucleons. NMR spectroscopy is hence limited to species with unpaired nuclear systems, with proton (hydrogen), carbon-13 and nitrogen-15 often used in organic material analysis.

Nuclear spins, just like electron spins, have directionality and can therefore occupy either a spin up or spin down state, usually denoted by a plus or a minus in front of the spin quantum number i.e. for a half spin system s = +1/2 or s = -1/2, there is no net

energy difference between these two states. In cases where an atom has a non-zero value of nuclear spin, it will also have a non-zero magnetic dipole moment. This is exploited for NMR spectroscopy where unpaired spins within a sample can align parallel (lowest energy state) or anti parallel (higher energy state) to an applied external magnetic field, as shown in Figure 3.19.

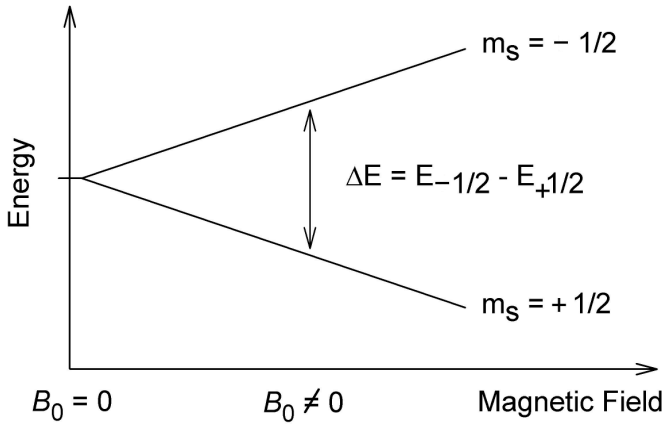

Figure 3.19: NMR energy level splitting (taken from [67])

Electromagnetic radiation can be absorbed by such systems in the presence of a magnetic field, causing the unpaired nuclear spins to align anti-parallel and thus occupy the higher energy level. The frequency of the absorbed electromagnetic radiation is a function of the strength of the applied magnetic field and is typically in the radio wave region of the electromagnetic spectrum. In order to exploit this phenomenon for spectroscopy, a sample is usually pulsed with a broad spectrum of radio waves, whilst a static magnetic field is applied. Unpaired nuclear states will absorb and emit radio waves at a specific resonant frequency that is dependant on the applied filed. In a sample with numerous different nuclear spins, this will cause as many simultaneous absorptions and emissions of characteristic radio waves. This complex spectra is then processed as a Fourier series which separates out the individual absorbed radio wave frequencies into a characteristic spectra.

The characteristics of the resultant NMR spectra come from shielding, where the local

electronic structure of a molecule changes the energy levels between the nuclear spin states of an atom relative to the same type of atom on a dissimilar molecule. Without this phenomena, the NMR signal generated by an atom from one molecule would be identical to that of the same atom on a dissimilar molecule, significantly reducing the usefulness of this technique. The generation of characteristic spectra is very useful for identifying possible daughter products generated, however NMR is not particularly sensitive for analysing impurities, and samples must be dissolved into a solvent, as solid state NMR is not locally available. This presents problems for materials that are particularly insoluble, such as TATB. Additionally, as HMX, PETN and TATB are solids, it is possible that changes induced through irradiation may be altered or lost by dissolution of the materials within a solvent.

Electron spin resonance (ESR)

Electron Spin Resonance which is also known as Electron Paramagnetic Resonance (EPR) is an analogous analytical technique to NMR, but quantifies the effect of unpaired electron rather than unpaired nuclear spin. In instances where electrons are unpaired, for example in free radicals, the subatomic particle will have a non-zero magnetic moment which, by the application of a magnetic field, can have its energy levels split in the same manner as NMR, i.e. Figure 3.19. Resonant electromagnetic radiation, in this case microwave rather than radio, can be absorbed by an unpaired electron, which is again a function of the the magnetic field strength. Much like NMR, the spectral characteristics which aid identification come from the interaction of the unpaired spin with local environments, in this case, the interaction between the unpaired electron and nuclear spins, called hyperfine coupling.

There are many combinations of microwave frequency and magnetic field strength that can yield an electron resonance and hence produce an ESR signal, which can significantly complicate identification. As a result, most modern ESR spectrometry is undertaken at

either a fixed microwave frequency and with swept magnetic field, or the opposite; the former is available for solids, liquids and gaseous samples using an X-Band microwave source.

One of the key advantages of ESR spectrometry is its sensitivity, with the ability to generate spectra for paramagnetic species in very low concentrations. This is partly due to the lack of competing signals and subsequent noise generation as other paramagnetic bodies are unlikely to occur naturally for long lifetimes, unlike NMR where there is a natural abundance of unpaired nuclear spins (especially for protons), for even for the most well controlled specimens.

Chapter 4

Computational Investigation

Suitable calculations need to be selected in order to support the research topic presented within this thesis. As previously mentioned, computational chemistry can be used to calculate characteristic electronic spectra, as well as thermodynamic properties. Unfortunately, no computational chemistry method is available that directly predicts the product(s) resultant from ionisation of a molecule. Rather, by using chemical understanding, literature review and experimental evidence, the thermodynamic properties and electronic spectra of a selection of potential daughter products (as well as the parent molecule) can be calculated, in order to assess if they are credible products resultant from ionisation. It is acknowledged that there is a shortcoming in the method, as potential daughter products/species may be overlooked and hence not considered, which may cause the incorrect conclusion to be drawn. There is no solution to this potential shortcoming other than to try and cover as many possible relevant daughter products that time permits in order to minimise the risk.

All calculations need to be available within a suitable software package in order to implement them for the study. Gaussian 16 a.03 [68] was utilised for all computational chemistry calculations with results visualised within the GaussView 6 [69], unless otherwise stated.

4.1 Optimisation

Computational chemistry calculations are based heavily upon the geometry and structure of the molecule in question. As a result, calculations need to be undertaken on molecules that have the most appropriate geometry and structure to real life as possible. As such, one of the first calculations that must be undertaken is a geometry optimisation, where the structure of a molecule is adjusted using the requested method, level of theory and basis set, in order to find a minimum in terms of the molecule's potential energy, as described by the net force and displacement across the molecule.

Spin-state and charge also need to be considered and separate optimisations are required for similar molecules that differ in these parameters, as the resultant structure and geometry will be significantly different, i.e. HMX in the ground state and HMX excited to the first triplet state require separate optimisations prior to any further calculation. This has an obvious impact when considering possible daughter products generated by fragmentation of an ionic parent molecule due to charge convention. In the case of an ionised molecule fragmenting into two species, it is unknown which species will remain charged, therefore optimisations (and subsequent calculations) will need to be undertaken for each daughter species and fragment in each possible spin-state, significantly increasing the number of molecules being optimised.

In addition to providing the correct structure for subsequent calculations, geometry optimisations of radical species will, by their very nature, identify the most energetically favourable location for the radical to be located on the molecule in question. This is achieved without inputting any information that may bias the outcome other than that the molecule is a radical by simply selecting the correct charge and spin-state of the molecule.

In the case of ionisation through gamma radiation, this results (prior to fragmentation) in ionic radicals that are in the doublet state (spin multiplicity of 2) which have a charge of +1.

The location of the radical (visualised by subsequent calculations that generate anisotropic hyperfine coupling) on the resultant optimised parent molecule can then be used to suggest which bonds may break/rearrange forming daughter products through fragmentation and/or rearrangement. Using this methodology to predict potential mechanisms does have a key approximation, in that upon ionisation the parent molecule undergoes internal rearrangement to the ground state of the ionised molecule, prior to any fragmentation. Despite the random nature of gamma radiation (i.e. any electron including non-valence could be removed upon interaction), this approximation is believed to be sound, especially for TATB where the conjugated system permits a radical resonance that induces stability [41]. In the case of a non-valence electron being removed, is it well documented through the Franck-Condon principle [52] that a valence electron can replace the lower energy orbital (through mechanisms such as florescence which may cause secondary interactions) much faster than a molecule may re-arrange, i.e. valence and non-valence ionisations can be treated the same.

The optimisation of a molecule is non-trivial and is heavily dependant on the starting structure of the molecule, level of theory, basis sets and shallowness of the potential energy surface. Optimisations are typically achieved by guessing the molecular geometry based upon a starting structure and a matrix of the second-order partial derivatives of the energy function of the molecule, also known as the Hessian matrix. Optimisations are usually undertaken with an approximation of a molecule's Hessian matrix, which typically proves effective. However, in difficult cases i.e. radical, ionic and other highly stressed states, the approximation may not be suitable and can often yield failed optimisations. In such cases, the explicit calculation of the Hessian matrix may be required for

each guessed structure to achieve optimisation; this is very computationally expensive. A somewhat less demanding methodology is to calculate the explicit Hessian matrix for the initial starting structure only i.e. not the subsequent guess, which may result in a converged optimisation.

Symmetry is often used in computational chemistry to reduce the cost of each calculation by only requiring analysis of a portion of a molecule. Whist this method is useful, it can often yield failed optimisations, where such a treatment causes the global minima on a molecule's potential energy surface to be missed. In order to ensure that optimisations (and subsequent calculations) are successful, symmetry was explicitly ignored for all calculations.

Molecular optimisations require target parameters in order to define whether or not a molecule is optimised. This is typically related to the potential energy of the molecule, more specifically the net force and displacement across the molecule, with values closer to zero indicating a higher probability that a minima has been achieved. Tightening the convergence criteria therefore has obvious benefits in that the resultant geometry should yield more accurate structure and results in subsequent calculations, but will require additional computational resources. Gaussian 16 permits three pre-set values of convergence tightness (standard, tight and very-tight) against four parameters; force, displacement, Root Mean Squared (RMS) force and RMS displacement, with very tight being the most desirable.

Due to the trade-off between accuracy, computational resources and the importance of geometry, optimisations are often completed using a stepwise methodology, gradually building the complexity until optimisation is achieved at the desired level. Where optimisations fail, the Hessian of the starting structure shall be explicitly calculated and the optimisation re-attempted. If this fails, the matrix shall be re-calculated at every guessed structure

within the optimisation. Resultantly, every selected molecule will be optimised using the following stepwise method towards the desired level of theory (DFT using MH06-HF hybrid functionals) using the selected target triple zeta basis set (Dunning's aug-cc-pVTZ) and achieving a very-tight level of convergence.

1. Optimise to a tight criteria using the Semi-Empirical (PM6) Level of theory [48]
2. Optimise to a tight criteria using the DFT (MH06-HF) level of theory and Pople Basis set 6-31
3. Optimise to a ttight criteria using the DFT (MH06-HF) level of theory and Pople Basis set 6-311++g(d,p)
4. Optimise to a very tight criteria using the DFT (MH06-HF) level of theory and Dunning Basis set aug-cc-pVTZ

A further consideration for optimisation (and subsequent calculations) is the use of restricted and unrestricted methods. In cases where there are unpaired electrons within a molecule, by definition there will be molecular orbitals that are singularly occupied. Conversely, in cases where all electrons are paired, all molecular orbitals will be fully occupied. Where there are singularly occupied orbitals i.e. radicals, these must be treated with unrestricted methods as restricted methods will not account for the unpaired orbital, slightly increasing the computational requirement.

After the successful optimisation of a molecule, it will then be analysed vibrationally to confirm that the optimisation was successful.

4.2 Vibrational

The vibrational analysis of the structure/bonds of a molecule that has been successfully optimised, affords two pieces of vital information; the thermodynamic, and IR absorption

properties of the molecule. Of primary importance are the IR absorption properties as, in addition to providing an excellent fingerprint of the molecule's electronic structure, they permit a check as to whether or not the prior optimisation was successful. This check is achieved by the consideration of any negative or imaginary frequencies resultant from the vibrational analysis. If one such frequency is observed this is typically indicative of a transition state [48]; any more than one imaginary frequency suggests that the structure is non physical.

As transition states are not being considered, any vibrational analyses resulting in one or more negative/imaginary frequencies are considered not to be representative and must be re-optimised and re-analysed vibrationally until no such frequencies exist. The chance of negative/imaginary frequencies being present is related to how representative the structure is to ideal, and is hence why the optimisation convergence is tightened prior to this and other subsequent calculations.

In order to ensure accuracy and a true test of a molecule's structure, the vibrational analysis must be undertaken using the same level of theory and basis sets as those used to optimise the structure, i.e. DFT (MH06-HF) and aug-cc-pVTZ basis set.

If the vibrational analysis proves the optimised structure to be sound, then the thermodynamic properties, also calculated as part of the vibrational analysis, can be assumed to be representative for the molecule. Thermodynamic calculations have been used in computational chemistry for a number of years, with rates of reaction, heats of formation and activation energies all being readily calculable. These methods can be used to predict daughter product speciation based upon favourable thermodynamic properties between parent and daughter molecules, i.e. where the net enthalpy of reaction is negative, and therefore contributes rather than requires energy from the system.

In quantum chemistry these calculations are reasonably easy, as contributions from rotation, vibration, translation and electronic motion are afforded through vibrational analysis. Therefore calculating the enthalpy and/or free energy of reaction can be undertaken using simple addition and subtraction according to Equation 4.1. Careful selection of the correct contribution must be made in order to calculate the correct property. For heats of formation, the sum of the calculated electronic ε_0 and thermal enthalpies H_{Corr} should be used and for the free energy of reaction, the sum of the calculated electronic ε_0 and thermal free energies G_{Corr} should be used, as described within [70].

$$\Delta_r H^\circ = \sum_{Products} \Delta_f H^\circ_{Prod} - \sum_{Reactants} \Delta_f H^\circ_{React} \tag{4.1}$$

Using this methodology, purported reactions can be tested to see if they are thermodynamically favourable. However, as previously mentioned, this research considers ionisation processes and as such, consideration must be given to the spin-state and charge of any molecule being tested. Calculation of the thermodynamics of the optimised ground state of the parent explosive materials and their ionic radical counterparts, does not offer any insight into potential daughter product speciation, however it does provide a measure as to the amount of energy required to ionise each molecule, i.e. the ionisation potential energy. This does provide useful insight as to the lowest amount of energy required to ionise the parent explosive.

4.3 Electronic

After successful optimisation and vibrational analysis, electronic properties (in addition to the IR) may be calculated based upon the optimised structure. This may be used alongside experimental evidence to elucidate any daughter product speciation resultant from the ionisation of a parent molecule. Of particular note is the provision of nuclear spin data (hydrogen, carbon, nitrogen, oxygen) that may be determined experimentally using

a NMR spectrometer. Anisotropic electron spin data can also be calculated which may be measured using an Electron Spin Resonance (ESR) spectrometer (also known as Electron Paramagnetic Resonance (EPR) spectrometer). UV-Vis light absorption data (UV-Vis) can also be calculated and may be measured by a spectrometer; this is is of particular importance for TATB as a colour change is well documented.

4.3.1 Nuclear magnetic resonance (NMR)

NMR shielding tensors may be calculated for each optimised structure utilising the same level of theory and basis set as that used to optimise. The Gauge-Independent Atomic Orbital (GIAO) method was selected (default in Gaussian 16) as it is acknowledged to provide accurate results as long as the initial optimisation was undertaken at a sufficiently high level of theory. As with experimental NMR, a suitable reference is required in order to calculate the chemical shifts of the molecule with respect to that reference. For hydrogen and carbon, the standard Gaussian 16 tetramethylsilane (TMS) reference was used. For nitrogen, the standard Gaussian 16 ammonia (HN_3) reference was used. Although rarely used, for oxygen, the standard Gaussian 16 water (H_20) was used. Each of these standards were available pre-optimised using DFT, the B3YLP hybrid functional and the Pople 6-311+g(2d,p) basis set.

4.3.2 Electron spin resonance

The anisotropic hyperfine coupling and electron spin *g* tensors may be calculated for molecules that have a non-zero net electron spin. The computation of such parameters affords two key pieces of information; firstly an ability to generate an ESR spectra which may be used alongside experimental evidence to fingerprint radicals (such as those potentially generated through gamma ray irradiation) and secondly, the ability to identify the potential location of the radical on the molecule in question after optimisation.

The same level of theory (DFT MH06-HF) may be used to calculate the various ESR electrostatic properties, however an ESR specific basis set should be used in order for calculations to be as representative as possible. This is an acknowledged departure from using Dunning's correlation consistent basis sets. However, as with the vibrational and NMR analysis, the ESR specific basis sets are simply testing the structure which has been optimised using the complex Dunning basis set. The basis set selected for the analysis needed to be compatible with DFT and resultantly the double zeta with polarisation functionals of Barone [71] called EPR-II, was selected. As with all other computational chemistry calculations so far, the various ESR constants may be calculated using the Gaussian 16 software package [68], however the visualisation of the radical location and the generation of an ESR spectrum is not possible in the GaussView visualisation software [69].

In order to visualise the location of the radical, a piece of software called Spinach [72] may be utilised to read the output of any ESR calculations undertaken with Gaussian 16. Both nuclear (NMR) and electron (ESR) couplings (J and Hyperfine) may be read into the software along with other related data (chemical shifts and the G-Tensor), allowing visualisation of both phenomena. However, the ESR properties (anisotropic hyperfine coupling constants and the g tensor) are of main interest for this calculation to enable radical location identification. This is highlighted in Figure 4.1, where the nuclear and electron spin couplings can be visualised for the neutral Phenyl radical.

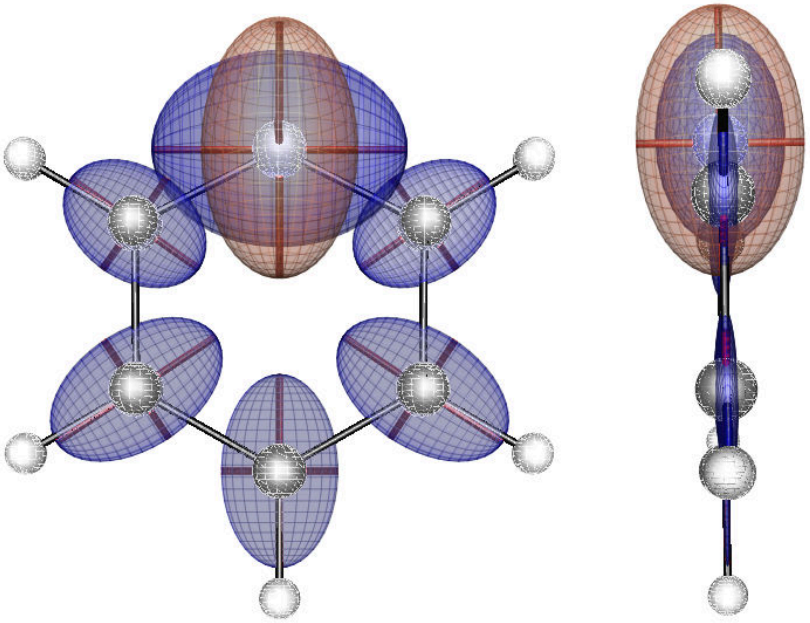

Figure 4.1: J-coupling (blue) and hyperfine coupling (orange) of the phenyl neutral radical [72]

Care must be taken upon the interpretation of results from Spinach, as it generates anisotropic hyperfine tensors based upon isotopes of atoms, and does not take into account relative abundance. Consider the phenyl radical example in Figure 4.1, an unpaired electron requires a non-zero nuclear spin in-order to interact, carbon-12 has a net nuclear spin of zero and therefore would give rise to no hyperfine coupling. Its isotope carbon-13, on the other hand, does have a net nuclear spin of $I = 1/2$ and therefore can give rise to hyperfine coupling interactions.

By default, Spinach assumes that all atoms are in an isotopic state such that it will lead to the generation of hyperfine coupling interactions. This can be corrected by normalising the coupling against the relative abundance of each isotope. An example of this is shown in Figure 4.2, where it can be seen that once relative atomic abundance is taken into account, the majority of hyperfine coupling originates from the unpaired spins of the hydrogen atoms.

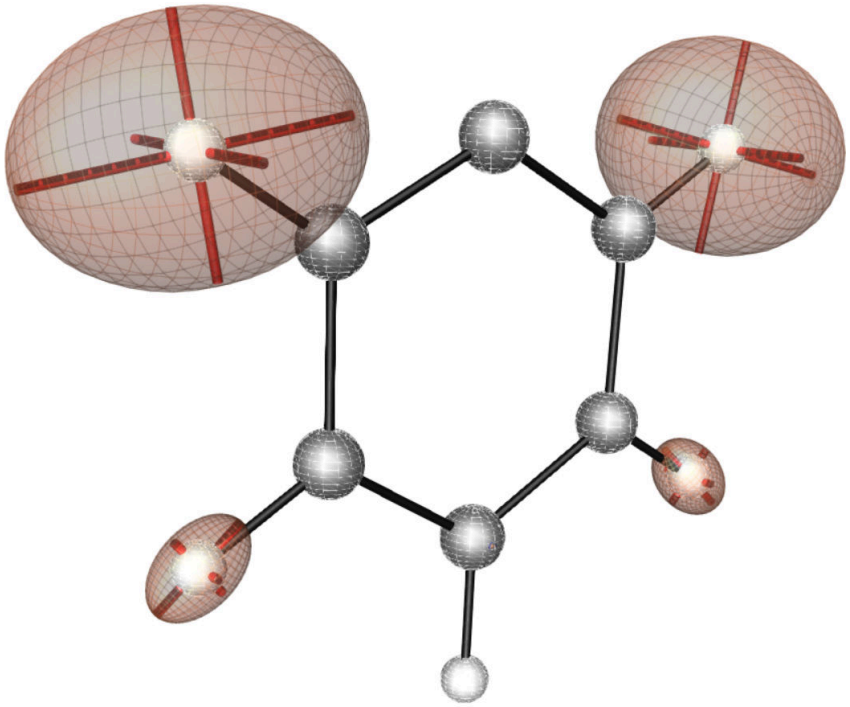

Figure 4.2: Corrected hyperfine coupling of phenyl neutral radical

The generation of uncorrected hyperfine coupling tensors is actually very useful as it does provide excellent evidence as to the location of the radical. This is because hyperfine coupling will be greatest the closer a radical is to a body with unpaired nuclear spin. Therefore the strongest hyperfine couplings will occur when a radical interacts with its own unpaired nuclear spin. Without the utilisation of isotopes, this detail would be missed for atoms that are abundant with no net nuclear spin, for example carbon-12 or oxygen-16.

The generation of predicted ESR spectra for radical molecules is also very valuable, affording useful comparisons to those typically obtained experimentally using ESR spectrometers. As with the generation of the visualisations of the nuclear and electron couplings, this cannot be achieved within the Gaussian software. Such simulated spectra can however be obtained through a MATLAB [73] toolbox called EasySpin [74], which can take the various electrostatic parameters from the ESR calculation, as well as experimental parameters such as spectrometer characteristics.

EasySpin [74] has a selection of different simulation functions available, which differ in applicability based on the type of analysis required. The pepper function was selected for all analyses as this is most suitable for the measurements and materials that are detailed within the latter experimental section, i.e. the generation of continuous wave (CW) ESR spectra for powders and crystals.

EasySpin computes the predicted ESR spectra based on each molecule's spin system, the so called g value and associated anisotropic hyperfine coupling. This is quite simple for isotropic systems which can be defined by single values for these three parameters, however this is a significant simplification and not applicable to complex systems such as the ionic radical species being considered. Resultantly the full g and hyperfine tensors calculated by Gaussian need to be utilised.

This does however come with a significant computational penalty and is practically impossible to calculate if contributions from the electron systems of each atom is considered for systems containing more than 6-7 atoms. A compromise needs to be achieved between treating the molecule isotropically versus using the anisotropic hyperfine tensor of each atom's electronic spin system.

This can be achieved by using the full g and hyperfine tensors but only for electron systems with significantly large anisotropic hyperfine coupling values within the tensor, i.e. only considering electron systems that have a significant contribution to the resultant signal. This methodology permits the calculation of an ESR signal using the full detail of the electronic systems of key atoms rather than significantly simplifying the electronic structures of every atom, of which the majority have little to no influence on the resultant signal.

An example of this is shown in Figure 4.3 where the top most spectra is generated from

the hyperfine coupling of the two closest (to the radical centre) hydrogen atoms only, with the bottom most spectra considering all five hydrogen atoms. It can be seen that the spectra are quite different.

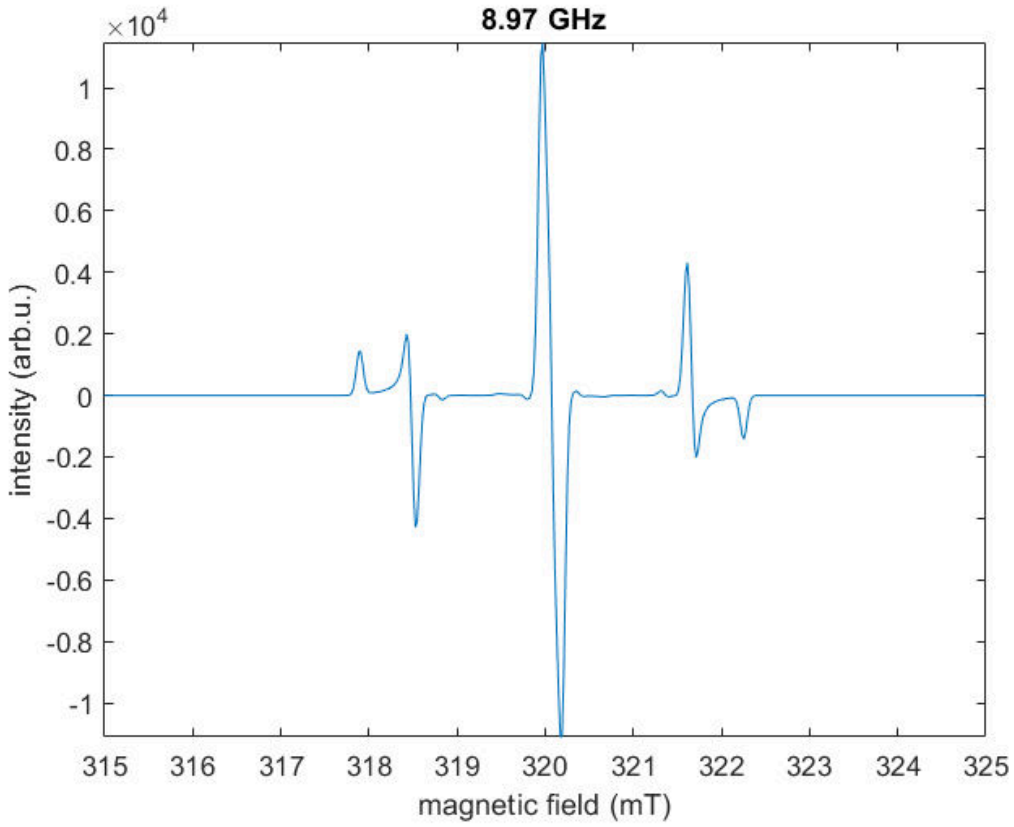

(a) Non-complex ESR spectra

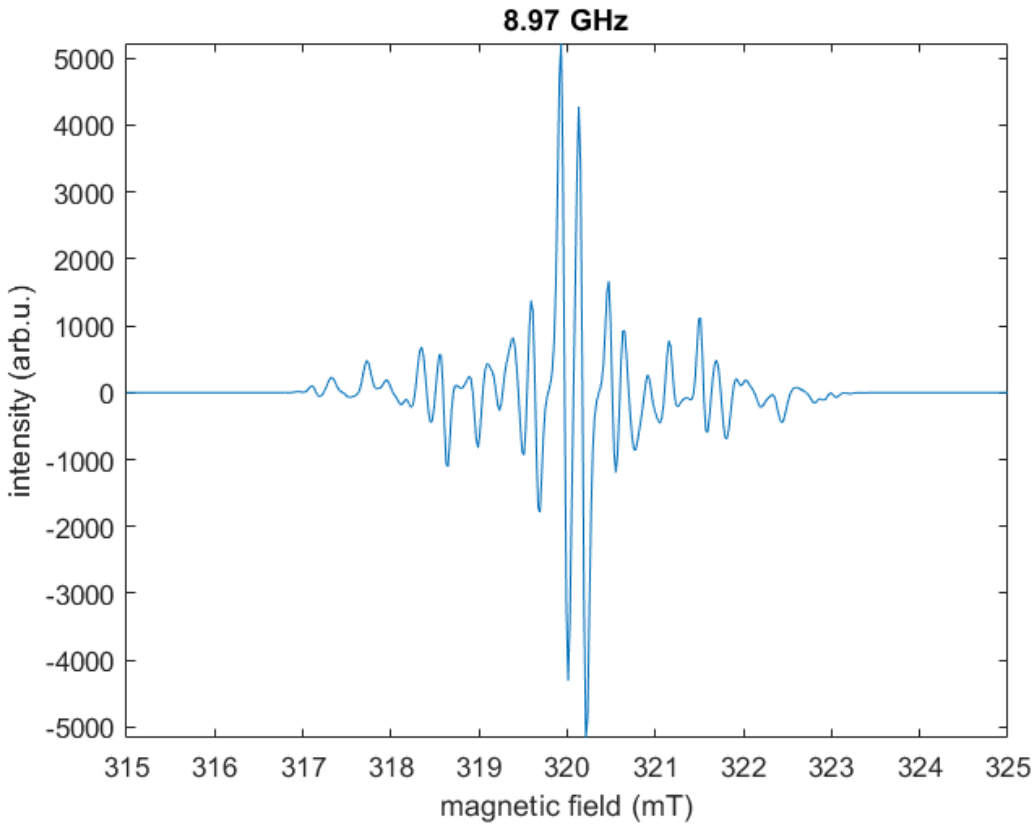

(b) Complex ESR spectra

Figure 4.3: Comparative predictive spectra of the phenyl radical

In addition to experimental parameters, EasySpin [74] requires a finite value of line broadening, otherwise the calculated spectra will be infinity sharp and uncharacteristic of real life measured spectra. This is quite a subjective parameter and care needs to be taken not to under or over broaden the calculated spectra. For all calculations, these broadenings must be considered on an individual basis, and shall be treated isotropically and defined by the peak-to-peak distance between the first derivative of the spectra.

An example of an over-broadened spectra can be seen in Figure 4.4, which is derived from the same hyperfine coupling contributions and g-tensor of the five hydrogen atoms that generated the spectra seen in Figure 4.3b.

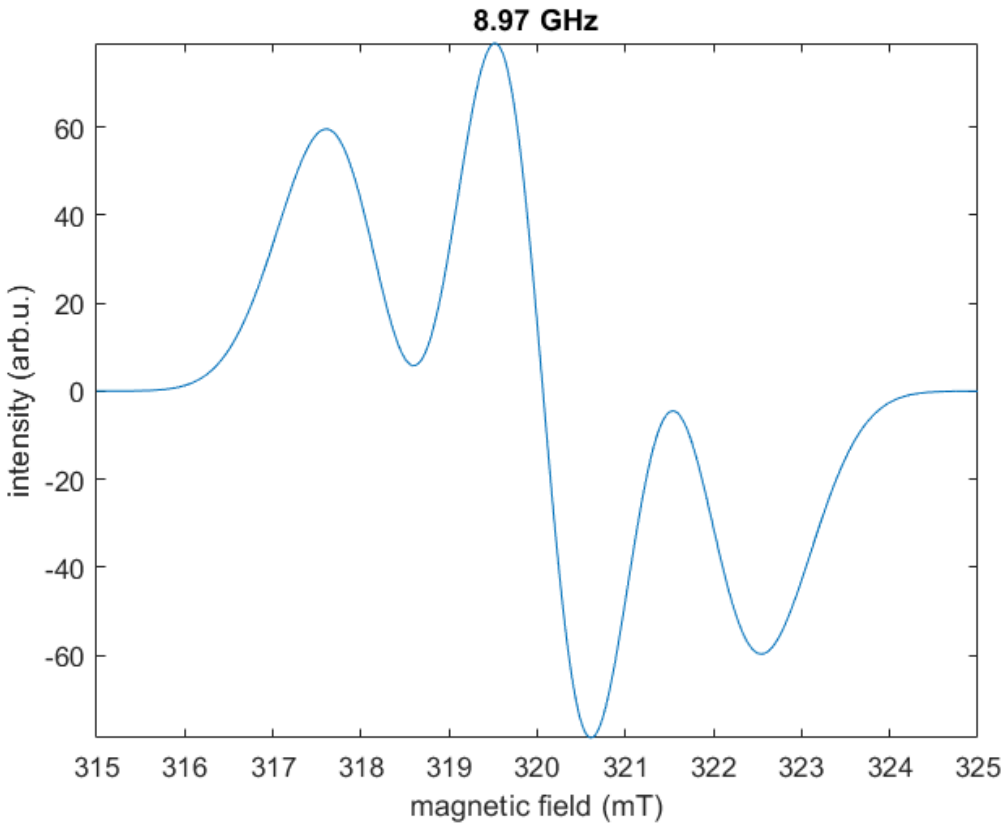

Figure 4.4: Over broadened predicted ESR spectra of phenyl radical

4.3.3 UV-VIS

The UV-Vis absorption spectra of predicted species can provide additional evidence that may be used alongside experimental data. There are numerous computational methods for obtaining the UV spectra, the vast majority of which are based upon the Franck-Cordon principle [48] which states that electron excitation/de-excitation processes occur within a molecule over such small time scales, that the geometry and structure of the molecule remains unchanged throughout the process. This approximation is key in permitting the calculation of electronically excited states of molecules based on the optimised structure of the molecule in its ground state. Without this approximation, such a calculation would require optimised structures for each electronically excited state, massively increasing the computational cost to the point of it being out of reach, except for only the most simple of systems.

There are four main types of calculation available in order to generate the UV-Vis absorption properties of a molecule; Semi-Empirical, Configuration Interaction (singlet excitations only) (CIS), Time Dependant Hartree-Fock (TD-HF), and Time Dependant Density Functional Theory (TD-DFT).

Semi-empirical calculations, such as those undertaken by Manaa [46] are of comparably low accuracy, with CIS, TD-HF and TD-DFT methods considered to be significantly more accurate [48]. However, for open shell systems such as radicals that require unrestricted methods, errors become significant for calculations undertaken at the semi-empirical, CIS and TD-HF level of theory and are much more acceptable for TD-DFT [48, 75]. In addition to this advantage, all ground state optimisations are undertaken using DFT, meaning that all structures would not need to be re-optimised at a different level of theory in order to obtain an accurate UV-Vis spectra. It was therefore concluded that the same level of theory, DFT, including electron-exchange hybrid functional MH06-HF, would be utilised for the required time dependant calculations.

One of the key questions with excited state calculations is the type and number required to be calculated. In real life, there are a huge number of potential excited states that an electron can be promoted to; calculation of all of these states is computationally prohibitive and almost impossible for all but the most simple of molecules. A compromise therefore needed to be achieved between the low fidelity pre-set of Gaussian (six singlet states) and the attempted calculation of all states. This compromise was the computation of the first fifty excited states, equally split between singlet and triplet excitations i.e. twenty five of each. This does not necessarily mean that the first fifty states are *real* and some calculated transitions may have a zero intensity, indicating that they are quantum mechanically forbidden. Therefore the correct interpretation of the simulation is that the first twenty five states are tested in both the singlet and triplet state to see if they are real. If they are, the corresponding absorption wavelength and magnitude are calculated, and spectra provided.

4.4 Approximation of solid state

One of the key advantages of employing an implicit (i.e. PCM) method vs explicit (i.e. ONIOM, PBC), is that the computational cost is comparatively minute, permitting the treatment of a molecule with very high levels of accuracy. However the disadvantage is that phenomena such as directional specific interactions, such as pi stacking, which is a known for TATB, will be treated as a unidirectional average interaction. Consideration was given to all methods, and despite the disadvantage of the implicit solvent method, its advantages of using a higher level of theory and reduced computational requirements (especially considering the number of molecules requiring simulation) led to its selection over the ONIOM and periodic boundary conditions.

For explosive molecules that are part of complex crystal structures consisting of massive

numbers of identical molecules in every direction, this is believed to be a fair approximation to determine thermodynamic and spectral properties. It is acknowledged that as daughter products and possible crystal defects grow with increasing radiation dose, this approximation may become less suitable and molecular dynamic simulations more so. It is envisaged that the utilisation of implicit solvent methods on individual molecules will be utilised to ascertain the main interactions of gamma radiation on the selected materials, with the results of this study informing future work that is beyond this study, which can then focus on a reduced number of molecules using either molecular dynamics or ONIOM/PBC methods, with high levels of quantum mechanical treatments.

Specifically, the implicit solvent method selected was the Polarisable Continuum Model which considers contributions from electrostatic, dispersion-repulsion and cavitation, due to its relative simplicity and availability within Gaussian for DFT (and HF) methods. The required inputs for the model are the solvent's stoichiometry, used alongside the Universal Force Field method [48] to calculate the cavitation radius, and the dielectric properties ε_0 of the solvent. Literature values were obtained for TATB [76], HMX [77]and PETN [77] and are shown in the below Table 4.1. For vibrational calculations only, the dynamic dielectric properties ε are also required, however, these could not be found in the literature for these materials, and as such were approximated to the static dielectric constant.

Name	Stoichiometry	$\varepsilon/\varepsilon_0$
TATB	$C_6H_6N_6O_6$	4.0
HMX	$C_4H_8N_8O_8$	3.81
PETN	$C_5H_8N_4O_{12}$	2.71

Table 4.1: PCM model parameters

In an effort to understand the impact of applying the implicit solvent approximation, all calculations were undertaken in both the gas and pseudo solid state, effectively doubling

the required number of calculations for each molecule.

4.5 Employed process flow for computational investigation

Figure 4.5 shows a summary process flow for the computational chemistry calculations. Steps 1 and 2 are required for each molecule, however step 3 is discretionary and applicable to select molecules, i.e. ESR calculations shall only be undertaken on species with unpaired electron systems and UV-VIS calculations on materials with a suspected chromophore.

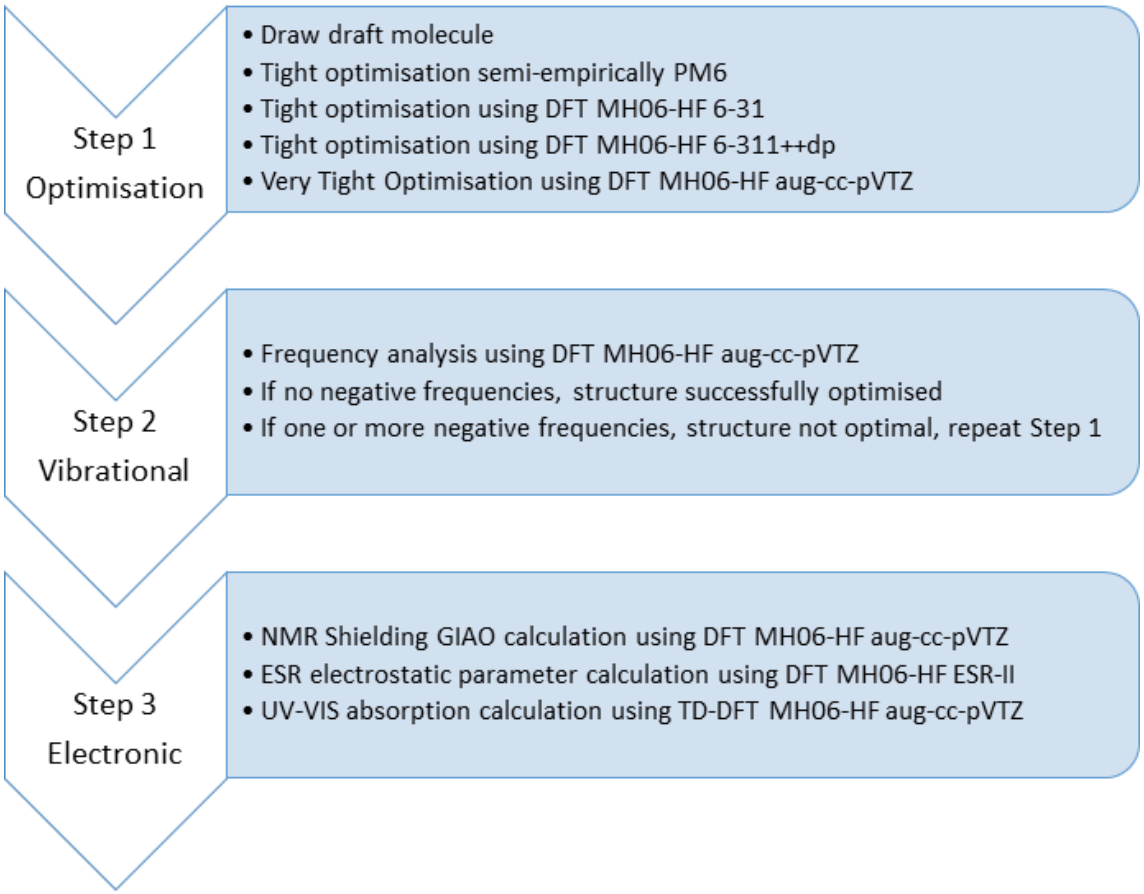

Figure 4.5: Modelling flow diagram

4.6 Selected molecules

As alluded to previously, no computational method exists that will predict the decomposition mechanisms or resultant product(s) from gamma ray ionisation, rather a selection of daughter products need to be tested to see if the thermodynamics are favourable for them to exist. This information, coupled with any derived electronic structure data, and corroborating experimental data ultimately provides evidence that a purported mechanism and daughter product is real. Resultantly, a list of molecules was generated from as many literature sources as possible in order to determine the most likely daughter product(s) and mechanism resultant from ionisation of the three parent molecules, TATB, HMX and PETN.

As charge must be conserved, any decomposition product(s) resultant from gamma ray ionisation must be positively charged. This net charge must remain as further decomposition steps occur. However, in cases where fragmentation occurs, it is unknown which fragment will retain the charge and which will not. As a result each fragment will need to be simulated in each state, with the combination yielding the most favourable thermodynamics the most likely. This causes a significant increase in the number of molecules required to be simulated, which is again exacerbated with each molecule being simulated in both the gas and pseudo solid states. This is highlighted in Figure 4.6, which considers molecule A being ionised and fragmenting to molecules B and C. With the inclusion of the implicit solvent model, this interaction requires twelve molecules to be considered.

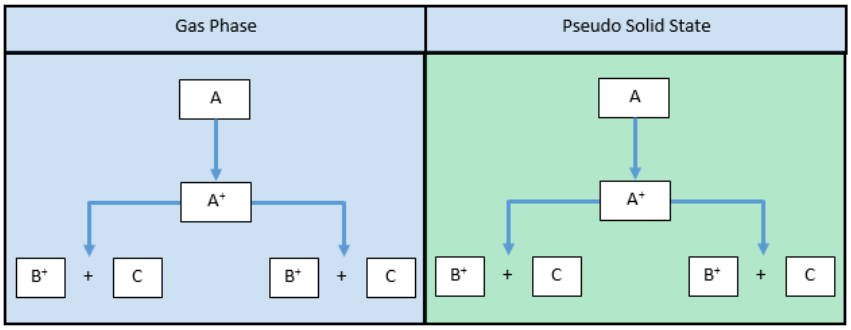

Figure 4.6: Example fragmentation

As seen from Chapter 3, only a very limited amount of computational modelling has been undertaken which considers the effect of gamma radiation on explosive materials. Published works mainly focus on predicting various properties of purported decomposition products [46], with few papers additionally considering the thermodynamic requirements to form the suggested daughter products resultant from gamma radiation i.e. from an ionic and radical state [78, 79]. Of particular note is Nguyen [79], who used computational chemistry to predict the fragmentation of TNT that has been ionised through negative and positive electrospray (i.e. not gamma radiation), used in mass spectrometers that are often coupled to analytical techniques such as liquid and gas chromatography. He correctly considered the thermodynamics of the purported fragmentations and decompositions from the parent ionic and radical TNT molecule.

TATB

TATB has been perhaps the most studied explosive with regard to gamma radiation, with a selection of works [46, 80, 43, 52, 44, 42, 49, 53, 78] experimentally and theoretically exploring, suggesting and potentially identifying a number of daughter products. Two key molecules have been strongly suggested as possible daughter product resultant from the exposure of TATB to ionising gamma radiation in a debate covering decades; a mono-furazan and a mono-nitroso derivative of TATB. There has also been suggestions that

the degradation of TATB continues past the mono-furazan and mono-nitroso derivatives, resulting in di-furazan and di-nitroso equivalents [42]. One of the more recent pieces of work, Ying [52], suggested that a phenoxyl radical is also a possibility. These five molecules form the basis of the daughter products to be tested for the degradation of TATB through ionisation, however a few additional molecules have also been added as potential hybrids. These include reactions that consider the isomerisation of a nitro group to a nitrite prior to rearrangement and/or fragmentation as well as complete loss of NO_2 and NH_2 groups.

The reaction pathways have been mapped out, as shown in Figure 4.7, with the first reaction A representing the initial ionisation of TATB. It can be seen from the map, that there are a significant number of molecules requiring simulation, at first glance it would appear that 20 such species exist if small fragments such as H_2O and O_2 are included. However as previously alluded to, it is unknown which species will retain the positive charge in the case of fragmentation, therefore each molecule needs to be simulated in both the ground and ionic radical state. The only exception to this is where molecules do not undergo fragmentation but undergo re-arrangement, where the charge must be retained by the molecule. These bodies are identified within the maps by a set of square brackets. In total this takes the number of species required to be simulated to 37, which effectively doubles to 74 due to the analysis being undertaken in both the gas and pseudo solid states.

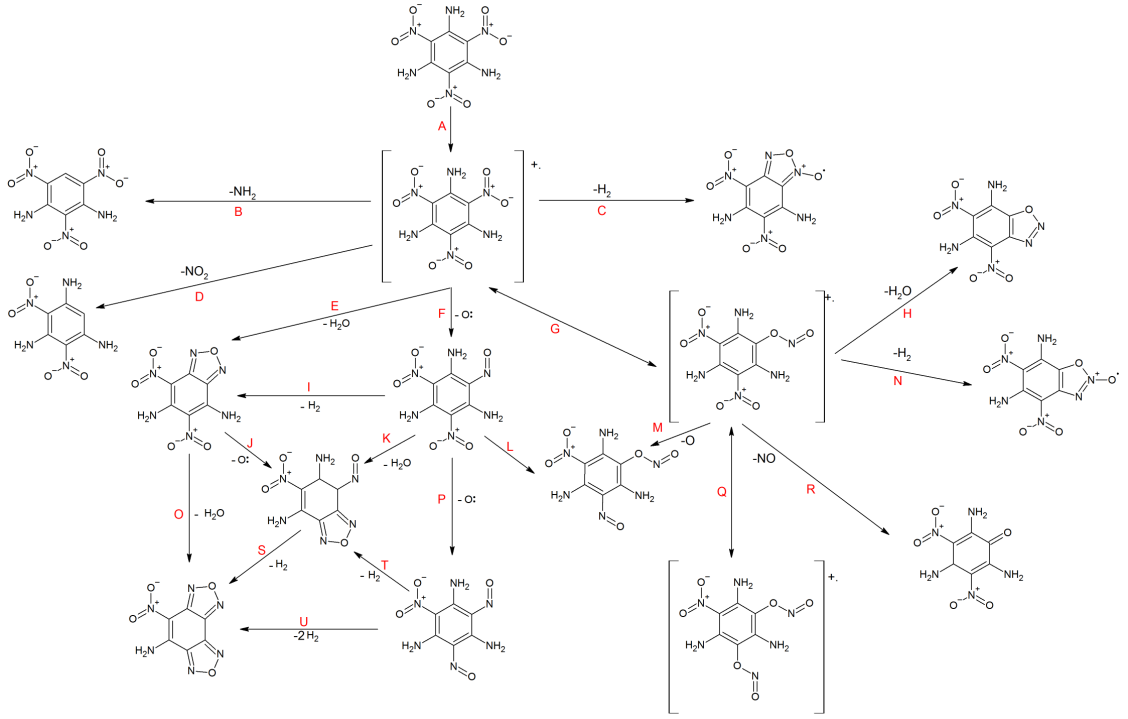

Figure 4.7: TATB decomposition map

HMX

HMX has garnered a similar amount of interest to TATB with regard to its interaction with gamma radiation up to and including the 1990's [28, 30, 31, 36, 37, 40]. There is a fair amount of literature available addressing potential thermal, UV and organic (bacterial) decomposition mechanisms of HMX, however most of this work concludes that HMX is markedly resistant to such reactions. There are limited works covering potential daughter products resultant from gamma radiation of HMX. Perhaps most notably is Miles [36, 37], who tentatively identified the generation of the chain terminating NO_2 radical and Thomas [28] who measured a significant generation of gaseous N_2 amongst other gasses to a lesser extent. Beard [40] undertook X-Ray irradiations of RDX (considered applicable to HMX due to their chemical similarity), and suggested some purported decomposition pathways based upon the photolysis i.e. non-ionisation of the N-NO_2 bond. Despite this difference, Beard's suggested decomposition pathways can be tested using

the computational technique to investigate if they are favourable for decomposition due to ionisation. Consideration of the cleavage of bonds other than N-NO_2, potentially suggests the loss of hydrogen from the C-H bond, and also potential ring opening resultant from the breakage of the C-N bond.

Based upon these works and consideration of other possible bonds breaking, a decomposition map for HMX resultant from ionisation has been generated and is shown in Figure 4.8. As with TATB, consideration must be made as to the charge and spin-state of all fragments and resultant combinations in order to find the most energetically favourable pathway, increasing the number of required simulations. In cases where a re-arrangement occurs prior to fragmentation, the molecule can only possibly exist in the ionic doublet spin-state, resultant from the loss of an electron; these are shown by square brackets in Figure 4.8.

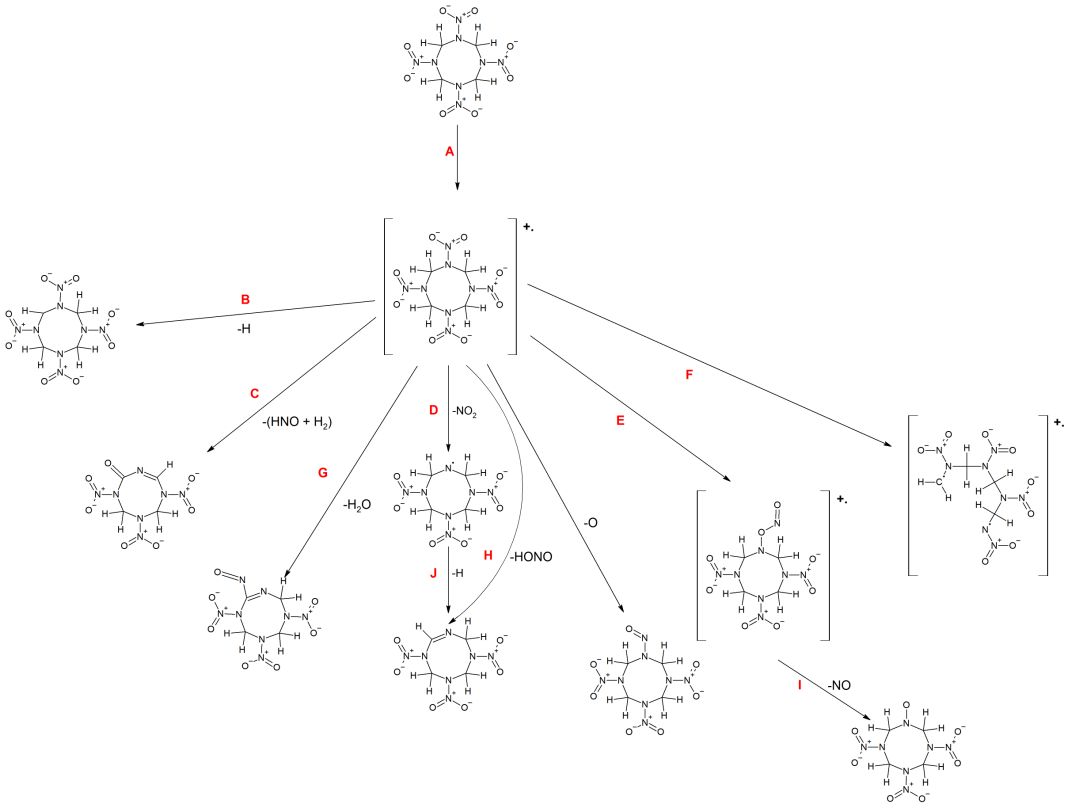

Figure 4.8: HMX decomposition map

PETN

PETN has received interest comparable to that of HMX, with more attention being given to the material in the previous century than the current. One of the more pertinent findings was that of Miles et al [38] that identified a long lived chain terminating radical when PETN is irradiated, which was purportedly assigned to the NO_2 radical. This suggests that the O-N bond may be the most susceptible to cleavage upon gamma radiation, however this was identified as a chain terminating radical, with other spectra observed prior.

As with the other materials, the relative ease of exposing PETN to UV over gamma radiation has caused an increased wealth of literature covering decomposition through processes such as photolysis. One of the more relevant papers is the computational and experimental study of Yu and Bernstein in 2011 [81] which considers the decomposition of PETN resultant from electronic excitation. Whilst this work does not cover ionised electronic states, the decomposition pathways may be valid for ionised PETN, and have therefore been considered. Figure 4.9 details the summarised decomposition pathways and products that are considered plausible for ionised PETN that will be tested using computational chemistry.

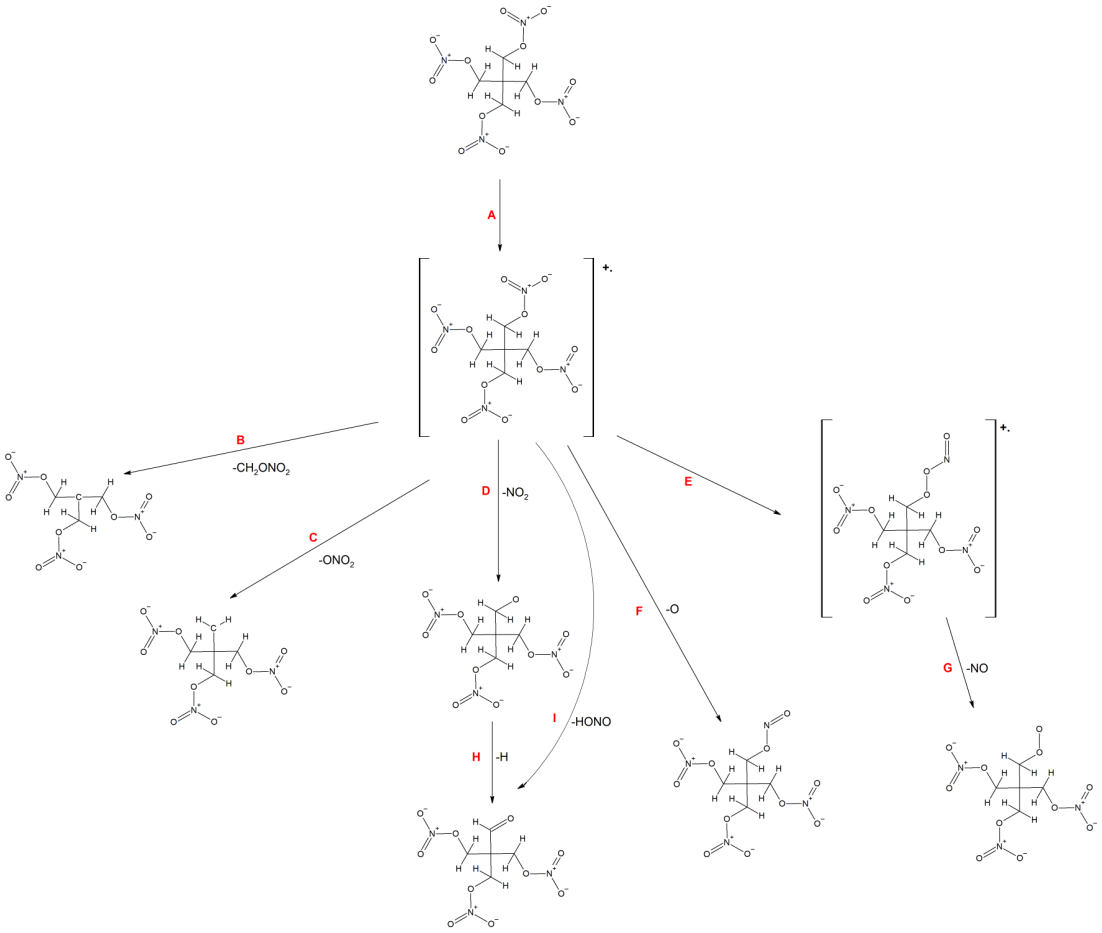

Figure 4.9: PETN decomposition map

4.7 Results

The following details key computational results obtained from this part of the study for TATB, HMX and PETN. A brief discussion of the results is presented where appropriate, however a more in-depth analysis and discussion can be found later in Chapters 6, which considers both computational and experimental evidence for each material independently.

4.7.1 TATB and derivatives

Due to the significant number of species being considered, presentation of each molecule's optimised geometry, thermochemical and electronic structure (IR, NMR, ESR and UV-Vis) data and spectra is of limited value and hence data for only key molecules of interest, namely TATB, mono-furazan, mono-nitroso, mono-nitrite and the mono-phenoxyl derivatives are presented at this level of detail. Extensive data and spectra for each molecule can, however, be found in the appendix.

The thermochemical data for all molecules will be considered in order to assess the thermodynamically favourable decomposition route for TATB upon irradiation.

TATB baseline and ionic radical

TATB and its ionic and radical equivalent (charge +1, doublet spin state) were both successfully optimised in both the gas and pseudo solid states to the required level of theory and to the required convergence threshold. The optimisation for the gas phase ground state TATB molecule was particularly difficult, believed to be attributed to a very shallow potential energy surface. This is unsurprising as TATB is a symmetrical molecule that has complex intra-hydrogen bonding with nitro groups that are free to rotate and contort, with small adjustments to both of these parameters generating numerous local, but not global, minima on the potential energy surface. This is exacerbated in the gaseous ground level state, as no external force is applied to constrain the molecule through use of the PCM model, or asymmetry present due to the lack of an electron.

Optimisation for the gas phase ground state equivalent required the Hessian matrix to be calculated explicitly at each optimisation iteration; almost 300, each taking approximately 5 hours to complete on a 500 processor cluster. The other three molecules were comparatively simple to optimise, however the pseudo-solid state did require the explicit

Hessian to be calculated at the start of the first optimisation iteration, in order to achieve a successful optimisation at the required very tight criteria.

The resultant ground state molecules appear as expected, with the difference in geometry, electron density and electrostatic properties, as shown in Figure 4.10 being negligible between the gas and pseudo solid states. There is a notable difference, also shown in Figure 4.10, when compared to the equivalent structures of the ionic TATB in both the pseudo solid and gas states. There is an obvious twist on one of the nitro groups compared with the baseline molecule, and perhaps unsurprisingly, a reduction in the the electron density and subsequent electrostatic properties of the molecule.

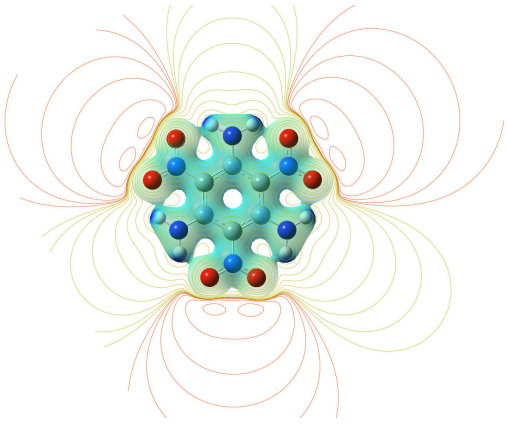

(a) TATB - gas phase

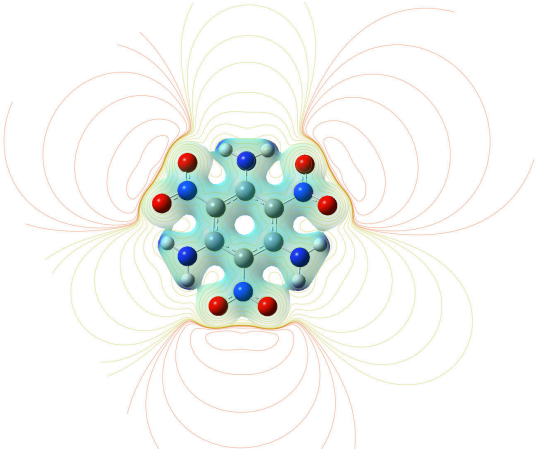

(b) TATB - pseudo solid state

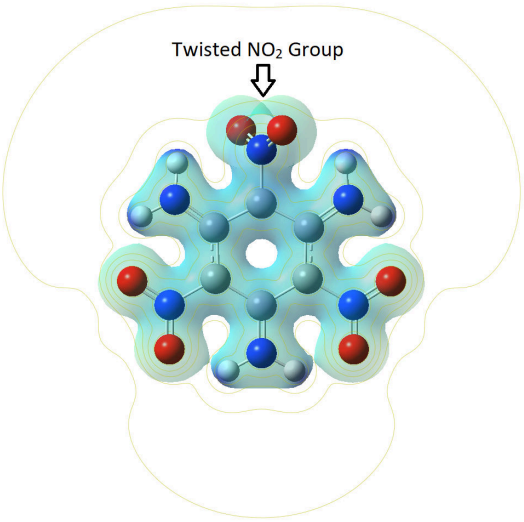

(c) Cation radical derivative of TATB - gas phase

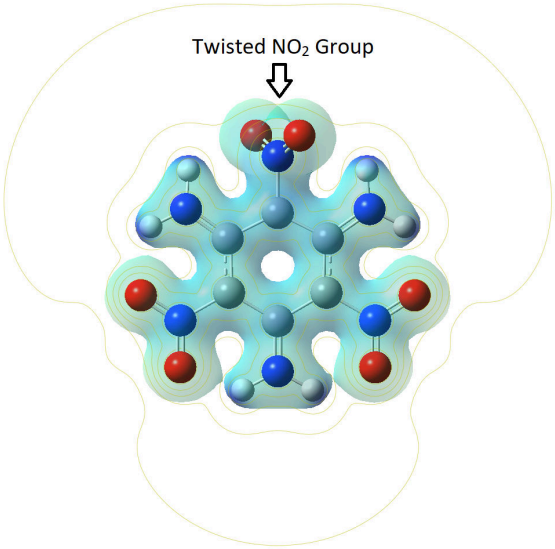

(d) Cation radical derivative of TATB - pseudo solid state

Figure 4.10: Optimised structures, electron densities and electrostatic potentials of TATB and its cation radical derivative

Both structures were submitted for vibrational analysis which yielded no negative frequencies for all four molecules, indicating that the structures had been successfully optimised. There was a negligible difference in the calculated vibrational/IR spectra between the gas and pseudo solid states, which is unsurprising as the analysis is undertaken on the optimised structures which were very similar. There was, however, a notable difference in the data obtained for the ionic radical when compared against the baseline; again this is unsurprising as there was a clear difference between the optimised structures. Corre-

sponding IR spectra for baseline and ionic TATB in the pseudo solid state can be found in Figure 4.11 with the resultant calculated thermochemical data for all four vibrational analyses shown in Table 4.2.

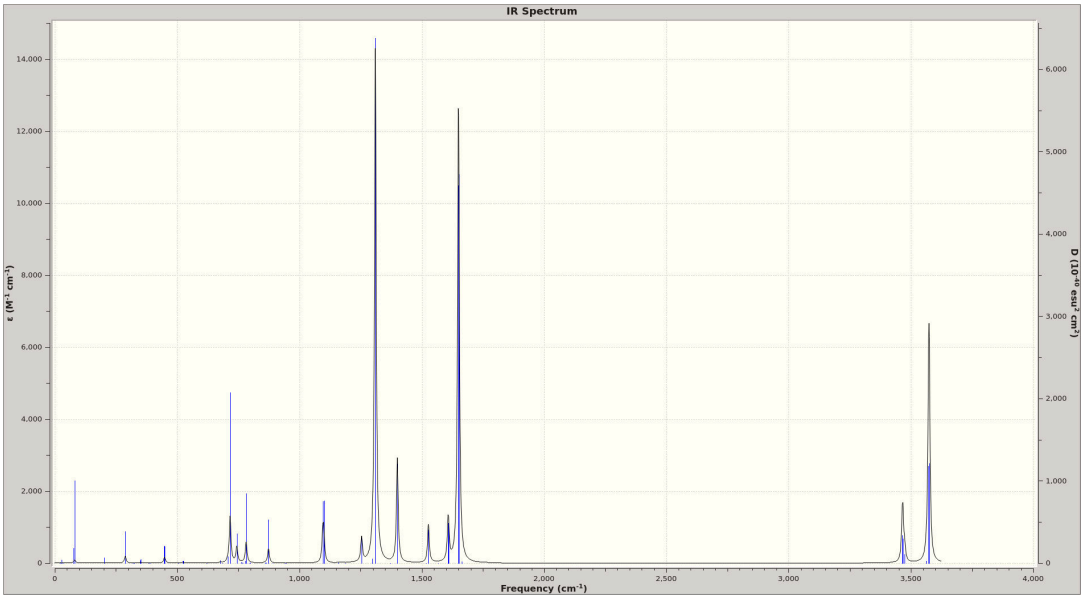

(a) TATB

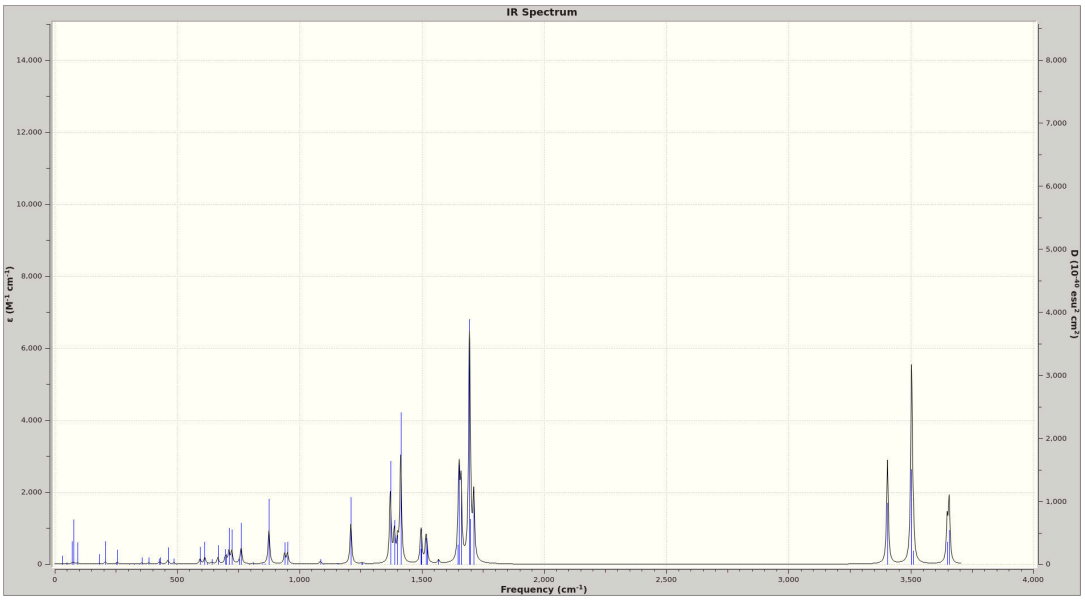

(b) Cation radical derivative of TATB

Figure 4.11: Predicted IR spectra of TATB and its cation radical derivative

Phase	Charge	Spin	ε_0	ε_{ZPE}	E_{tot}	H_{corr}	G_{corr}	C_v
Gas	0	1	-1012.0148	0.162840	0.17725	0.178194	0.115935	54.087
Solid	0	1	-1012.0235	0.162199	0.176592	0.177536	0.117709	54.392
Gas	+1	2	-1011.6635	0.162601	0.177502	0.178446	0.117825	55.728
Solid	+1	2	-1011.7290	0.162424	0.177301	0.178245	0.118361	55.926

Table 4.2: TATB thermochemical data (DFT MH06-HF - aug-cc-pVTZ)

Where ε_0 - Electron Energy (Hartrees), ε_{ZPE} - Zero-point Energy Correction (Hartrees), E_{tot} - Thermal Correction to Energy (Hartrees), H_{corr} - Thermal Correction fo Enthalpy (Hartrees), G_{corr} - Thermal Correction to Free Energy (Hartrees) and C_v - Heat Capacity (cal mol^{-1} Kelvin^{-1})

The differences between the gas and pseudo solid states for both TATB and its ionic and radical equivalent are reasonably small, and in line with expectations from the small differences seen in the corresponding spectra obtained through vibrational analysis. There is, however, a much more notable difference in the calculated energies between the baseline and ionic radical species of TATB which corresponds to the loss of the electron and is equivalent to the first ionisation potential energy E_1 of TATB, which is calculated as the difference in the total electron energy between TATB and its ionic radical and is presented in Table 4.3.

The calculated numbers for the ionisation potential of TATB are orders of magnitude lower than that of any gamma ray, indicating that ionisation will be all but certain upon such an interaction. Using the Planck-Einstein relationship [12] the equivalent ionisation wavelength may also be calculated and is also presented within Table 4.3. The resultant ionisation wavelengths sit towards the higher end of the UV spectra in terms of energy and tentatively suggest that the affect of gamma and UV radiation on TATB may be comparable, a point that is not surprising considering the reported greening for both UV and

gamma ray exposures [46, 52, 43, 66].

Phase	E_1 (eV)	λ (nm)
Gas	9.56	129.71
Pseudo Solid	8.01	154.81

Table 4.3: First ionisation potential of TATB

The UV-Vis wavelength spectrum is of particular interest for TATB, due to the widely reported discolouration seen in the material when exposed to ultraviolet, x-ray and/or gamma radiation. The optimised structures of both baseline TATB and its ionised equivalent were analysed in both the gas and pseudo solid states using Time Dependant Density Functional Theory to generate an absorption spectra in the UV-Vis region.

As with the vibrational analysis, differences between the calculated spectra of the gas phase and pseudo solid state were negligible with the main difference being in the magnitude rather than the frequency/wavelength of the absorption peaks. There was, however, a much more notable difference, as shown in Figure 4.12, between the TATB and its ionised equivalent regardless of being simulated in either the gaseous or pseudo solid state. Both spectra are dominated by absorptions within the ultraviolet region and lower wavelengths of visible light, unsurprising for TATB which, when pristine, appears whitish-yellow. The significance of the UV-Vis spectral results will be examined in more detail later on, however it is noted that two absorption are present around 500 nm which corresponds to the colour red. Such absorptions make a material look comparatively more blue, which could mix with the yellow of TATB to look green overall.

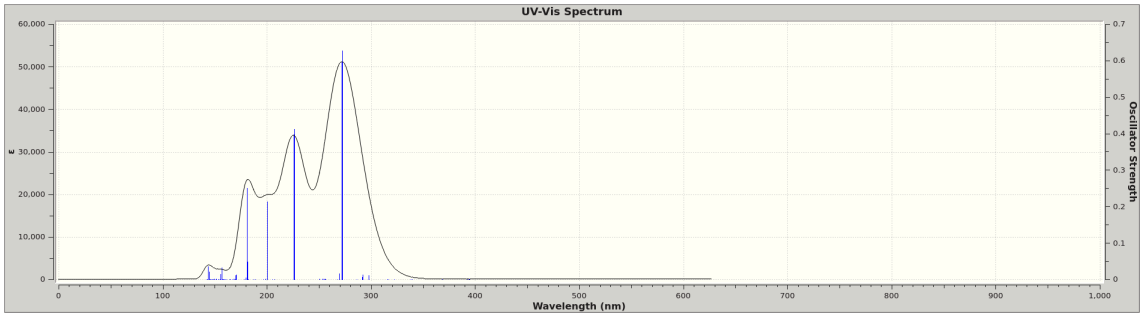

(a) TATB

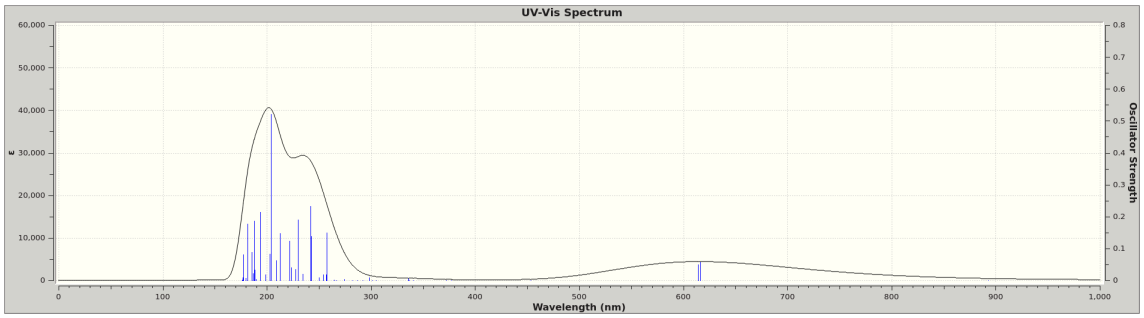

(b) Cation radical derivative of TATB

Figure 4.12: Simulated UV-Vis absorption spectra of TATB and its cation radical derivative

The nuclear magnetic resonance properties for both molecules in the gas and pseudo solid states were successfully calculated. The predicted NMR spectra mirrored that which had been observed within the vibrational analysis, in that there was a slight difference between the gas state and pseudo solid states for both the TATB and its ionic radical degradation product, where spectra generated in the pseudo solid-state suffered some expected anisotropy compared to the much more symmetrical gas phase predictions.

In keeping with the previous analyses, a marked difference was observed in the spectra between the baseline and ionic radical variants of TATB. The chemical shifts, relative to the appropriate reference, of the hydrogen, carbon, nitrogen and oxygen atoms closest to the twisted nitro group of the ionic radical species showed a significant difference when compared to the atoms of other equivalent groups of the molecule. This difference, as highlighted for the predicted proton chemical shifts against TMS in Figure 4.13, indicates a significantly different local magnetic field for atoms within the twisted nitro group. As

these local magnetic fields are dominated by the local molecular orbitals/electrons, this difference suggests a significantly different local electronic structure which, in this case, must be indicative as to the location of the withdrawn electron.

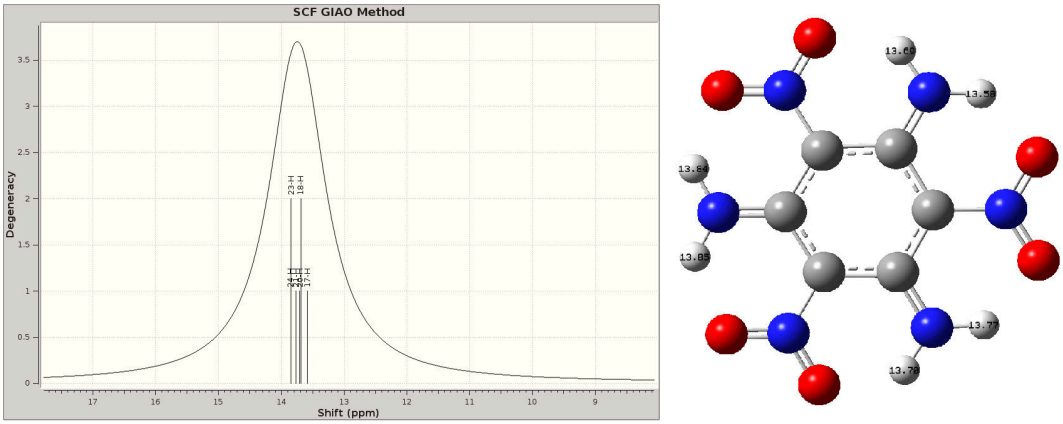

(a) TATB

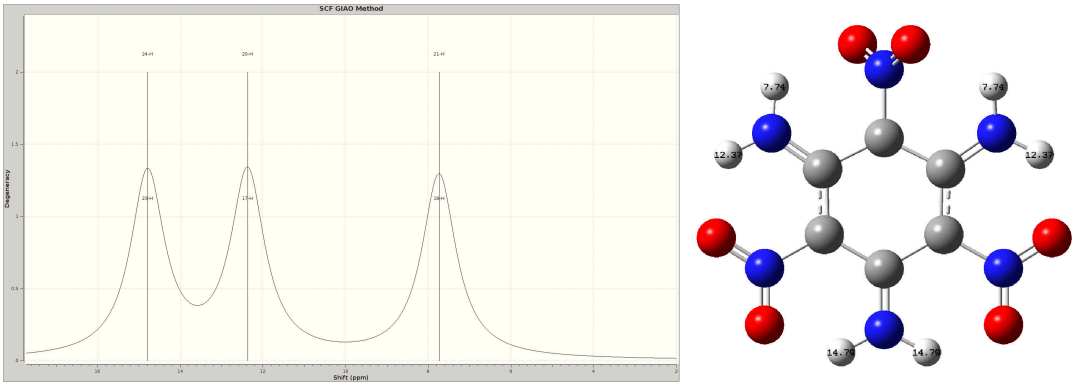

(b) Cation radical derivative of TATB

Figure 4.13: Simulated proton NMR spectra of TATB and its cation radical derivative

The electrostatic properties of both the ground and ionic radical states were also calculated successfully for both the gas and pseudo solid states. Although the calculation is redundant on molecules with no net electron spin, it was deemed valuable to undertake on one non-radical molecule as well as its ionic radical equivalent to show that any differences can be attributed to the lack of an electron. The calculations successfully generated an isotropic g-tensor and no hyperfine coupling constants for the non radical baseline TATB, indicating that there is no net unpaired spin in the molecule. For the ionic radical

equivalent, anisotropic hyperfine coupling and g tensors were generated indicating the presence of a non-zero net spin for the molecule.

The output from both files was processed through Spinach [72] which highlighted the lack of hyperfine coupling for the non radical but also the strong coupling of the electronic structure of the carbon atom connected to the twisted nitro group, indicating the location of potential electron deficiency in the molecule; this was also confirmed by the analysis of the atomic charges of the molecule, derived using the Mulliken population analysis [48]. Representations of the molecules can be found in Figures 4.14a and 4.14b, where the blue field indicates the NMR chemical shift tensors and the orange field indicates the electron hyperfine coupling tensor. The resultant electronic anisotropic hyperfine coupling structure for the ionic derivative of TATB suggests that the radical species should be carbon centred and located at the bottom of the twisted nitro group. There are small contributions from the anisotropic hyperfine coupling of adjacent carbon atoms, suggesting that this is the most energetically favourable position for the radical and lends itself to the theory of radical stabilisation through pi-bonding resonance.

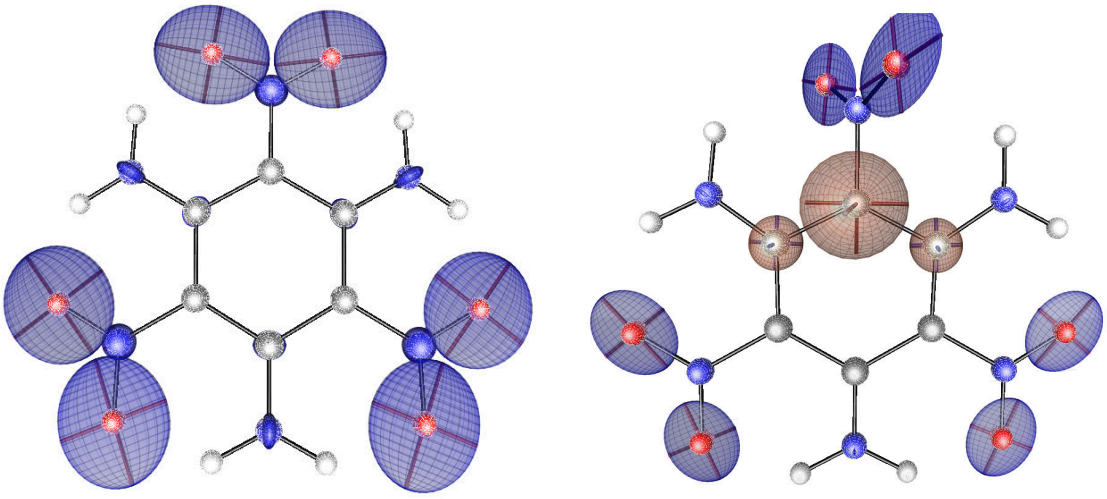

(a) TATB

(b) Cation radical derivative TATB

Figure 4.14: Structure of TATB and its cation radical derivative with hyperfine (orange) j-coupling (blue) tensors

As mentioned previously, care should be taken when interpreting hyperfine coupling tensors produced from Spinach. The large contributions suggested from the carbon atom are based upon the radical interacting with the unpaired neutron present within a carbon-13 isotope. Whist this technique is useful for identifying the preferential location of a radical, relative abundance must be taken into account in order to ascertain real life couplings, the significant majority of coupling comes from the adjacent nitrogen of the twisted nitro group, as shown in in Figure 4.15.

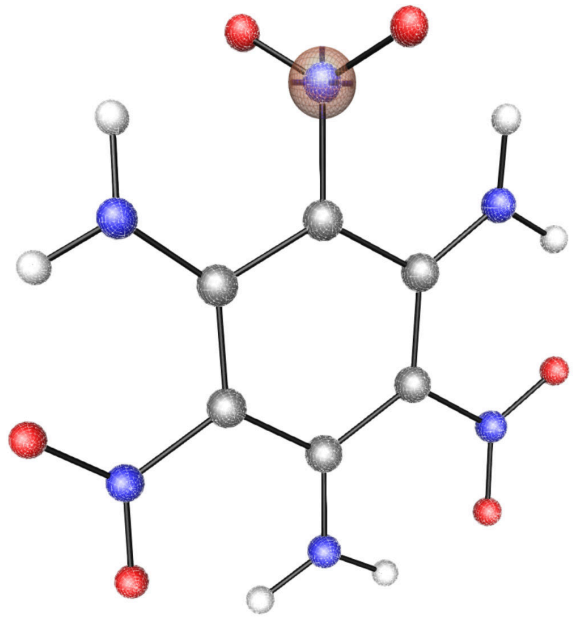

Figure 4.15: Structure of TATB cation radical with hyperfine coupling adjusted for atomic abundance and anisotropy

The computed g-factor (g) and hyperfine coupling (A) constants for the nitrogen atom (both in tensor form) are presented below. Both the g and the hyperfine coupling tensors were corrected for anisotropy before spectra generation:

$$g = \begin{pmatrix} 2.004794 & 0.000000 & 0.001373 \\ 0.000000 & 2.004035 & 0.000000 \\ 0.001373 & 0.000000 & 2.004989 \end{pmatrix} A = \begin{pmatrix} -0.601308 & 0.000000 & 0.036090 \\ 0.000000 & -0.636255 & 0.000000 \\ 0.036090 & 0.000000 & -0.562404 \end{pmatrix}$$

A simulated ESR spectra was generated using these derived computed parameters. In an effort to make the simulation as comparable as possible to future experimental evidence, additional variables (such as a cavity frequency of 8.97 GHz) were derived from the available ESR spectrometer. The resultant symmetrical three peaked spectra is shown in Figure 4.16 and is typical for a single unpaired electron interacting with a nitrogen-14 atom, which has a nuclear spin of 1.

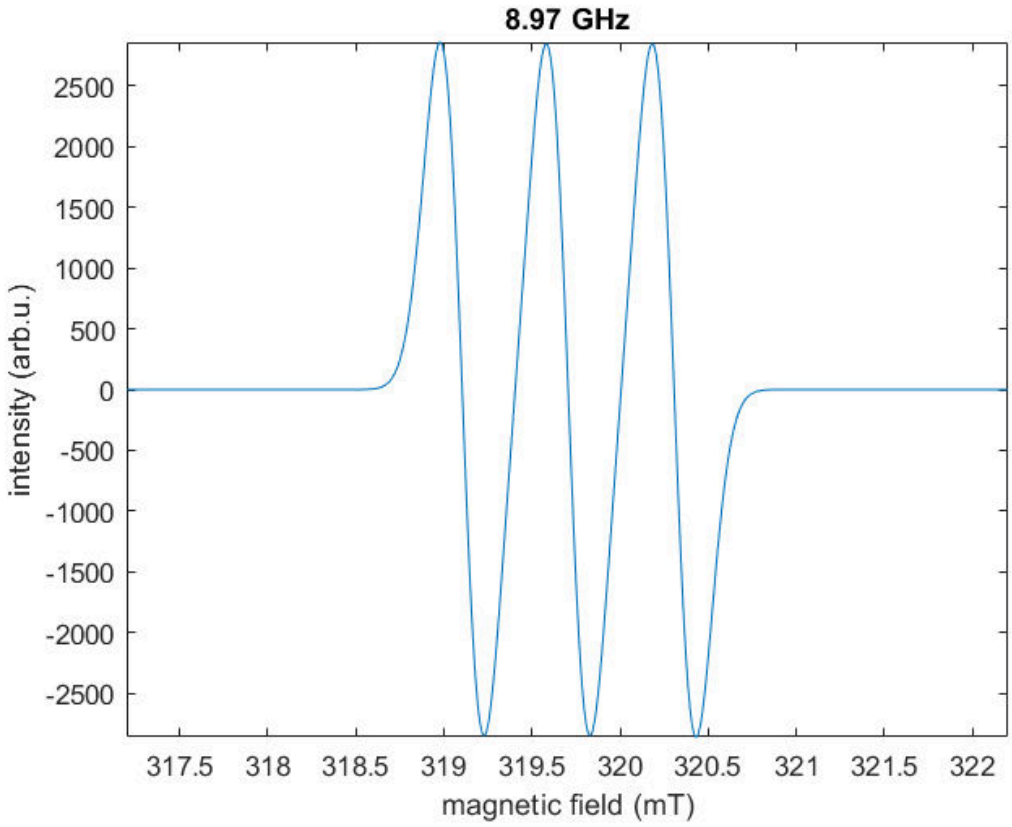

Figure 4.16: Simulated ESR spectra for cation radical derivative of TATB

Mono-furazan TATB derivative

Optimisation was successful to the required level of theory for both the ground state mono-furazan and its ionic radical derivative, in both the gas and pseudo solid states. Resultant molecular geometries appeared to be very similar between the ground and ionic radical state molecules with the exception of a slight twist to one of the nitro groups of the ionic-radical compared to the ground state, in keeping with that observed for the TATB molecule and its ionic radical derivative. A similar difference was observed within the electron density and electrostatic potentials between ground and ionic radical states, as shown in Figure 4.17, and only small differences could be seen between each molecule in the gas and pseudo solid state.

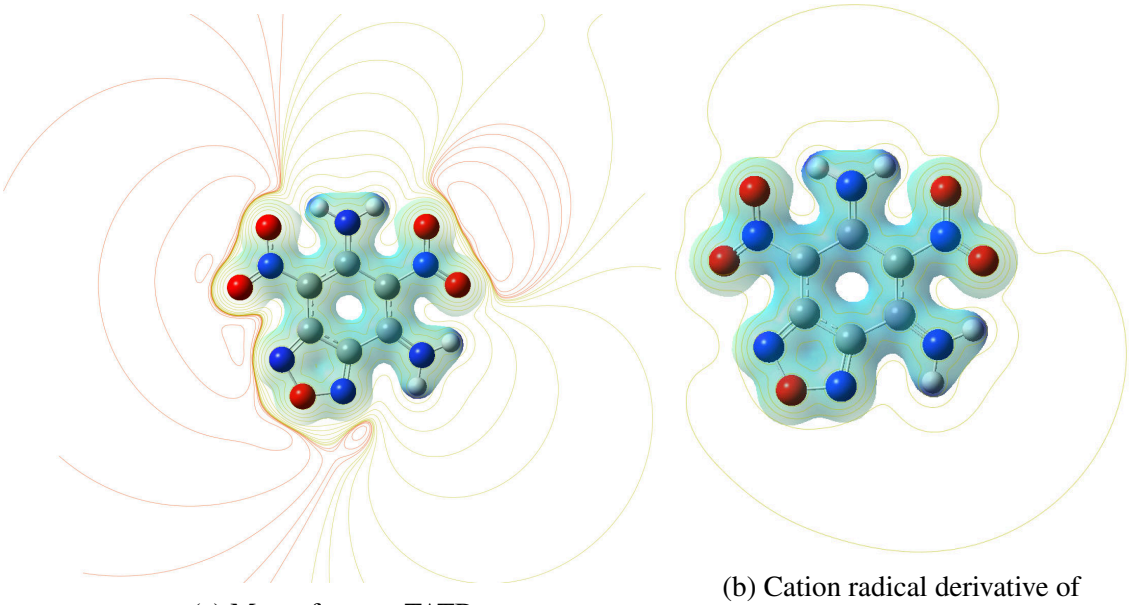

(a) Mono-furazan TATB

(b) Cation radical derivative of mono-furazan TATB

Figure 4.17: Optimised structures, electron densities and electrostatic potentials of mono-furazan TATB and its cation radical derivative

Vibrational analyses were undertaken successfully for both molecules in both states yielding no negative frequencies, indicating a successful optimisation. The subsequent thermochemical data is presented in Table 4.4, with ionisation potential in both phases calculated and presented in Table 4.5 alongside the equivalent wavelength of light.

Phase	Charge	Spin	ε_0	ε_{ZPE}	E_{tot}	H_{corr}	G_{corr}	C_v
Gas	0	1	-935.56176	0.136401	0.149053	0.149998	0.095899	48.120
Solid	0	1	-935.5739	0.135869	0.148538	0.149482	0.095342	48.195
Gas	+1	2	-935.22192	0.135535	0.148279	0.149223	0.09407	47.973
Solid	+1	2	-935.28876	0.135536	0.148357	0.149302	0.093555	48.066

Table 4.4: Mono-furazan TATB thermochemical data (DFT MH06-HF - aug-cc-pVTZ)

Where ε_0 - Electron Energy (Hartrees), ε_{ZPE} - Zero-point Energy Correction (Hartrees), E_{tot} - Thermal Correction to Energy (Hartrees), H_{corr} - Thermal Correction fo Enthalpy

(Hartrees), G_{corr} - Thermal Correction to Free Energy (Hartrees) and C_v - Heat Capacity (cal mol^{-1} Kelvin^{-1})

Phase	E_1 (eV)	λ (nm)
Gas	9.25	134.04
Pseudo Solid	7.76	159.77

Table 4.5: Mono-furazan TATB first ionisation potential

The optimised structures were successfully submitted for analysis by TD-DFT and GIAO NMR, affording UV-Vis and NMR Spectra. Continuing the theme observed so far, differences in properties between gas and pseudo solid states were observable but small, whereas differences between ground and ionic radical states were much more significant. As observed with TATB, the calculated UV-Vis absorption spectra for the mono-furazan derivative, Figure 4.18, shows a significant difference between the ground and ionic states with the latter having absorptions in the 500 nm region.

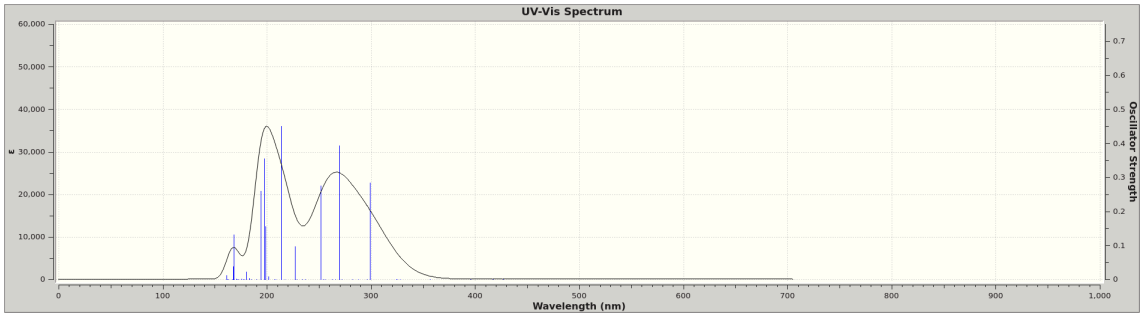

(a) mono-furazan TATB

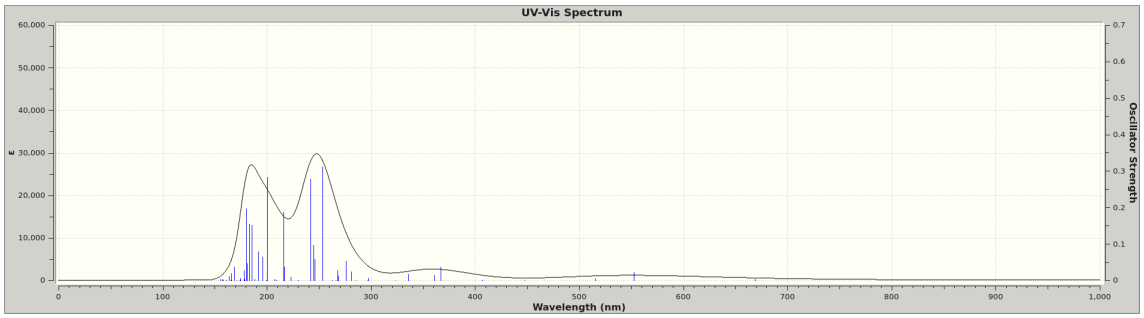

(b) Cation radical derivative of mono-furazan TATB

Figure 4.18: Simulated UV-Vis absorption spectra of mono-furazan TATB and its cation radical derivative

The electrostatic properties of the ionic and radical derivative of TATB was derived and processed through Spinach [72] and EasySpin [74] to generate structures with hyperfine coupling tensors. In keeping with ionic TATB, it can be seen from the structure, as shown in Figure 4.19a, that the main contributions to the ESR signal come from the carbon atom adjacent to the slightly twisted nitro group, and appears to be a likely candidate as a radical centre. However, as with the TATB ion, this tensor is based upon the radical coupling to the carbon-13 isotope, and as with the ionic parent molecule, once relative abundance is taken into account, the main contribution to the signal actually originate from the adjacent nitrogen atom of the twisted nitro group. The nitrogen and hydrogens of the adjacent amine group also contribute to the coupling, as shown in Figure 4.19b.

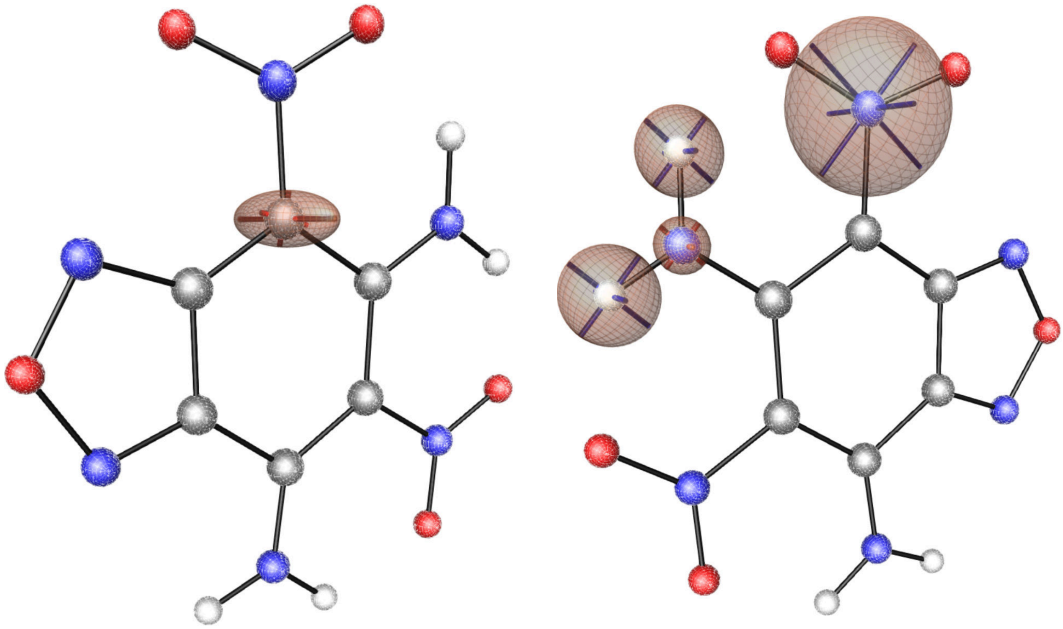

(a) Un-adjusted (b) Adjusted

Figure 4.19: Structure and hyperfine coupling of mono-furazan TATB radical cation

Like ionic TATB, the resultant spectra should feature three lines as the unpaired electron couples to the spin of the nitrogen-14 atom, however, with the inclusion of the additional coupling from the adjacent amine group the spectra becomes exceedingly detailed. This is shown in in Figure 4.20, where the top most spectra considers just the contributions from the nitrogen, and the bottom most spectra also considers the amine group.

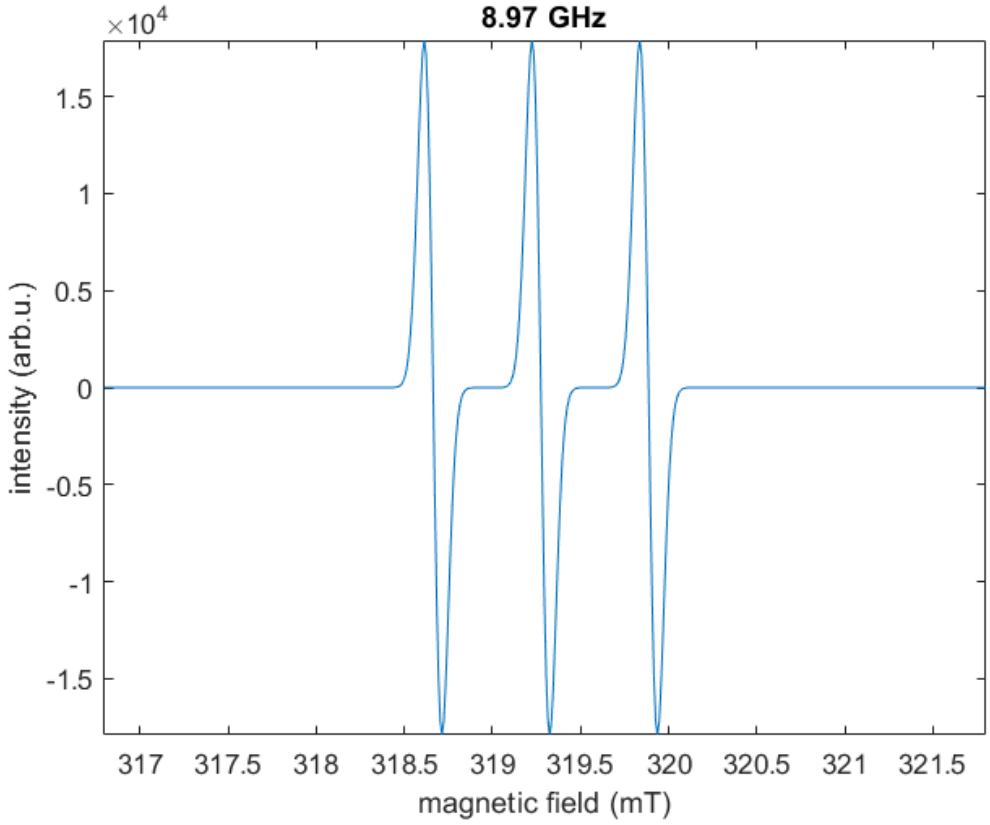

(a) Part complexity

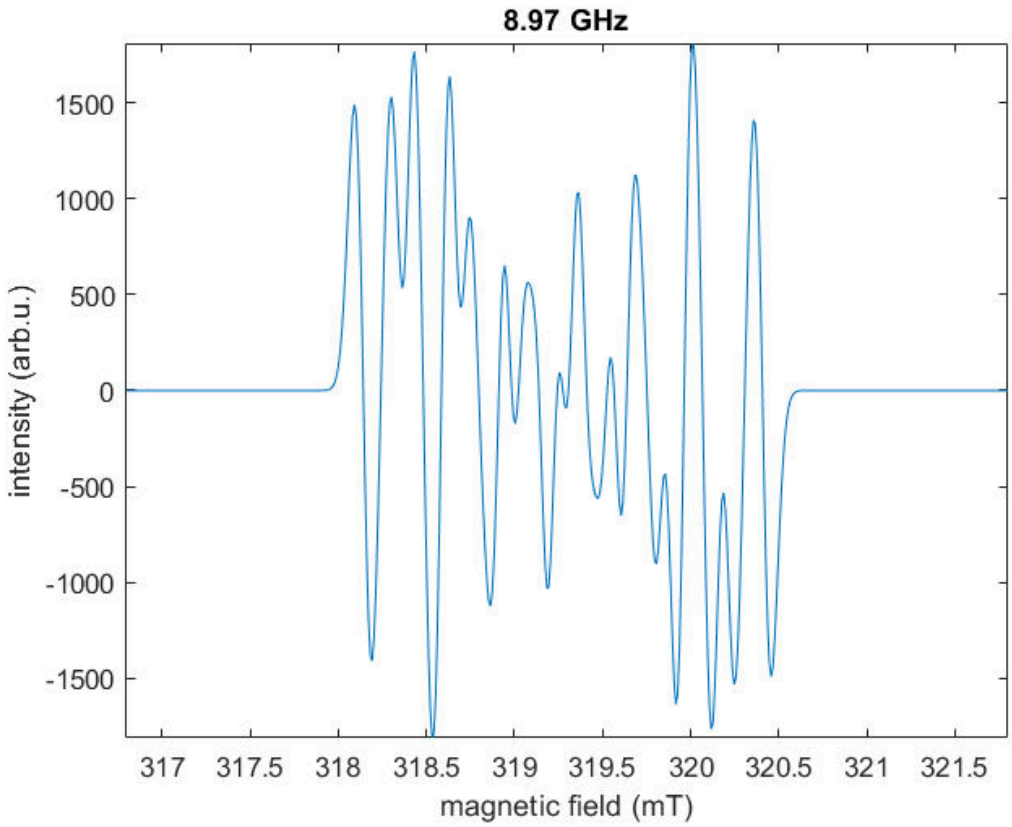

(b) Full complexity

Figure 4.20: Predicted ESR signal of cation radical derivative of mono-furazan TATB

The computed g-factor (g) tensor is presented below, the hyperfine coupling tensors for the adjacent nitrogen is also presented. Additional hyperfine coupling tensors for the adjacent amine group may be found in the appendix. Both the g and the hyperfine coupling tensors were corrected for anisotropy before spectra generation:

$$g = \begin{pmatrix} 2.011054 & -0.002760 & -0.002112 \\ -0.002760 & 2.007970 & 0.000738 \\ -0.002112 & 0.000738 & 2.002906 \end{pmatrix} A = \begin{pmatrix} -0.578500 & -0.029503 & -0.029707 \\ -0.029503 & -0.565749 & 0.031330 \\ -0.029707 & 0.031330 & -0.705902 \end{pmatrix}$$

Mono-nitroso TATB derivative

The mono-nitroso TATB derivative and its ionic radical equivalent were successfully optimised to the required level of theory in both the gas and pseudo-solid states, with the ionic radical derivative providing some resistance in both phases which required explicit initial Hessians to be calculated for the aug-cc-pVTZ optimisation step. Both molecules in both states produced planar molecules, with no evidence of the nitro-group twist that has been seen for the ionic radical derivatives of TATB and the mono-furazan daughter product. In keeping with these two molecules, the mono-nitroso and its ionic radical derivative also showed notable but small differences between the gas and pseudo solid states, with a more significant difference observed between the two electronic states. The optimised structures with electron densities and electrostatic potentials can be found in Figure 4.21.

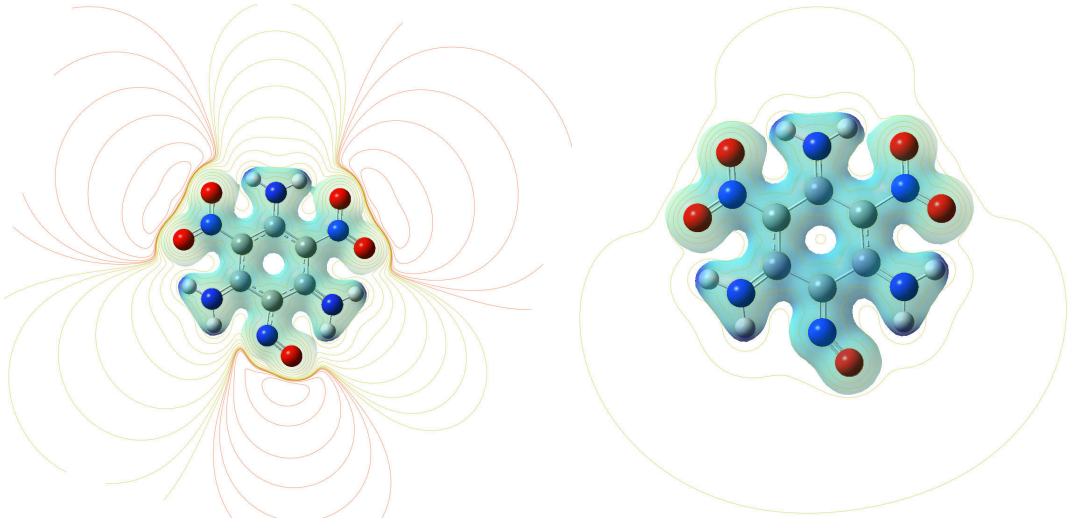

(a) Mono-nitroso TATB (b) Cation radical derivative

Figure 4.21: Optimised structures, electron densities and electrostatic potentials of mono-nitroso and its cation radical derivative

Vibrational analysis on both molecules in both states successfully yielded no imaginary frequencies, suggesting that the optimised structures were at a global minima, with resultant thermochemical and ionisation potential data presented within Tables 4.6 and 4.7 respectively.

Phase	Charge	Spin	ε_0	ε_{ZPE}	E_{tot}	H_{corr}	G_{corr}	C_v
Gas	0	1	-936.81547	0.157733	0.171412	0.172356	0.11587	52.329
Solid	0	1	-936.82406	0.156822	0.170615	0.17156	0.114506	52.630
Gas	1	2	-936.50492	0.15863	0.172485	0.173429	0.115613	52.605
Solid	1	2	-936.56939	0.158296	0.172186	0.17313	0.115036	52.686

Table 4.6: Mono-nitroso thermochemical Data (DFT MH06-HF - aug-cc-pVTZ)

Where ε_0 - Electron Energy (Hartrees), ε_{ZPE} - Zero-point Energy Correction (Hartrees), E_{tot} - Thermal Correction to Energy (Hartrees), H_{corr} - Thermal Correction fo Enthalpy (Hartrees), G_{corr} - Thermal Correction to Free Energy (Hartrees) and C_v - Heat Capacity

(cal mol^{-1} $Kelvin^{-1}$)

Phase	E_1 (eV)	λ (nm)
Gas	8.45	146.73
Pseudo Solid	6.93	178.91

Table 4.7: Mono-furazan first ionisation potential

As with the other molecules considered so far, the optimised structures were submitted for TD-DFT, GIAO NMR and, where applicable, (i.e. ionic radical species) electrostatic property analysis, yielding UV-VIS and NMR spectra as well as hyperfine coupling and g tensors. The resultant UV-Vis spectra continues the trend where differences between gas and solid states for both molecules is negligible. However, in contrast to what has been seen for the other two molecules, there is also a negligible difference between the baseline and the ionic radical derivatives of the mono-nitroso molecule (in both simulated states) as shown in Figure 4.22. The resultant predicted UV-Vis spectra for both molecules in both simulated states, lacks any absorptions in the correct visible region for them to appear green. This disagrees with the semi-empirical analysis undertaken by Manaa [46], as absorptions in the 600 nm range are not observed.

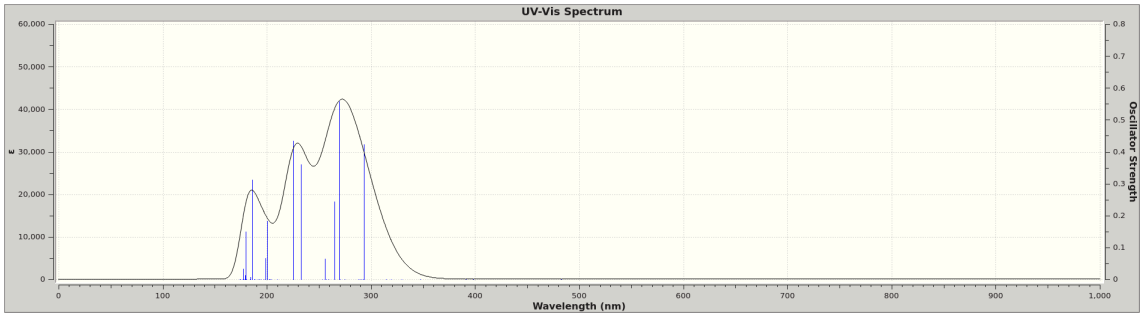

(a) Mono-nitroso TATB

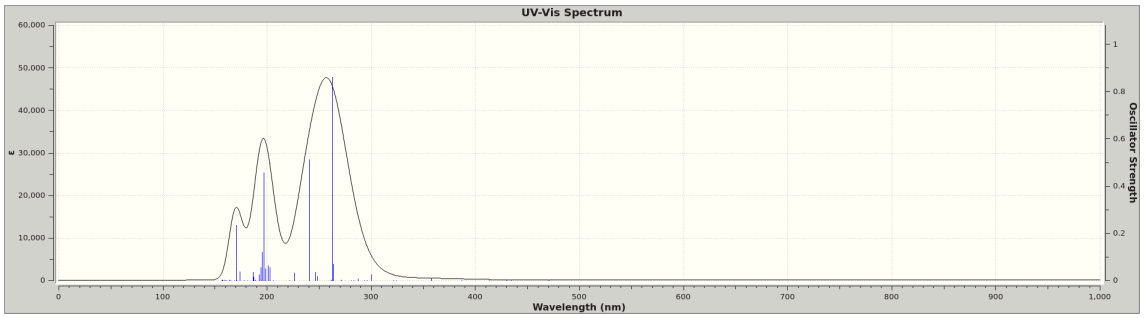

(b) Cation radical derivative of mono-nitroso TATB

Figure 4.22: Simulated UV-Vis absorption spectra of mono-nitroso and its cation radical derivative

The output from the electrostatic properties calculation was processed through Spinach [72] resulting in visualised hyperfine coupling (and chemical shifts) of the structure as shown in Figure 4.23a. The unadjusted hyperfine coupling suggests that the radical could be centred on either the nitrogen or oxygen of the nitroso group, or even the adjacent carbon within the aromatic ring in keeping with previous observations, although the coupling is strongest on the oxygen. This data, corrected for relative abundance, is shown in Figure 4.23b, where it can be seen that any coupling will be dominated by the nitrogen atom.

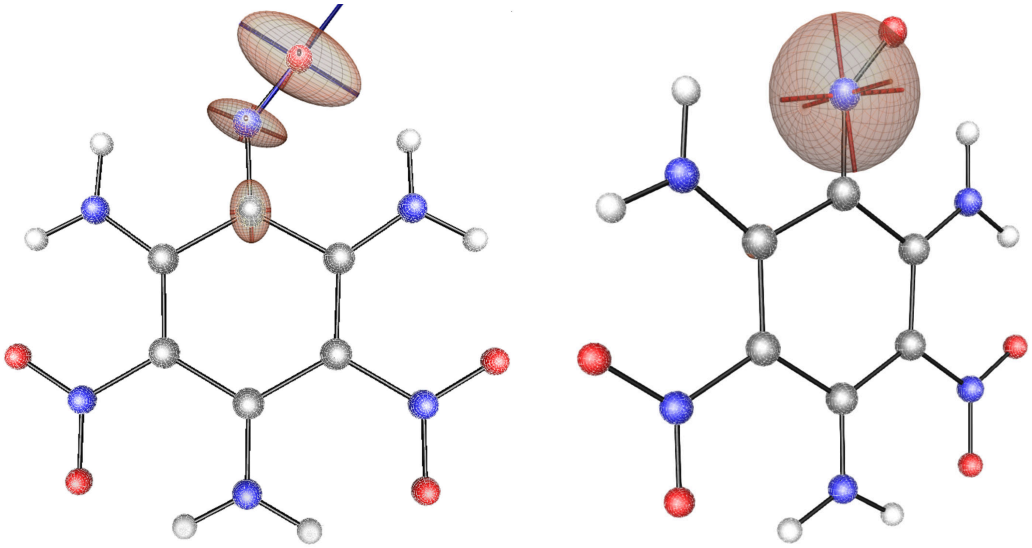

(a) Un-adjusted (b) Adjusted

Figure 4.23: Structure and hyperfine coupling of mono-nitroso TATB radical cation

The predicted ESR spectra for the mono-nitroso derivative of TATB would be expected to feature mostly contributions of the nitrogen atom within the nitroso group, resulting in three clean peaks. This is indeed observed, as shown in Figure 4.24a, where just the nitrogen hyperfine coupling is used to generate a spectra. Consideration of small contributions of coupling from adjacent hydrogens results in superposition and a much more complex structure, as shown in Figure 4.24b.

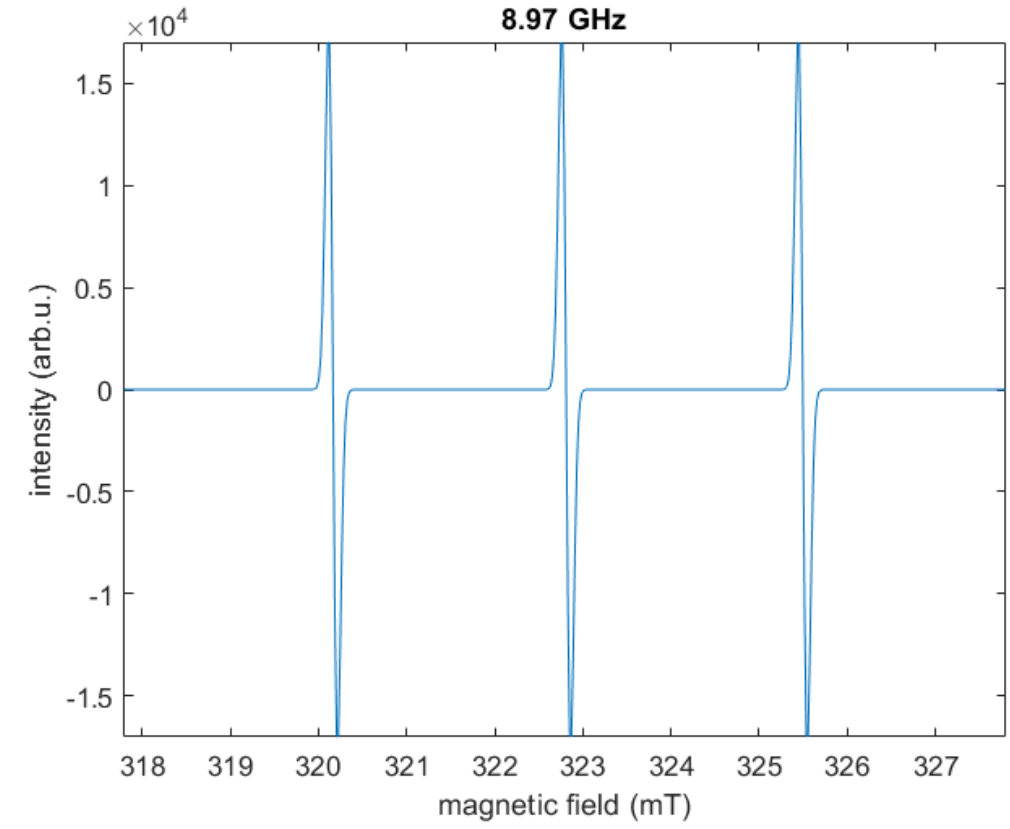

(a) Simple

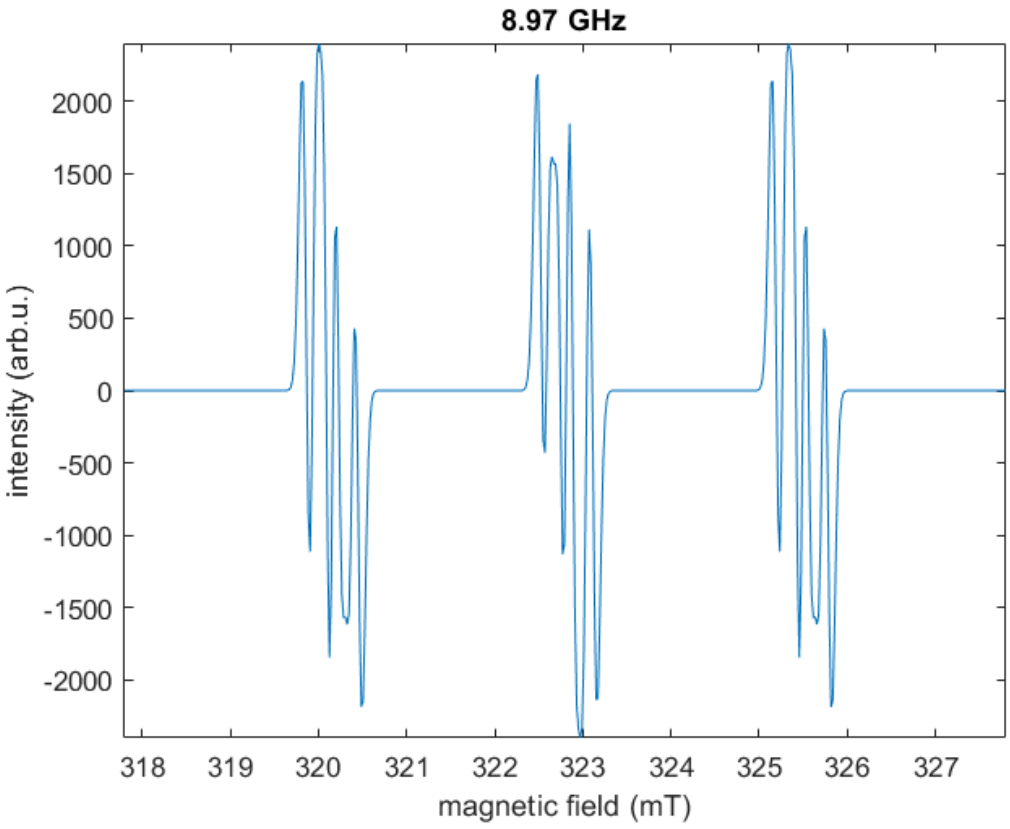

(b) Complex

Figure 4.24: Predicted ESR signal of cation radical derivative of mono-nitroso TATB

The computed g-factor (g) and hyperfine coupling (A) constants for the nitrogen atom (both in tensor form) are presented below, additional hyperfine coupling tensors for the hydrogen may be found in the appendix. Both the g and the hyperfine coupling tensors were corrected for anisotropy before spectra generation:

$$g = \begin{pmatrix} 1.957062 & -0.042279 & -0.002862 \\ -0.042279 & 1.963710 & -0.003036 \\ -0.002862 & -0.003036 & 2.008249 \end{pmatrix} A = \begin{pmatrix} 3.399647 & -1.045038 & -0.093746 \\ -1.045038 & 2.534987 & 0.038949 \\ -0.093746 & 0.038949 & 2.129146 \end{pmatrix}$$

Phenoxyl radical

Optimisation of the phenoxyl racial in both ionic and ground states was successful but difficult and often required re-starting at various points. In order to achieve optimisation the utilisation of the computationally expensive quadratically convergence method for the Self Consistent Field (SCF) calculations within each optimisation step, was required. The spin state of this structure is a departure from that of previous molecules as the ground state molecule is a radical, meaning that the spin state will be doublet for the ground state and singlet for the cationic derivative. In keeping with the other derivatives so far, minimal differences were noted between gas and solid states, and in this case between the ionic and ground state structures, although some atomic distances are notably different. Structures, with electron density surfaces and electrostatic potential contours are shown in Figure 4.25.

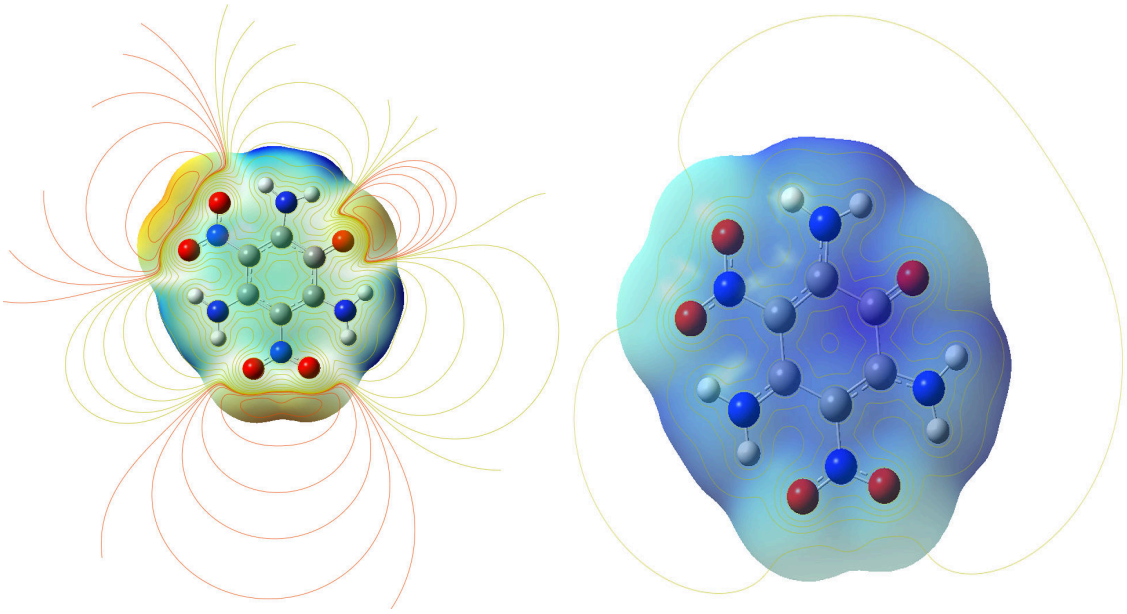

(a) Mono-phenoxyl TATB radical

(b) Cation derivative

Figure 4.25: Optimised structures, electron densities and electrostatic potentials of phenoxyl radical and its cation derivative

Vibrational analysis on the optimised structures yielded no negative frequencies, indicating optimisation success, and produced the thermochemical data presented in Table 4.8, which was used to generate the ionisation potential shown in Table 4.9; in keeping with previous calculations minimal differences were noted between gas and pseudo solid states.

Phase	Charge	Spin	ε_0	ε_{ZPE}	E_{tot}	H_{corr}	G_{corr}	C_v
Gas	0	2	-882.105128	0.153086	0.165932	0.16687	0.112323	49.729
Solid	0	2	-882.114165	0.152336	0.165274	0.166218	0.111342	50.000
Gas	1	1	-881.831312	0.154815	0.167722	0.168667	0.113690	48.953
Solid	1	1	-881.896192	0.154997	0.167783	0.168727	0.114594	48.841

Table 4.8: Phenoxyl radical thermochemical data (DFT MH06-HF - aug-cc-pVTZ)

Where ε_0 - Electron Energy (Hartrees), ε_{ZPE} - Zero-point Energy Correction (Hartrees), E_{tot} - Thermal Correction to Energy (Hartrees), H_{corr} - Thermal Correction fo Enthalpy

(Hartrees), G_{corr} - Thermal Correction to Free Energy (Hartrees) and C_v - Heat Capacity (cal mol^{-1} Kelvin^{-1})

Phase	E_1 (eV)	λ (nm)
Gas	5.685	218.08
Pseudo Solid	5.9314	209.03

Table 4.9: Phenoxyl radical first ionisation potential

UV-VIS and ESR calculations were undertaken successfully on the optimised structures, again with minimal differences being noted between gas and pseudo solid states. The resultant UV-Vis spectra, as shown in Figure 4.26 for the uncharged radical, and Figure 4.26b for its positively charged equivalent, show no absorptions greater than 450nm. Although discussed in greater detail in the conclusions section, it should be highlighted that these calculated UV-Vis spectra are in disagreement with those published by Ying et al [52] who saw a strong peak at 611 nm that led him to conclude that the ground state phenoxyl radical was the cause of the greening of TATB.

Despite using the same level of theory i.e. TD-DFT, albeit with a basis set much reduced in complexity (Pople 6-311++g(d,p)) and a lesser hybrid function (B3LYP), Ying claimed that the peak seen at 611 nm was from the second singlet excitation, and as such would have been considered by the calculation presented here, which consider the first 25 singlet (and triplicate) states. Although not particularly visible in the spectra presented in Figure 4.26a, there is a calculated absorption at 631nm. However, the strength of this absorption is negligible (10 orders of magnitude less than the strongest peak) and contributes little to the spectra, and hence suggests that this cannot be the cause of the greening seen in TATB.

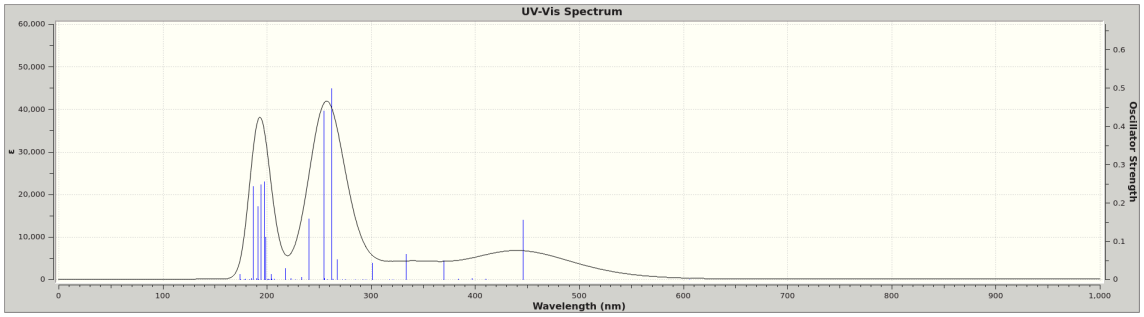

(a) Mono-phenoxyl TATB radical

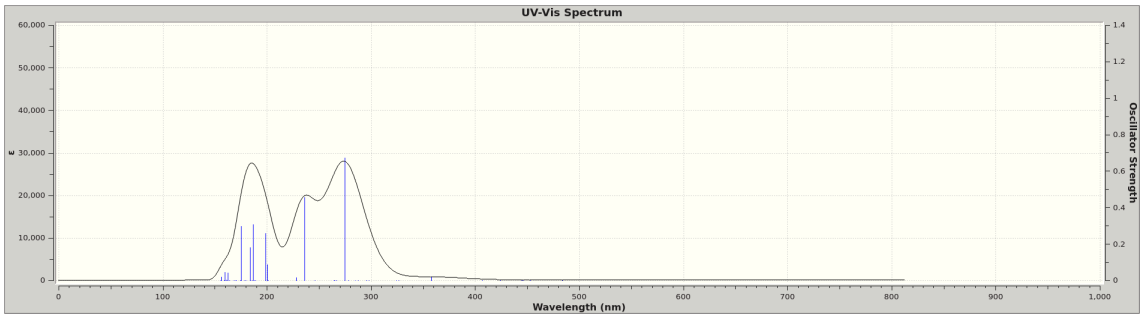

(b) Cation derivative of mono-phenoxyl TATB radical

Figure 4.26: Simulated UV-Vis absorption spectra of mono-phenoxyl TATB radical and its cation derivative

The calculated electrostatic properties were successfully processed through Spinach with the resultant structure shown in Figure 4.27. Unsurprisingly, the uncorrected structure suggests that the radical is located on the lone oxygen atom, as shown by the unadjusted structure with hyperfine coupling based on oxygen-17 being present. Taking into account relative abundance, the coupling of the radical appears to be dominated by numerous hydrogen and nitrogen atoms on adjacent amine groups, this results in a multi peaked spectra, as shown in Figure 4.28.

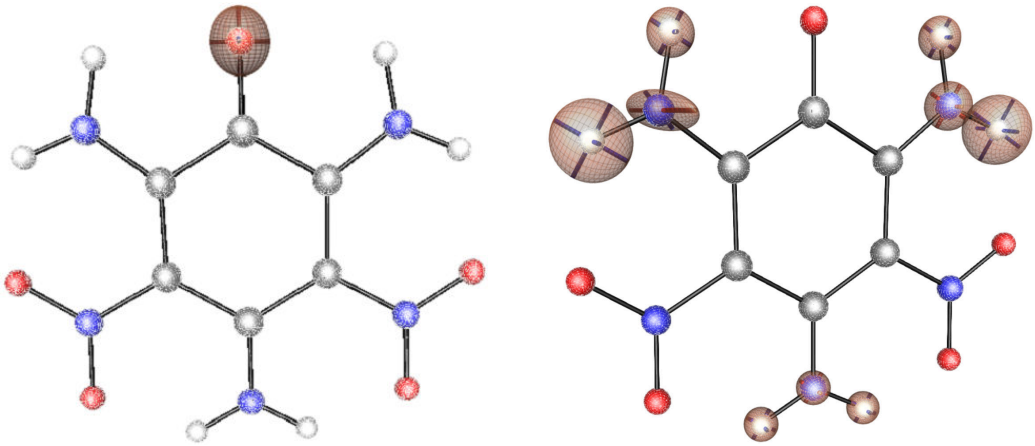

(a) Un-adjusted (b) Adjusted

Figure 4.27: Structure and hyperfine coupling of mono-phenoxyl TATB

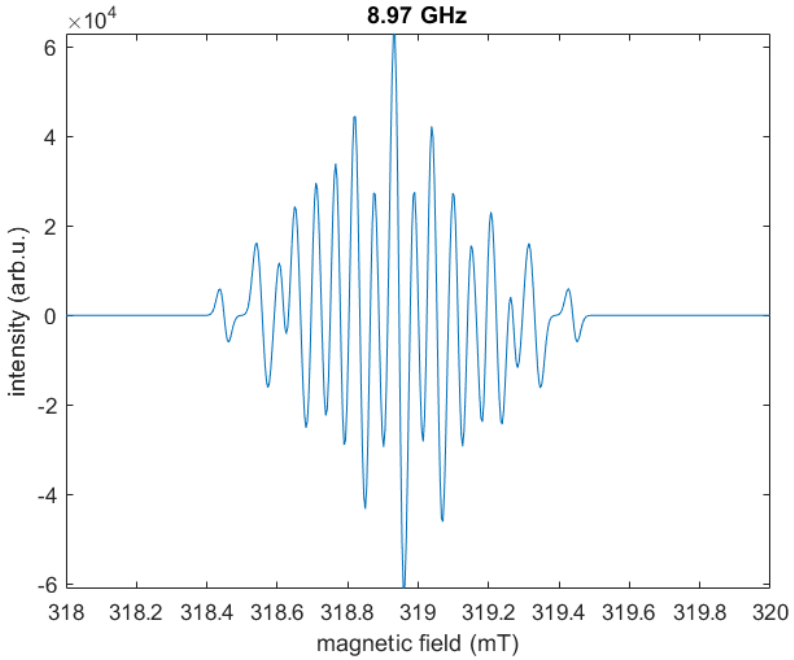

Figure 4.28: Predicted ESR spectra of phenoxyl TATB derivative

The computed g-factor (g) for the molecule is presented below, as the hyperfine coupling is based on multiple tensors (i.e. from contributions of several hydrogen and nitrogen atoms) these have not been reproduced, but are available in the appendix. Both the g and the hyperfine coupling tensors were corrected for anisotropy before spectra generation:

$$g = \begin{pmatrix} 1.957062 & -0.042279 & -0.002862 \\ -0.042279 & 1.963710 & -0.003036 \\ -0.002862 & -0.003036 & 2.008249 \end{pmatrix}$$

Preferential thermodynamic pathway for TATB

The remaining molecules, as identified within the purported TATB decomposition pathways, were each successfully optimised in both the gas and pseudo solid states and submitted for vibrational, NMR, TD-DFT and Electrostatic properties analysis (where appropriate). The most pertinent data is the thermodynamic data obtained from the vibrational analysis which allows an insight into the decomposition pathway that ionised TATB may undergo.

Each reaction (A→S), as identified within the TATB decomposition pathways shown in Figure 4.7, was tested using appropriate thermodynamic data calculated from the molecules in question. Any reaction that resulted in a net loss of energy to the system was determined to be energetically favourable. Any reaction that required energy was deemed not to be energetically favourable, allowing an insight into the potential decomposition pathway for TATB once ionised. The calculated thermodynamic data for each reaction is summarised in Table 4.10.

			Gas-Phase			Pseudo Solid Phase		
Path	Reactant	Products	$\Delta_r H^o$	$\Delta_r G^o$	Rate(s^{-1})	$\Delta_r H^o$	$\Delta_r G^o$	Rate(s^{-1})
A	TATB	TATB Ion	923.04	927.34	2.14E+150	775.24	775.09	1.01E+123
B	TATB Ion	DATB & NH_2 Ion	774.53	724.90	6.27e-115	500.41	450.38	7.77E-67
		DATB Ion & NH_2	668.02	615.94	7.67E-96	477.74	425.70	1.64E-62
C		CL-14 & H_2 Ion	838.13	809.45	4.27e-28	1464.49	1433.86	3.90E-239
		CL-14 Ion & H_2	257.41	228.73	5.27E-28	1026.87	998.87	7.41E-163
D		TADB & NO_2 Ion	426.35	377.51	4.52E-54	341.38	290.14	9.20E-39
		TADB Ion & NO_2	290.66	234.90	4.37E-29	281.02	233.74	6.99E-29
E		mono-furazan & H_2O Ion	330.34	289.27	1.30E-38	213.48	170.36	8.85E-18
		mono-furazan Ion & H_2O	-7.14	-48.97	2.36E+21	-22.67	-68.01	5.10E+24
F		mono-nitroso & O Ion	1082.80	1049.21	9.55E-172	958.19	921.17	2.58E-149
		mono-nitroso Ion & O	436.70	401.33	3.04E-58	436.10	398.71	8.77E-58
G		mono-Nitrite Ion	-225.49	-240.15	7.34E+34	-219.46	-231.90	2.64E+53
H	monoNitrite Ion	Benzo TATB & H_2O Ion	492.22	515.80	2.69E-78	372.57	340.52	1.37E-47
		Benzo TATB Ion & H_2O	282.93	258.66	3.01E-33	248.21	218.51	3.25E-26
I	mono-nitroso	mono-furazan and H_2	198.11	165.58	6.10E-17	189.14	157.98	1.31E-15
	mono-nitroso Ion	mono-furazan and H_2 Ion	860.13	827.48	6.69E-133	709.30	677.41	1.31E-106
		mono-furazan Ion and H_2	270.12	238.32	1.10E-29	264.53	231.88	1.48E-28
J	mono-furazan	mono-furazanmono-nitroso & O	552.19	516.23	2.25E-78	549.84	513.96	5.63E-78
	mono-furazan Ion	mono-furazanmono-nitroso & O Ion	1126.27	1091.37	3.93E-179	996.53	963.15	1.14E-156

		mono-furazanmono-nitroso Ion & O	541.18	495.24	1.07E-74	516.61	480.02	4.99E-72
K	mono-nitroso	mono-furazan-mono-nitroso & H_2O	36.33	-6.81	9.68E+13	15.67	-26.02	2.25E+17
	mono-nitroso Ion	mono-furazan-mono-nitroso & H_2O Ion	97.34	52.82	3.47E+03	57.83	13.94	2.25E+10
		mono-furazan-mono-nitroso Ion & H_2O	445.59	404.17	9.68E-59	327.21	286.25	4.40E-38
L	mono-nitroso	mono-nitroso-mono-nitrite	3.70	1.88	2.91E+12	2.66	2.11	2.65E+12
	mono-nitroso Ion	mono-nitroso-mono-nitrite Ion	-34.27	-37.07	1.94E+19	-23.35	-25.55	1.86E+17
M	monoNitrite Ion	mono-nitrite-mono-nitroso & O Ion	1311.99	1291.23	3.79E-214	1180.31	1155.18	2.60E-190
		mono-nitrite-mono-nitroso Ion & O	627.91	604.41	8.04E-94	632.22	604.42	7.99E-94
N		Benzoxy TATB and H_2 Ion	1003.58	985.08	1.64E-160	848.87	665.19	1.80E-104
		Benzoxy TATB Ion and H_2	544.52	532.58	3.09E-81	499.64	320.82	3.88E-44
O	mono-furazan	di-furazan & H_2O	-5.46	-49.16	2.54E+21	-10.70	-54.24	1.98E+22
	mono-furazan Ion	di-furazan & H_2O Ion	53.39	7.66	2.82E+11	34.52	-7.88	1.49E+14
		di-furazan ion & H_2O	332.02	289.08	1.41E-38	225.45	184.13	3.43E-20
P	mono-nitroso	di-furazan & O	554.48	519.45	6.16E-79	551.77	517.37	1.42E-78
	mono-nitroso Ion	di-furazan & O Ion	1200.58	1167.32	1.94E-192	1064.24	1040.47	3.25E-170
		di-furazan ion & O	549.16	345.74	1.67E-48	716.22	513.54	6.68E-78
Q	monoNitrite Ion	di-nitrite Ion	51.82	56.69	7.28E+02	58.36	59.76	2.10E+2
R	monoNitrite Ion	Phenoxyl TATB & NO Ion	218.98	190.64	2.48E-21	119.44	88.73	1.77E-3
		Phenoxyl TATB Ion & NO	9.22	-22.35	5.12E+16	4.76	-28.75	6.77E+17
S	mono-nitrosomono-furazan	di-furazan & H_2	156.32	123.23	1.60E-09	162.78	129.76	1.15E-10
	mono-nitrosomono-furazan Ion	di-furazan & H_2 Ion	757.33	725.50	4.91E-115	640.77	609.23	1.15E-94

		di-furazan Ion& H_2	226.18	192.82	1.03E-21	241.22	210.07	9.80E-25
T	di-nitroso	mono-furazan-mono-nitroso & H_2	195.82	162.36	2.23E-16	187.21	154.57	5.17E-15
	di-nitroso Ion	mono-furazan-mono-nitroso & H_2 Ion	262.16	395.69	2.96E-57	232.21	33.12	9.78E+06
		mono-furazan-mono-nitroso Ion & H_2	863.16	997.97	9.06E-163	710.21	512.59	9.81E-78
U	di-nitroso	di-furazan & $2H_2$	352.14	285.59	5.76E-38	349.98	284.33	9.56E-38
	di-nitroso Ion	di-furazan & H_2 & H_2 Ion	488.34	588.85	4.27E-91	306.14	408.43	1.74E-59
		di-furazan & $2H_2$	1019.48	1121.19	2.34E-184	705.69	807.59	2.04E-129

Table 4.10: Thermodynamic evaluation of purported decomposition pathways of TATB - energetically favourable highlighted in green

Where $\Delta_r H^o$ - Enthalpy of reaction (kJ/mol) and $\Delta_r G^o$ - Gibbs free energy of reaction (kJ/mol).

It can be seen from the above table that there are only a select number of the decomposition pathways that are energetically favourable, where the enthalpy and/or Gibbs free energy is negative; namely subsets from within reaction pathways E, G, K, L, O and R. Investigation of these reactions leads to the conclusion that only reaction pathways E, O, R and G may be credible, as the precursor molecules for reactions K and L are unlikely to be formed as their preceding reactions are not energetically favourable. The investigation of thermochemical data of the each reaction permits the generation of an updated TATB decomposition pathway, as presented in Figure 4.29.

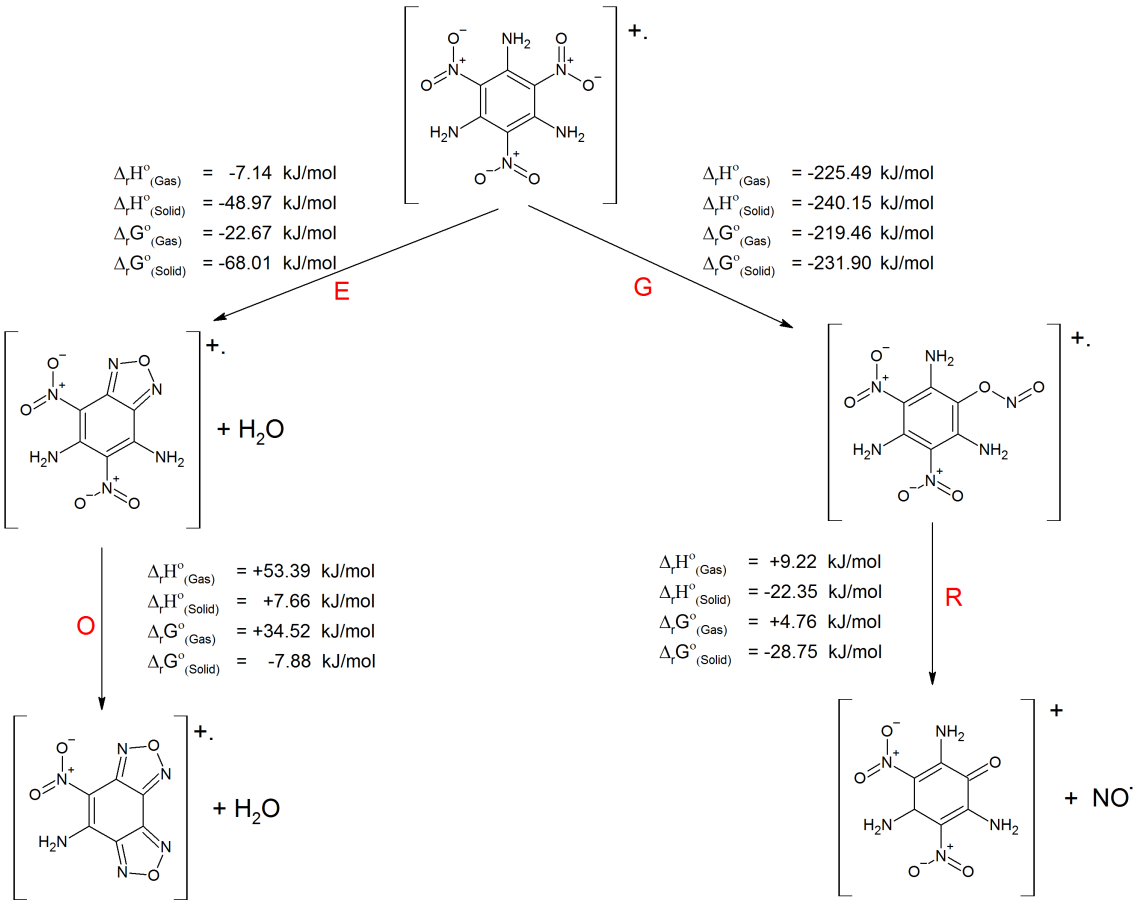

Figure 4.29: Energy favourable decomposition of Ionic TATB

It is of particular note that the mono-nitroso derivative does not feature in updated decomposition pathways and upon inspection of the associated thermochemical data, appears to be one of the most energetically unfavourable decomposition products. The pur-

ported phenoxyl radical also does not appear to be energetically favourable, however its nitrite based pre-cursor and its ionic non-radical equivalent appears to be energetically favourable, with the latter marginal.

Interestingly, the mono-furazan derivative also appears to be energetically unfavourable, however, much like with the phenoxyl, its positively charged radical equivalent does appear to be energetically unfavourable. Further decomposition to the di-furazan is marginally unfavourable with the exception of the Solid state calculations, where the Gibbs Free energy of reaction crosses into the energetically favourable region. It is noted that all purported decomposition products are ionic, with the exception of the phenoxyl radical, suggesting that long lived radicals are likely to accumulate in the material, a known observation from experimental analysis [53].

4.7.2 HMX and derivatives

HMX baseline and ion

Both HMX and its ionic radical equivalent were successfully optimised to the required convergence criteria using the highest level of theory (DFT MH06-HF) and basis sets (aug-cc-pVTZ) requested. In keeping with TATB, there was negligible difference between optimised structures in the gas and pseudo solid phases. In contrast to TATB, there was negligible difference between the ground state and ionic geometries, however, the same significant reduction in electron density and electrostatic potential can be seen between both states, as shown in Figure 4.30.

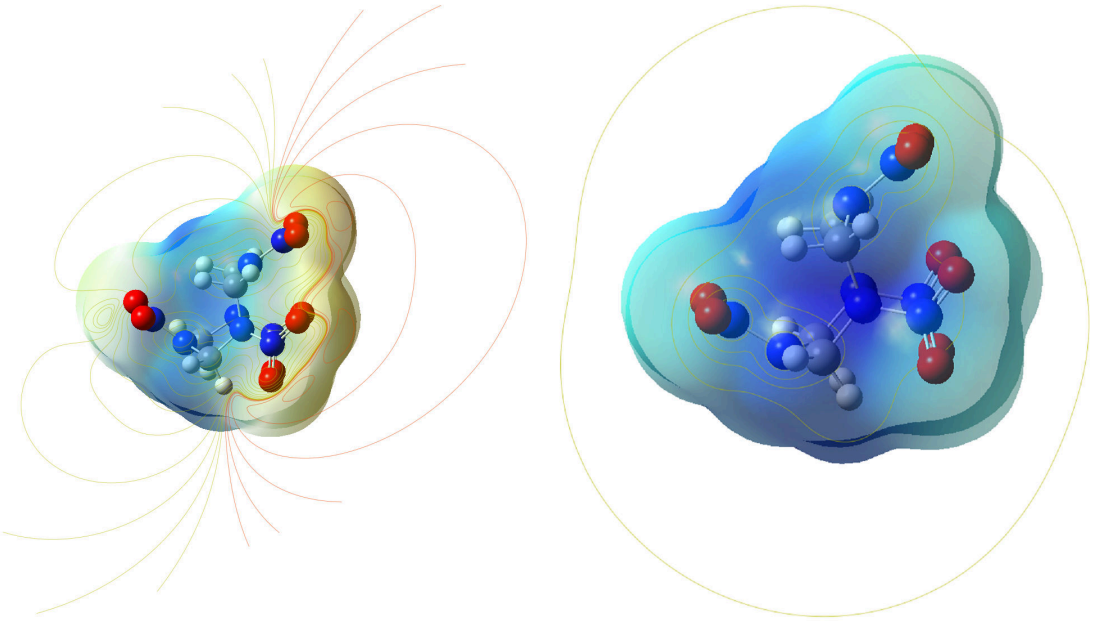

(a) HMX (b) Cation radical derivative

Figure 4.30: Optimised structures, electron densities and electrostatic potentials of HMX and its cation radical derivative

Both structures in both phases were submitted for vibrational analysis which yielded no imaginary frequencies, suggesting that the four structures were at a global minima on their potential energy surfaces. In keeping with observations from TATB, the predicted vibrations for both HMX and its ionic radical equivalent were negligibly different between gas and pseudo solid states. However, a more notable difference can be seen between the baseline and ionic radical species themselves, regardless of the simulated state. The predicted IR spectra between HMX and its ionic radical equivalent, in the pseudo solid state, demonstrates this difference, as shown in Figure 4.31.

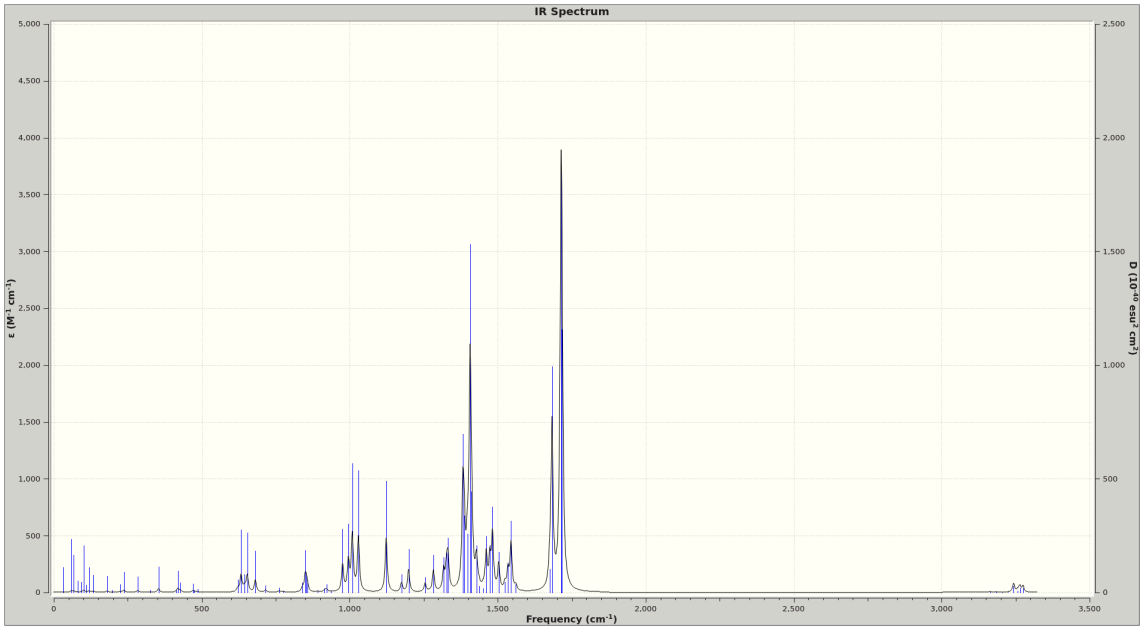

(a) HMX

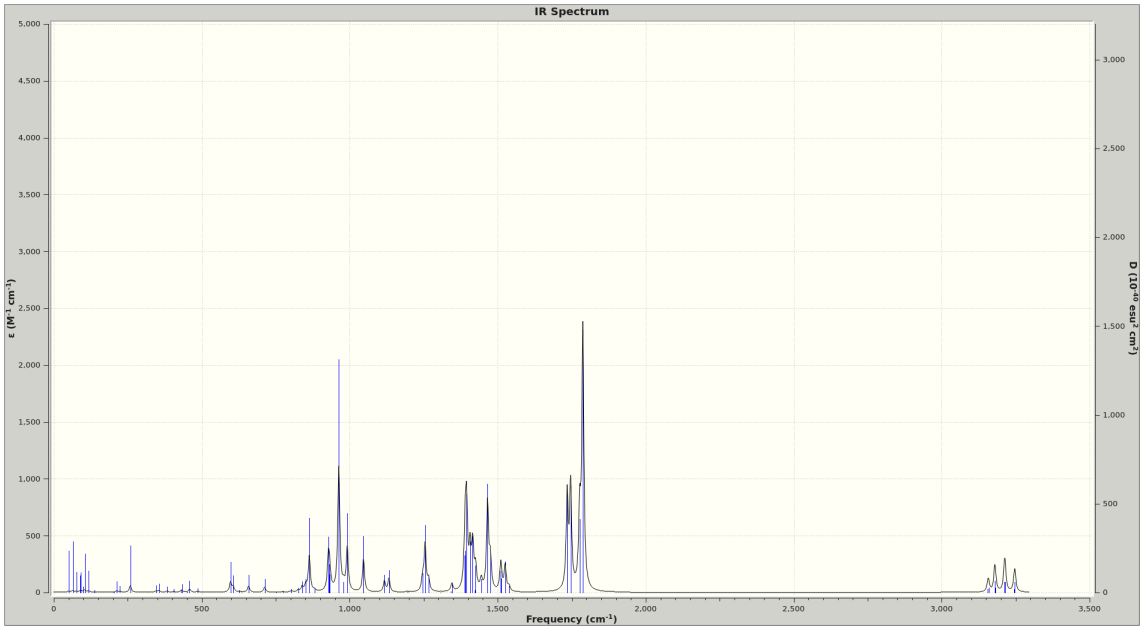

(b) Cation radical derivative of HMX

Figure 4.31: Predicted IR spectra of HMX and its cation radical derivative

Thermochemical data was successfully generated from the vibrational analysis and is summarised in Table 4.11. From this data, the ionisation potential for HMX in both states and its equivalent wavelength of light was calculated, and is presented in Table 4.12. In keeping with TATB, it can been seen form the ionisation potentials that ionisation can be

achieved by application of UV light as well as gamma radiation, implying that the interaction will be similar between the two radiations.

Phase	Charge	Spin	ε_0	ε_{ZPE}	E_{tot}	H_{corr}	G_{corr}	C_v
Gas	0	1	-1196.763947	0.200143	0.216562	0.217507	0.154605	59.475
Solid	0	1	-1196.777604	0.199882	0.216360	0.217304	0.154114	59.516
Gas	1	2	-1196.367438	0.197813	0.216111	0.215055	0.15245	60.214
Solid	1	2	-1196.430566	0.197961	0.214211	0.215155	0.152766	60.164

Table 4.11: HMX thermochemical data (DFT MH06-HF - aug-cc-pVTZ)

Where ε_0 - Electron Energy (Hartrees), ε_{ZPE} - Zero-point Energy Correction (Hartrees), E_{tot} - Thermal Correction to Energy (Hartrees), H_{corr} - Thermal Correction fo Enthalpy (Hartrees), G_{corr} - Thermal Correction to Free Energy (Hartrees) and C_v - Heat Capacity (cal mol^{-1} Kelvin^{-1})

Phase	E_1 (eV)	λ (nm)
Gas	10.79	114.91
Pseudo Solid	9.44	131.34

Table 4.12: HMX first ionisation potential

HMX and its ionic radical equivalent were not selected for TF-DFT analysis as a UV-Vis spectra was deemed not to be required as there has been no reported changes in colour with gamma radiation. Both molecules in both states were, however, submitted for NMR analyses which were successful in their generation of chemical shifts and associated spectra. As with TATB and its ionic radical equivalent, there were small differences between the gas and pseudo solid states, with the latter inducing some anisotropy. Unsurprisingly and in keeping with TATB, there was a notable difference between ground and ionic

electronic states for both gaseous and pseudo solid states, as highlighted in the predicted proton spectra for ionic HMX, shown in Figure 4.32. The spectra shows significant differences between the proton signals indicating potential radical locations.

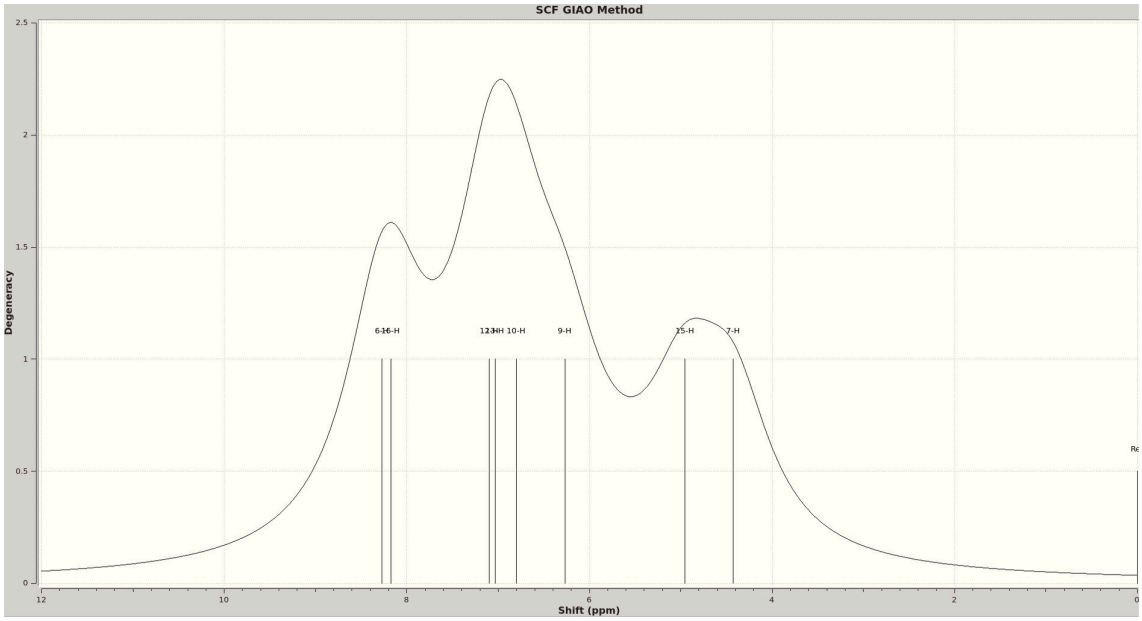

Figure 4.32: Simulated proton NMR spectra of the cation radical derivative of HMX

The ionic radical derivative of HMX, in both the gas and pseudo solid states, was also submitted for electrostatic property analysis in an effort to generate the hyperfine coupling and g tensors which provide evidence as to the location of any unpaired electrons and the ability to generate simulated ESR spectra. The calculations were successful and the output processed through Spinach [72] providing a visualisation of the potential locations of any unpaired electron spins; this is shown (for the solid state) in Figure 4.33. As can be seen from the calculation, hyperfine coupling is present on half of the hydrogen internal nitrogen atoms of the molecule. In stark contrast to the TATB derivatives, none of the carbon or oxygen atoms couple to the radical, indicating that the radical is likely centred on one of the internal nitrogen atoms, and is probably the result of lacking an aromatic centre that supports resonance.

The output from Spinach was corrected for relative atomic abundances and processed through EasySpin [74] with the resultant spectra shown also in Figure 4.33. As expected from the multiple contributions of the hyperfine coupling of nitrogen and hydrogen superimposed upon each other, a very detailed ESR spectra results. Inspection of the atomic charges of the structure, derived from the Mulliken population approximation [48], confirmed that the internal nitrogen atoms were each both partially charged (i.e. +0.5 each) and are therefore likely locations for a potential radial to reside. This may then lead to the N-NO_2 bond fragmenting, which may be supported by the thermodynamic analysis.

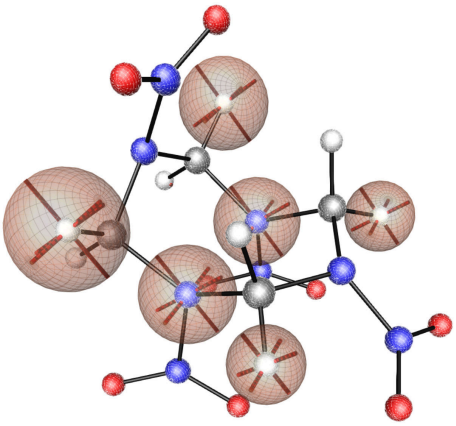

(a) Structure with adjusted hyperfine coupling

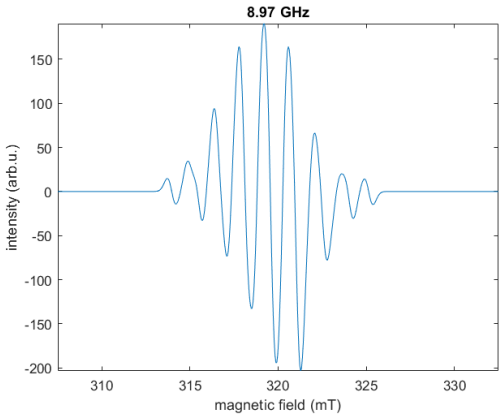

(b) Predicted ESR signal

Figure 4.33: Electrostatic properties of HMX radical cation

The computed g-factor (g) for the molecule is presented below, as the hyperfine coupling is based on multiple tensors (i.e. from contributions of several hydrogen and nitrogen atoms) these have not been reproduced, but are available in the appendix. Both the g and the hyperfine coupling tensors were corrected for anisotropy before spectra generation.

$$g = \begin{pmatrix} 2.006901 & 0.003343 & 0.000637 \\ 0.003343 & 2.006569 & -0.000080 \\ 0.000637 & -0.000080 & 2.002873 \end{pmatrix}$$

Preferential thermodynamic pathway for HMX

As for TATB, each reaction (A→I), as identified within the HMX decomposition pathways, Figure 4.8, was tested by using appropriate thermodynamic data calculated from the molecules in question. A summary of reaction thermodynamics can be found in Table 4.13.

			Gas-Phase			Pseudo Solid Phase		
Path	Reactant	Products	$\Delta_r H^o$	$\Delta_r G^o$	Rate(s^{-1})	$\Delta_r H^o$	$\Delta_r G^o$	Rate(s^{-1})
A	HMX	HMX Ion	1034.60	1035.38	2.53E-169	905.50	907.61	6.13E-147
B	HMX Ion	H Eliminated HMX & H Ion	673.46	638.39	8.96E-100	510.95	474.05	5.53E-71
		H Eliminated HMX Ion & H	261.30	227.68	8.03E-28	259.54	225.04	2.33E-27
C		HMX Path C & HNO &H_2 Ion	532.37	435.80	2.79E-64	400.69	305.08	2.22E-41
		HMX Path C & HNO Ion &H_2	57.30	-36.93	1.83E+19	-73.32	-116.68	1.72E+33
		HMX Path C Ion & HNO &H_2 Ion	152.13	55.96	9.76E+02	140.45	49.78	1.18E+04
D		NO_2 Eliminated HMX & NO_2 Ion	199.94	147.48	8.01E-14	126.65	152.72	1.09E-14
		NO_2 Eliminated HMX Ion & NO_2	38.41	-17.4	6.95E+15	36.91	-20.64	2.56E+16
E		HMX Nitrite Ion& O Ion	-178.12	-185.51	1.97E+45	-171.03	-182.22	5.20E+44
F		HMX Opened Ion& O Ion	48.02	46.2	4.86E+4	31.87	31.03	2.27E+7
G		Path G & H_2O Ion	164.09	110.70	2.51E-07	64.00	10.60	8.65E+10
		Path G Ion & H_2O	-165.61	-225.24	1.79E+52	-174.06	-232.50	3.36E+53
H		nitroso HMX & O	940.47	899.78	1.44E-145	825.95	782.50	5.07E-125
		nitroso HMX Ion & O	392.75	353.30	7.91E-50	391.72	353.18	8.28E-50
I	HMX Nitrite Ion	Phenoxyl HMX & NO Ion	165.59	120.48	4.85E-09	72.10	29.89	3.60E+07
		Phenoxyl HMX Ion & NO	56.99	11.63	5.70E+10	42.76	-2.22	1.52E+13
J	NO_2 Eliminated HMX	IMINE HMX & H	152.73	122.53	2.12E-09	151.42	121.4	3.39E-9
	NO_2 Eliminated HMX Ion	IMINE HMX & H Ion	618.53	585.89	1.41E-90	454.67	423.38	4.18E-62

	Ionic IMINE HMX & H	340.45	301.27	1.03E-40	336.51	304.51	2.78E-41

Table 4.13: Thermodynamic evaluation of purported decomposition pathways of HMX - energetically favourable highlighted in green

Where $\Delta_r H^o$ - Enthalpy of reaction (kJ/mol) and $\Delta_r G^o$ - Gibbs free energy of reaction (kJ/mol).

As can be seen from the table, aspects of pathways C, D, E, G and I are favourable with the latter being marginally unfavourable, but due to the small values, it has been included. This data has been used to generate updated decomposition pathways for Ionised HMX as shown in Figure 4.34.

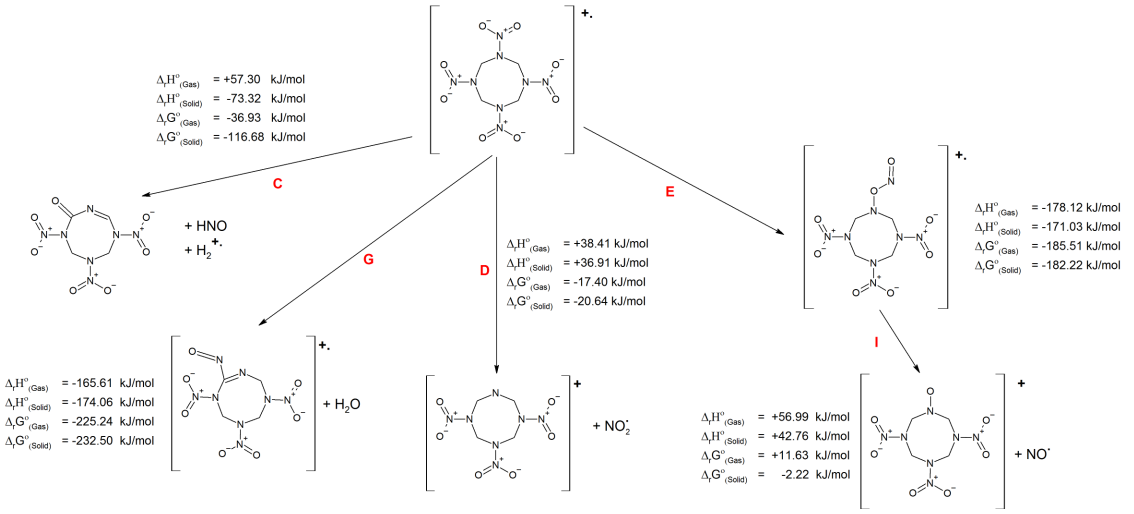

Figure 4.34: Energy favourable decomposition of ionic HMX

All but one of the purported energetically favourable products results in the much larger molecule remaining ionised, a continued theme from the calculations of TATB. Despite the four hydrogen atoms being a significant source of the anisotropic hyperfine coupling on the parent HMX ion, the hydrogen eliminated derivative is particularly unfavourable. The charge being centred around the internal nitrogen atoms may explain why the derivatives from reaction paths C and G are favourable.

A further inspection is possible of the radical species, by the analysis of the hyperfine coupling through Spinach and the subsequent generation of predicted ESR species as shown in Figures 4.35, and 4.36 and for the non charged NO_2 radical that may form as part of path D shown in Figure 4.37. Unfortunately the NO radical that may be formed as part of path I would not converge using the EPR-II basis set despite numerous attempts, whilst this suggests that the radical would be very unstable, it does mean that a spectra

and hyperfine coupling constants could not be generated for this molecule.

A couple of interesting observations can be made from the structure and spectra of the cationic c-nitroso radical derivative of HMX, as shown in Figure 4.35. Firstly, is that during the optimisation the fragmentation of N=O has resulted, indicating that the target molecule is very unstable and would almost immediately degrade by release of the N=O fragment.

Further observations suggest that the positive charge is split between the unpaired nitrogen on the larger molecule and the nitrogen of the gaseous fragment. This is further supported by the hyperfine coupling being present on both atoms and the generation of a complex spectra.

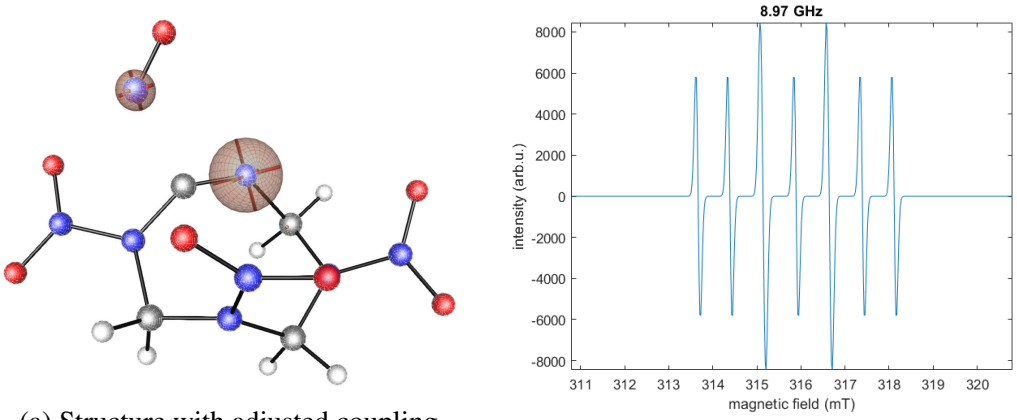

(a) Structure with adjusted coupling

(b) Predicted ESR signal

Figure 4.35: Predicted electrostatic properties of c-nitroso HMX radical cation

The computed g-factor (g) for the c-nitroso derivative is presented below, as the hyperfine coupling is based on multiple tensors these have not been reproduced, but are available in the appendix. Both the g and the hyperfine coupling tensors were corrected for anisotropy

before spectra generation.

$$g = \begin{pmatrix} 2.019927 & 0.025281 & -0.011645 \\ 0.025281 & 2.049788 & -0.025438 \\ -0.011645 & -0.025438 & 2.016709 \end{pmatrix}$$

Analysis of the cationic nitrite derivative, as shown in Figure 4.36, continues the trend from the c-nitroso, where the fragmentation NO appears to result from the optimisation. Inspection of the atomic charges, suggests that the radical sits either on the nitrogen or the oxygen of the resultant C-N-O moiety. This is in agreement with the thermochemistry that suggests that further decomposition from the nitrite to the R-C-N-O derivative, results in the larger molecule being cationic but the NO becomes the radical.

The resultant ESR spectra is complex and is dominated by the hyperfine coupling from the three highlighted hydrogen atoms in Figure 4.36.

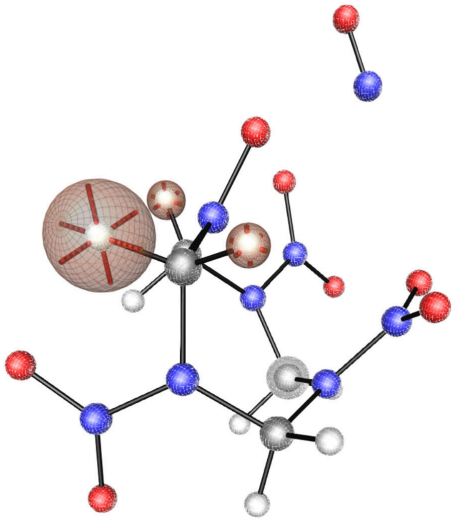

(a) Structure with adjusted coupling

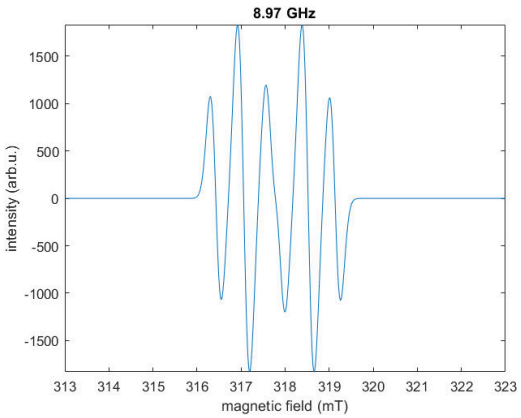

(b) Predicted ESR signal

Figure 4.36: Predicted electrostatic properties of HMX nitrite radical cation

The computed g-factor (g) for the nitrite derivative is presented below. As the hyperfine coupling is based on multiple tensors these have not been reproduced, but are available in the appendix. Both the g and the hyperfine coupling tensors were corrected for anisotropy before spectra generation.

$$g = \begin{pmatrix} 2.022090 & 0.014979 & 0.001840 \\ 0.014979 & 2.022051 & 0.007003 \\ 0.001840 & 0.007003 & 2.006010 \end{pmatrix}$$

The only two energetically favourable products that are a radical, are the NO and NO_2 fragments. Firstly, the NO_2 radical, as shown in Figure 4.37, produces a very characteristic three peaked spectra as the unpaired electron couples to the unpaired spin of the nitrogen atom.

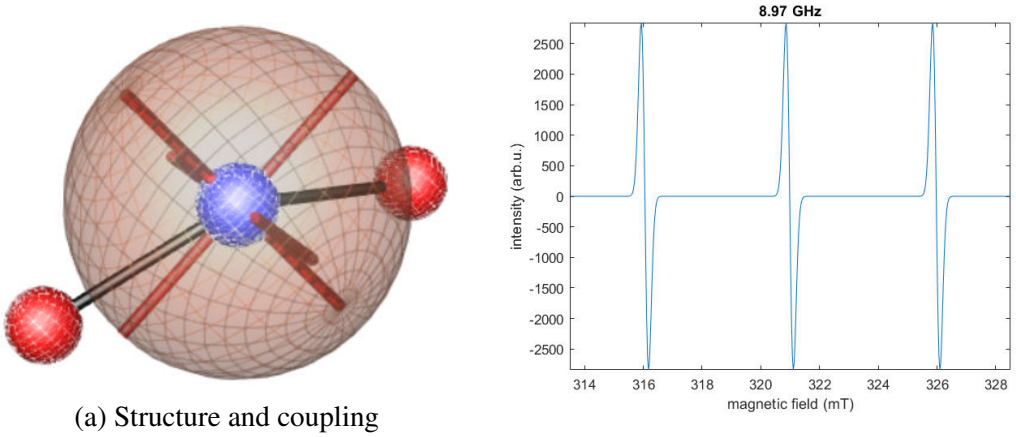

(a) Structure and coupling

(b) Predicted ESR signal

Figure 4.37: Predicted electrostatic properties of NO_2 radical

The computed g-factor (g) for the NO_2 derivative is presented below, as is hyperfine coupling tensor for the nitrogen atom. Both the g and the hyperfine coupling tensor were

corrected for anisotropy before spectra generation.

$$g = \begin{pmatrix} 2.006493 & 0.000771 & -0.001560 \\ 0.000771 & 1.984046 & -0.012408 \\ -0.001560 & -0.012408 & 1.998010 \end{pmatrix} A = \begin{pmatrix} 4.994610 & -0.548664 & 0.929933 \\ -0.548664 & 4.486348 & -0.748622 \\ 0.929933 & -0.748622 & 5.317571 \end{pmatrix}$$

4.7.3 PETN and derivatives

PETN baseline and ion

As with TATB and HMX, the baseline PETN molecule and its ionic equivalent were successfully optimised to the required level of theory with comparative ease. The resultant structures showed negligible difference between gas and solid state calculations, however a marked difference could be noted between ground and ionic states, this is shown in Figure 4.38 for the pseudo solid state only.

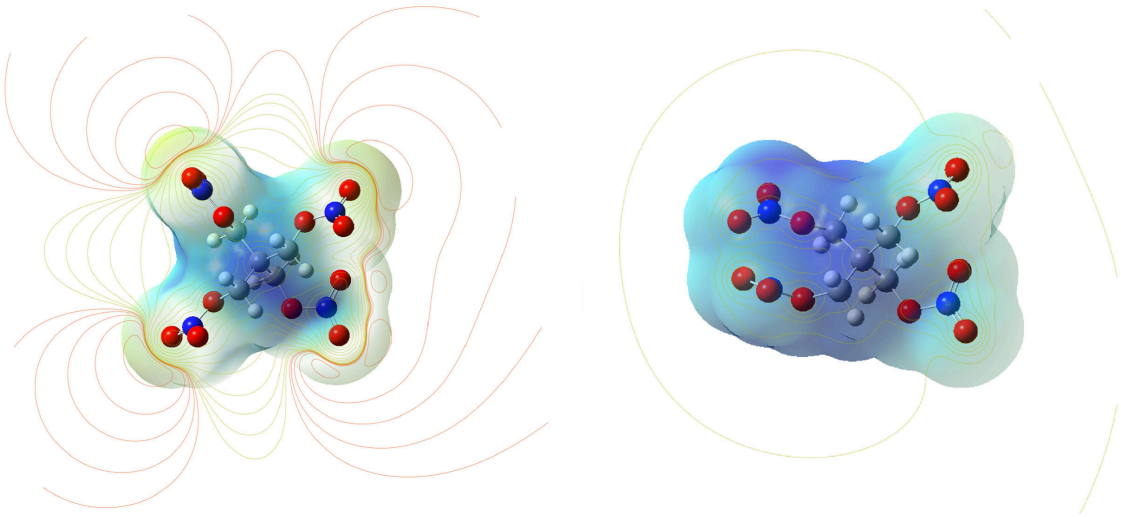

(a) PETN (b) Cation radical derivative

Figure 4.38: Optimised structures, electron densities and electrostatic potentials of PETN and its cation radical derivative

The optimised structures were submitted for vibrational analysis which afforded an IR absorption spectra with no negative frequencies, as shown in Figure 4.39. Thermochem-

ical data was analysed as presented in Table 4.14 from which the ionisation potential of PETN was determined, as presented in Table 4.15.

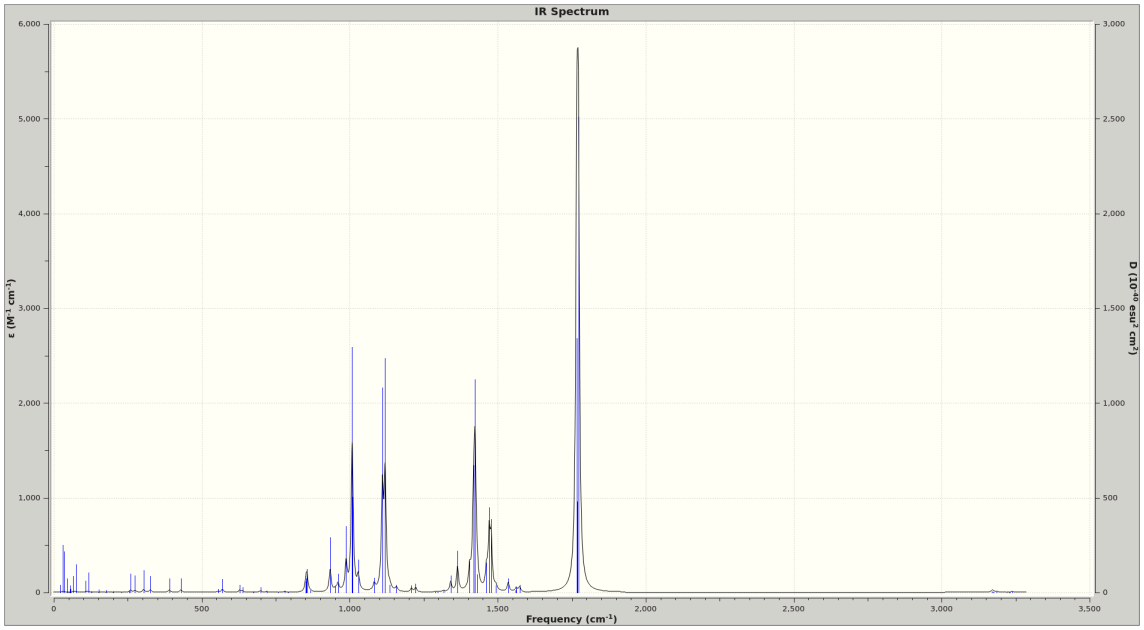

(a) PETN

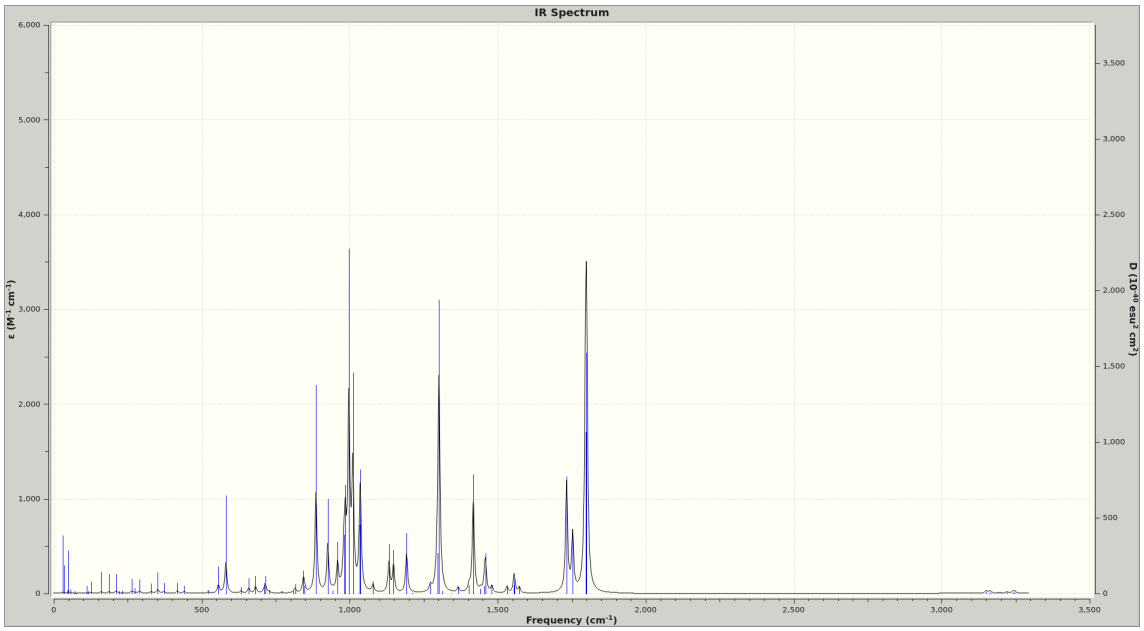

(b) Cation radical derivative of PETN

Figure 4.39: Predicted IR spectra of PETN and its cation radical derivative

Phase	Charge	Spin	ε_0	ε_{ZPE}	E_{tot}	H_{corr}	G_{corr}	C_v
Gas	0	1	-1316.67299	0.198027	0.217752	0.218697	0.144404	66.172
Solid	0	1	-1316.683719	0.197973	0.21762	0.215864	0.144926	66.136
Gas	1	2	-1316.225629	0.196198	0.215102	0.216046	0.145256	66.721
Solid	1	2	-1316.283308	0.231632	0.247552	0.248496	0.186378	59.969

Table 4.14: PETN thermochemical data (DFT MH06-HF - aug-cc-pVTZ)

Where ε_0 - Electron Energy (Hartrees), ε_{ZPE} - Zero-point Energy Correction (Hartrees), E_{tot} - Thermal Correction to Energy (Hartrees), H_{corr} - Thermal Correction fo Enthalpy (Hartrees), G_{corr} - Thermal Correction to Free Energy (Hartrees) and C_v - Heat Capacity (cal mol^{-1} Kelvin^{-1})

Phase	E_1 (eV)	λ (nm)
Gas	10.6030	116.93
Pseudo Solid	10.896	113.79

Table 4.15: PETN first ionisation potential

As with TATB and HMX, an electrostatic property calculation was undertaken on the ion to determine the hyperfine coupling and g-factor tensors. These were then processed through Spinach [72] to generate a visualisation of the hyperfine coupling of the molecule, which may be used to identify potential radical locations. The calculated tensors were then processed through EasySpin [74] to generate predicted ESR spectra, both structure and predicted spectra are shown in Figure 4.40.

Analysis of the ESR tensors and spectra that were not corrected for atomic abundances coupled alongside the atomic charges, suggests that two of the outer most oxygen atoms are likely radical centres. The significant majority of the contributions to the ESR spec-

tra are generated from the two nitrogen atoms once atomic abundances are taken into account, as shown by the hyperfine coupling tensors (orange) in Figure 4.40. This potentially suggests that the external N-O bond of the nitrite ester group of PETN may be the most susceptible to fragmentation.

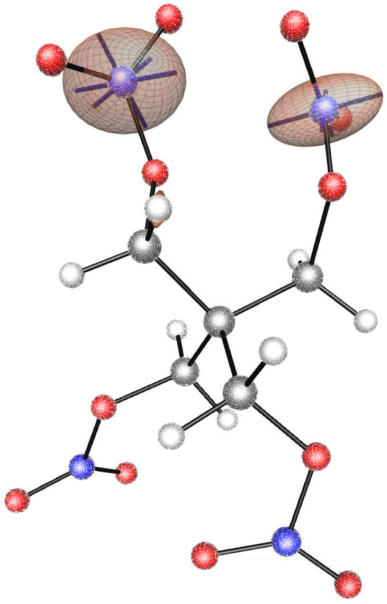

(a) Structure with adjusted coupling

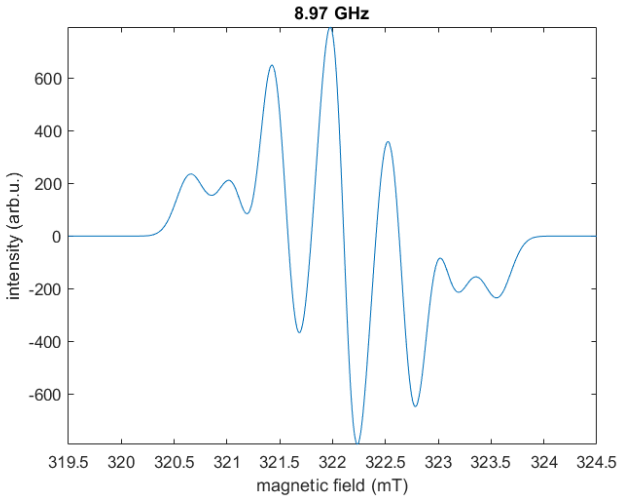

(b) Predicted ESR signal

Figure 4.40: Predicted electrostatic properties of cation radical derivative of PETN

The computed g-factor (g) for the cationic PETN radical is presented below, as the hyperfine coupling is based on tensors from two atoms these have not been reproduced, but are available in the appendix. Both the g and the hyperfine coupling tensors were corrected for anisotropy before spectra generation.

$$g = \begin{pmatrix} 1.999302 & -0.014312 & 0.047468 \\ -0.014312 & 1.998744 & 0.013447 \\ 0.047468 & 0.013447 & 1.970902 \end{pmatrix}$$

Preferential thermodynamic pathway for PETN

Each reaction (A→H), as identified within the HMX decomposition pathways shown in Figure 4.9, can be tested with the appropriate thermodynamic data calculated from the molecules in question to ascertain weather the reaction is energetically favourable, allowing an insight into the potential decomposition pathway.

			Gas-Phase			Pseudo Solid Phase		
Path	Reactant	Products	$\Delta_r H^o$	$\Delta_r G^o$	Rate(s^{-1})	$\Delta_r H^o$	$\Delta_r G^o$	Rate(s^{-1})
A	PETN	PETN Ion	1167.59	1334.05	1.20E-221	1129.87	1160.11	3.55E-191
B	PETN Ion	Ionic CH_2ONO_2 Eliminated PETN & CH_2ONO_2	-68.64	-126.63	9.52E+34	-173.61	-246.02	7.84E+55
		CH_2ONO_2 Eliminated PETN & CH_2ONO_2 Ion	-30.41	-104.47	1.24E+31	-125.93	-227.97	5.39E+52
C		ONO_2 Eliminated PETN Ion & ONO_2	46.80	-12.56	9.86E+14	-33.09	-118.02	2.95E+33
		ONO_2 Eliminated PETN & ONO_2 Ion	481.47	415.72	9.15E-61	343.07	254.33	1.72E-32
D		NO_2 Eliminated PETN Ion & NO_2	-252.93	-327.57	1.52E+70	-359.83	-440.19	8.16E+89
		Ionic NO_2 Eliminated PETN & NO_2 Ion	17.05	-43.51	2.61E+20	-130.61	-210.24	4.23E+49
E		PETN Nitrite Ion	-64.66	-79.74	5.79E+26	-143.47	-175.55	3.53E+43
F		nitroso PETN Ion & O	414.64	366.97	3.18E-52	313.44	252.22	4.04E-32
		nitroso PETN & O Ion	806.40	759.08	6.44E-121	459.93	386.77	1.08E-55
G	Ionic Nitrite PETN	Ionic NO Eliminated PETN & NO	159.60	118.25	1.19E-08	303.94	256.98	5.91E-33
		NO Eliminated PETN & NO Ion	15.81	-27.03	3.38E+17	-70.41	-120.77	8.93E+33
H	NO2 Eliminated PETN	HONO Eliminated PETN & H	101.82	72.09	1.46E+00	95.35	62.03	8.44E+01
	Ionic NO2 Eliminated PETN	Ionic HONO Eliminated PETN & H	431.49	403.05	1.52E-58	446.72	556.87	1.71E-85
		HONO Eliminated PETN & H Ion	676.07	654.33	1.45E-102	543.81	505.27	1.88E-76

Table 4.16: Thermodynamic evaluation of purported decomposition pathways of PETN - energetically favourable highlighted in green

Where $\Delta_r H^o$ - Enthalpy of reaction (kJ/mol) and $\Delta_r G^o$ - Gibbs free energy of reaction (kJ/mol).

As can be seen from Table 4.16 several reactions are favourable, as highlighted in green. As with TATB and HMX, this information has been used to generate purportedly favourable decomposition pathways, as shown in Figure 4.41, with each energetically favourable product being examined in more detail.

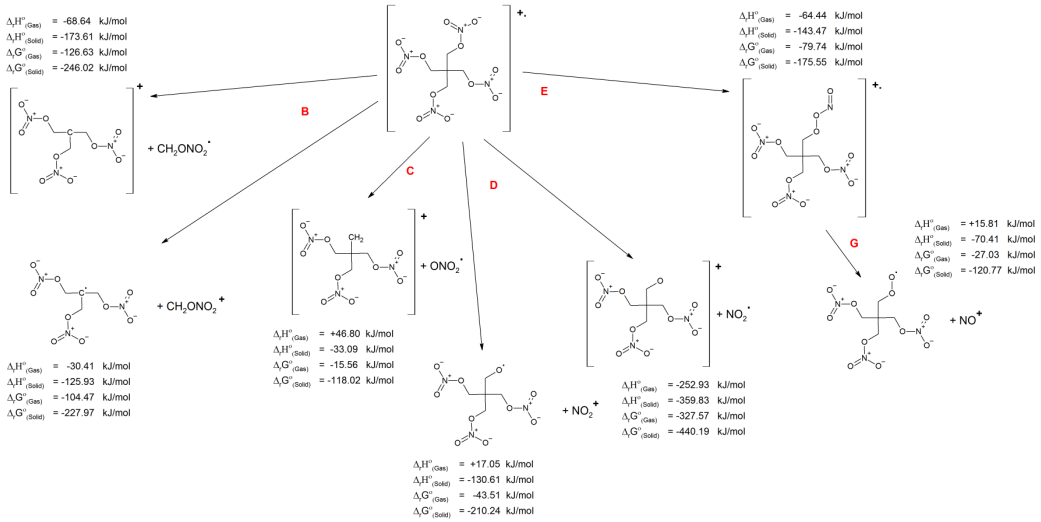

Figure 4.41: Energy favourable decomposition of cation radical derivative of PETN

The ionic form of the CH_2ONO_2 eliminated PETN is not a radical and the molecule appears to have closed the NO_2 group onto the internal carbon during the optimisation process, as shown in Figure 4.42.

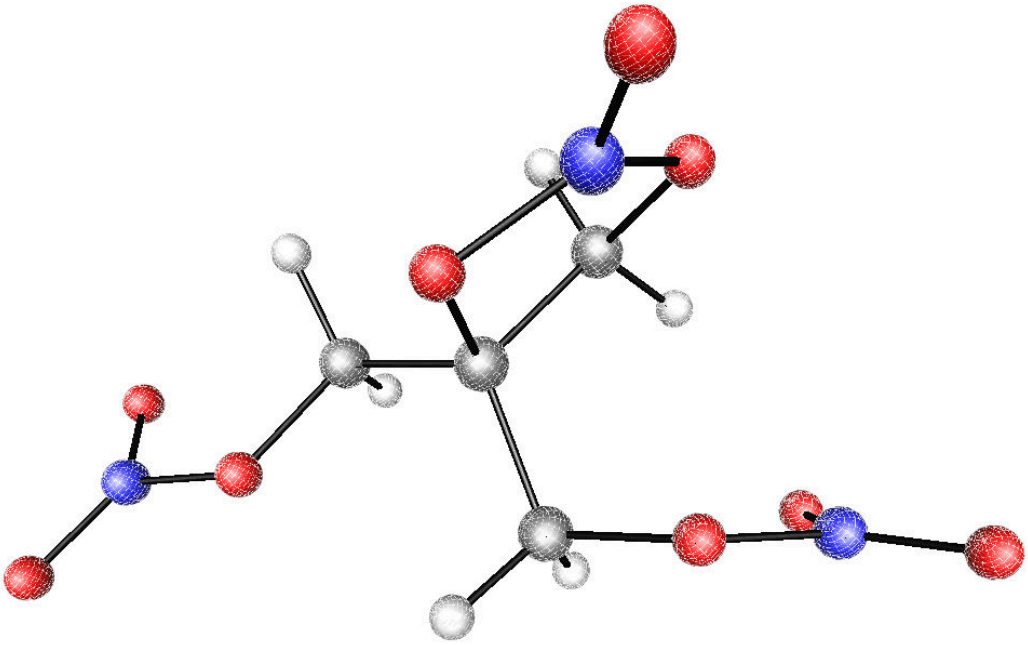

Figure 4.42: Structure of ionic CH_2ONO_2 eliminated PETN

The ground state CH_2ONO_2 fragment is a radical and, as shown in Figure 4.43a, the resultant hyperfine coupling tensor of the molecule strongly suggests that it is Carbon centred. As per previous examples, this hyperfine coupling is then corrected for atomic abundance, resulting in a the hyperfine coupling shown in Figure 4.43b, which is dominated by the two protons either side of the suspected radical centre.

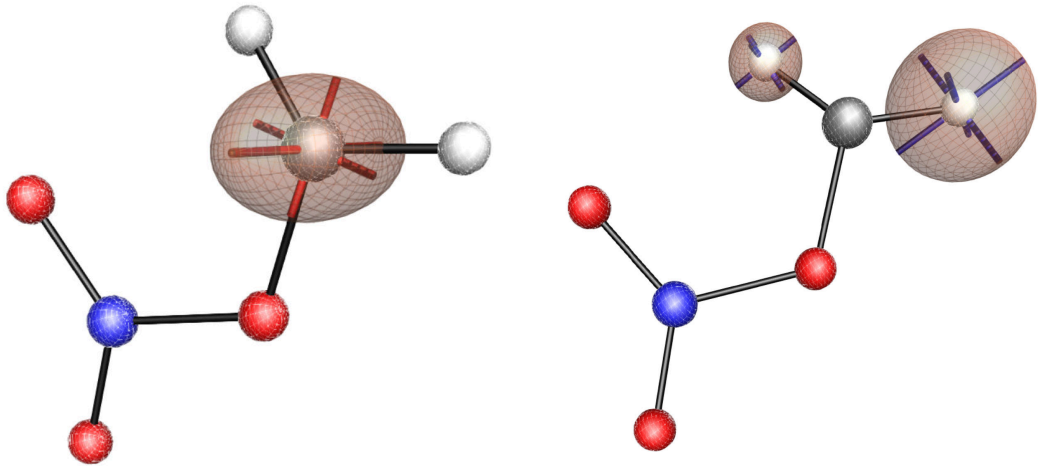

(a) Un-adjusted

(b) Adjusted

Figure 4.43: Structure and hyperfine coupling of CH_2ONO_2

The corrected hyperfine coupling and g-factor tensors were then used to generate a predicted ESR spectra as shown in Figure 4.44, which is typical for a single electron interacting with two hydrogen atoms that are non-equivalent, which results in two doublets and thus, four peaks.

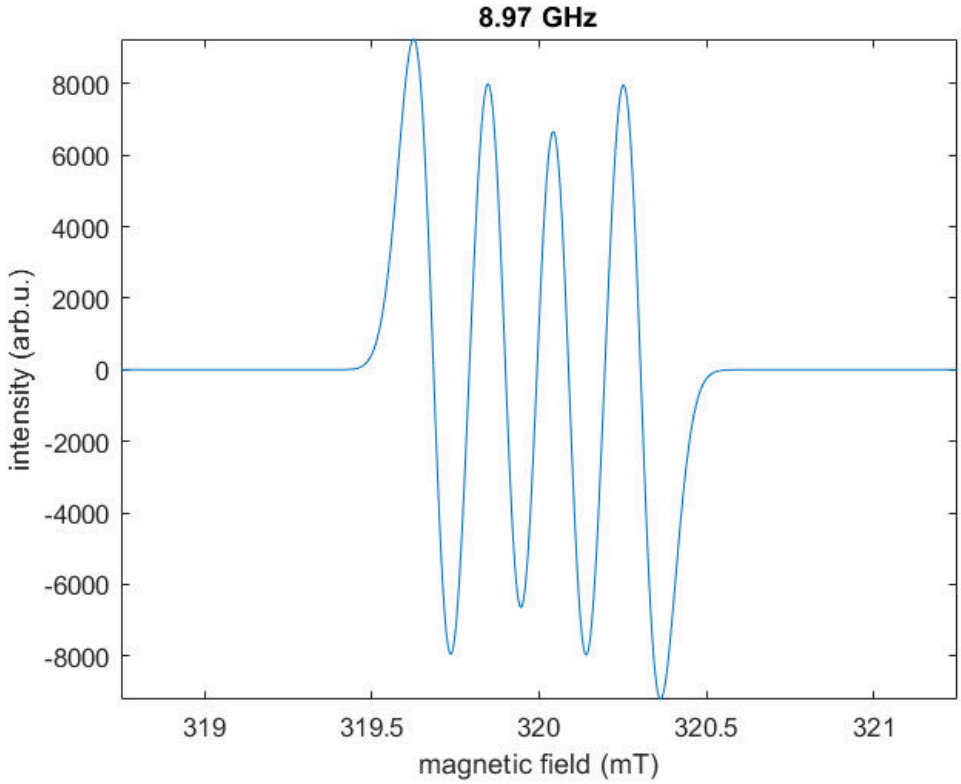

Figure 4.44: Predicted ESR signal of CH_2ONO_2 eliminated PETN radical

The computed g-factor (g) is presented below. The hyperfine coupling tensors for both hydrogens (and the small contribution from the Nitrogens) are available in the Appendix, however both were corrected for anisotropy before spectra generation.

$$g = \begin{pmatrix} 2.001660 & 0.000049 & -0.000315 \\ 0.000049 & 2.002621 & 0.000875 \\ -0.000315 & -0.000875 & 2.004093 \end{pmatrix}$$

Also energetically favourable, the non-ionic form of the CH_2ONO_2 is again a radical, with the optimised structure shown in Figure 4.45a. Again uncorrected for atomic abundance, the structure shows significant hyperfine coupling to the central carbon atom suggesting that this is where the radical is situated. Applying the correction for atomic abundance reveals that the main interactions for this carbon centred radical is with three hydrogen

atoms of which two have equivalent hyperfine coupling tensors.

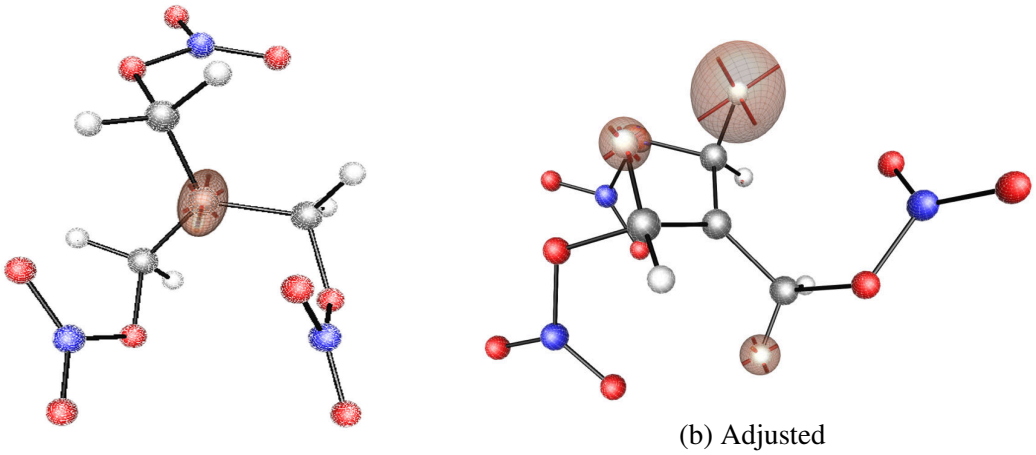

(a) Un-adjusted

(b) Adjusted

Figure 4.45: Structure and hyperfine coupling of CH_2ONO_2

The corresponding predicted ESR spectra, shown in Figure 4.46, demonstrates the two similar and one dissimilar hyperfine coupling tensors, where the two large peaks are from the singular dissimilar tensor and the three peaks are from the two similar hydrogen atoms.

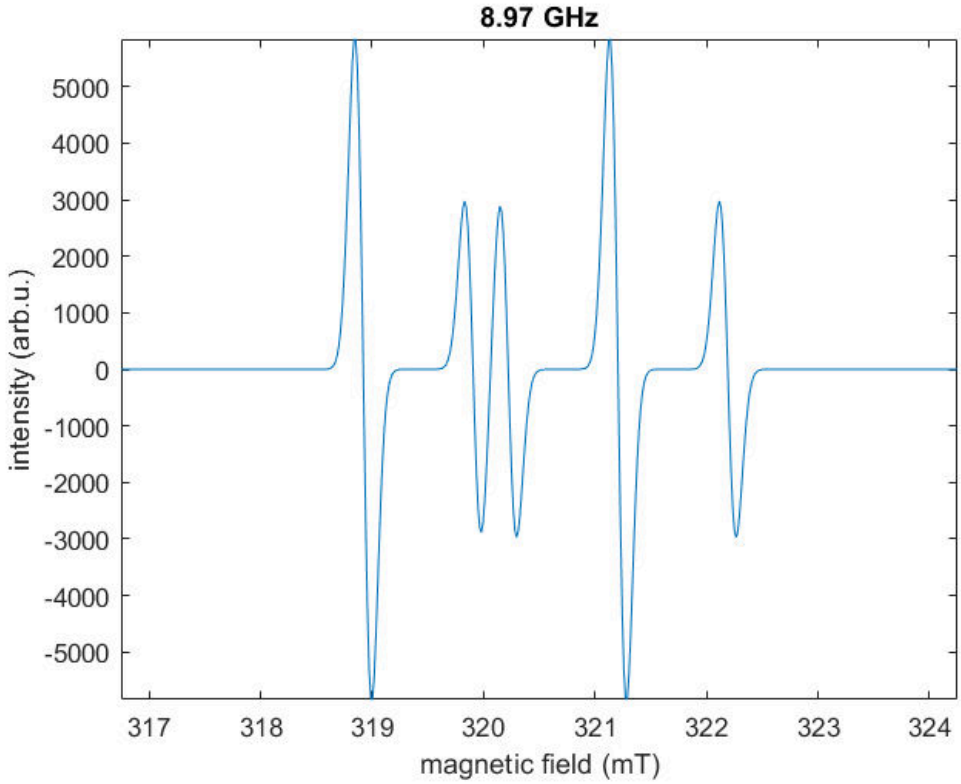

Figure 4.46: Predicted ESR spectra of CH_2ONO_2 radical

The ionic and non-radical ONO_2 eliminated derivative of PETN is energetically favourable, along with the ground state and radical ONO_2 fragment. During the optimisation, it appears that the outermost carbon atom bonds with the lone pair of electrons on the adjacent oxygen, as shown in Figure 4.47.

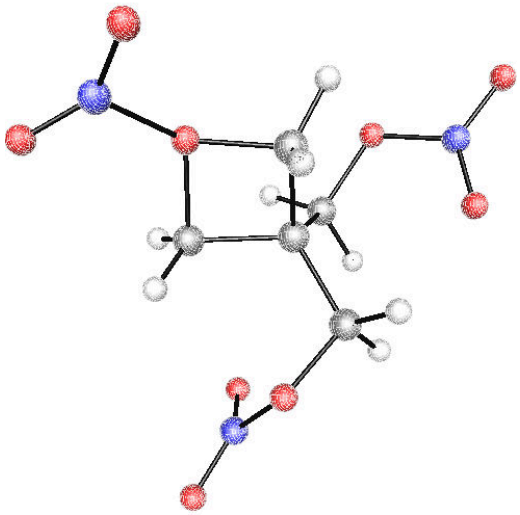

Figure 4.47: Structure of energetically favourable ONO_2 eliminated PETN cation

The resultant ONO_2 fragment is a radical, and its structure with uncorrected hyperfine coupling tensors is shown in Figure 4.48a alongside the structure with corrected hyperfine coupling tensors in Figure 4.48b. The uncorrected tensors suggest an oxygen centred radical, that will couple to the internal nitrogen atom, as shown by the corrected tensors.

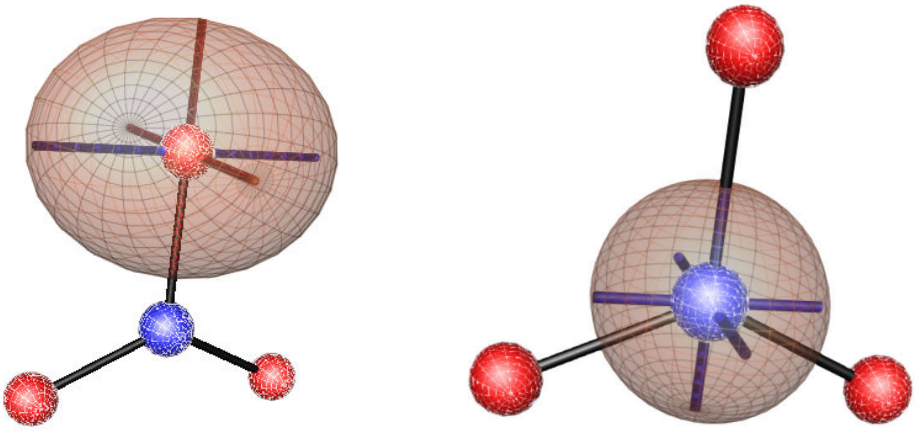

(a) Un-adjusted (b) Adjusted

Figure 4.48: ONO_2 radical structure

The corrected hyperfine coupling and g-factor tensors were then used to generate a predicted ESR spectra as shown in Figure 4.49, which is typical for a single electron inter-

acting with a nitrogen atom, consisting of three distinct peaks.

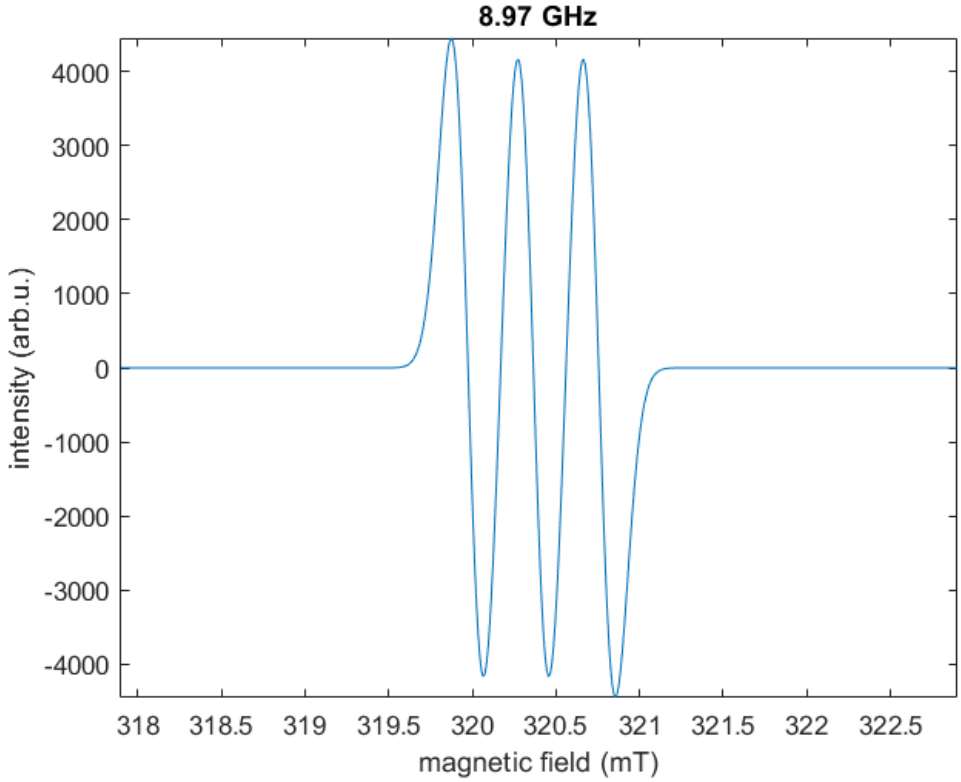

Figure 4.49: Predicted ESR spectra of ONO_2 radical

The computed g-factor (g) and hyperfine tensor of the nitrogen is presented below, both of which were corrected for anisotropy before spectra generation.

$$g = \begin{pmatrix} 2.001698 & -0.007558 & 0.000000 \\ -0.007558 & 1.991801 & 0.000000 \\ 0.000000 & 0.000000 & 2.007985 \end{pmatrix} A = \begin{pmatrix} -0.371701 & 0.001757 & 0.000000 \\ 0.001757 & -0.369399 & 0.000000 \\ 0.000000 & 0.000000 & 2.007985 \end{pmatrix}$$

NO_2 eliminated PETN appears to be energetically favourable regardless of whether the main product or the smaller NO_2 fragment is a cationic and the other a radical. However it is significantly more energetically favourable to form the larger fragment as a cation and the NO_2 fragment as a ground state radical. Starting with the least energetically

favourable, where the much larger NO_2 eliminated PETN is a radical and the NO_2 fragment is cationic, it can be seen that the radical is likely centred on the outer most oxygen atom. This is shown in Figure 4.50a, by the location of the uncorrected hyperfine coupling. When the correction for atomic abundance is applied, the majority of the hyperfine coupling can be seen to originate from the two adjacent protons, as shown in Figure 4.50b.

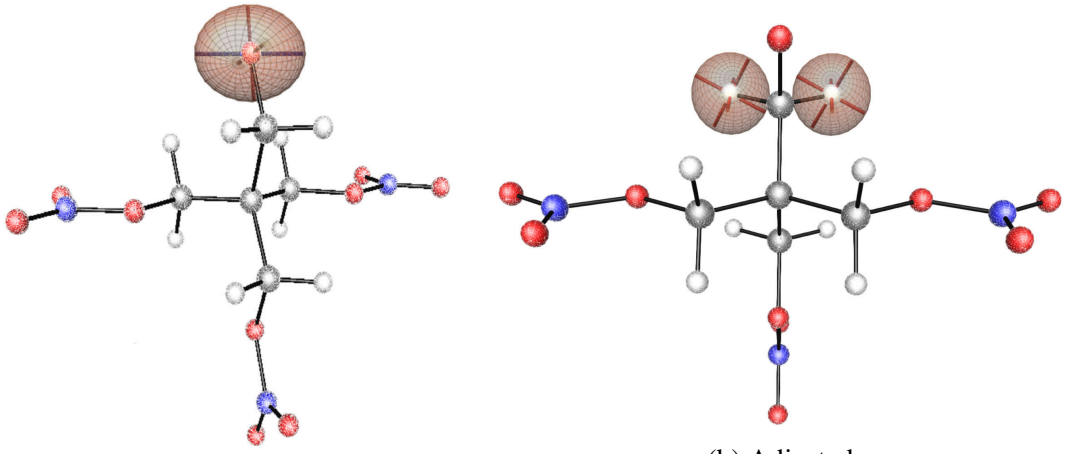

(a) Un-Adjusted (b) Adjusted

Figure 4.50: Structure and hyperfine coupling of NO_2 eliminated PETN

The g-factor and hyperfine coupling tensors of the hydrogen atoms were used to generate a predictive ESR spectra, as shown in Figure 4.51. The observed triplet is typical for a single electron interacting with two similar protons.

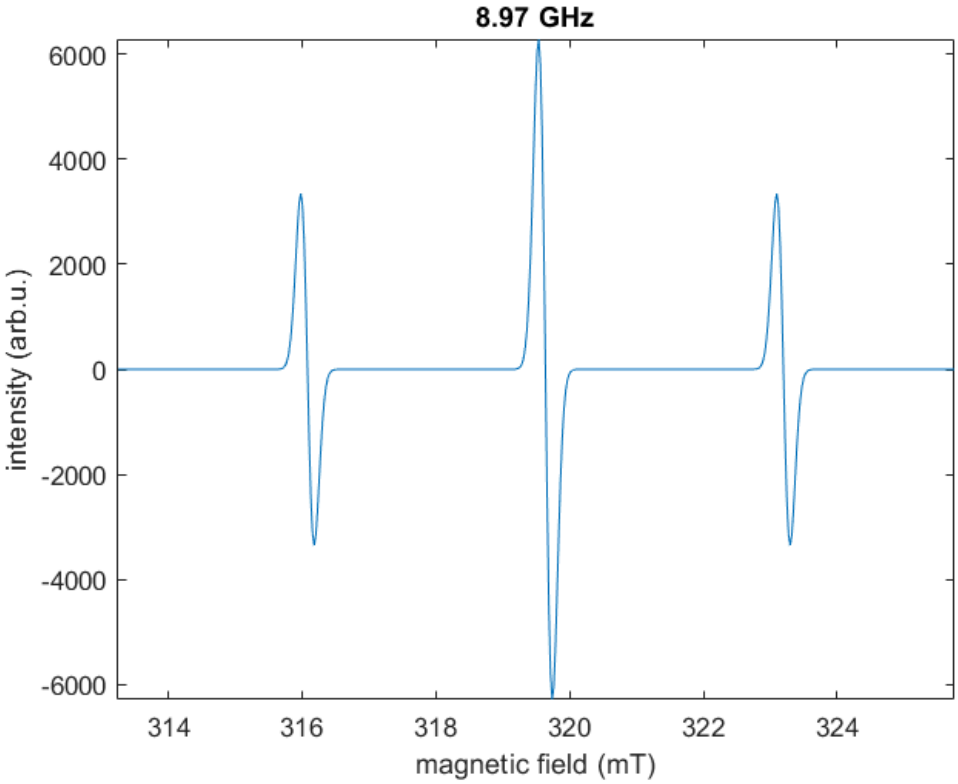

Figure 4.51: Predicted ESR spectra of NO_2 eliminated PETN radical

The computed g-factor (g) and hyperfine tensor of the identical hydrogens is presented below, both of which were corrected for anisotropy before spectra generation.

$$g = \begin{pmatrix} 2.000587 & 0.003141 & -0.005710 \\ 0.003141 & 1.996035 & 0.010280 \\ -0.005710 & 0.010280 & 2.018092 \end{pmatrix} A = \begin{pmatrix} 3.367390 & 0.039117 & -0.138635 \\ 0.039117 & 3.744196 & -0.377662 \\ -0.138635 & -0.377662 & 3.601687 \end{pmatrix}$$

The more energetically favourable equivalent, where the larger NO_2 eliminated PETN molecule becomes cationic and the NO_2 fragment is a radical, was difficult to optimise and, as shown in Figure 4.52, appears to be quite unstable. The structure suggests possible further release of NO_2 from an adjacent nitro group followed by the capture of a hydrogen atom from a CH_2 group.

The initially released NO_2 radical is well known, with the radical being centred on the nitrogen. The structure and corresponding predicted ESR spectra have already been displayed for the NO_2 radical as it was a suspected fragment resultant from HMX ionisation, it is shown in Figure 4.37.

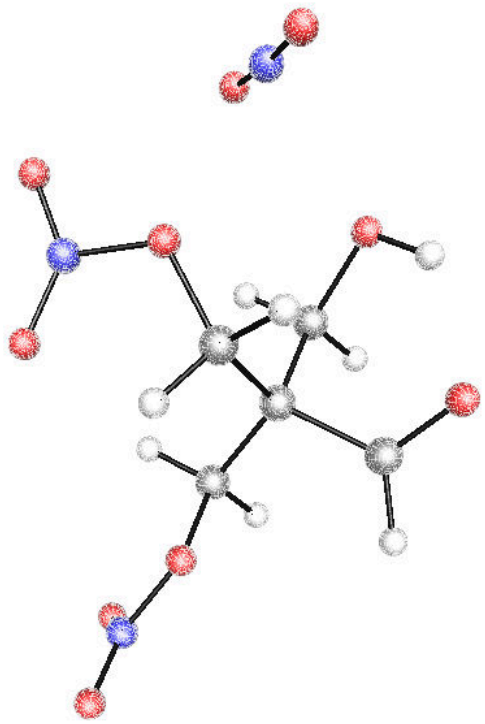

Figure 4.52: Structure of NO_2 eliminated PETN cation

The NO eliminated derivative of PETN is also energetically favourable, resulting in a potential oxygen centred radical derived from the uncorrected hyperfine coupling tensors of the optimised structure, as shown in Figure 4.53. Correcting for atomic abundance essentially nullifies any hyperfine coupling on the oxygen atom, indicating that the vast majority of coupling will come from the closer protons within the molecule, as shown in Figure 4.53b.

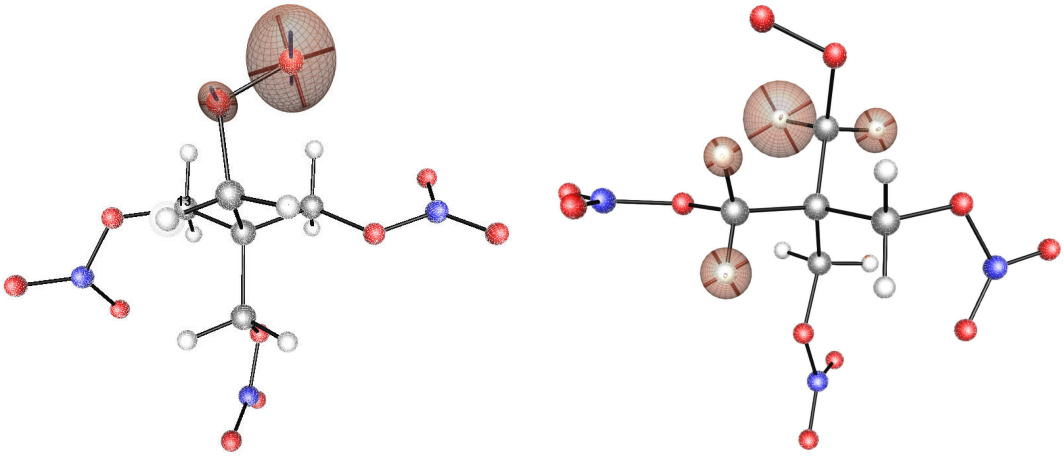

(a) Un-adjusted (b) Adjusted

Figure 4.53: Structure and hyperfine coupling of NO eliminated PETN radical

The g-factor and hyperfine coupling tensors of the hydrogen atoms were used to generate a predictive ESR spectra. As shown in Figure 4.54, the observed spectra complex and upon inspection of the individual tensors, consists of two singlets from dissimilar hydrogens and a triplet from two similar hydrogen atoms.

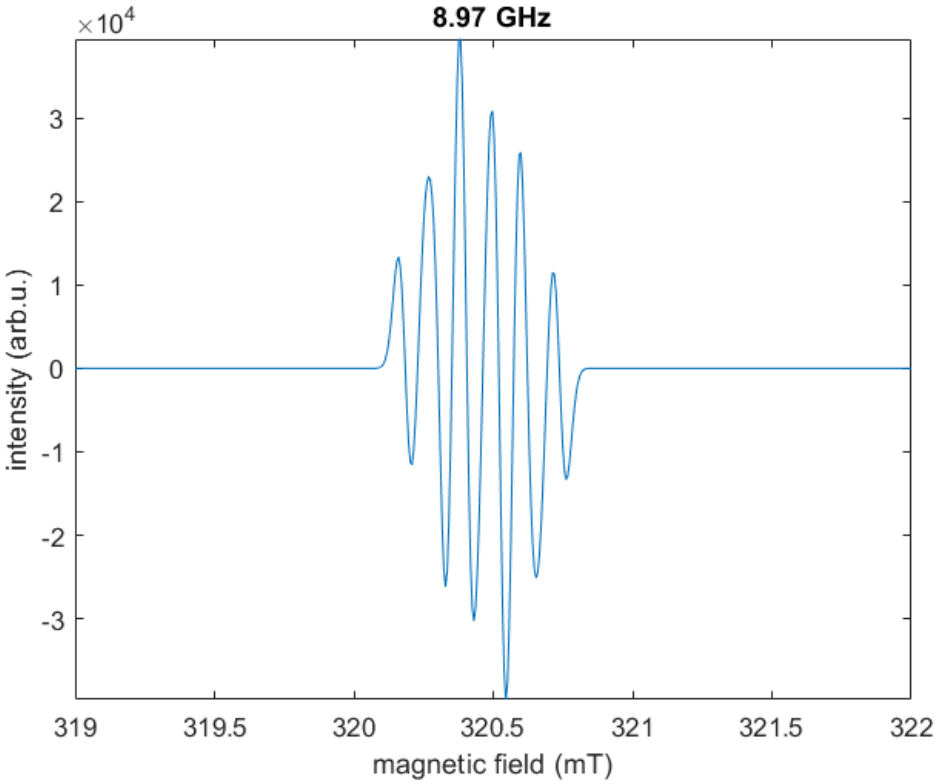

Figure 4.54: Predicted ESR spectra of NO eliminated PETN radical

The computed g-factor (g) is presented below and the hyperfine coupling tensors for the hydrogens is available in the Appendix, both of which were corrected for anisotropy before spectra generation.

$$g = \begin{pmatrix} 1.988991 & 0.013205 & -0.000873 \\ 0.013205 & 2.002803 & 0.009890 \\ -0.000873 & 0.009890 & 2.007827 \end{pmatrix}$$

The isomerisation of PETN to a nitrite derivative does not involve fragmentation, and as such cannot exist in an electronic ground state. The resultant optimised structure, as shown in Figure 4.55, is quite interesting as it suggests the potential release of NO_2. The remaining fragment is therefore equivalent to the NO_2 eliminated PETN fragment that has previously been considered.

The structure of the fragmented nitrite derivative suggests that the radical is located on the oxygen adjacent to the site of the NO_2 loss, as shown by the uncorrected hyperfine coupling in Figure 4.55a. This is in agreement to the previous analysis of the NO_2 eliminated PETN fragment. Correcting for atomic abundances yields strong hyperfine coupling to only one of the hydrogen atoms adjacent to the radical centre, with a small contribution from the adjacent hydrogen, as shown in Figure 4.55b.

This suggests that for the nitrite derivative, the presence of NO_2 group that appears to fragment from the parent molecule, is influencing the calculation.

Further analysis of the charge distribution suggested that the NO_2 fragment was cationic, and therefore the larger fragment would need to be a radical for the charges to balance. Additional evidence comes from the linear geometry of the NO_2 fragment which is only achieved when it is in the cationic state, whereas in its non-ionic radical state, it has a bond angle of approximately 134°, as shown in the previous structure analysis, Figure 4.37.

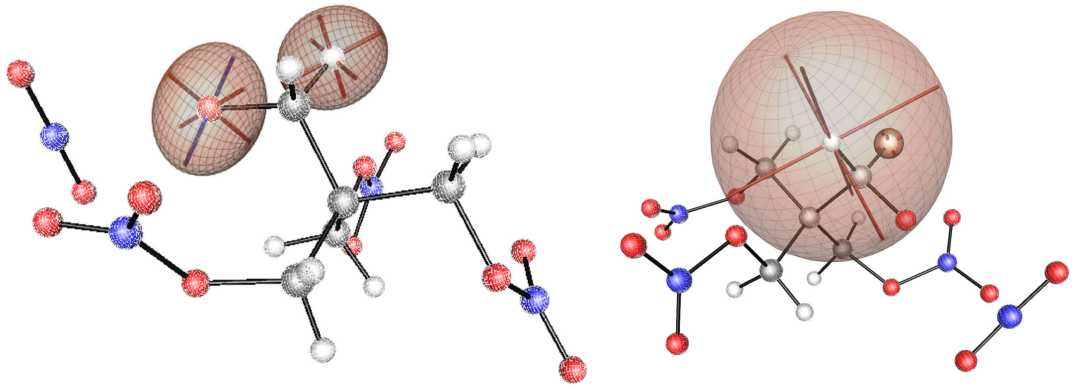

(a) Un-Adjusted (b) Adjusted

Figure 4.55: Structure and hyperfine coupling of radical nitrite derivative of PETN

The hyperfine coupling tensor for the two hydrogens was used, alongside the g-factor

tensor to generate a predicted ESR signal, as shown in Figure 4.56, which generated a typical doublet. This is in contrast to the previously generated triplet seen in the predicted spectra of the NO_2 eliminated PETN derivative, Figure 4.51.

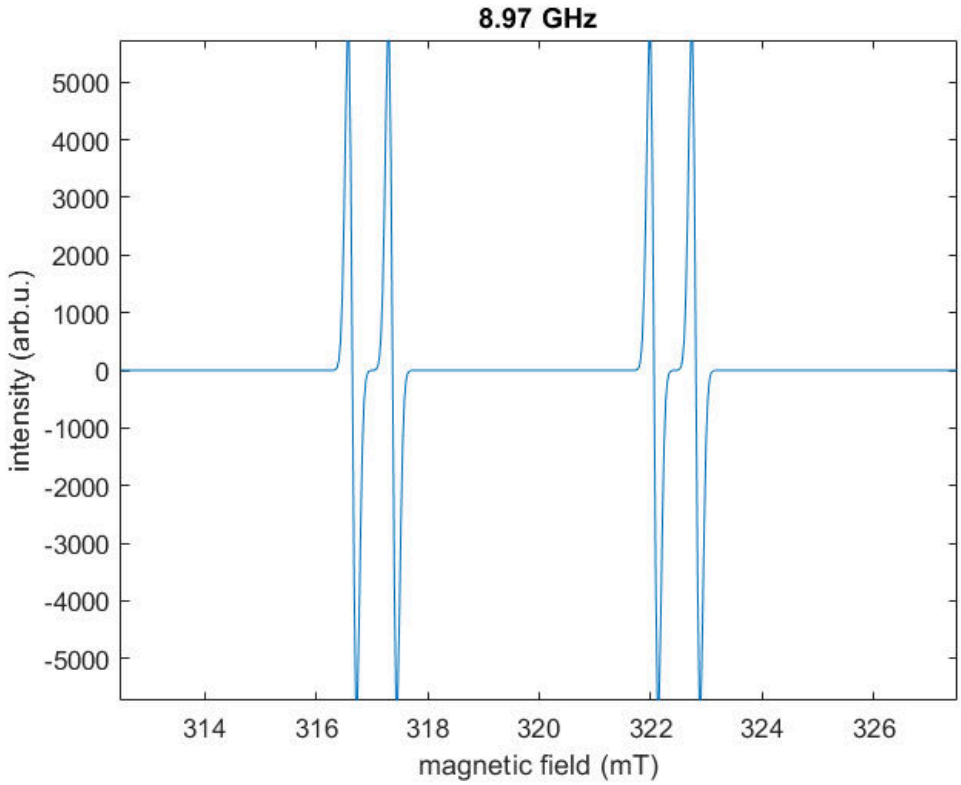

Figure 4.56: Predicted ESR spectra of ONO_2 radical

The computed g-factor (g) and hyperfine tensor of the identical hydrogens is presented below, both of which were corrected for anisotropy before spectra generation.

$$g = \begin{pmatrix} 2.001953 & -0.000358 & -0.001698 \\ -0.000358 & 2.019301 & -0.007596 \\ -0.001698 & -0.007596 & 1.991887 \end{pmatrix} A = \begin{pmatrix} 5.528688 & -0.154322 & -0.283668 \\ -0.154322 & 5.112822 & 0.210308 \\ -0.283668 & 0.210308 & 5.636513 \end{pmatrix}$$

Chapter 5

Experimental Investigation

Evidence gathered from any computational calculation, such as those undertaken in the previous chapter, should be validated against experimental evidence where possible, to demonstrate its validity. This is especially true considering that most models/calculations often do not explicitly represent all the known physics/chemistry occurring for a given scenario, and therefore approximations are often made which may likely induce error. The calculations that have been undertaken so far are no exception and several approximations have been made.

Experimental evidence is therefore required to support or refute the calculations and any conclusions that are drawn. Where dependencies lie between modelling and experimental evidence, consideration must be made to both the modelling and experimental effort to ascertain if they are correctly representing each other. If they are, then experimental data must take precedence as it provides true-to-life evidence with no approximations.

Chapter 3 provided some literature evidence as to the effect of gamma radiation on TATB, HMX and PETN. These experimental investigations are quite varied and all have been limited by the availability of a suitable gamma emitting source, meaning that most data sets have experienced different radioactive environments. As highlighted earlier in Chap-

ter two, this does not just effect the total dose, but the dose rate as well. Variations continue in both the thermal and gaseous environments employed within these investigations, sometimes causing significant differences [36, 37]. It was decided that additional experimental and analytical evidence over that present within the literature would enhance the available evidence to validate models and support conclusions. However, these experimental investigations would need to be well controlled in terms of thermal, gaseous and radiolytic environments in order to make them as applicable as possible.

5.1 Experimental plan

An experimental plan was drawn up based upon material, facility and analytical availability, in order to provide experimental evidence of the effect of gamma radiation on TATB, HMX and PETN. It was decided that an effort should be made where feasible to make any experimentation as physically simplistic as possible for two reasons; to maximise read-across between experimental evidence and any computational predictions and secondly, to ensure that an understanding of the interaction in these cases could be ascertained before consideration of more complex scenarios.

The experimental plan was broken into three areas. The irradiation of bulk materials followed by their subsequent analysis; the development of an in-situ gamma irradiative ESR technique; and some additional wet chemistry, targeted towards TATB, including the synthesis of a suspected daughter product which could be used as a marker compound during analysis.

5.1.1 Bulk material irradiation and analysis

As elucidated earlier, the ability to analyse HMX, PETN, and TATB that has been exposed to gamma radiation provides perhaps the best possible evidence as to the effect. In order to make any resultant data as applicable as possible to a nuclear weapon environment, consideration needed to be made to the appropriate radiation, gaseous and thermal environments. The exact environment encountered within different nuclear weapons is undoubtedly variable and (unsurprisingly) not available in the open literature due to security restrictions; however, a few approximations can be made: Firstly that a chemically inert gas would be present, as it is unlikely anything else would be used; the temperature would be elevated from ambient due to radiological heating effects; and finally, that the radiation environment would be dominated by gamma emission from either Uranium-235 or Plutonium-239, the two most commonly used fissile materials [82].

The gaseous environment initially presented difficulty as consideration was given to the irradiation of bulk material in chemically inert gasses such as nitrogen, argon or helium, but it was quickly realised that these gasses would become ionised themselves in the presence of gamma radiation, presenting the possibility of unknown side reactions. As a result, and in an effort to keep the investigation simple and make any subsequent data/findings more suitable for model validation, the most appropriate gaseous environment was considered to be a vacuum and was hence selected for any irradiative experiments. The thermal environment was decided to be set at 40°C as service representative temperatures were unknown and 40°C was deemed to be sufficiently far away from ambient that it should be easy to achieve and control accurately.

The radiolytic environment posed the most significant challenge as dose rates would need to be much greater than those observed within weapon environments in order to accelerate the effect. In order to obtain an increased dose rate of radiation that is comparable in incident energy to that of a nuclear weapon environment, significant quantities of the

same fissile material contained with such weapons would be required; this was clearly unachievable. Consideration of the available sources lead to a decision between utilising the JJ-Thomson facility cobalt-60 source, which has a significantly higher incident energy than that of Plutonium or Uranium, or using smaller, much lower activity laboratory point sources of other radio nuclides, including Uranium-235, and Americium-241, that have more comparable energy spectra.

It was decided that the JJ-Thomson facility would be used over point sources, due to its immediate availability to irradiate explosive samples safely in a proven way, with differences in the incident energy compared to service being addressed by the calculated mass attenuation function of each material. The use of such an active source permitted much greater dose rates and hence total doses to be achieved over a fixed time period. Values of dose rate needed to be reasoned, with increases in dose rate reducing facility demand and hence cost, whilst providing data earlier. However, concern was raised that higher dose rates would significantly increase the probability of radical-radical reactions that would not likely be seen throughout weapon service. The total dose that materials were to receive was equally challenging as relevance to service was desirable, however a sufficient enough effect to the material was required in order to undertake successful analytical investigations. Resultantly, a total dose of 200 kGy (dose equivalent to water) was agreed as this was the maximum permitted for explosive materials for the facility. Irradiations would be undertaken at the maximum dose rate that could be achieved throughout the project, i.e. 750 Gy hr^{-1}.

These decisions were also heavily influenced by the fact that a number of irradiative experiments had previously been undertaken in the JJ-Thomson facility, namely by Padfield and Connors [43, 66, 51, 49] and keeping the same experimental conditions allows not only read across to their data, but also access to samples of TATB that had already been irradiated to total doses varying between 10 kGy and 400 kGy. Although these samples

had been irradiated at a higher dose rate than what was achievable for this work, due to source decay, it was decided due to facility availability and cost not to repeat the irradiation of TATB as all other parameters were identical.

The provision of samples of raw PETN and HMX irradiated to 200 kGy at a dose rate of 750 Gy/hr was therefore planned to be undertaken within the JJ-Thomson facility. The explosive containment units, control unit and glass ampoules were used in an unmodified state to improve read-across, with the exception of a data logger being incorporated onto the control box with a secondary thermocouple channel to ensure irradiation temperatures were consistent. A total of 4 grams of each material was irradiated and split between six vials, that were evacuated then flame-sealed prior to being irradiated for approximately 266.7 hours at 40°C.

In order to have confidence in the dose rates and associated total doses, detailed dosimetry of the JJ-Thomson facility and the associated apparatus was also undertaken, as this had only been completed reasonably crudely several years prior to the start of this investigation.

Post irradiation, specimens were withdrawn from the facility and visually inspected prior to sampling and analysis of the gaseous head space, afforded through the break arm on the side of each ampoule and subsequent direct injection into a GC-MS. Samples were then removed from the ampoules by scoring and targeted breakage of the flame-sealed end of the glass ampoule. Collected material and a baseline sample was initially sent for hazard analysis, which consisted of a 10-shot Rotter test, to measure impact sensitiveness and spark test to ascertain the electrostatic hazard properties of the material; additional bulk hazard testing could not be afforded due to limited material availability. Materials, including remnants of irradiated TATB from Connors and Padfield [43, 66, 51, 49] and appropriate baselines were then also analysed using DSC, FT-IR, HPLC-MS, NMR and

ESR, where possible.

Analysis of the materials by DSC was undertaken at a heating rate of 2°C per minute in accordance with the compatibility STANAG [33] and were used to ascertain differences in phase change, decomposition onset and peak temperatures and infer changes in the thermal hazard properties. NMR would also be undertaken on dissolved specimens, which was acknowledged to be challenging for TATB due to its poor solubility and HPLC-MS would be undertaken, where specialist bi-phenyl and phenyl-hexyl columns were selected to separate the aromatic TATB from possible decomposition products.

ESR analysis was also planned to be undertaken on samples withdrawn from the JJ-Thomson facility, however due to the time period between retrieving a specimen and analysis, any detected radicals will be long lived chain terminating radicals, so any evidence of early time radical formation would likely be lost.

5.1.2 In-Situ ESR

The irradiations undertaken within the JJ-Thomson facility are acknowledged to focus on bulk changes resultant from large quantities of absorbed gamma radiation; with findings from subsequent analytical investigations providing evidence as to the end product of the interaction. As shown from the purported decomposition maps, there are potential intermediate steps, mostly involving ionic and radical species, that are likely to exist prior to the formation of the reaction terminating daughter product. The ability to detect some analytical evidence of intermediate states is highly desirable, as it would provide evidence to corroborate the computational chemistry predictions.

Due to the short lived nature of the suspected intermediate radical species, detection and quantification presents challenges. Irradiations undertaken within the JJ-Thomson facility

can only be achieved at ambient or higher temperatures, meaning that any short-lived radicals will likely have decayed to long lived daughter species, in fractions of a second after the cobalt-60 source is retracted, i.e. significantly longer than that required to retrieve and test the irradiated material. As a result, in-situ methods were considered which could provide some analytical evidence during the irradiation.

The only method that was considered potentially viable for samples under irradiation in the JJ-Thomson facility was using FT-IR with the light sent through fibre-optic cables, permitting the spectrometer to sit outside the radiation cell. A few trials were undertaken that showed that the method was not viable, due to the darkening of the glass ampoule upon irradiation and the decomposition of the fibre-optic cables, attributed to the intensity of the radiation field.

Consideration was then given to the possibility of undertaking ESR analysis of materials immediately after irradiation in the JJ-Thomson facility. This option was favourable as it would provide evidence that could directly corroborate predictions from the computational chemistry analysis. However, due to the lack of ability to undertake the irradiations at low temperature and the time required to access the samples, it was concluded that any detections would simply see chain terminating radicals. As an alternative, spin trapping was considered.

This methodology involves mixing a chemical species with a radical, which subsequently react together to form a more stable, albeit different, radical species. This longer lived spin-adduct may then be analysed within an ESR spectrometer. However, the main drawback with this method is that the identity of the short lived radical must be inferred from the spectra of the spin-adduct, adding significant complexity. In addition to this issue, the spin trap would have to be added to the sample prior to irradiation, meaning that the spin trap would then be exposed to exactly the same amount of radiation as the sample. The

spin trap would likely itself become an ionised radical and decompose to an unknown product. This methodology was therefore not considered further.

It became apparent that there was no viable method for in-situ analysis of samples being irradiated within the JJ-Thomson facility, mostly due to its power but also due to the multi-directional nature of the radiation field, i.e. equipment and/or other chemicals would be exposed along with the sample. The availability of smaller, lower activity point sources was investigated, with several options being viable for more 'bench-top' applications; this allowed additional in-situ methodologies to be considered. However, these point sources were of much lower activity compared to the JJ-Thomson facility, hence why they were not selected for bulk material irradiation, and as a result the analysis technique needed to be as sensitive as possible.

Fortunately, ESR analysis is known to be one of the most sensitive analytical techniques, with spectra achievable at very low radical concentrations as low as 10^{-6} molar percent [83]. It was therefore considered that ESR would be the best technique to develop an in-situ methodology for irradiating samples, and would provide excellent evidence to compare against the predicted ESR spectra of any intermediate species.

Typical ESR spectrometers, such as the one available at Shrivenham, are designed so that an external stimuli, such as ultraviolet radiation, can be applied to a sample whilst it is inside the spectrometer, i.e. in an in-situ arrangement. The instrument also has an environmental controller capable of reaching -170°C. This arrangement was adapted so that a gamma emitting source could be placed in-line with the sample whilst it was within the spectrometer, with the aim of irradiating samples of interest at the lowest achievable temperatures. These low temperature irradiations would significantly extend the lifetime of intermediate radicals when compared to room temperature, and permit the generation of an ESR spectra without having to raise the temperature of the sample.

As discussed previously, ESR spectrometers contain powerful electromagnets in order to generate the required characteristic spectra. Many radionuclides, such as cobalt-60, are ferromagnetic, which presented a potential safety concern where the application of a strong magnetic field could cause heating or even rapid movement of the radionuclide, both of which have the potential to cause unplanned dispersal of radioactive material within the laboratory; this was clearly not acceptable. A method was developed which allowed the electromagnet to be physically switched off and isolated whilst allowing the thermal controller to function. This allowed a sample to be irradiated at a controlled temperature, without the application of an electromagnetic field.

Consideration was also given to the radionuclide selected for the in-situ measurements, with two available types, cobalt-60 and americium-241; with the former having gamma quanta an order of magnitude greater in energy. The cobalt-60 option had the obvious advantage of being the same incident energy of the irradiations undertaken in the JJ-Thomson facility. However, as shown by some of the computationally calculated ionisation potentials, the interaction between the lower energy americium-241 should be identical, i.e. ionisation through Compton scattering. In fact the lower energy of the americium-241 was one of its advantages, as radiation at this energy would be absorbed more readily as a function of material thickness than that of cobalt-60. This was especially useful considering the limited quantity that would be exposed due to the small diameter (3.4 mm) of the ESR tubes. An additional advantage for the americium was that it is paramagnetic and not ferromagnetic like the cobalt, meaning that if the electromagnet were to accidentally become enabled, the effect on the material would be significantly reduced. As a result, americium was selected as the source of choice for these experiments.

Four americium-241 sources were available in varying activities ranging from 40 kBq to 1 GBq. All four samples were of different geometry and therefore needed to have

unique fixtures manufactured such that they could be mounted onto the ESR cavity and provide a collimated beam of gamma radiation to the sample. A standard approach was used, whereby an aluminium fixture would be attached to the ESR cavity port using nylon grub screws to secure. Each fixture would mount the radionuclide and collimate any emitted radiation through a hole 5 mm in diameter towards the sample in the cavity. Each fixture was manufactured in two parts, allowing the incorporation of the radionuclide into the fixture prior to its mounting onto the ESR. An example of one of the fixtures can be seen in Figure 5.1, and the port on the spectrometer on which it would mount can be seen in Figure 5.2.

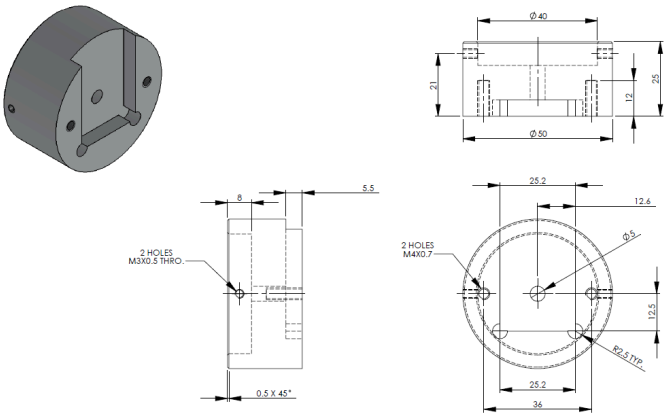

Figure 5.1: Schematic of source holder (courtesy of Brian Duguid - Cranfield University)

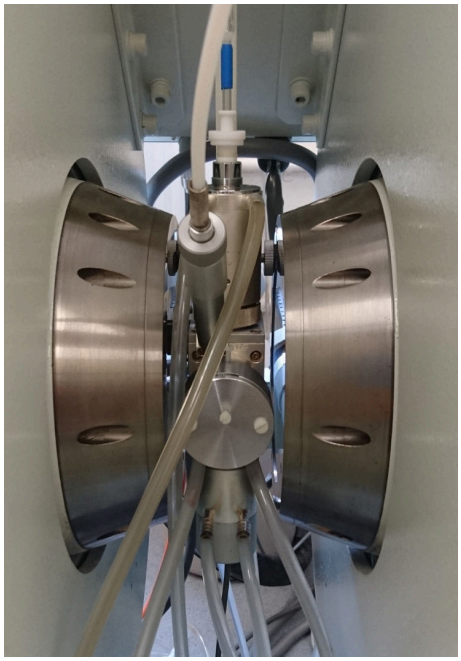

Figure 5.2: ESR spectrometer sample and source mounting

In order to provide read-across to the irradiations undertaken within the JJ-Thomson facility, samples of HMX, TATB and PETN would need to be sealed under vacuum. This presented a small challenge as ESR vials are typically manufactured from quartz or an equivalent, to reduce any signals from impurities found in typical laboratory glassware. A technique was developed that allowed powdered samples to be added to an ESR tube, which would be subsequently evacuated and then flame-sealed in an manner akin to the method used for evacuating and sealing ampoules used within the JJ-Thomson facility. In order to achieve this, the ESR tubes were modified using graded glass seals which allowed the addition of a section of lab-typical borosilicate glass at a much greater diameter. This permitted sample addition, evacuation and flame-sealing, whilst ensuring that only quartz was present alongside the sample in the microwave cavity. Using this method, samples of HMX, PETN and TATB were all sealed under vacuum, each containing approximately 0.5 grams of material.

One of the significant issues with the designed arrangement was that dosimetry was not

possible, primarily due to the fact that a detector could not be incorporated into the microwave cavity based on size restrictions. It was therefore impossible to measure the amount of radiation, from any source, that was reaching the sample. A measurement between the location of source and the sample within the cavity was made using a calliper (76.82 mm), permitting an approximation of the amount of radiation likely to be incident on a sample.

This was based on the known activity of each radionuclide, the inverse square law and the expected absorption from air. Based upon the activity of the most powerful point source (approx. 1 GBq) and the inverse square law, it can be calculated that the expected activity at 76.82 mm would be 74,158 Bq per square millimetre. This is achieved, as detailed in Equation 5.1, by dividing the activity of the point source $\dot{A}_{Source}$ by the area of a sphere with radius 76.82 mm, the distance from the source to the sample. This results in an areal activity, $\dot{A}_{Shpere}$, of 13,500 Bq per square millimetre.

$$\dot{A}_{Shpere} = \frac{\dot{A}_{Source}}{4\pi r^2} \tag{5.1}$$

The total activity that would be incident of the sample $\dot{A}_{Incident}$ is therefore simply this value $\dot{A}_{Shpere}$ multiplied by the area (3.4 mm by 50 mm) of the ampoule, the resultant calculated activity is approximately 2.29 MBq.

This value reduces further, due to absorption from the 76.82 mm of air between the point source and the sample. Using literature values for the mass-absorption coefficient μ/ρ for air 60 keV of 0.1888 [17] and the Beer Lambert law as shown in Equation 2.1, this corrects the incident activity $\dot{A}_{CorIncident}$ to approximately 541 kBq, as shown by Equation 5.2, where x is distance.

$$\dot{A}_{CorIncident} = \dot{A}_{Incident} e^{-\mu x/\rho} \tag{5.2}$$

The wall of the glass ampoules also presents a further absorption prior to the actual specimen, this consists of 0.8 mm of silicon dioxide. Again by using literature values for the mass-absorption coefficient for silicone at 60 keV, 0.2417 [17], the reduction was calculated and determined to be minimal, resulting in an activity of 530 kBq actually incident on the sample $\dot{A}_{SampleIncident}$, as per Equation 5.3.

$$\dot{A}_{SampleIncident} = \dot{A}_{CorIncident} e^{-\mu x/\rho} \tag{5.3}$$

Knowing that approximately 530 kBq would be incident on the sample, a further calculation was undertaken to determine the proportion of the incident radiation that would be absorbed by a sample. This calculation was again based upon the Beer-Lambert law, but rather than using a material's mass-attenuation coefficient, the mass-energy attenuation coefficient was used to calculate the amount of radiation that would be absorbed, rather than what would be lost through interactions such as absorption *and* scattering.

PETN has the lowest calculated mass-energy attenuation coefficient compared to TATB and HMX, and hence was used as a worst case. Using the the theoretically determined value for the mass-energy coefficient detailed within Chapter 2 of 0.0289 and the sample thickness of 3.4 mm, an activity $\dot{A}_{PETNAbsorbed}$ was calculated as per Equation 5.4, resulting in an activity of 525 kBq.

$$\dot{A}_{PETNAbsorbed} = \dot{A}_{SampleIncident} e^{-\mu_{en} x/\rho} \tag{5.4}$$

Unfortunately, this final step proved to be flawed and led to an incorrect assessment of the number of interactions that a sample would expect to experience. This is explored in more depth in the next chapter, but was only discovered after the experiment was attempted.

5.1.3 Synthesis of marker compounds

One of the key findings of Connors's work was a purported mono-furazan derivative of TATB. This conclusion was born from finding a peak in the chromatograph of irradiated TATB vs pristine that gave a peak in the mass spectrum of 240 atomic mass units, which is 18 less than TATB, signifying the loss of water. Whilst this is strong evidence for the presence of such a compound, positive identification against a marker compound was deemed highly desirable for the material. Unfortunately, a synthesis for the mono-furazan derivative was not found in the literature. However, one was found [46, 84] for TATB's other popular purported degradation product from gamma radiation; the mono-nitroso derivative. Synthesis of this compound would allow a study to be undertaken alongside irradiated samples of TATB, providing evidence for or against its generation.

5.1.4 Re-crystallisation

The work undertaken by Tian [53] suggested that the discolouration of TATB was not caused by the generation of a daughter product with a green or blue chromophore, but was caused by dislocations within the crystal structure. In addition, numerous literature have suggested that the increase in sensitiveness seen for some irradiations of TATB, HMX and PETN especially to impact, may be caused by the generation of gaseous fissures within the crystal structures. As a result, the re-crystallisation of irradiated samples of TATB, HMX and PETN were planned in order to see if changes were reversible through reformation of the crystal structure.

5.2 Experimental results

Dosimetry

Prior to any experimental work being undertaken, the radiological activity of the cobalt-60 source within the JJ-Thomson facility needed to be fully characterised. This was to ensure that the radiolytic environment to which selected materials may be exposed, was well understood. This characterisation would not only allow an understanding of the total amount and rate of radiation a sample may receive, but it would also allow future calculations, for example using mass-attenuation coefficients to calculate the actual received dose, to be based upon accurate initial data. In addition, and due to the relatively short half life of cobalt-60, the activity of the source at the planned end date of the research project needed to be accurately predicted so that experiments could be irradiated at the same dose rates throughout the duration of the project. This predicted activity required calculation based upon well founded predictions of typical radioactive decay [12], and again needed to be based on accurate, traceable data.

Various methods exist for conducting dosimetry of point sources of gamma emitting radionuclides with subsequent measurements providing different physical meanings. Air KERMA (Kinetic Energy Release per unit MAss) is often used as standard in gamma ray spectroscopy and hence most electrometers are calibrated to this standard. The physical meaning of air KERMA is essentially the amount of energy transferred to a unit mass of standard air from an incident photon beam, which has the SI unit of Gray (Joules per Kilogram).

Dosimetry was undertaken using a PTW Unidos Webline Electrometer and a NE2571 0.6 cm^3 ion chamber, which are typical for such measurements, both of which were loaned and calibrated to a traceable standard by the Atomic Weapons Establishment (AWE) to Air KERMA [85]. Measurements of dose and rate were taken as averages across three

readings, of a period of sixty seconds. A longer exposure time would have potentially reduced uncertainty in measurement, however it was not advisable due to the activity of the source, as it would have reduced the life of the ion chamber. Measurements were undertaken at three distances relative to the closest side of the aluminium can of the cobalt-60 source. This was undertaken in both free air and inside the explosive containment units where the ion chamber was placed within the central sample location.

Air KERMA readings were then converted to dose equivalence to water in accordance with ISO 4037-2:1996 [86], specifically Equation 5.5. Source data for the relevant variables is summarised in Table 5.1, with measured values for the explosive unit presented in Table 5.2.

$$(D_w)_r = M_r N_k [(L/\rho)_{w,a}][(1-\bar{g}_a)k_{att}k_m]_c \tag{5.5}$$

Symbol	Units	Meaning	Value for cobalt-60
(Dw)r	Gray	Dose rate to Water	NA
$M_r.N_k$	Gray	Air KERMA Dose Rate	NA
$(L/\rho)_{w,a}$	Unit-less	Restricted-mass collision-stopping power	1.1325[86]
$1-\bar{g}_a$	Unit-less	Factor for Bremsstrahlung Radiation	0.9970 [86]
$K_{at}K_m$	Unit-less	Factor for NE2571 ion chamber	0.985[87]

Table 5.1: Air KERMA to dose equivalent to water parameters

Distance from source (M)	Dose rate air KERMA (Gy hr^{-1})	Dose rate to water (Gy hr^{-1})
0.177	1079	1200
0.210	833	927
0.220	757	842
0.300	479	533

Table 5.2: Dosimetry values

Knowledge that the activity of the source can be described by standard exponential decay as per Equation 5.6, and that radiation flux will also decay as a function of distance exponentially according to the Beer-Lambert law, repeated here in Equation 5.7, predicted dose equivalences to both Air KERMA and water may be calculated as a function of both distance (from the source) and time.

$$\dot{A} = \dot{A}_0 e^{-\lambda t} \tag{5.6}$$

Where $\dot{A}$ = Dose Rate at time = t, $\dot{A}_0$ = Dose Rate at time = 0, λ = Decay Constant and t = time

$$\dot{A} = \dot{A_0} e^{-\mu x/\rho} \tag{5.7}$$

Where μ is the mass attenuation coefficient of air and x is the reference thickness.

Using this principle, it can be calculated that the highest achievable dose rate in July 2018 for explosive samples, i.e. samples contained within the explosive containment unit placed at the minimum stand-off to the side of the aluminium can of 5 cm, is approximately 750 Gy hr-1, dose equivalent to water. This is achieved by plotting the measured activity from the dosimetry measurements against distance from the source can on a natural log plot. A linear function can then be plotted, which is essentially the Beer-Lambert

law from Equation 5.7, this is shown as the red dotted line in Figure 5.3. This line is then adjusted to take into account changes in activity by using Equation 5.6, and results in the dotted blue line in 5.3. The equation for this line is then used to calculate the achievable dose rates at the requested date of irradiation.

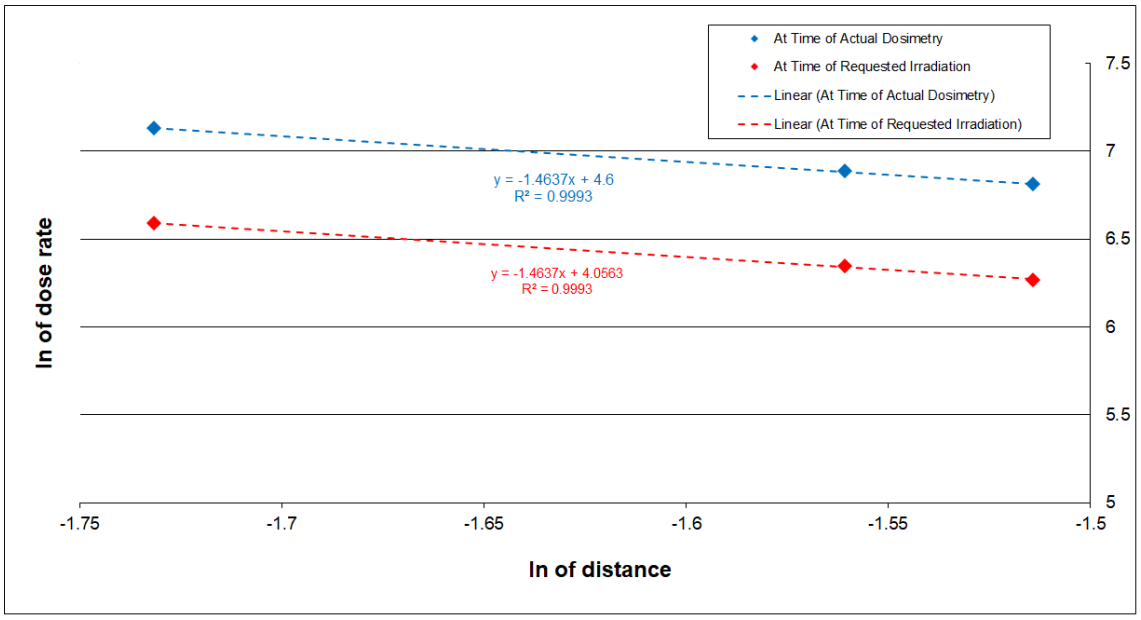

Figure 5.3: Activity vs. distance at time of dosimetry and on 31st July 2018

It is acknowledged that there is some uncertainty in the values measured during the dosimetry, which will propagate through to any predictions of dose and/or distance to the source. It is thought that the largest source of error would have been the measurement of distance within the JJ-Thomson facility as this was undertaken as accurately as possible with metre rule, with millimetre markings. Repeat measurements of the dosimetry were not possible due to the significantly large activity of the source, which would have reduced the life of the ion chamber. However, during the sixty second exposure time the dose rate was very stable, indicating good accuracy.

5.2.1 Sample preparation

Twelve ampoules, six of HMX and six of PETN, were successfully flame-sealed using the methodology developed by Connors. Three modified quartz ESR tubes containing HMX, PETN and TATB were also successfully evacuated and flame sealed for the In-Situ ESR experiments. Irradiations within the JJ-Thomson facility were not undertaken concurrently. With HMX being irradiated approximately three months prior to the PETN, slight adjustments were made to the distance between the explosive containment unit and the cobalt-60 source to address the slight reduction in activity between the two dates. Historical samples from Connors and Padfield were inspected, where pressed pellets and powders of TATB that had been gamma irradiated from 10 to 400 kGy dose equivalent to water, were found to be in good condition (and still of various shades of green). In addition, baseline un-irradiated TATB, and a sample of powder that has been UV irradiated for a total of 120 days (that had an almost blue/blackish appearance) was also obtained.

5.2.2 General findings

In keeping with findings from Padfield and Connors, the radiation environment had turned the glass ampoules a very dark brown which impeded the ability to use FT-IR techniques to analyse the head-space. The head-space of each irradiated ampoule was retrieved using a modified method to that of Connors. A design was generated where a glass side arm was mounted to a number of standard gas GC-MS vials of volume 10 mm^3 that were sealed with a septum. This was then connected to the side break tube of the sample ampoules by plastic tubing, fitted with vacuum grease. The modified GC vial was flushed with argon (spiked with krypton) for five minutes, as this was the carrier gas selected for the GC-MS. Due to the density of argon (and krypton) the apparatus was arranged such that the irradiated ampoule was held directly underneath the modified GC vial during flushing to ensure that all atmospheric species would be removed.

After five minutes, flushing was halted and the side break arm on the irradiated ampoule was broken through the connecting plastic tubing. Upon breakage of the side arm on each sample of irradiated HMX and PETN, the septum of the modified GC vial became slightly concave indicating that a vacuum was still present in each of the vials. The sample was then left for a further 15 minutes to allow equilibration between the irradiated ampoule and the GC-MS vial, before being sampled manually by a 1 micro-litre gas syringe which was injected directly into the sample port on the GC-MS. Unfortunately, only atmospheric gas species were detected in their typical ratios for air, indicating that either gasses were generated in such minute quantities that they were below the limit of detection, or, more likely, the gas sampling method was flawed.

In order to test if the sampling methodology was at fault, four samples of nitrocellulose wetted by 30 % isopropyl alcohol were vacuum-sealed within pristine glass irradiation vials and subjected to three weeks of accelerated ageing at 90°C, known to generate significant quantities of NOx species that should be detectable using the GC-MS methodology. Upon retrieval from the oven, two of the samples had undergone what was likely autocatalytic decomposition, where the material has turned from white and fluffy to a black solid; the other two samples retained their white and fluffy initial appearance. Gas sampling was undertaken using the same methodology, except when the break arm was fractured on all four vials the septum became slightly convex, indicating the presence of a significant quantity of a decomposition gas. However, upon injection of the same volume into the GC-MS, the same atmospheric species were detected, suggesting that the methodology was flawed. The equipment and chromatography method(s) were checked by testing a prepared gas standard that yielded expected results, indicating the equipment was working correctly. All samples of HMX and PETN were tested as the material needed to be retrieved for hazard testing, meaning that method development could not be undertaken on these materials. It was decided that the methodology would be re-visited prior

to future planned irradiations of HMX and PETN, using thermally aged nitrocellulose as a test.

Unfortunately during the course of the experimental programme, the JJ-Thomson facility suffered a mechanical failure rendering it unavailable after the first set of irradiations of PETN and HMX, meaning that future gas head-space analysis was not possible. Furthermore, and as will be explored in further detail below, the hazard properties of the retrieved irradiated samples of PETN and HMX were significantly affected. On safety grounds, the significant majority of these materials were disposed of, permitting only a very limited set of experimental analyses on the recovered material.

5.2.3 Bulk material irradiation analysis - TATB

Hazard properties

Due to the limited quantities, no hazard testing was possible for the 400 kGy gamma or 120 day UV irradiated samples. Connors and Padfield demonstrated notable changes to the hazard properties of the exact same TATB irradiated by gamma radiation to 200 kGy, therefore it was expected that the hazard properties of the 400 kGy and 120 day UV irradiated TATB would likely be worse; the material was therefore handled accordingly and minimal quantities used.

Thermal properties

Samples of baseline, 400 kGy and 120 day UV irradiated TATB were analysed by DSC undertaken with a heating rate of 2°C in a 40 micro litre aluminium sample holder with a pierced lid, as per the compatibility STANAG 4147 [33]. The resultant thermograms are shown compared against each other in Figure 5.4. A notable difference between the ma-

terials is observed with the onset of decomposition and peak decomposition temperatures being reduced for UV and gamma irradiated TATB, when compared to its baseline.

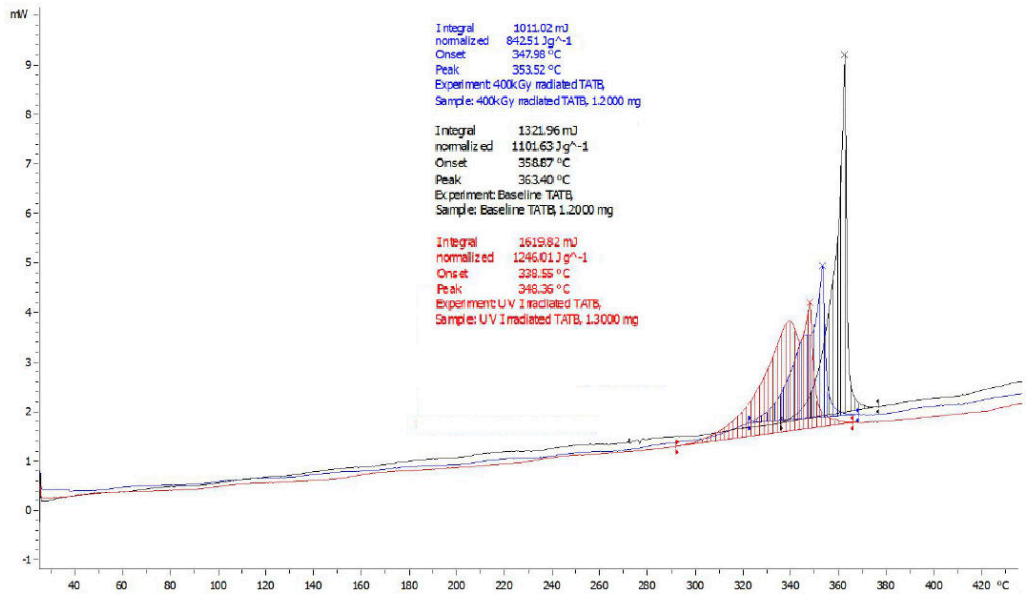

Figure 5.4: TATB thermograms

Microscopy

Optical microscopy was undertaken on samples of pristine, 400 kGy gamma and 120 day UV irradiated samples of TATB that were prepared on optical glass slides. Images were obtained at a magnification of x500 and an effort was made to obtain focused images as a function of depth by imaging every 5 microns over a total depth of 200 microns and applying reconstructing techniques. The resultant images are presented in Figure 5.5, where no crystal fissures can be observed and the greening of the material is clearly visible. There appears to be a notable difference in the powder morphology and particle size between the three images (same scale), with perhaps the most pronounced being with the UV aged material. It appears that the baseline material has a greater particle size than the 400 kGy irradiated which itself appears greater than the UV irradiated sample, the same trend can be said regarding the fluffiness of the crystals. All three materials were labelled with the same batch number and described in the documentation as TATB Type C, suggesting that

the change might be the result of irradiation, or perhaps samples had been miss labelled.

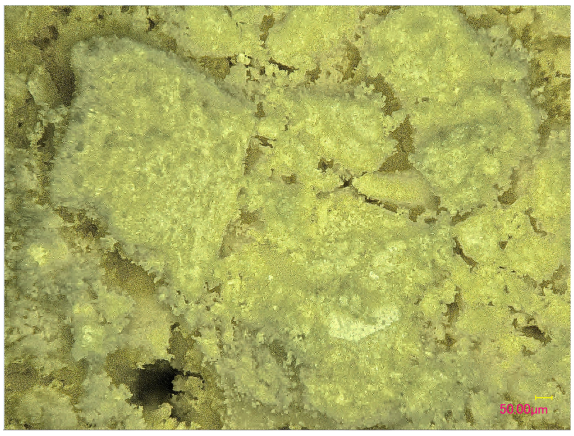

(a) Baseline

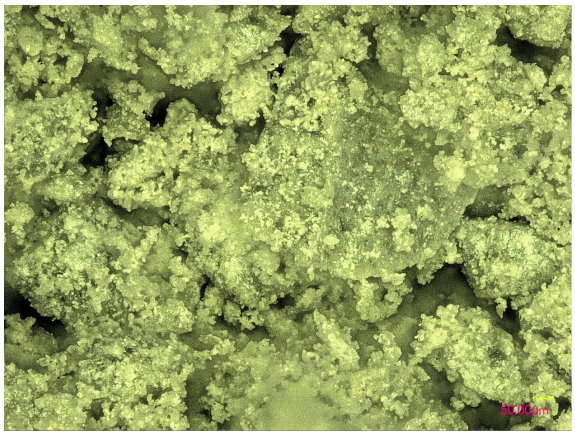

(b) 400 kGy gamma irradiated

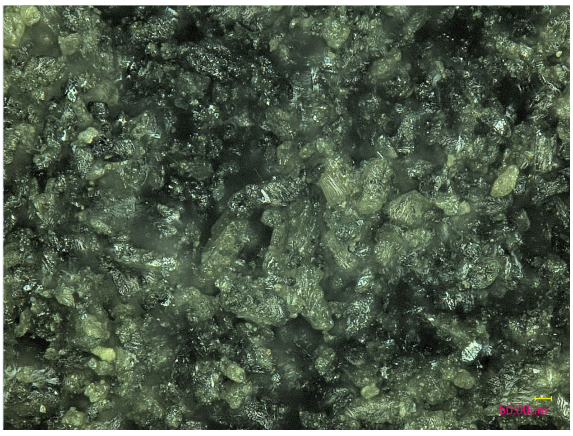

(c) UV irradiated

Figure 5.5: Optical microscopy of TATB

NMR

Due to the poor solubility of TATB in typical NMR solvents such as d-chloroform, d-acetone or even d-DMSO, specialist deuterated concentrated sulphuric acid (D_2SO_4) was obtained. Samples were prepared by dissolving pristine, 400 kGy gamma and 120 day UV irradiated TATB powders into this solvent, that were then submitted for proton, carbon and nitrogen NMR analysis using 128, 1024 and 1000 scans respectively. Even for the most sensitive proton scans, as shown in Figure 5.6 for the UV irradiated sample, no difference was detected between the three materials with identified peaks typical of pristine TATB. In the carbon and nitrogen scans, spectra could not be detected for even pristine TATB, highlighting the poor solubility of the material, even in D_2SO_4.

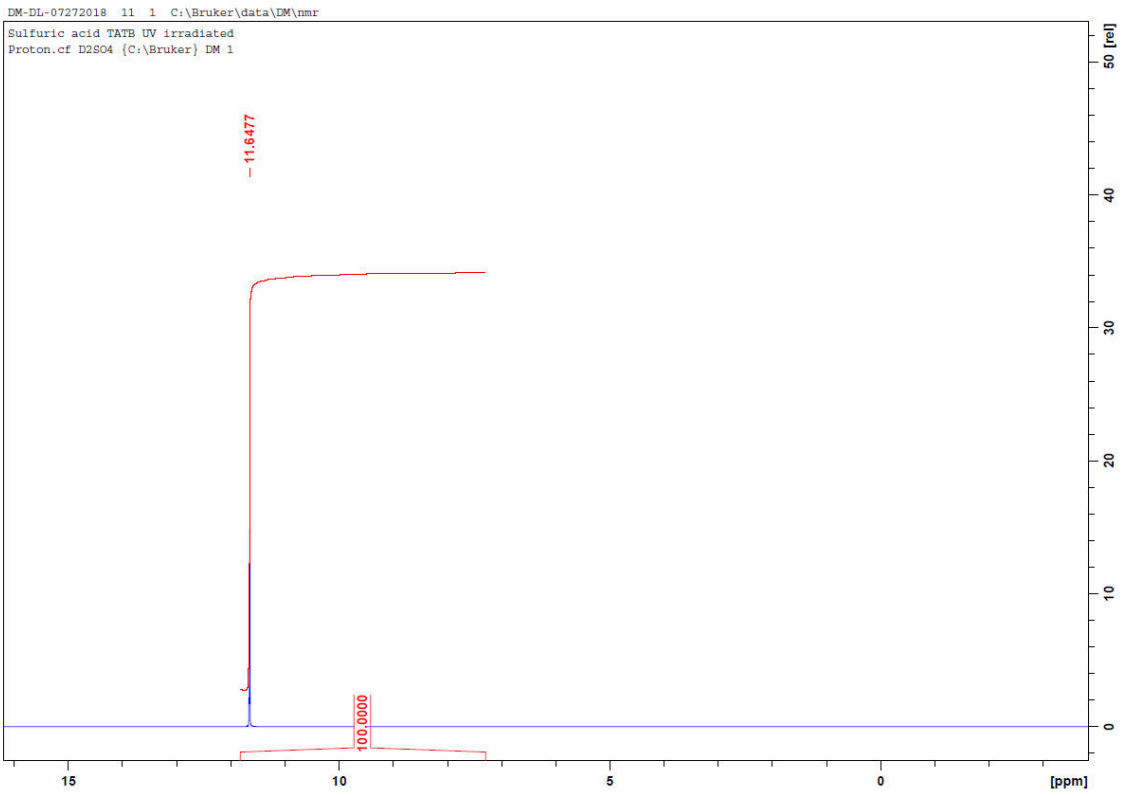

Figure 5.6: Proton NMR spectra of UV irradiated TATB in D_2SO_4

ESR

Samples of the baseline, 400 kGy gamma irradiated and 120 day UV irradiated TATB powders were submitted for analysis by ESR. The microwave cavity was successfully tuned prior to sample preparation where materials were transferred into specialist quartz ESR vials that were inserted into the instrument at room temperature, at which a magnetic field sweep measurement was undertaken at the fixed microwave frequency of the cavity. Spectra were observed for all three powders, where a maximum signal strength was observed for the UV irradiated sample, an intermediate level for the 400 kGy sample and a barely detectable signal for the baseline TATB, assumed to be attributed to the accumulation of radicles from stray sunlight.

Figure 5.7 shows individual spectra generated after a period of ESR parameter optimisation. Figure 5.8 shows the spectra of the 400 kGy and baseline samples using the optimised parameters from the UV irradiated sample, permitting a comparison between all three materials as to their radical concentration. It can be seen the 400 kGy spectra is much weaker than that of the UV irradiated sample and that a signal cannot even be detected for the baseline TATB.

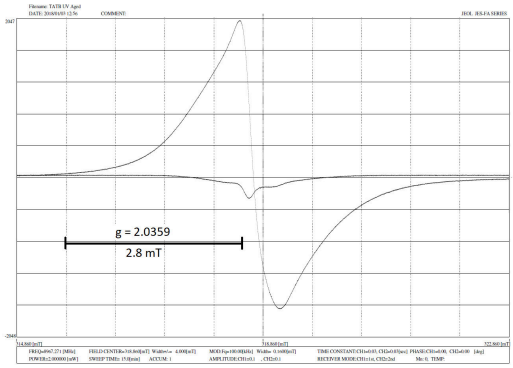

(a) UV irradiated

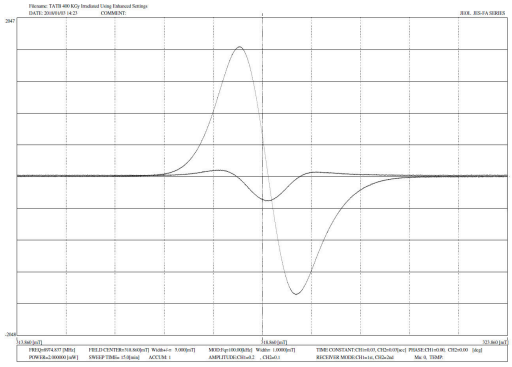

(b) 400 kGy gamma irradiated

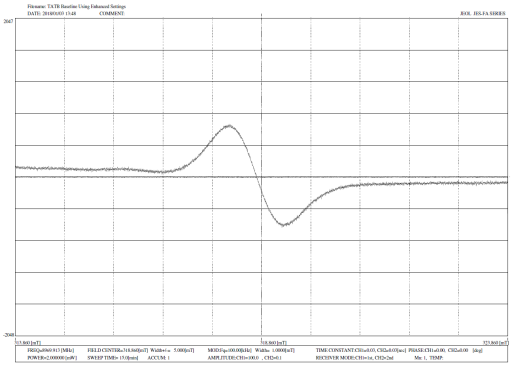

(c) Baseline

Figure 5.7: ESR Spectra - individual optimised settings

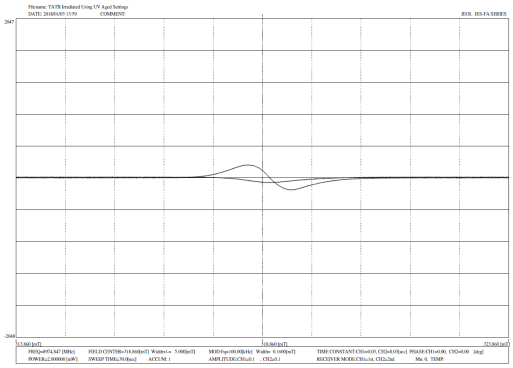

(a) 400 kGy gamma irradiated

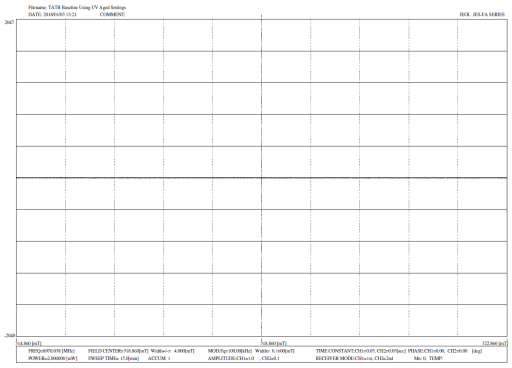

(b) Baseline

Figure 5.8: ESR Spectra - UV irradiated optimised settings

UV-VIS

UV-Vis analysis was undertaken on samples of un-irradiated, 400 kGy gamma irradiated and 120 day UV irradiated samples of TATB dissolved in DMSO. The resultant solutions

all appeared to be the same straw yellow colour with the resultant spectra not containing any characteristic differences, as shown in Figure 5.9, where differences are likely due to concentration alone.

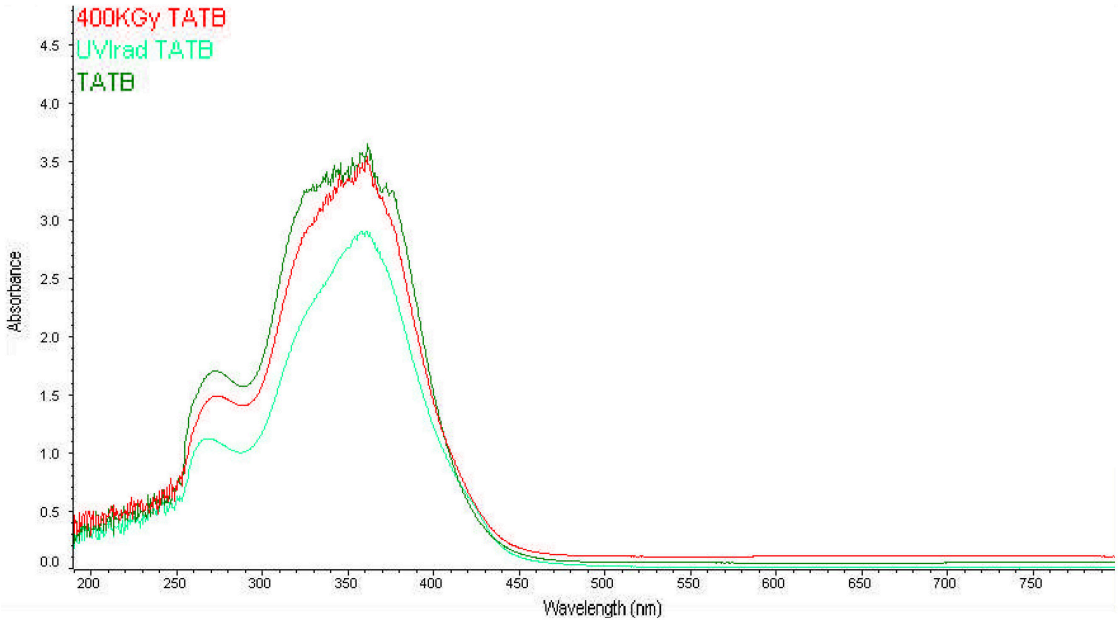

Figure 5.9: UV-Vis analysis

5.2.4 Bulk material irradiation analysis - HMX

Hazard properties

The impact sensitiveness of the irradiated HMX increased significantly when compared to the baseline material, which had a Figure of Insensitiveness (FoI) of 65. An equivalent value could not be ascertained for the irradiated sample as the material was initiating from even the lowest drop heights available on the Rotter apparatus. This indicated a FoI of less than 20, comparable in impact sensitivity to primary explosives. Resultantly, the material was immediately quarantined with no additional hazard testing permitted. Aside from a very small sample (approx. 100 mg) that had been kept for concurrent thermal analysis, the remaining bulk of this material was destroyed on safety grounds.

Thermal Properties

DSC analysis was undertaken at 2°C per minute in pierced 40 micro litre aluminium pans in a Mettler DSC 30, in accordance with the chemical compatibility STANAG 4147 [33]. A suitable baseline of non-irradiated material, from the same batch of HMX, was run concurrently for comparison. DSC results for baseline and irradiated HMX are shown in Figures 5.10 and 5.11 respectively.

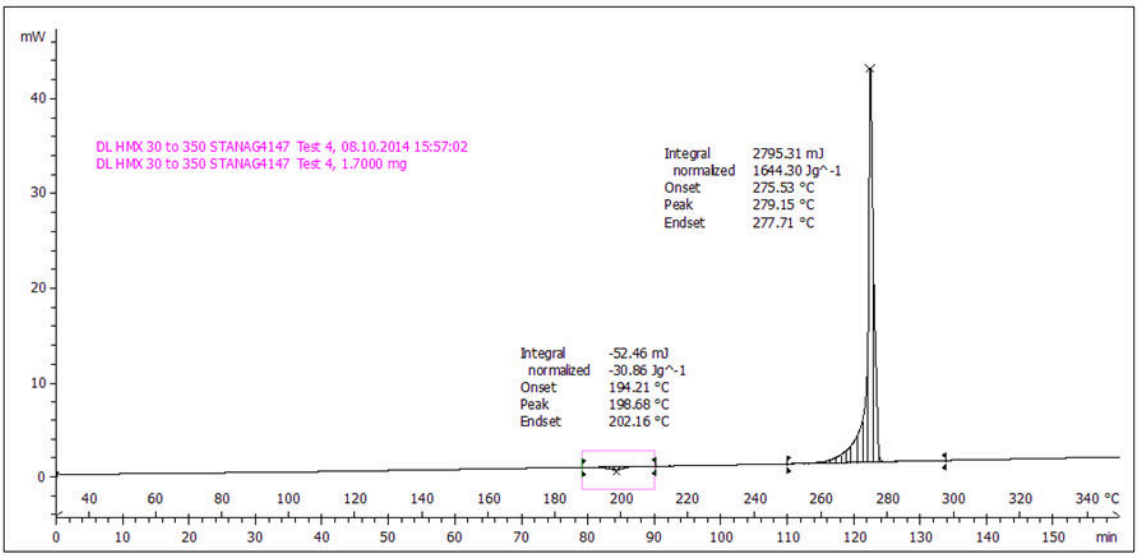

Figure 5.10: Thermal response of baseline HMX

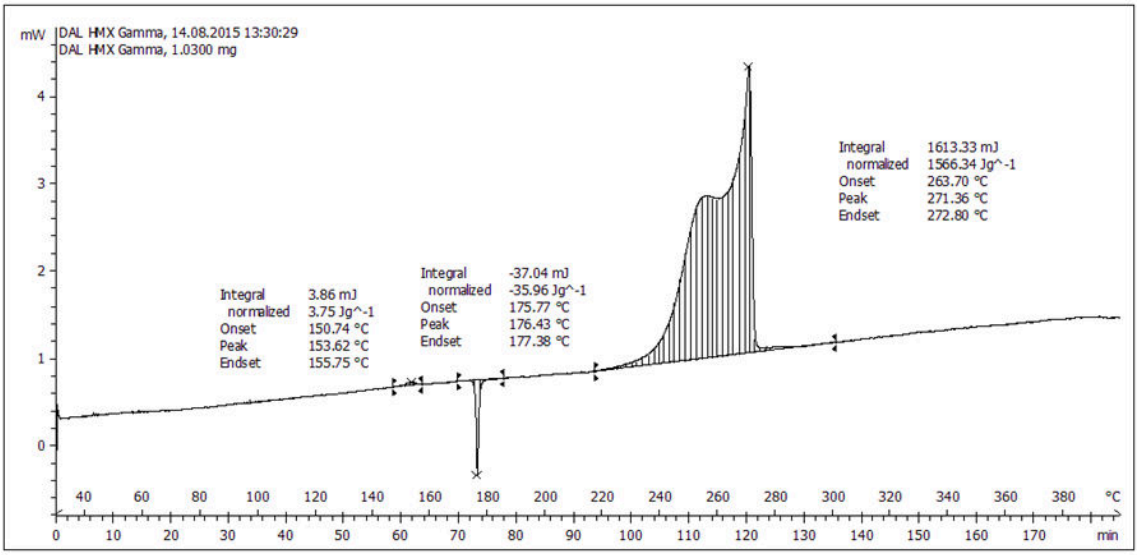

Figure 5.11: Thermal response of HMX irradiated to 200 kGy in vacuum

NMR

Samples of irradiated and baseline HMX were prepared and submitted for NMR analysis in deuterated acetone. Initial NMR scans yielded a negative result, as generated spectra were indistinguishable from the baseline. These were repeated with the irradiated and baseline HMX being dissolved into deuterated dimethylsulfoxide in case any daughter products had decreased in solubility. Extensive proton, carbon and nitrogen scans were undertaken using 190,000, 1280 and 120 scans respectively. Results showed negligible difference between baseline materials which were run at the same time. Example proton results (in d-DMSO) are shown in Figure 5.12 for the un-aged baseline and in Figure 5.13 for 200 kGy irradiated HMX.

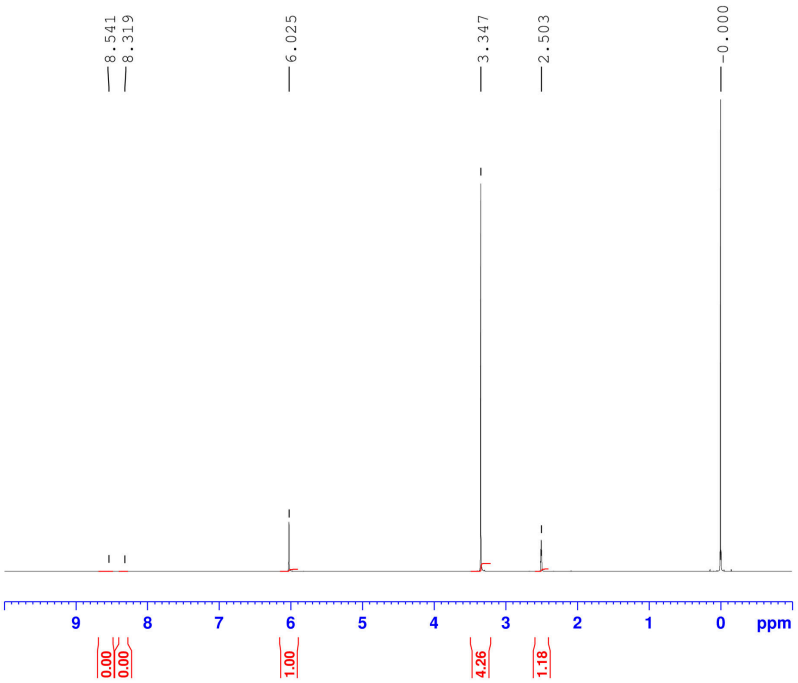

Figure 5.12: Proton NMR spectra of un-aged HMX in d-DMSO

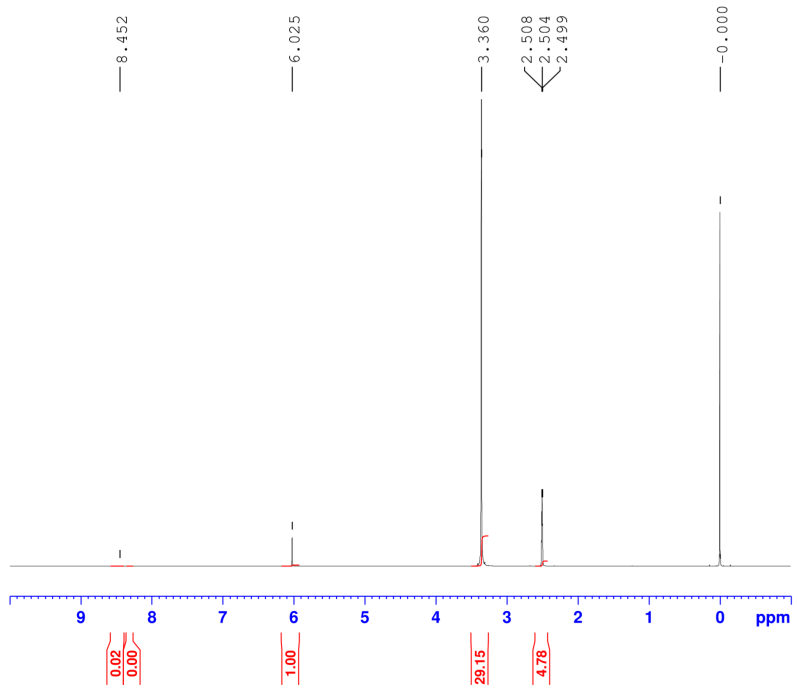

Figure 5.13: Proton NMR spectra of 200 kGy irradiated HMX in d-DMSO

HPLC

Samples of irradiated and baseline HMX were prepared for analysis by HPLC, by dissolution in acetonitrile to a concentration of 50 parts per million. Samples were run through the HPLC with UV and MS detectors. No difference between the baseline and irradiated material was observed despite a concentrated analysis on the UV detector output across the main peak of the chromatogram. An example output from the detector can be seen in Figures 5.14 and 5.15, where negligible significant difference can be observed.

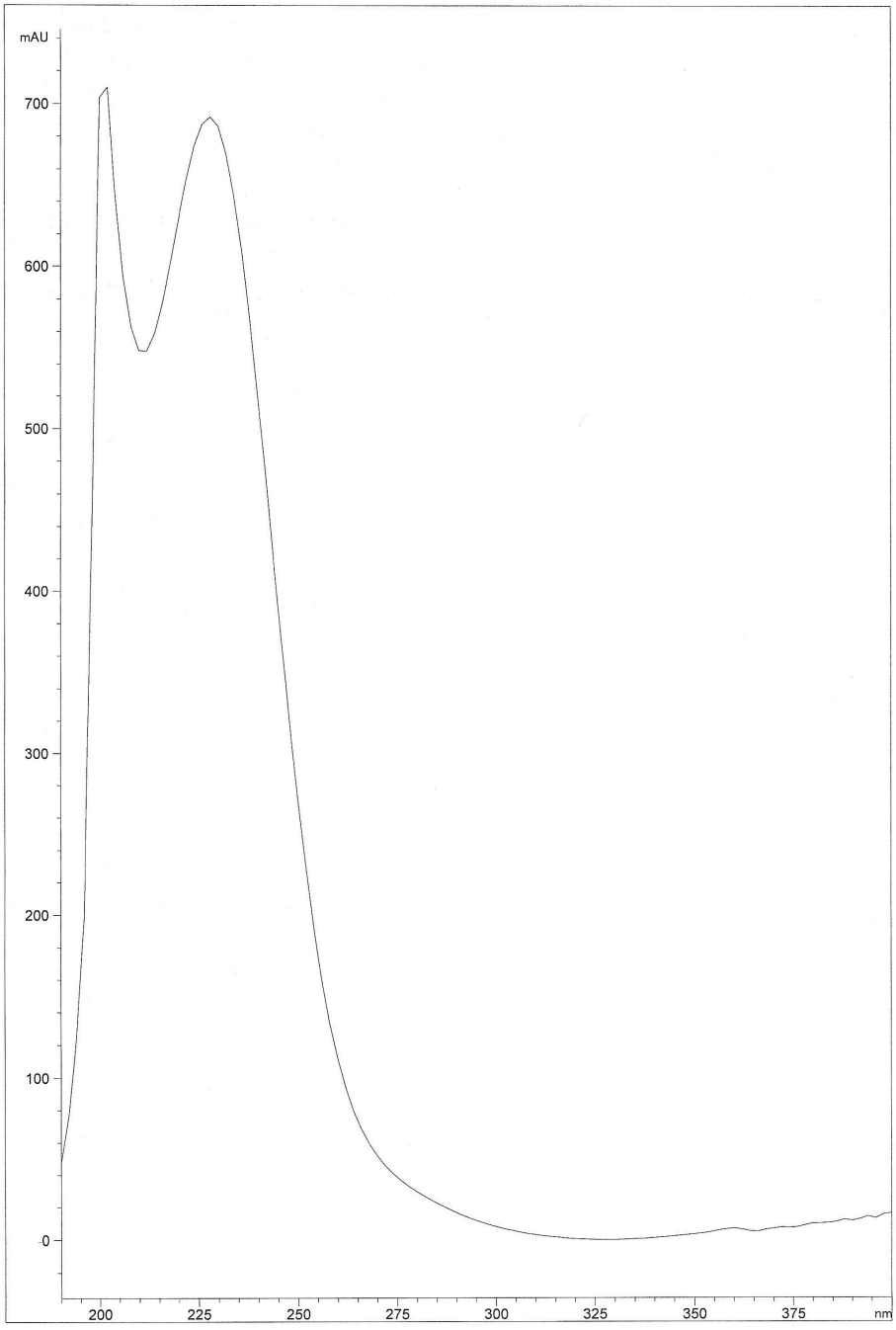

Figure 5.14: Baseline

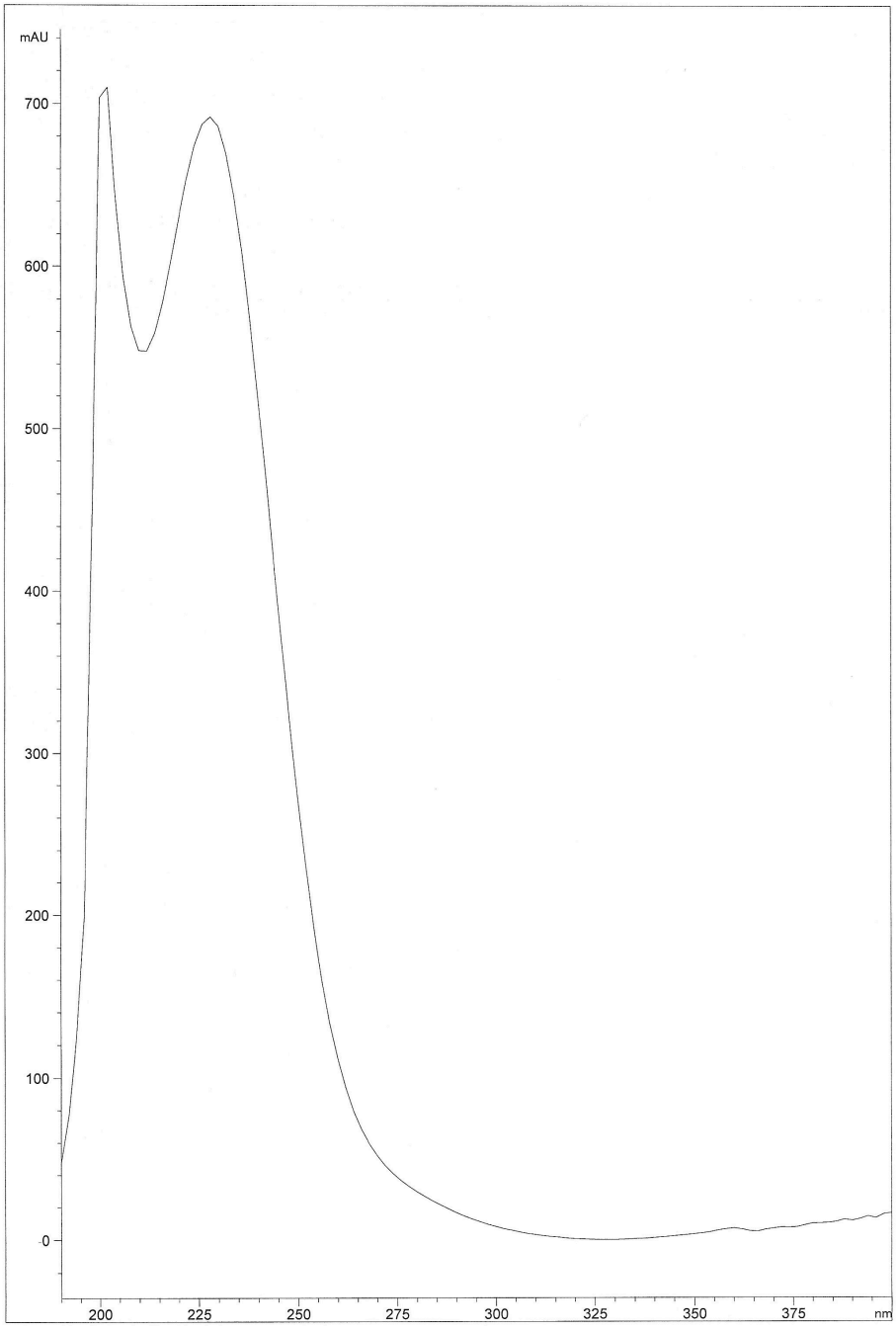

Figure 5.15: 200 kGy gamma irradiated

ESR

Due to samples being disposed of, analysis by ESR was not possible despite a small quantity of material remaining available.

5.2.5 Bulk material irradiation analysis - PETN

Hazard properties

In a similar manner to HMX, the impact sensitiveness of the irradiated PETN was altered significantly, reducing from a baseline FoI value of 81 to 26, which is again in the region of some of the most sensitive explosive materials. The PETN was tested prior to the HMX, but within the same series of hazard testing. As with the HMX, the PETN material was quarantined and ultimately disposed of, again on safety grounds, with only a small (approx. 500 mg) sample retained for some small amount of testing.

Thermal properties

Despite the similar alteration in impact sensitiveness as seen in HMX, the PETN thermograms showed negligible difference between baseline and irradiated samples, as shown in Figure 5.16; analysis of the irradiated material was repeated, confirming the observation.

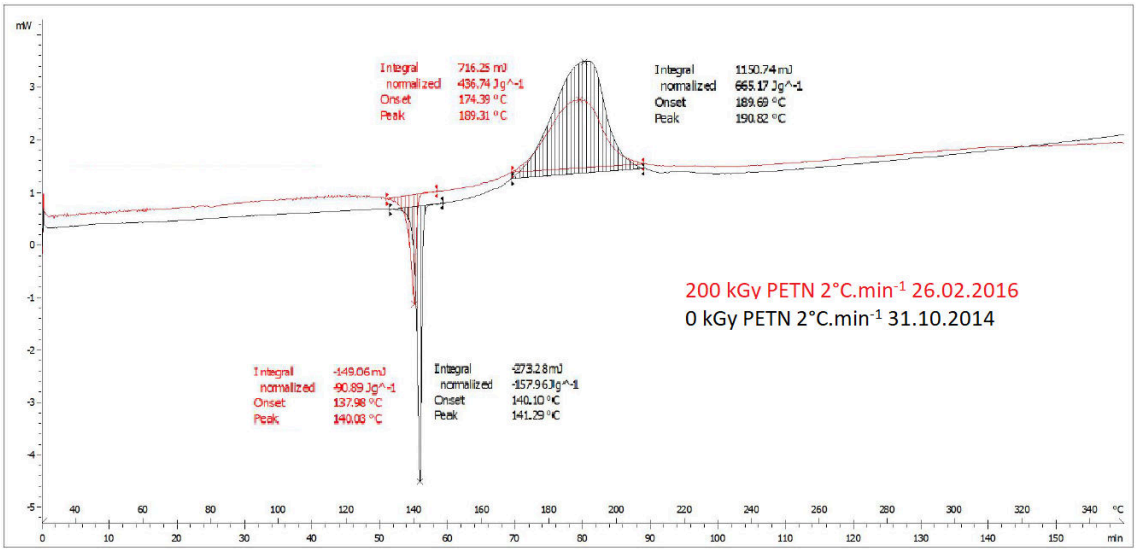

Figure 5.16: Combined thermogram of baseline and 200 kGy gamma irradiated PETN

NMR

As with HMX, a sample of the irradiated and baseline PETN was dissolved in both deuterated acetone and DMSO and submitted for proton, carbon and nitrogen NMR analysis. In keeping with the observations from HMX, no difference was observed between the irradiated and baseline NMR spectra for any scan type despite a significant change in the impact sensitiveness. The proton NMR spectra is shown in Figure 5.17 for 200 kGy irradiated PETN in d-acetone, which is typical of standard PETN.

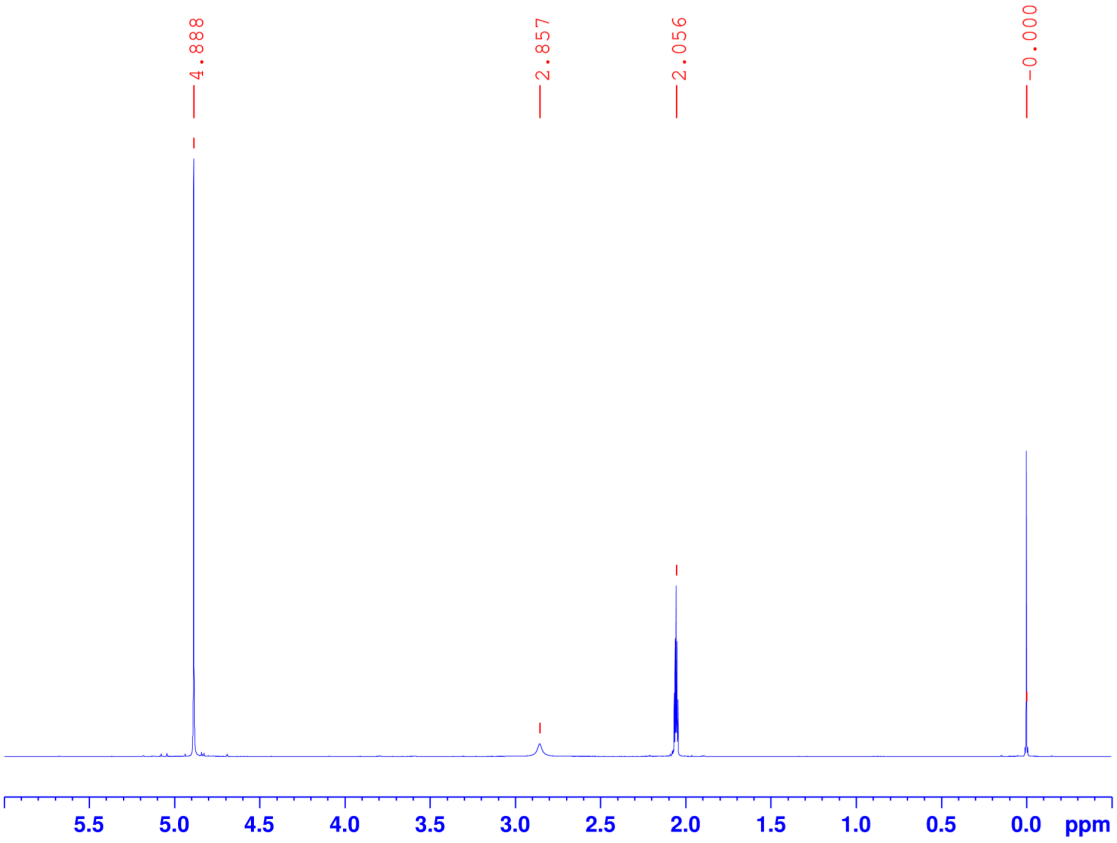

Figure 5.17: Proton NMR spectra of 200 kGy gamma irradiated PETN

HPLC

A sample of irradiated and baseline PETN was prepared for HPLC analysis using the same method used for HMX, dissolution in acetonitrile to 50 parts per million. As with the HMX, no difference could be ascertained between the baseline and highly irradiated

material despite a significant effort to improve separation and detection.

ESR

Due to more irradiated PETN being available compared to the HMX, (after the bulk had been quarantined and disposed of due to the concerning impact hazard results), an analysis of the material within the ESR was possible. The PETN material was irradiated approximately one year prior to the ESR spectrometer being available at Shrivenham. Despite this significant period of time, a long lived radical that differed from that observed for TATB was detected, as shown in Figure 5.18. This measurement was repeated again over a year later, resulting in an identical spectra signifying that the radical is particularly long lived.

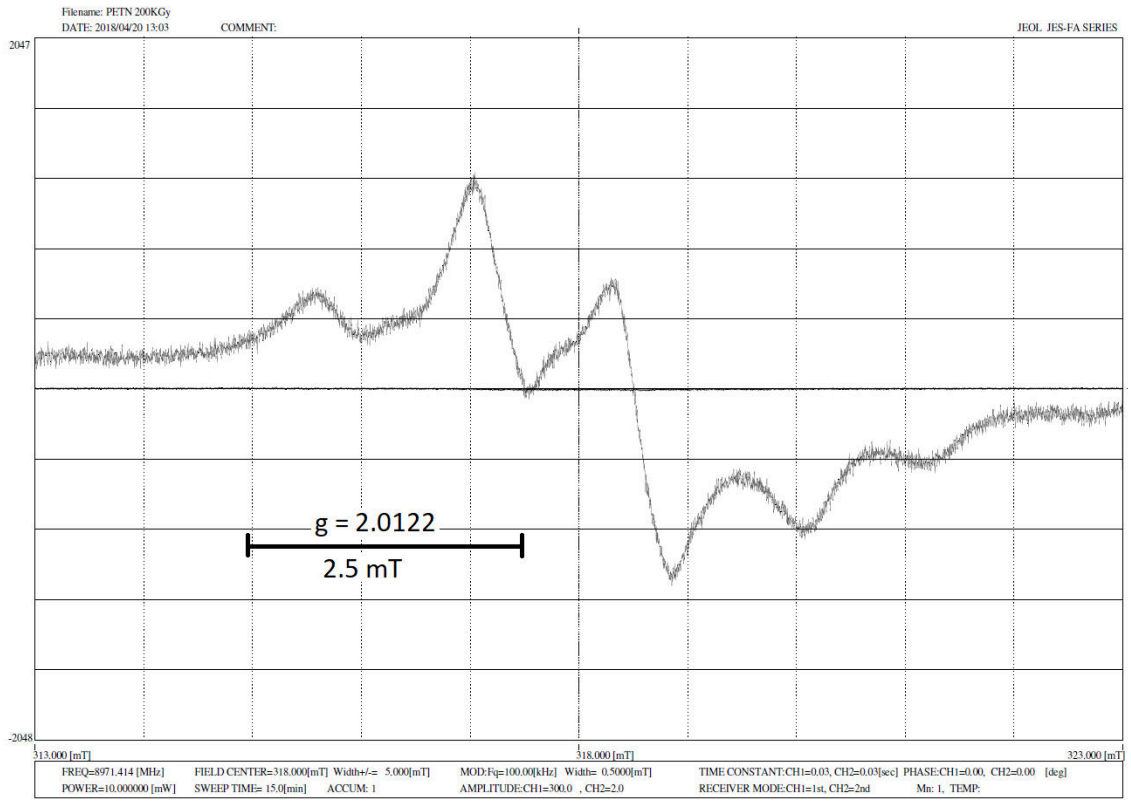

Figure 5.18: Long lived radical in 200 kGy gamma irradiated PETN

In order to confirm that this radical was due to the irradiation, a sample of baseline PETN was run using the same variables for the ESR spectrometer. This yielded no spectra indicating that no radicals were present, as shown in Figure 5.19.

Figure 5.19: Nil spectra for baseline PETN

5.2.6 In-Situ ESR

Samples of PETN, HMX and TATB vacuum-sealed in ESR ampoules were subjected to sub-ambient irradiations using the 400 kBq Americium source. At intervals of 15 minutes, the radionuclide was removed and the electromagnet and microwave bridge powered on in order to undertake an analysis. Unfortunately, at each interval, no spectra was observed and were identical to that shown in Figure 5.19, with the exception of TATB which had a detectable spectra in the baseline material identical to that shown in Figure 5.7c that did not change with the periodic irradiations, attributed to radicals formed from stray sunlight. After an hour, the samples were gradually returned to room temperature and the

400 kBq source was swapped for the more powerful 1 GBq radionuclide.

As with the 400 kBq source, spectra were attempted to be ascertained every fifteen minutes and in keeping with the lower activity source, no spectra were obtained, that differed from the baseline (i.e. no spectra for PETN and HMX, as per Figure 5.7 and a low concentration simple single peak spectra for TATB, as per Figure 5.7c). Further irradiations were attempted that yielded negligible results with the limiting factor being the availability of liquid nitrogen. The maximum duration at which the spectrometer could operate at low temperature i.e. less than 150°C was determined to be approximately 1.25 hours. This was due to the available quantity of liquid nitrogen in the attached bespoke dewar which could not be topped up mid-irradiation without causing the instrument to return to room temperature, which would remove any generated short term radicals, invalidating the experiment.

5.2.7 Synthesis and analysis of mono-nitroso TATB derivative

The synthesis of the mono-nitroso derivative of TATB (2,4,6-triamino-1,3-dinitro-5-nitroso benzene) was taken from literature sources [46, 84] where TATB, dissolved in DMSO, is held at 60-90°C for three to four hours in the presence of the strong base sodium ethoxide and the reducing agent hydroxylamine hydrochloride, after which the reaction mixture is neutralised by the addition of acid.

The synthesis was achieved with prior preparation of sodium ethoxide by the reaction of sodium hydride and ethanol. 5 g of sodium hydride (40 % oil wet by mass i.e. 3 g of sodium hydride) was added under inert atmosphere (nitrogen) to a round-bottom flask. To remove the oil, the sodium hydride was twice washed with hexane, which was itself removed by syringe, prior to the drop-wise addition of 5.76 g of ethanol at 40°C, under stirring. The reaction was left for one hour to ensure completion. A 0.25 M solution of

hydroxylamine hydrochloride was then prepared in 500 ml of DMSO, which was subsequently added to the sodium ethoxide within a 1 litre round bottom flask. The reaction mixture was then heated to 70°C, at which point 0.45 g of TATB was then added to the mixture, calculated to be the maximum quantity that could be dissolved in 500 ml of DMSO at 70°C [88], where the reaction mixture turned from an off white colour to orange, immediately upon the addition.

The reaction mixture was allowed to progress for four hours, by which point the reaction mixture has turned to a vivid orange/red (Figure 5.20), rather than the purple observed previously. The solution was allowed to cool to 50°C at which point it was neutralised by the drop-wise addition of concentrated hydrochloric acid. 250 ml of distilled water was then added to the mixture causing a solid precipitate to form. The mixture was then added to 1 litre of distilled water to crash precipitate as much solid as possible and was left overnight to settle.

Figure 5.20: Initial reaction products

The following day, a solid was clearly observable at the bottom of the mixture which was recovered by gradual filtration through a buchner funnel. The yellow/lime green solid residue was washed with water and hexane in an attempt to remove any remaining reactants or impurities, such as oil from the sodium ethoxide preparation, and was dried within a desiccator. The dried product was weighed at a calculated yield of 46.67 % $\pm$ 1.63 %.

Characterisation of the synthesised product was undertaken by NMR by preparation of a sample dissolved in deuterated sulphuric acid. The resultant spectra (proton is presented within Figure 5.21) showed significant differences when compared against baseline, 400 kGy and UV irradiated TATB samples which were themselves indistinguishable from each other.

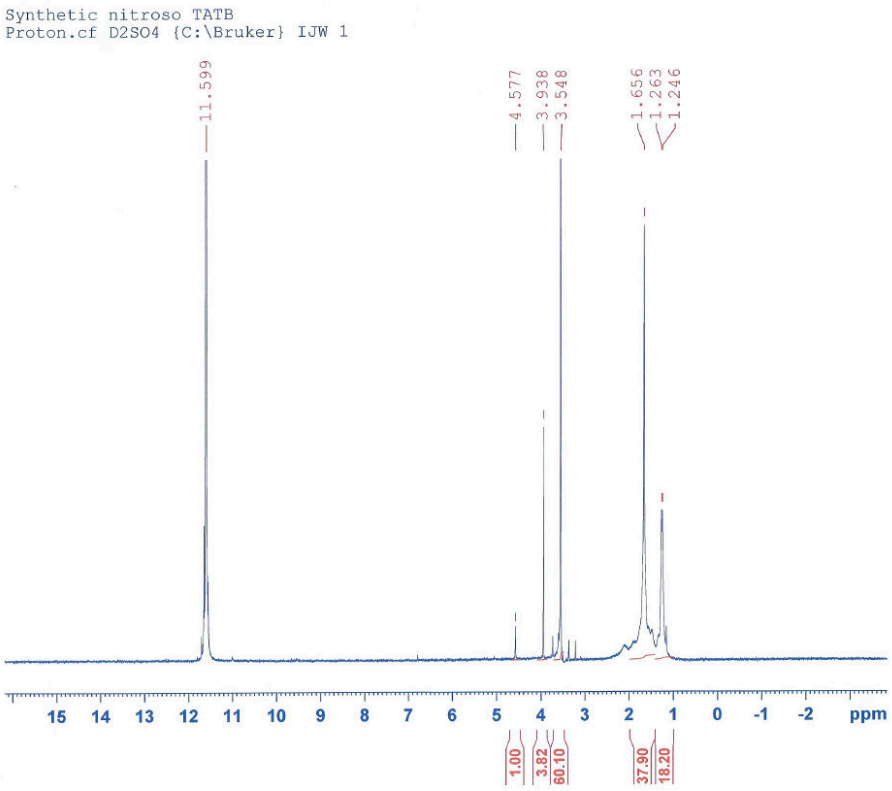

Figure 5.21: Synthetic mono-nitroso TATB proton NMR spectra

Additional characterisation by means of DSC was undertaken on the synthetic material and is shown in Figure 5.22, combined with the thermograms from baseline, 400 kGy Gamma and UV irradiated samples. A clear difference can be seen between all four traces, with the potential trend of increasing concentration of the mono-nitroso with decreasing onset and peak decomposition temperatures being observed.

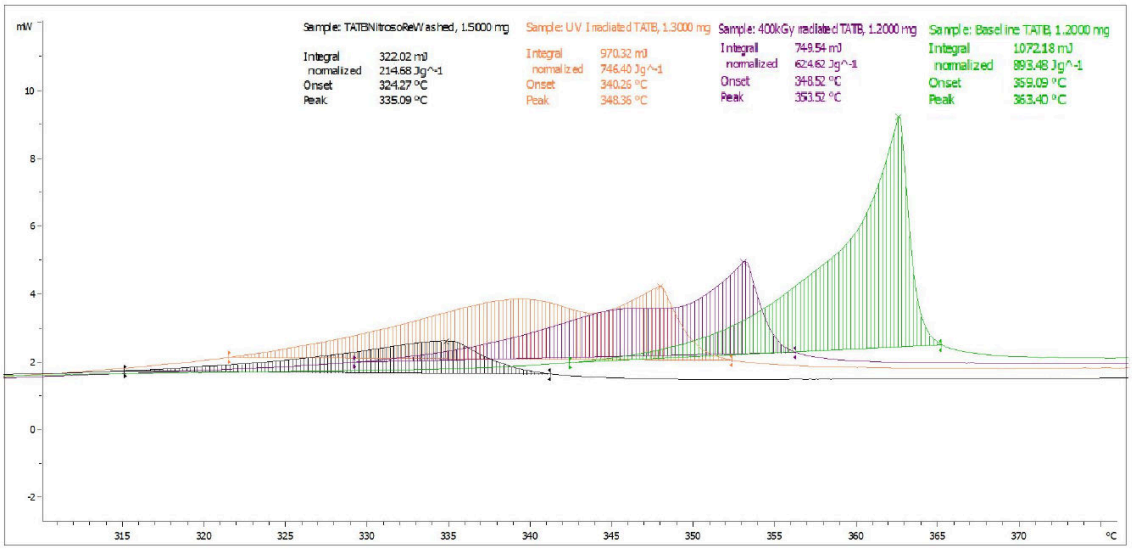

Figure 5.22: Combined thermogram

5.2.8 Recrystallisation of irradiated TATB

The most heavily gamma irradiated TATB (400 kGy) was selected for recrystallisation as it was thought that any differences would be most apparent for this material. As with the synthesis of the mono-nitroso TATB derivative, DMSO was selected as the solvent of choice, due to TATB's poor solubility in other easily accessible laboratory solvents. 0.46 g of 400 kGy irradiated TATB was added to 500 ml of DMSO at room temperature in a round-bottom flask under stirring, which resulted in a green mixture with most of the TATB remaining undissolved as a solid matter in suspension. The mixture was then heated to 70°C and held under these conditions for two hours.

During the first 30 minutes, the majority of remaining solid irradiated TATB successfully dissolved into the solution. A further 250 ml of DMSO was added to ensure that all the remaining solid matter dissolved. This was successfully achieved once the solution had retuned to 70°C after the addition. Over the course of the following hour, the mixture turned from a lime green colour (Figure 5.23a) to golden yellow/orange which subsequently turned to yellow (Figure 5.23b) upon cooling to room temperature, where a solid particulate could be observed within the solution.

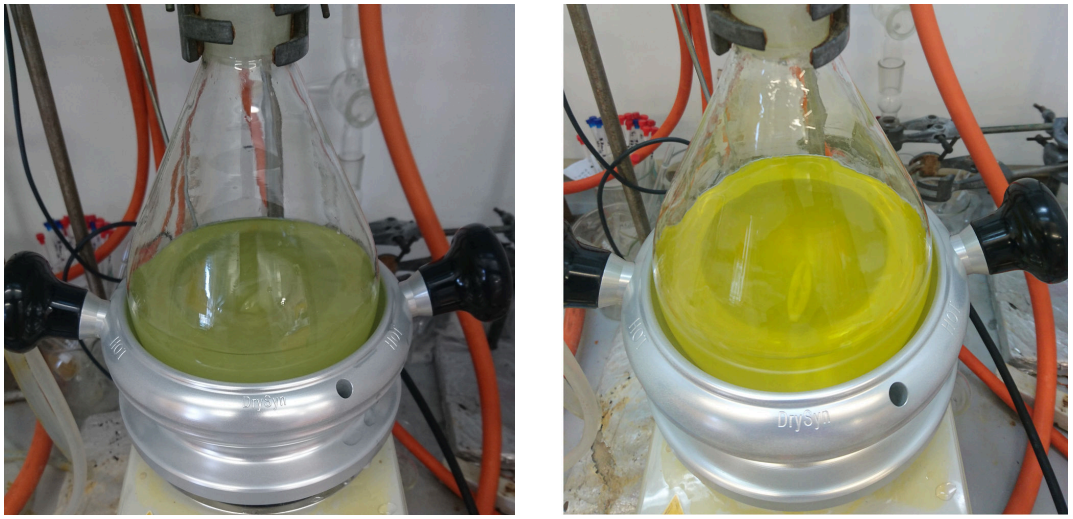

(a) Time zero (b) 90 minutes later

Figure 5.23: 400 kGy TATB during recrystallisation

This mixture was then poured into a conical flask containing 1 litre of distilled water in an effort to crash precipitate a solid from the mixture. A translucent white/yellow solution resulted (Figure 5.24a), suggesting a very fine solid precipitate had formed. This mixture was then filtered using a buchner funnel, however the solid could not be recovered and appeared to remain in the solution. A further 1 litre of distilled water was added along with sodium chloride and magnesium sulphate in an attempt to drop the TATB from the solution, due to their higher affinity for DMSO and water than TATB. The solution was left in the dark (wrapped in foil to minimise subsequent decompositions resultant from stray UV and visible light) for one week, at which point a solid particulate was observed

to have separated from the solution, yielding a clear liquid above a yellow precipitate (Figure 5.24b).

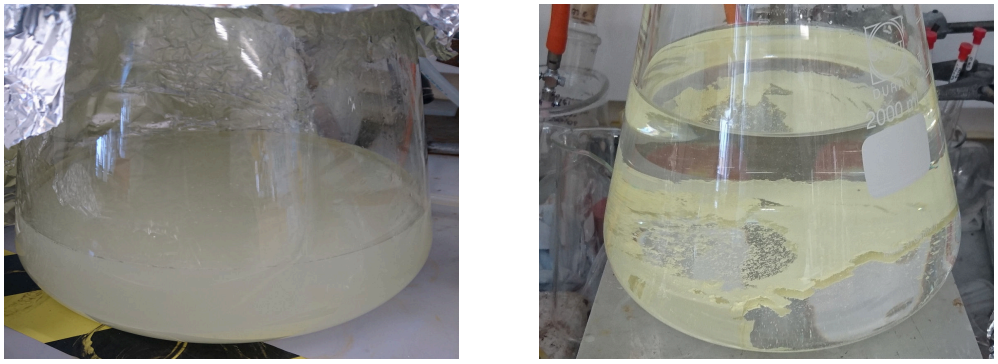

(a) Time zero (b) After one week

Figure 5.24: 400 kGy TATB Re-crystallisation

The solution was then gradually filtered through a buchner funnel using a 2.5 micron filter paper, resulting in the successful recovery of a pale yellow solid particulate (Figure 5.25) and a clear filtrate. The recovered material was then washed with copious amounts of distilled water ensuring that residual traces of sodium chloride and magnesium sulphate were removed; the solid was then dried in a foil wrapped desiccator for approximately four weeks. After drying, the recovered material was weighed at 0.4546 g compared to the initial 0.46 g of starting TATB, indicating a yield of 98.826 % $\pm$ 1.55 %. Unfortunately, the measurement of the initial 400 kGy TATB was undertaken on a balance of poor accuracy (to 0.005 g) causing most of the uncertainty in yield.

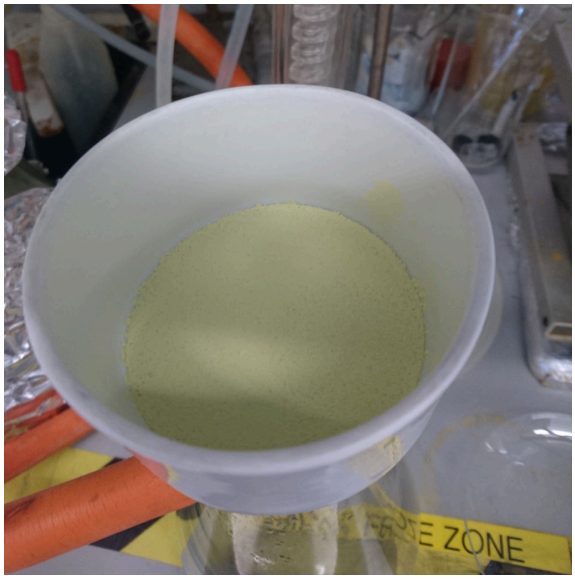

Figure 5.25: Recovered solid particulate

Analysis of the recovered solid was undertaken by DSC as it was technique which has proven to be the most sensitive method for detecting changes induced through radiation. The DSC thermogram for the recovered product, is shown in Figure 5.26 against the equivalent prior to recrystallisation.

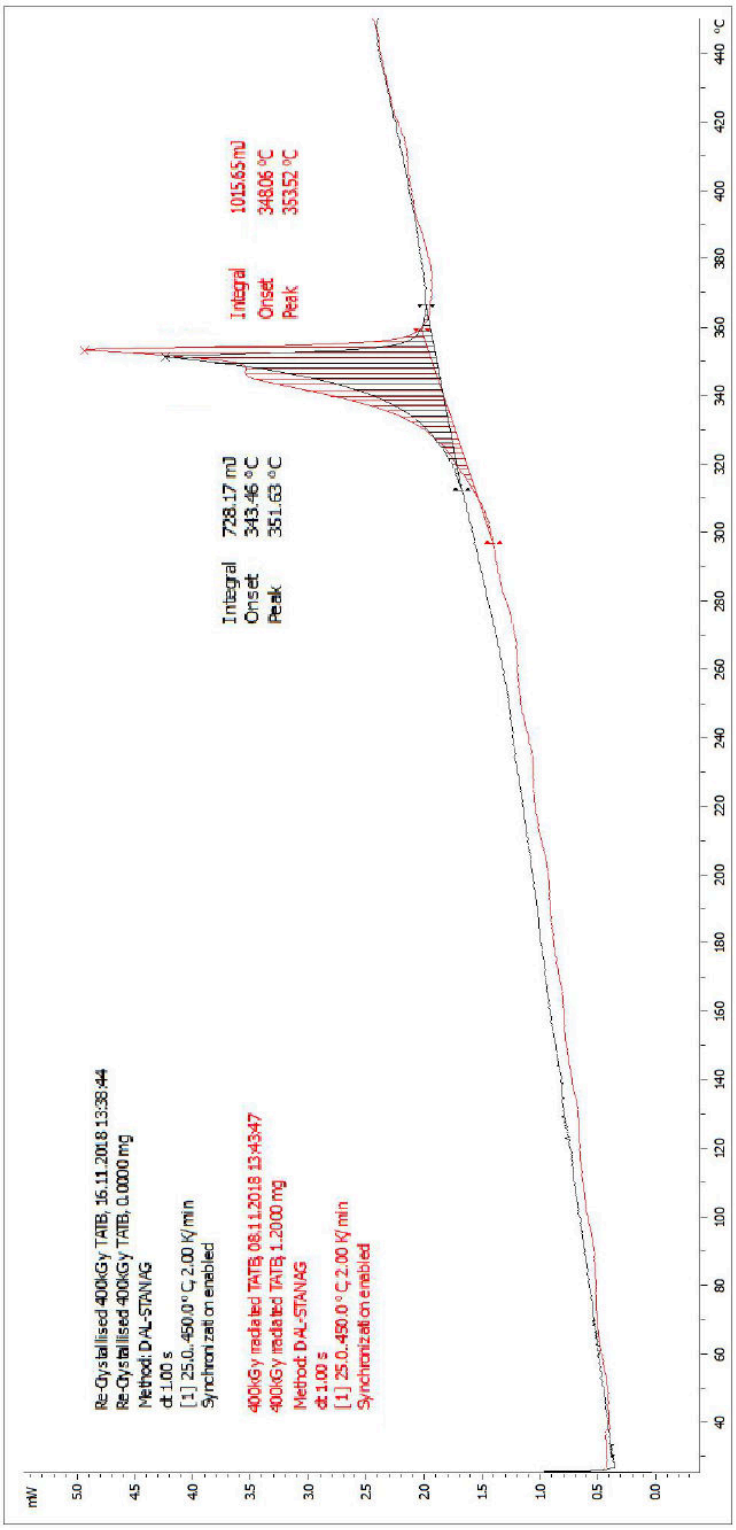

Figure 5.26: Thermogram of re-crystallised 400 kGy TATB

Chapter 6

Discussion of investigation

Observations from both the experimental and computational investigation into the effect of radiation on TATB, HMX and PETN were varied and shall be discussed in more detail below. However, beforehand a few general, material non-specific observations can be discussed.

6.1 General

Firstly is the calculated ionic potentials for all three materials, which were of order 10 electron volts. This signifies the minimum amount of energy required to achieve ionisation and can be equated to specific wavelengths of light, for all molecules this was within the lower region of ultraviolet radiation. This is significant, as it suggests that incident photons of light, whether they are from x-ray, UV or gamma ray, that are greater in wavelength/energy than this threshold should result in the removal of an electron from the molecule. Upon the ionisation, the subsequent reactions should be identical regardless of the source. However, the higher the energy of the photon, the less likely the ejected electron can be recaptured. In short, ionisation should result in the same fundamental chemistry for each molecule. This allows future work to be undertaken using UV lamps, which are much more easy to access than high output gamma ray sources.

6.1.1 In-situ ESR

Based on the limitation placed on the total radiation time by the liquid nitrogen dewar of one hour, and the calculations previously detailed, an approximation as to the maximum number of radical generating interactions (worst case, based upon PETN) that a sample could experience without returning to room temperature was made at approximately $2.4x10^6$. This number was derived by using the calculated rate of absorptions (525 kBq) for the material with the smallest mass-energy attenuation coefficient, PETN, and multiplying it by the maximum achievable period of irradiation time of one and a quarter hours in seconds (4500 s). This was believed to be sufficient in order to generate a signal within the ESR cavity.

Upon the unsuccessful ESR experimental campaign these were reviewed and a mistake identified which considered the amount of radiation a sample would absorb. This was the application of the Beer-Lambert law across the 3.4 mm of sample in the cavity, where it was initially thought that by using the mass energy-attenuation, rather than the mass attenuation coefficient, the calculation would describe the amount of radiation absorbed by the material. This is incorrect and the calculation, shown in Equation 5.4, represents the amount of radiation that would not be absorbed by the material and would actually be the resultant activity incident on the back wall of the ESR tube.

The correct calculation is to take the difference between the activity incident on the sample and the resultant activity using the mass-energy attenuation coefficient. This difference must be the activity absorbed by the material and therefore result in radical formation, this is shown in Equation 6.1 which should have been used rather than Equation 5.4, where x = 0.34 cm, the thickness of the PETN sample. This results in a rate of absorption two orders of magnitude lower than that originally calculated, 5.180 kBq compared to 525

kBq.

$$\dot{A}_{PETNAbsorbed} = \dot{A}_{SampleIncident} - \dot{A}_{SampleIncident} e^{-\mu_{en} x/\rho} \tag{6.1}$$

As a further step this number can be used to approximate the molar concentration of the radicals within the sample. Firstly, the number of molecules of the material within the ampoule of which is exposed to radiation needs to be approximated. Utilising the same geometries of a inner radius (r) for the ampoule of 3.4 mm and a sample length (l) of 50 mm, an exposed sample volume (V) can be determined by Equation 6.2.

$$V = l\pi r^2 \approx 454 \tag{6.2}$$

Using the density (ρ) of PETN (again the worst case due to its low value), of 1.77 x10^{-9} Kg mm^{-3} [89], a mass (m) can be calculated by Equation 6.3.

$$m = V\rho \approx 8.04\, x10^{-7} \tag{6.3}$$

By using the molar mass (M) of PETN, the number of moles (Mol) within this mass can be equated using Equation 6.4, with the factor of 1000 converting between Kilograms and grams.

$$Mol = 1000m/M \approx 2.54x10^{-6} \tag{6.4}$$

By using Avagadro's constant N_a and the number of moles (Mol) of PETN, the number of molecules of PETN (N_{PETN}) within the ampoule can be equated by their product as per Equation 6.5.

$$N_{PETN} = N_a Mol \approx 1.53x10^{18} \tag{6.5}$$

Finally the maximum molar concentration (M_{conc})after a period of irradiation (t=4500) can be equated by Equation 6.6.

$$M_{conc} = \dot{A}_{PETNAbsorbed} t / N_{PETN} \approx 1.52x10^{-9} \quad (6.6)$$

This calculated value is very low, and beyond the limits of detection for ESR spectrometers [83]. Based upon this number, in-situ irradiations would need to be undertaken for approximately 50,000 hours (over 5 years) using the current source and sample size in order to achieve recommended levels of radical concentration.

6.2 Material specific

6.2.1 TATB

The computational results for TATB and its purported daughter products provides some significant insight into the effect of ionising radiation on the material. The calculated geometry of the parent TATB ionic radical and associated hyperfine coupling tensor, as shown in Figure 4.14, indicates that the radical will be located within the aromatic structure of the molecule, suggesting that radical stabilisation though aromatic resonance is indeed likely to occur. The resultant structure suggest a twisting of the nitro group closest to the radical centre. Such a twist may also affect the graphitic crystalline structure, due to a potential disruption in the complex intra molecular hydrogen bonding. However, this twist may not occur in the solid state, due to this hydrogen bonding.

As with HMX and PETN, thermodynamically favourable decomposition products of TATB resulted in the larger fragments remaining cationic, with only the mono-furazan and nitrite derivative being energetically favourable, before they themselves may fragment to further decomposition products. The stability of the ionic TATB parent molecule is demonstrated by the low number of energetically favourable decomposition products, and resultant difficulty in optimisation due to many local minima being apparent, as the radical resonated

around the constitutive aromatic ring.

Looking towards some of the experimental evidence and despite the visually observed greening of TATB, the liquid state experimental UV-Vis spectroscopy showed negligible differences between the baseline, 400 kGy and UV irradiated samples of TATB and broadly agreed with the computationally predicted UV-Vis spectra of pure TATB. A comparison is shown below in Figure 6.1, where a dependency of 100 nm is apparent between the predicted and liquid measured UV-Vis results, potentially due to differences in states.

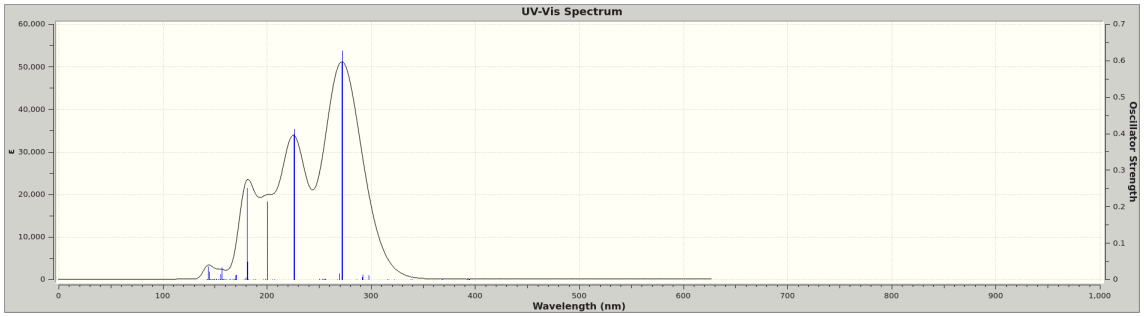

(a) Predicted

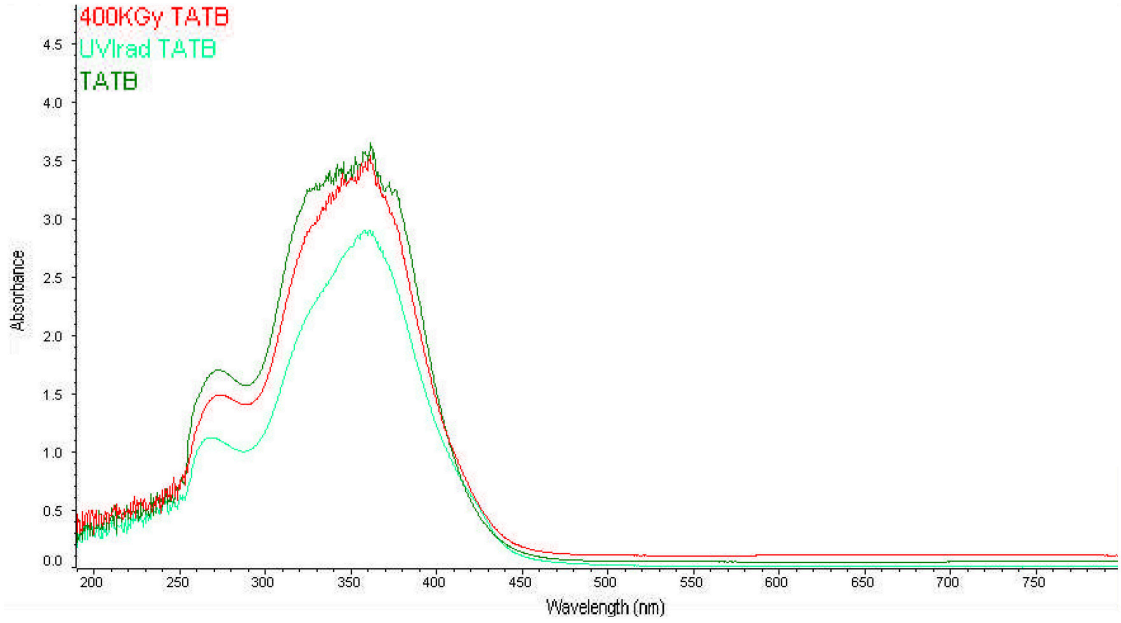

(b) Measured

Figure 6.1: UV-Vis Spectra of TATB

This observation is in contrast to previous work undertaken by Ying [52] and Padfield [49] who showed differences in solid state UV-Vis reflectance between 0 kGy, 50 kGY, 100 kGy, 200 kGy and 400 kGy gamma irradiated TATB, as shown earlier in Figure 3.13. Padfield's reflectance data was located, re-processed and converted to absorbance, as shown in Figure 6.2. This enables direct comparison to computationally derived UV-Vis spectra, and to the measured spectra of Ying [52]. These converted spectra agree with that of Ying, where a broad peak, with a maximum at approximate 650 nm, can be seen to increase as a function of radiation dose.

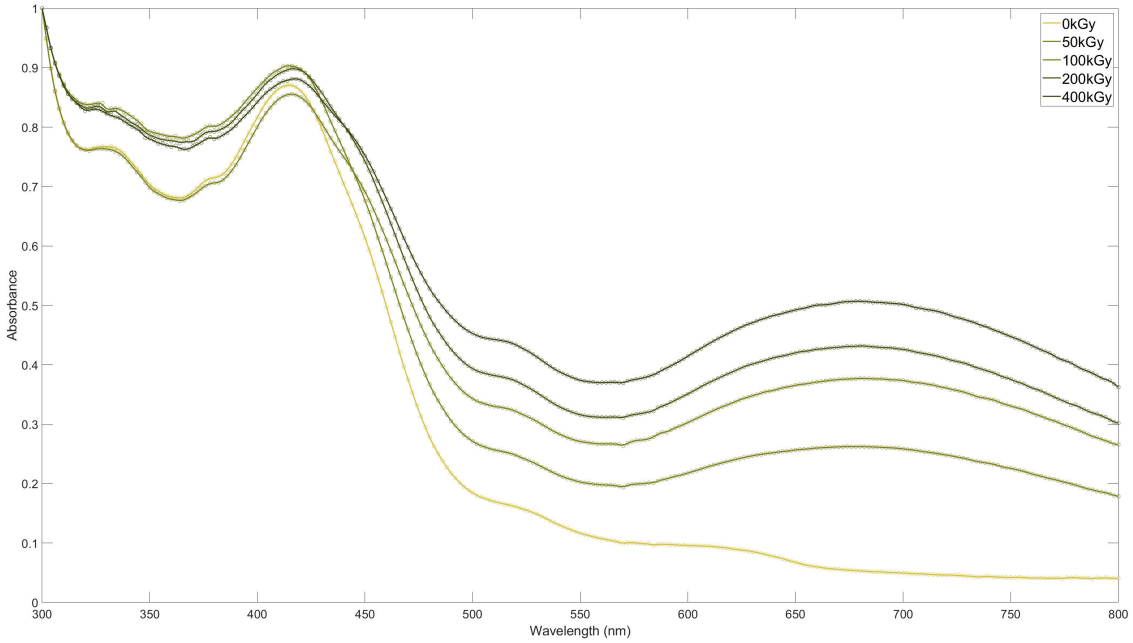

Figure 6.2: UV-Vis analysis of irradiated TATB

The calculated UV-Vis spectra of the ionic derivative of TATB, is of significant interest, as it contains by far the most prominent absorption peaks in the region on the electromagnetic spectrum that corresponds to the colour blue, as shown here in a reprocessed form for clarity, in the below Figure 6.3. Equivalent calculations of the mono-furazan, mono-nitroso and the phenoxyl radical derivatives of TATB have not shown such absorptions, despite the calculations made by Ying [52] and Manaa [46]. The methods undertaken

within this research are more complex, by virtue of a more complex theory, hybrid functional and much larger basis set. This improved complexity does not conclusively prove that this is the source of the colour change, as more complex calculations are available than those undertaken within this research. However, whereas it is likely to see significant changes between lower and mid level calculations i.e. between semi-empirical and DFT with low basis set complexity, it is unlikely to see changes between high and extreme levels of accuracy as the results converge to real life representation, for this reason these results can be interpreted with moderately high confidence.

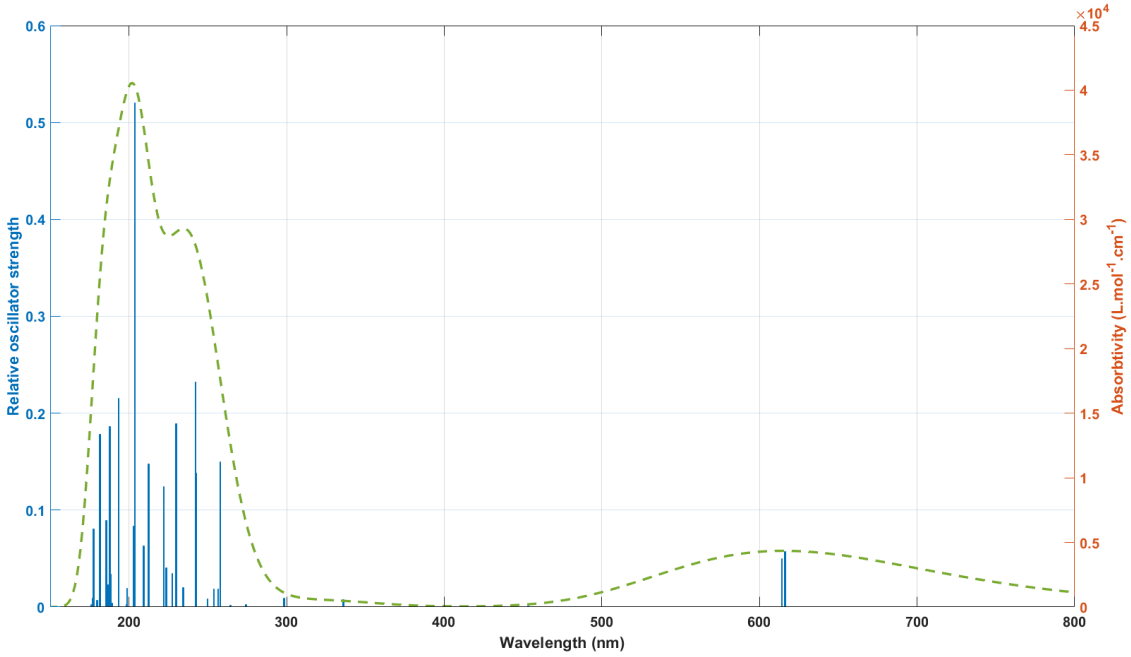

Figure 6.3: Reprocessed UV-Vis analysis of TATB cation radical

The calculated UV-Vis spectra of the ionic TATB agrees well with the converted spectra of Padfield, as shown in Figure 6.2, and that of Ying [52], improving confidence in the result of the simulation. Looking at the predicted UV-Vis spectra of the ionic TATB in more detail, it can be seen that the two absorption peaks of interest appear at 616.3 nm and 614.1 nm which actually correspond to red light in the visible spectrum. However, consideration must be made to the fact that the simulated spectra represents spectral *ab-*

sorptions and not *emissions*. Using this correct interpretation, any light incident on the material that is reflected back will be comparatively deficient in the red wavelength than its TATB baseline counterpart.

This interplay between colour through absorption and reflection of light is perhaps counter-intuitive, but is well described visually by a simple colour wheel, which highlights the phenomenon where light that is deficient in one colour/wavelength will appear to be of the opposite colour. Using this relationship, which is shown pictorially in Figure 6.4, it can be seen that light which is deficient in red, such as the cation radical TATB derivative, will likely appear blue. It is thought that mixing of the blue ionic TATB derivative, with the yellow of the unadulterated parent TATB, is potentially why irradiated materials appear green, and why in some extreme cases discolouration does indeed appear to progress further to a blue/black colour [42].

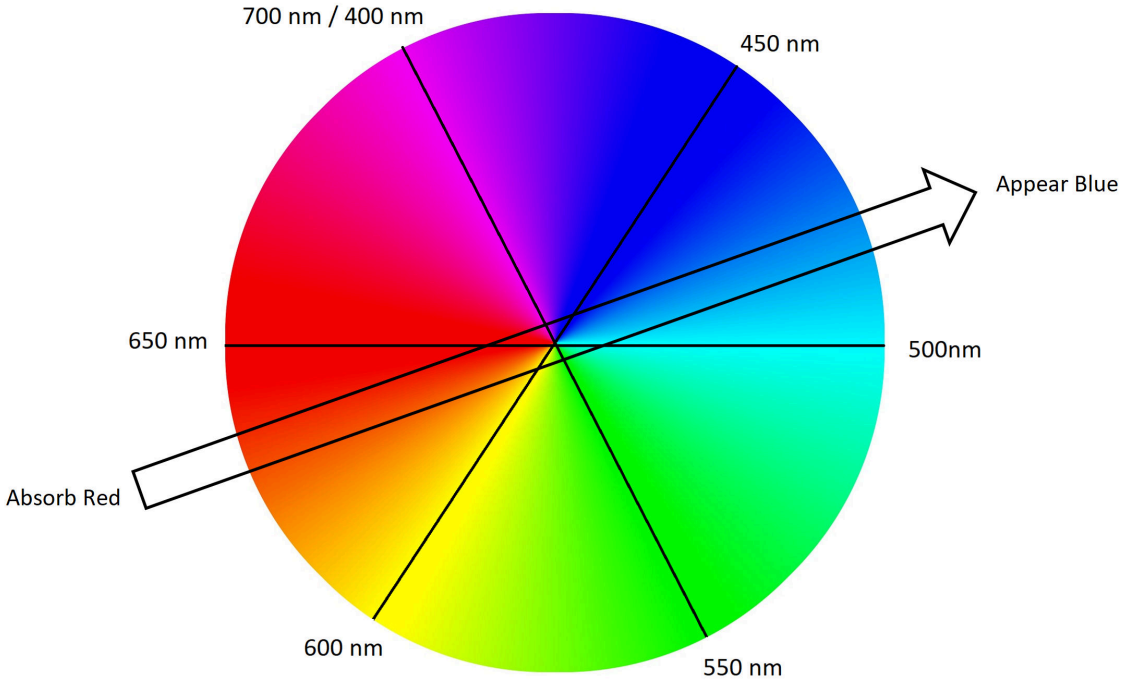

Figure 6.4: Colour wheel showing red absorption

Padfield [51] showed that the change in colour was a linear relationship with the absorbed

dose, as shown earlier in Figure 3.12. This makes sense, and corroborates the ESR signals that were measure experimentally that also increase with dose. Within experimental error, Padfield's correlation suggested a near unity relationship with dose and colour, indicating that a relative dose twice that of another, would make that TATB twice as green. This again makes perfect sense as the data used to generate the relationship was derived from samples that had experienced differing multitudes of exposure time to the same irradiation source. Therefore, and as shown by the Beer-Lambert law and the calculated mass-energy attenuation coefficient for TATB, the samples had experienced ionisation interactions at the same rate, just for different periods of time. Due to the apparently long lived nature of the TATB radical, the concentration of radicals within the material is also going to be a linear function of the dose, i.e. twice as long exposure to the source causes twice as many radicals to be formed, causing the TATB to look twice as green. Perhaps unsurprisingly, the observed strength of the ESR spectra and hence inferred radical concentration appear to correlate linearly with absorbed radiation dose. This ESR data also suggests that the radicals are very long lived, with no depreciation of the signal observed within years of measurement, further supporting the theory of the radical being stabilised through aromatic pi bonding resonance.

Some past works [43, 46, 53] have suggested that concentrations of impurities within TATB may be very low as the impurity may be acting as a dye, where low concentrations are used to change the colour of a material due to a particularly strong chromophore. Whilst there may be some truth in this assessment, the radical concentration in the UV irradiated TATB was so high it was clipping the detector in some cases, and was comparatively 50 times in magnitude when compared to a laboratory standard of tempol at a concentration of 10^{-5} M. Although quantification of radical concentration by this comparison is not possible due to differences in microwave absorptivity for example, it allows a qualitative assessment that significant concentrations of radicals are present within the irradiated material.

The fact that both the greenness and radical concentration within irradiated TATB appear to strongly correlate linearly with total dose, evidences that the discolouration observed within TATB must be due to a species that has unpaired electrons. Theories that suggest ground state decomposition products such as mono-nitroso and furazan products are responsible must be incorrect as these products cannot give rise to the observed ESR signal, unless these molecules are formed from a parent molecule that has an unpaired electron. This is feasible, as it has been shown that the cationic derivative of TATB may decompose to various products. However, if the parent cationic TATB were the cause of the ESR signal, but a further decomposition product, such as the mono-nitro derivative were responsible for the change in colour, then the colour of TATB should continue to change with time beyond the initial irradiation; this is not observed.

Two possibilities remain feasible; the first is that the radical and discolouration are unrelated (i.e. a species with a green/blue chromophore and a paramagnetic species are formed independently) and form coincidentally at the same rate. Whilst this is plausible, it is also very difficult to prove or disprove. Consideration of the evidence gained from the computational UV-VIS analysis of these products, where none of them appear to be strongly coloured, coupled with visual observations that the synthetic mono-nitroso and reported synthetic mono-furazan [90] were not strongly coloured, suggests that these products are not the source of the discolouration. Although evidence from these synthetic products is not proven (i.e. conformation of them being the target species), this evidence does suggest that the cause of the discolouration in TATB is potentially due to the second feasible possibility, a paramagnetic and coloured impurity.

Of all the potential paramagnetic decomposition products formed from irradiating TATB, it is simply the cationic radical derivative of TATB that has UV-Vis absorptions in the correct region corresponding to blue. Ying [52] had a similar conclusion, that his purported

phenoxyl radical was the source of the discolouration and, by nature of being a radical, was responsible for the widely reported ESR signal. Although the work undertaken in this investigation does not corroborate Ying's [52] claims that the phenoxyl radical is blue, the work presented here questions this further, as the predicted ESR signal does not match that observed experimentally. In contrast, the cationic radical derivative of TATB appears blue, but also doesn't match the experimentally derived ESR spectra well, as shown again in Figure 6.5.

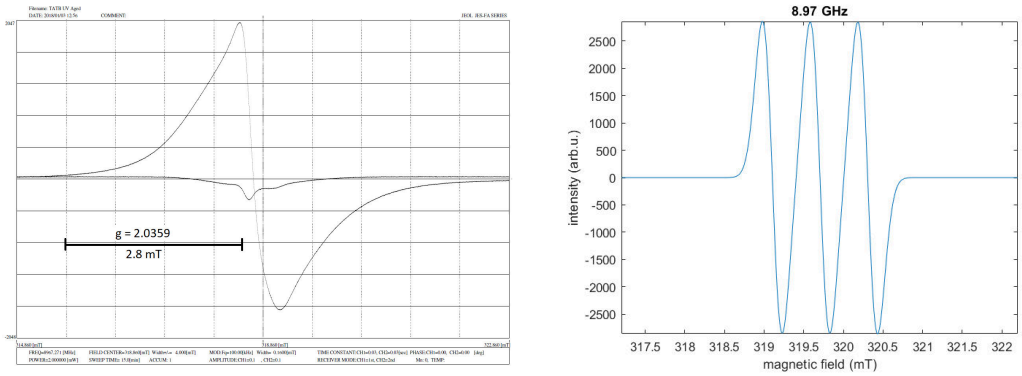

(a) Experimental

(b) Predicted

Figure 6.5: ESR signals of TATB

The simulated ESR signal for cationic TATB features three distinct peaks typical of a single electron interacting with an adjacent nitrogen atom. The experimental spectra of one peak suggests no hyperfine coupling, implying that the signal is generated from a free electron that is isolated from protons and nitrogen atoms, which simply cannot be true. A potential explanation as to why a single peak is observed, is due to the purported radical resonance of the molecule, where at any one point in time, there will be a broad distribution of signals from ionic TATB that are too varied in order to view all of the significantly intricate hyperfine coupling, thus generating a comparatively broad singlet peak. This is highlighted in Figure 6.6, where increased broadening results in a single peak that is similar to experimental measurements.

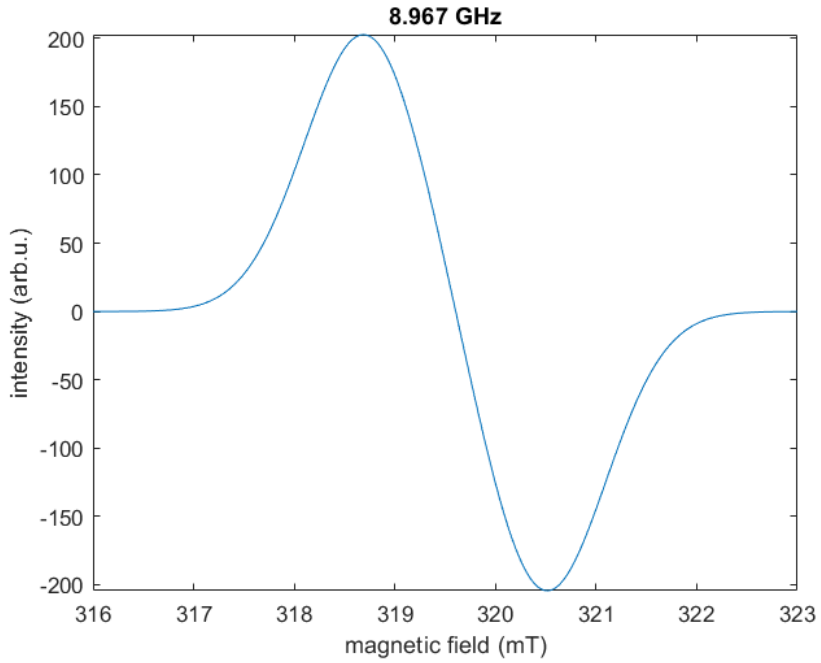

Figure 6.6: Broadened predicted ESR signal of TATB cation

Providing further evidence that it is the cationic TATB radical responsible for the discolouration and the ESR signal, is the result of the recrystallisation of the 400 kGy TATB, where a colour change from green to yellow was clearly visible during the dissolution. It is much more likely that the cationic radical derivative of TATB, once freed from its crystalline state, recaptures an electron and reforms the parent TATB, rather than the phenoxyl radical being present and converting to another non coloured impurity, as it could not possibly return to TATB. This is mainly backed up through the DSC thermogram, (Figure 5.26), which shows that the thermal properties of irradiated TATB reverted back to its unaltered baseline, after the recrystallisation.

A couple of issues exist with this evidence; firstly, is the possibility that the impurity was significantly more soluble than TATB and was therefore not collected and that the accuracy of the balance used for the initial weighing out of TATB limited the accuracy of the reported yield, only allowing an indicative but not firmly conclusive assessment that the mass was recovered in its entirety. Unfortunately, whist this should be looked at

in the future, due to TATB's solubility, undertaking a recrystallisation and achieving full mass recovery is significantly challenging. However, the fact that the collected washings from the recrystallisation were clear and subjected to copious amounts of water, sodium chloride and magnesium sulphite, it is unlikely that other dissolved products were within the solution and if present, they were colourless and not responsible for the blue in TATB.

The second issue is that the re-crystallisation procedure potentially quenched the ionic TATB radical by forming a radical spin-adduct and it was performed in DMSO, a known radial scavenger and spin-trap [91]. In order to test this theory, a small sample of the re-crystallised TATB was submitted for ESR analysis, where no signal was observed, indicating that either the ionic TATB radicals have captured unbound electrons and returned to TATB, or that the spin adduct was soluble in a salted 75:25 water to DMSO mixture.

Moving on to the NMR results, these were particularly disappointing, especially considering the efforts to obtain specialist solvents to increase the solubility of the material. The spectra showed no daughter product speciation, although good agreement between simulated and measured NMR spectra of baseline TATB was achieved, as shown in Figure 6.7.

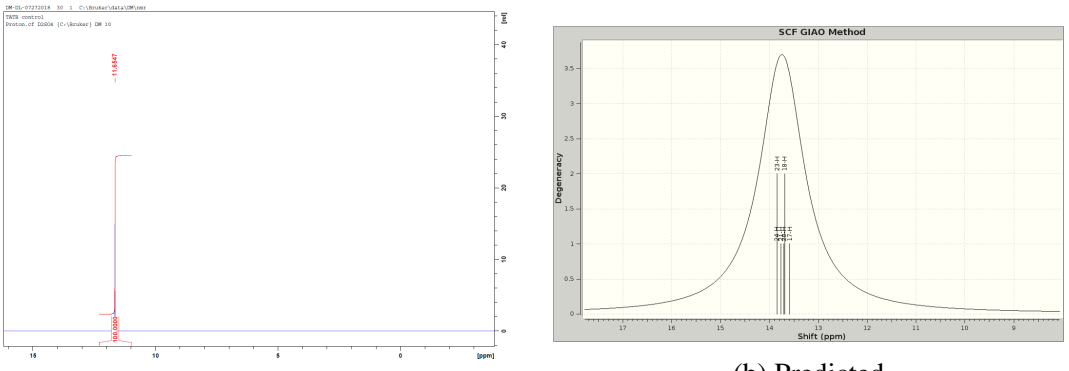

(a) Measured

(b) Predicted

Figure 6.7: TATB NMR spectra

The synthesis of the mono-nitroso derivative was of questionable success, although the synthesis was followed successfully and a lime green coloured material recovered, only DSC and NMR analysis was available in order to characterise the potential decomposition product. The NMR result was inconclusive and did not compare well to that predicted using the same methods that gave good comparison for pure TATB, this is shown in Figure 6.8.

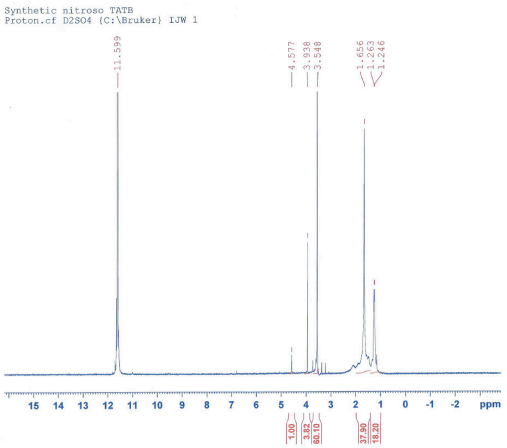

(a) Measured

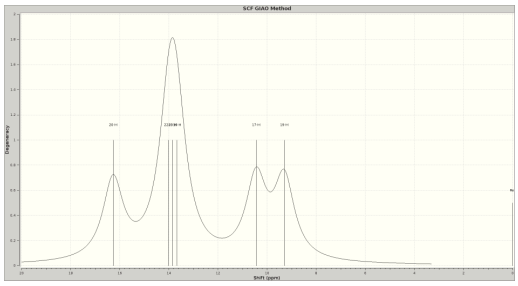

(b) Predicted

Figure 6.8: Mono-nitroso NMR

The thermal properties of the synthetic material, as determined by DSC, does show a reduction in the onset of decomposition, a trend seen in irradiated TATB as a function of total dose. However, the onset for the synthesised product is much lower than both UV and 400 kGy which are significantly more discoloured than the mono-nitroso when compared to unadulterated TATB. These observations, coupled with the fact that the mono-nitroso derivative is not paramagnetic, further suggest that it is not the source of the discolouration.

Summary

One of the most perplexing issues around the effect of gamma irradiation on explosives is the numerous analytical investigations, which have concluded that changes to the physical and explosive properties are caused by the presence of trace levels of impurities, and that this is why techniques such as NMR, HPLC FT-IR are unsuccessful, despite significant changes to some properties such as impact sensitiveness. In terms of TATB's thermal, explosive and optical properties, which become markedly altered upon irradiation, it is likely that these changes may simply be attributed to the presence of the cationic radical derivative of TATB. It appears that the resonance structure of the molecule may be stable enough to accommodate a radical centre for prolonged periods of time and give rise to the widely reported colour change. However, despite this stability, this cationic radical structure is comparatively much more stressed than that of unadulterated TATB. This comparative reduction in stability is potentially the cause as to the observed reduced explosive hazard [43] and thermal properties.

It appears likely, through observations made within this investigation and those preceding it, that changes to TATB through gamma (or UV) radiation are limited to the solid state, and that once irradiated TATB is no longer in the sold state, the damage appears to be reversible. This explains why most analytical methods in the liquid state are unsuccessful in detecting a change to the material, whilst solid state measurements such as impact testing, ESR and DSC are successful in doing so. This is further evidenced by the UV-Vis result that showed negligible change in the liquid state but significant change in the solid. This theory does not explain some historical results where decomposition products have been detected in the liquid state, namely that of Connors and Skidmore [43, 42]. Detections of very small quantities of mono-nitroso and mono-furazan decomposition have been inferred from experimental results. The computational investigation suggests that the formation of some daughter products (although not the mono-nitroso) are energetically favourable. It is therefore perfectly plausible that observed bulk material changes

are caused by the presence of the cationic TATB radical when it is in the solid state, but upon dissolution, a small fraction of the radicals degrade to energetically favourable decomposition products, although the vast majority are likely to simply recapture unbound electrons are reform TATB.

6.2.2 HMX

One of the most significant findings of the experimental section of this work was the marked increase in the sensitivity to impact of the irradiated HMX, when compared to the baseline. This marked increase in sensitivity is not surprising considering the work undertaken by Miles et al [36]. This measurement informs on the missing data in his work as noted by the comment "We have not yet studied the vacuum room temperature irradiation". This result certainly indicates that, in the presence of gamma radiation and under vacuum, the sensitivity of HMX can be greatly increased independently of temperature. As the experimental evidence gathered here cannot be directly compared to that of Miles due to differences in total dose, temperatures, grade of HMX and more, it is highly recommended that the same batch of HMX is irradiated under identical conditions within a representative gaseous atmosphere i.e. no vacuum, and the hazard properties determined for comparison.

The computational study of the influence of gamma radiation on HMX suggested that a potential radical could be located in one of two central nitrogen atoms. Hyperfine coupling was observed between these nitrogen and surrounding hydrogen atoms yielding a complex spectra. This is a marked difference from TATB, where the coupling was localised, and is most likely caused by the lack of aromatic resonance for HMX. This lack of resonance may mean that the decomposition of HMX by gamma irradiation is much more random in nature when compared to TATB, as the initial ionisation may cause fragmentation/isomerisation prior to the electronic stabilisation through pi bond resonance.

The potential location of the nitrogen based radical centre in ionised HMX suggests that the N-NO_2 bond is susceptible to breakage, which is supported by the thermodynamic investigation.

The analysis of energetically favourable decomposition products suggests a number of potential molecules that, in agreement with TATB, favour the larger fragment remaining ionised with the smaller in its electronic ground state. Although ESR analysis of irradiated HMX was not achievable due to sample disposal, the analysis undertaken by Miles et al [36] provided spectra for short lived radicals within the gamma irradiated HMX, this has been reproduced below in Figure 6.9. The computationally predicted ESR spectra from the energetically favourable decomposition products of HMX do not match the spectra observed by Miles well, with the exception of the NO_2 radical, which Miles tentatively assigned to the signal, this is also displayed in Figure 6.9.

(a) Experimental, reproduced from [36]

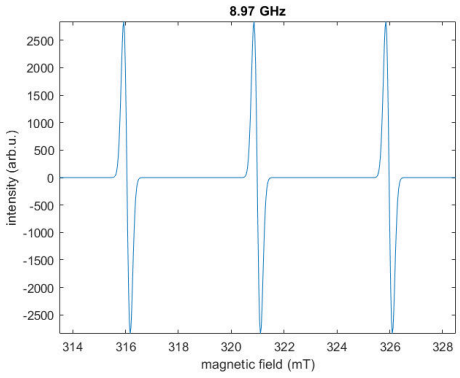

(b) Predicted

Figure 6.9: ESR Signal of suspected NO_2 radical

Consideration of the energetically favourable pathways studied within the computational investigation and the potential presence of the NO_2 suggests that the D path may be active upon irradiation of HMX, which results in an cationic (but non-radical) derivative of

HMX. This, unfortunately, does not agree with the work of Avrami [30] who detailed gas generation results of irradiated HMX (as shown in Figure 3.4), that were dominated by the generation of N_2 gas.

The ESR signals observed by Miles were very time and temperature dependant, indicating a marked reduction in radical stability, when compared to TATB. This suggests that either further decomposition reactions are occurring, or unbound electrons are being recaptured by the material. The experimental (hazard and thermal) analysis of irradiated HMX that was undertaken as part of this work that showed a significant change in the properties from a baseline sample was achieved approximately three months after the irradiation. It can be inferred from Miles's work that it would be expected that all radicals will have decayed within this time, and therefore changes to the thermal and hazard properties must be attributed to non paramagnetic decomposition products. This could be caused by the NO_2 eliminated cationic derivative of HMX with the NO_2 undergoing further decomposition reactions to form N_2.

The DSC scans of irradiated HMX provides an interesting insight into the effect of the radiation on the thermal properties of the material. The thermogram of HMX irradiated in vacuum offers three key pieces of information; a small exothermic peak at approximately 154°C, a sharp endothermic peak akin to a melt rather than the expected beta to delta phase transition at approximately 176°C, and a double humped exothermic decomposition peak that starts at 220° and continues up until 270°C. It is interesting to note that the small exotherm at 154°C has been observed previously in irradiated materials by Avrami [30], but has not been commented upon. It is also interesting to note that this is the approximate temperature that nitrous acid (one of the predicted energetically favourable fragments) boils, potentially indicating the presence of the imine derivative of HMX [92]. Furthermore nitrous acid is unstable and can disassociate, potentially producing the NO_2 radical, the same radical that Miles attributed his ESR spectra to.

The sharp endothermic peak is also of interest, potentially indicating an impurity, or perhaps simply a stressed state of HMX, i.e. the ionic form, rapidly re-arranging itself to a more stable state once the crystalline state is able to move. One of the initial theories for the increased sensitiveness of the HMX was a potential phase transition from beta to alpha, known to be much more impact sensitive [89]. This would not explain the significantly altered main decomposition peak as any alpha HMX would have transitioned to delta HMX prior to decomposition. A further potential theory is the presence of linear nitroamines that may have been formed by chain opening due to bond scission. This theory may explain the apparent melt observed in the material rather than the beta to delta phase transition and also the double peaked main exothermic decomposition peak.

As detailed by Miles [36, 37] changes to the impact sensitivity of HMX can be achieved by gamma irradiation. His work covered irradiations at low temperature in both atmospheric and vacuum conditions as well as at room temperature in atmospheric conductions only. The hazard results achieved within the investigation work presented here complete his test regime by showing that irradiations at, albeit slightly elevated temperature compared to room of 40°C, in vacuum significantly effect the sensitiveness to impact for HMX. Upon assessment of both sets of data, it can be concluded that it is not the effect of temperature, but rather the use of vacuum to irradiate HMX that significantly alters the impact sensitivity of HMX.

Returning to the thermal properties of irradiated HMX, they also appear to be significantly affected by the atmosphere (or lack of) in which HMX is irradiated. An analogous study undertaken by Padfield [51] showed negligible change in thermal or hazard behaviour when HMX was irradiated to 100 kGy in air. Additionally, and as part of a parallel investigation, a PBX containing 91 % HMX was also irradiated to a similar level in the presence of air and in vacuum. The sample irradiated in the presence of air showed

no change to the thermal properties when compared to a baseline. However, the PBX sample irradiated in vacuum showed equivalent thermal behaviour to the HMX irradiated in vacuum from this investigation; this is shown in in Figure 6.10.

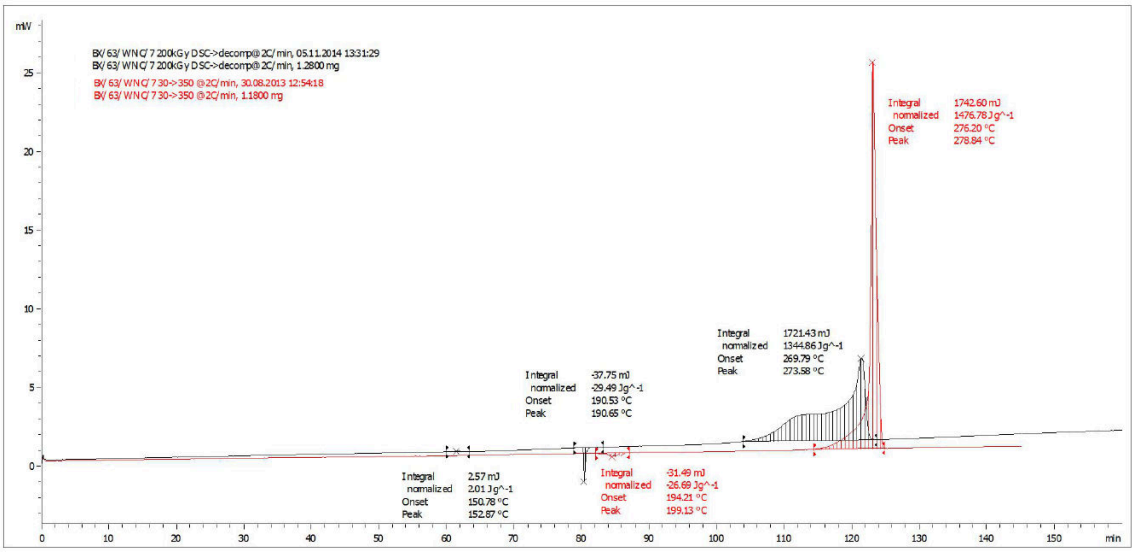

Figure 6.10: PBX baseline and 200 kGy gamma irradiation

Consideration of the liquid phase experimental investigation, NMR and HPLC analysis of irradiated HMX showed no difference when compared to baseline samples despite numerous runs and some method development. If the nitrous acid, suggested by the small exothermic peak at 154°C in the DSC was present, this should have been clearly detected on proton scan of the NMR. Similarly, any generated decomposition product such as the purported NO_2 eliminated HMX cation or linear nitroamine should have a completely different retention time compared to the parent HMX in the HPLC.

Summary

There are significant similarities and differences between the computational and experimental results of HMX, when compared to that of TATB. It is clear from the hazard and thermal properties that the presence of atmosphere is of significant importance, with all

data from irradiations undertaken in atmosphere showing negligible differences to these properties, whereas in vacuum significant changes are observed; these differences must therefore at least initially, be chemical in nature. The liquid experimental analysis provides strong evidence that daughter products are not being generated in any appreciable quantity. The evidence from Miles' work on the short lived (compared to TATB) ESR signal of the NO_2 radical suggests that any paramagnetic species are short lived, however, and this is key, these measurements are believed to have been undertaken in atmosphere and not in vacuum.

The ESR result shows that the NO_2 radicals decay over a matter of minutes, and are suggested to react with atmospheric oxygen to form more stable proxy type radicals that will escape into the head space, and allow the HMX to reform to its ground state, and original hazard and thermal properties. In the absence of atmosphere and more specifically oxygen, these radicals cannot form more stable radical moieties and it is suspected, although not evidenced, that ESR analysis of vacuum irradiated HMX would yield a long lived radical that is responsible for the measured differences in thermal and hazard properties that are not observed for irradiations undertaken in the presence of air.

It is thought that when HMX is irradiated in vacuum, any highly reactive radicals such as those hypothesised within the computational section cannot react with oxygen, and the crystalline structure must therefore compensate electronically by sharing electrons between adjacent molecules, by rearrangement and by the decay of the short lived to potential longer lived radical species. This causes the HMX crystal to be within a pseudo stressed state, that is responsible for the altered thermal and hazard properties observed only for vacuum irradiated materials. Post irradiation, when crystals are exposed to atmosphere, any radical species still present will likely be much more stable due to this rearrangement and are likely long lived and will not react with the oxygen or other species within the atmosphere, i.e. HMX properties will not return to their original state and

changes are permanent.

This theory goes on to explain why any liquid (NMR and HPLC) experimental investigation yielded negligible results, but testing in the solid state (DSC and impact testing) yielded notable differences, as once dissolved, the HMX molecules are free to reform by capturing unbound electrons. This theory is very similar to that of the TATB, however changes to the properties of TATB are much smaller in magnitude with the exception of the colour change, both of which can be attributed to the aromatic resonance of the molecule. The presence of this resonance allows TATB to suffer significant loss of electrons without significant alterations to its physical and thermal properties, however it does so at a cost to its colour. As HMX does not benefit from such aromatic resonance, HMX in the crystalline state is much more susceptible to ionising radiation.

As a final note on HMX, a concern was that changes to the thermal and hazard properties may have been resultant from the material being stored in a vacuum at elevated temperature for the approximately 11 day period of irradiation, i.e. the effect was not due to the radiation, but the vacuum storage. In order to test this theory, two ampoules of HMX were evacuated, flame-sealed and stored for 266.7 hours at 40°C. Thermal testing was undertaken, as the method had proved to be sensitive for the irradiated HMX, with the resultant thermogram, Figure 6.11, showing no difference between the baseline and these new samples, suggesting that observed changes can be attributed to the exposure to gamma radiation alone.

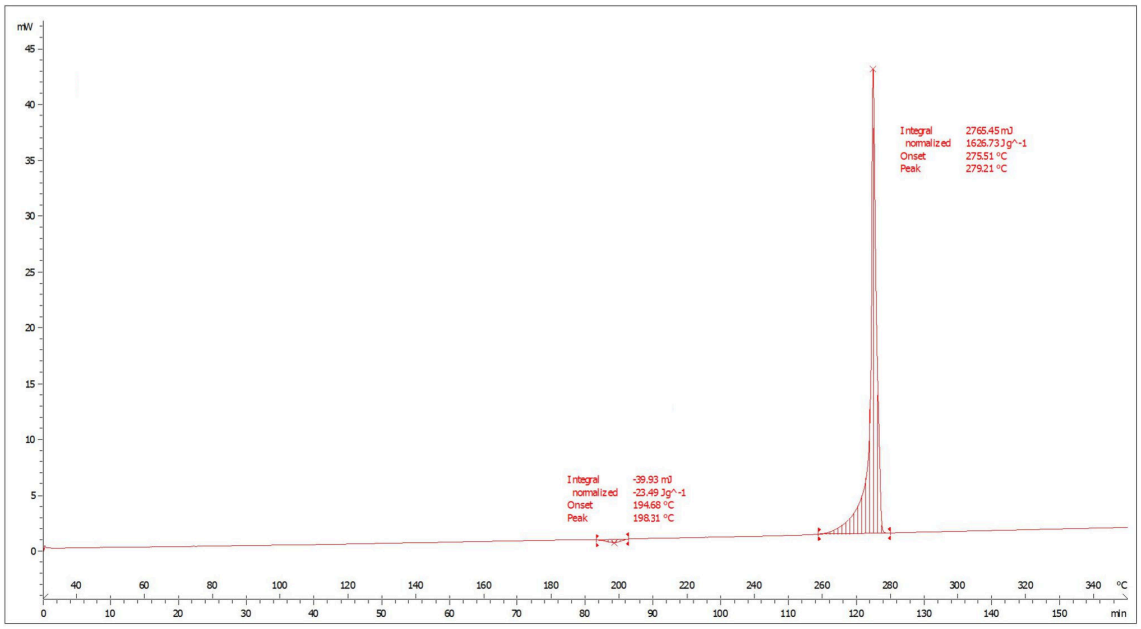

Figure 6.11: PBX baseline and 200 kGy gamma irradiation

6.2.3 PETN

PETN showed similarities and differences in both experimental and modelling investigations when compared against both TATB and HMX. Of particular note was the marked increase in sensitiveness to impact, resulting in a Figure of Insensitivity of 26, reduced from the baseline measurement of 81. This is comparable to that observed in the HMX sample and resulted in a material that was highly impact sensitive, resulting in its disposal. With only a small quantity left, the same techniques that were employed for the investigation of the limited quantities of irradiated HMX were used, which yielded a null result for both HPLC and NMR analyses. This indicates that the effect again may be limited to the solid state.

DSC analysis, however, showed a marked difference for the irradiated PETN when compared to HMX and TATB, as no significant change was observed between baseline and irradiated PETN. There is potentially peak depression observed in the thermograms for both the decomposition exotherm and the melt endotherm which would agree with other

literature evidence [30], however there is nothing to suggest significant alterations in the material's chemistry, caused by either daughter product speciation or potential stressed crystalline states.

Despite the disposal of the material due to its sensitivity to impact, more was retained when compared to the HMX. This material permitted an ESR measurement that yielded a small but detectable radical signal indicating the presence of a long lived radical. Miles [38] recorded two long lived radicals in PETN and attributed one to NO_2 and the other to an unknown, he also claimed that they were still in detectable concentrations days after irradiation. The PETN irradiated as part of this work was analysed almost three years after the initial irradiation and showed that significant concentrations of the radical were still present. However, the measured spectra here does not agree with that published by Miles, despite both reportedly being irradiated under vacuum, albeit with different incident energies.

Despite the lack of an altered DSC thermogram, HPLC chromatogram and NMR spectra, the ESR spectra does suggest changes in the chemistry of the PETN, whilst in the solid state. The change to impact sensitiveness was measured at the same time as the HMX, approximately three months after samples were irradiated, however a significant period of time, of order years, had passed prior to the thermal and ESR analyses. It is possible that the radical is responsible for the altered hazard properties, and that the concentration had decreased to such a low level that the thermal characteristics had not been altered, or simply that the radical does not effect the thermal properties. Unfortunately, the scarceness of this material means that re-analysis is all but impossible as changes appear to be time dependant, with properties perhaps reverting as radical concentrations reduce. This continues the theory that changes to these materials are dominated by the fact they are in the solid state.

The computational study on PETN suggests a variety of differing initial decomposition reactions, with several of them identifying the release of NO_2 either in an ionic or radical form. The most energetically favourable decomposition product was the loss of the NO_2 radical, resulting in an unstable ionic derivative of PETN that appeared to further decompose to a secondary intermediate and the subsequent release of ionic and non radical NO_2. Calculation of the electrostatic response for the purported radical species generated ESR spectra of varying complexity that can be compared to the long lived signal observed experimentally.

The oxygen centred radical of ionic PETN showed two potential equivalent sites for the radical to be located within the molecule which gave rise to a complex spectra. In real life radicals cannot be split, so it is likely that there will be a distribution of these locations. The simulated ESR spectra of the parent cation radical takes this into account, and reveals arguably the best agreement between the experimentally obtained and theoretically predicted spectra, this has been reproduced below in Figure 6.12.

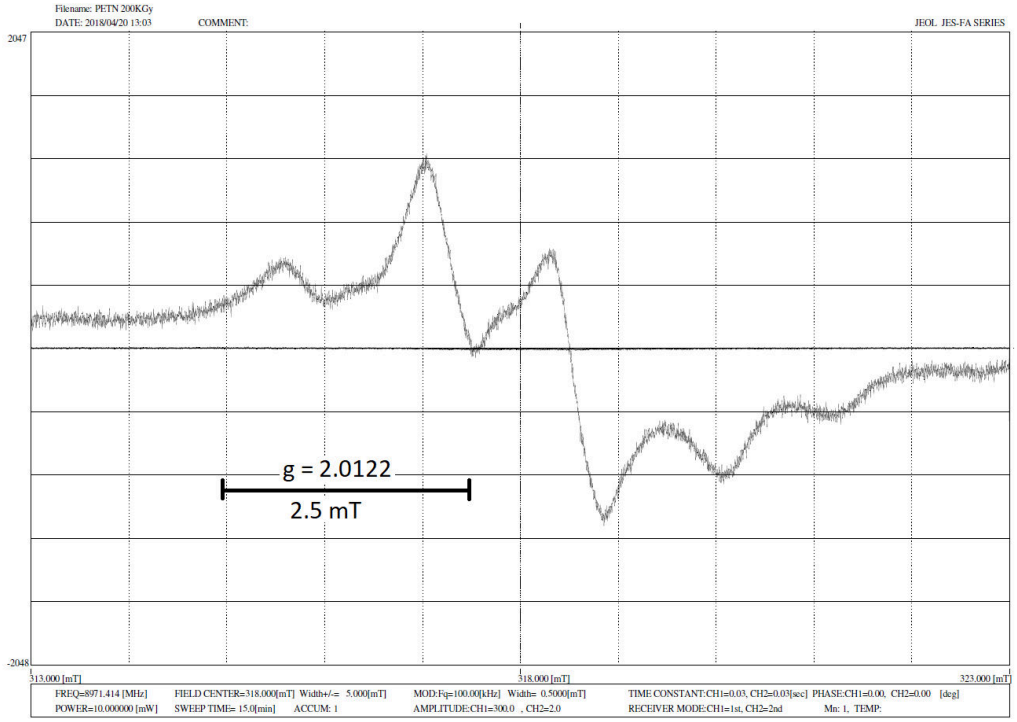

(a) Experimental derived spectra

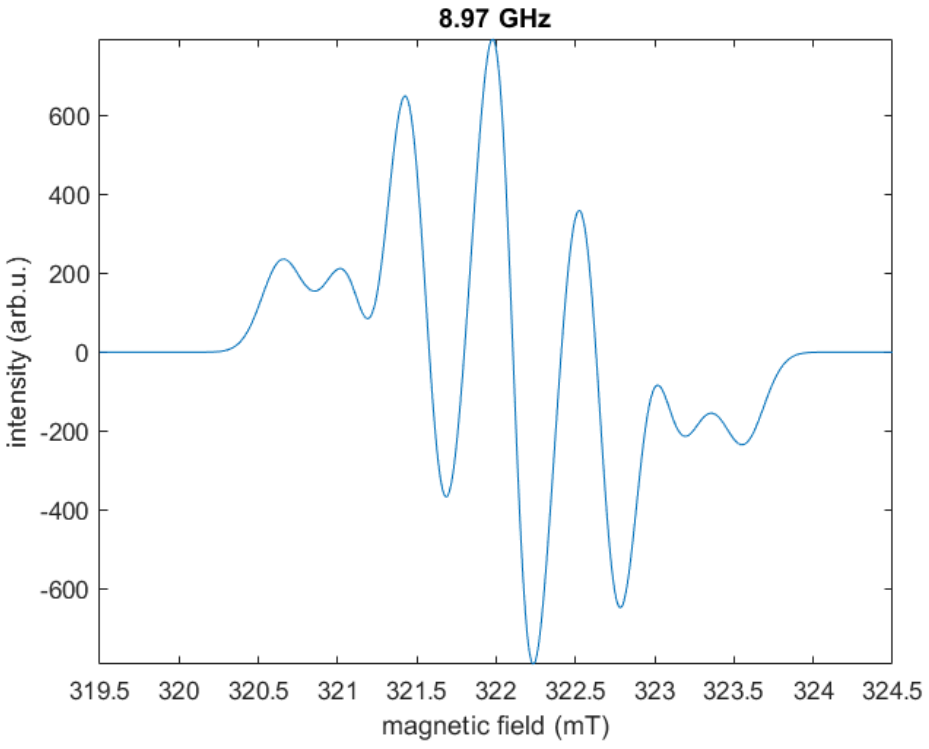

(b) Predicted

Figure 6.12: Experimental vs predicted ESR spectra of ionic PETN

Despite the thermodynamically favourable decomposition pathways, the possibility that

the long lived radical in irradiated PETN is simply just the PETN cation, fits with the observations from TATB and HMX and the theory that changes to the physical properties of these materials, is due to stressed charged equivalents, rather than daughter products, that are trapped within the solid state. Such cations would essentially revert to their parent form, once released from their crystalline structure, hence the liquid state analysis was unsuccessful whilst the impact properties were significantly altered.

Summary

The computational and experimental investigation for PETN was very similar to that of HMX, with the exception of the unadulterated thermal properties of the irradiated explosive crystal. It is thought that the same mechanisms are at play and that a stressed crystalline state of PETN is at fault for the observed increased sensitiveness to impact. It is possible that the lack of an effect on the thermal properties of PETN may be attributed to its comparatively low and broad decomposition temperature and that the presence of radical stressed states simply does not effect this property as much as HMX.

Chapter 7

General conclusions and future work

Throughout the literature there is no general mechanism that describes the interaction between gamma radiation and explosive materials. This is not particularly surprising, as although grouped together as a selection of materials by an intended application, their chemistries are quite different. Of particular note is the difference between explosive materials that contain aromatic groups, such as TATB, and materials that do not, i.e. HMX and PETN. It is well documented [41] that aromatic structures afford radiation resistance through radical resonance throughout the conjugated pi bonding structure, there is no reason that explosive materials would not follow this trend. There are two primary schools of thought as to the cause of measured changes to the explosive and physical properties of irradiated materials; firstly the formation of daughter products [43, 52, 46, 42, 51] and secondly, the generation of stressed crystal structures [27, 30, 22].

It has been shown by the computational calculations presented within Chapter 4, and by some that are detailed within the literature [79, 52], that the formation of several purported daughter products may be energetically favourable from an ionised parent PETN, HMX or TATB molecule. These calculations are significant approximations to what may occur in the solid state, and despite tactics to increase the relevance of the calculations, such the use of Implicit Solvent Methods, there is significant uncertainty as to the applicability of

these methods to the solid state of which these materials exist. It is perfectly plausible that the formation of these decomposition products is hindered by the trapping of these molecules in the crystal lattice in which they are located. Furthermore, ionising radiation is indiscriminate, and as such any electron and hence bond within a molecule is vulnerable to scission through ionisation, questioning whether the interaction causes repeatable and predictable decompositions or whether they are random, akin to the incident radiation.

In an effort to ascertain whether the interactions are random or predictable, the computational chemistry optimisations undertaken of the ionic species considered within this work, have demonstrated energetically favourable locations for radicals to reside on these molecules. However, this is based upon the approximation that upon ionisation, such molecules will re-arrange to obtain this energetically favourable state prior to fragmentation/isomerisation and hence potential daughter product formation. This is perhaps most valid for molecules that contain aromatic moieties, such as TATB, where radical rearrangement may occur through resonance, prior to fragmentation/isomerisation, if such movement is permitted in the solid state. A further, and potentially more credible possibility considering the experimental evidence, is that disruptions to, and the presence of, stressed crystal structures are responsible for the apparent bulk property changes.

Some general observations can be made from literature as well as the computational and experimental effort undertaken within this work. Firstly is that raw explosive materials that are exposed to large quantities of gamma radiation appear to become more impact sensitive with dose; secondly, the gaseous environment in which they are irradiated appears to have a significant effect on the resultant impact sensitiveness; and thirdly, computation of the ionisation potentials of TATB, HMX and PETN suggest that interactions of these materials with gamma radiation should be identical for X-Rays and UV photons above approximately 2 eV.

Irradiation of HMX, PETN and TATB in vacuum has been shown to affect the physical, thermal and hazard properties to differing extents, with the hazard properties of HMX and PETN and the optical properties of TATB being the most striking. Changes to these materials are almost always detected within the solid state. The main exception to this is TATB, where a number of external literatures have found chromatographic evidence of daughter product speciation. Long lived radicals of PETN and TATB (and short lived for HMX from literature [36, 37]) suggest that cationic species are present within these materials and are believed to be the cause of the increase in sensitivity, particularly to impact. This is further evidenced by the computational study of TATB, which concluded that the greening, which unsurprisingly correlates with total dose and radical concentration, appears to be attributed to the simple cationic radical derivative of TATB, and not a daughter product. This theory is supported by the evidence that the greening of TATB is reversible by re-crystallisation, with the resultant material devoid of any radical signal in the ESR, and a DSC thermogram that is practically identical to the initial baseline material.

It is thought that the aromatic resonance of TATB allows its cationic radical derivative to last for significant periods of time in the solid state and that, once dissolved, it may return to TATB though electron capture, or decomposition to a daughter product such as mono-furazan or mono-nitroso. It is likely that there is no one single daughter product, and that there will be a distribution of products formed within solution. As none of these daughter products are highly coloured, this may explain why decomposition products can be detected through analytical methods such as HPLC, whilst the recrystallisation reverted the colour from green to yellow.

Radicals seen in PETN and those reported for HMX [38, 37] appear to be more time sensitive than TATB and indicate decomposition in the solid state, although this is markedly more rapid for HMX compared to PETN. The decomposition reactions computationally predicted for HMX and PETN are complex and signify a collection of potential daugh-

ter products that may be responsible for the increased sensitivity, however it is possible that the strained cationic derivatives of the parent molecules are responsible for the bulk changes to the material.

The first ionic potentials of HMX, TATB and PETN are all of order single electron volts, which correspond to the mid Ultraviolet. Despite several different physical mechanisms, the interaction of electromagnetic radiation above this energy will result in the ionisation of the material, up until extreme energies in excess of 10s of MeV where pair production dominates and does not result in ionisation. This essentially means that radiations of these materials should have the same behaviour whether it is by X-Rays, Gamma rays or most UV quanta, allowing future work to be undertaken without requiring very specialised gamma irradiative facilities. As shown by the calculations of the mass and mass-energy linear attenuation coefficients, increased energies of incident electromagnetic radiation correspond to a lower rate of absorption, meaning that UV irradiation (of the same flux) represents a worst case in terms of the effect on the material. Again, as shown by the attenuation coefficient functions, the main difference between these electro magnetic quanta is the fact that higher energy photons are much more penetrative, due to their poorer rates of absorption, when compared to lower energies.

This fact means that future experiments can be undertaken using much more easily obtainable UV and X-Ray sources when compared to those that emit gamma radiation. Care must be made as to volumetric effects due to the poorer penetrative ability of these quanta, and as such experiments should be designed such that sample thickness is minimised in order to reduce this effect.

7.1 Future Work

A question remains as to whether the changes in physical and hazard properties are caused by alterations in the chemistry of each molecule, either by the presence of decomposition products or by stressed cationic states, or whether they are caused by changes to the crystal structure of each material. It is therefore suggested that future work should be undertaken on these materials to ascertain whether changes to the physical crystal structure are resultant through gamma irradiation, with analyses such as X-Ray diffraction and Scanning Electron Microscopy being suggested techniques.

Investigations into potential crystalline defects and stressed states induced through gamma radiation may also be complemented by further computational work that utilises molecular dynamic simulations or computational chemistry simulations that utilise ONIOM or periodic boundary conditions; these simulations may also be validated by potential x-ray diffraction experiments. Further decomposition products of TATB, HMX and PETN could be evaluated using the same computational method detailed within this work, as it is unknown if the purported products are final. Furthermore, as only initial and suspected final states are considered, the energy barrier and hence activation energy could also be calculated between these states, by the consideration of transition intermediaries.

Recrystallisation of TATB should also be undertaken in other materials, such as ionic solvents, where the solubility of TATB is increased relative to DMSO, allowing the recrystallisation to occur at lower temperature (i.e. room).

The computationally derived ionic potentials for TATB, HMX and PETN shows that an electron can be removed with energy of order 1 eV, indicating that mild radiation should have the same effect on these materials as gamma radiation, with the only significant difference being the penetrative power of gamma vs UV. It is therefore recommended that the in-situ ESR experiments at low temperatures are re-attempted using UV light, as

not only will the flux of ionising radiation be orders of magnitude greater than that of the most powerful AM-241 source currently available, but the absorption of this lower energy quanta should be much improved. This investigation can continue the understanding of the initial chemistry that occur when these materials are irradiated, and may help validate the purported decomposition pathways within this work.

Appendix A

Computational Data

A copy of the outputs from computational chemistry calculations may be found in the GaussianOutputData folder, within the attached CD. A naming convention has been used in order to identify the correct file, this is summarised within Figure A.1. In keeping with he modelling flow diagram shown in Figure 4.5, there are four main types of calculation, optimisation (OPT), vibrational (FRQ), time-dependent DFT (UVVIS) and electrostatic properties (ESR).

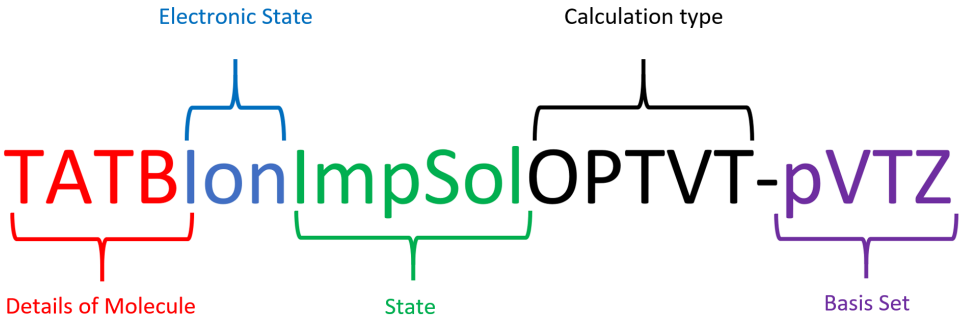

Figure A.1: Computational chemistry naming convention

A copy of the spreadsheet, including all raw data and the linear interpolation code developed to generate the predicted mass-attenuation functions can also be found within the accompanying CD, as MassAttenuationCalculations.xlsm.

A copy of the spreadsheet used to determine the thermodynamics of each of the considered reactions can also be found on the accompanying CD, as ThermochemistryCalculations.xlsx.

A copy of the MATLAB scripts used to generate the predicted ESR spectra may also be found within the accompanying CD, within the EasySpinMatlabCode folder.

Appendix B

A Note On Hotspots

Throughout this study, various references to daughter products, stressed states and crystalline defects have been made with regard to the observed increased explosive sensitiveness, especially to impact stimuli. The underlying explanation of why such defects/imperfections causes this increased sensitiveness can be explained by "hot spot" theory [55]. This details a selection of mechanisms that describe localised heating within an energetic material, bourn through adiabatic collapse of gaseous voids and frictional effects, which, under mechanical strain, can be aided by plastic flow. If this localised heating reaches a critical temperature for a particular duration, it will cause decomposition of local energetic molecules, releasing additional thermal energy. This in turn, causes the temperature to raise further and can result in the deflagration of energetic materials, which, under the correct circumstances can transition to detonation.

In cases where the crystalline structures of energetic materials are compromised, either with point defects, stacking faults, dislocations or grain boundaries, this can increase the probability of successful deflagration/detonation through "hot spot" formation. This is due to a combination of increased hot spot locations, due to pockets of gas trapped within a crystal, and the increased probability of frictional heating thought adiabatic shear banding and plastic flow of the material itself. When considering radiation damage on en-

ergetic materials, the formation of daughter products, whether they are solid or gaseous is likely to cause such compromising defects within the crystal structures which may be attributed to the observed increase in sensitiveness to impact.

References

[1] Byrnes, J., *Unexploded Ordnance Detection and Mitigation, ISBN: 9781402092534*. NATO Science for Peace and Security Series B: Physics and Biophysics, Springer Netherlands, 2008.

[2] Wikipedia contributors, "Polymer-bonded explosive." Electronic, Apr. 2019. Accessed 6-April-2019, `https://en.wikipedia.org/wiki/Polymer-bonded_explosive`.

[3] Wikipedia contributors, "Pentaerythritol tetranitrate — Wikipedia, The Free Encyclopedia," 2019. Accessed 6-April-2019, Licensed under Creative Commons Attribution Wikipedia, `https://en.wikipedia.org/wiki/Pentaerythritol_tetranitrate`.

[4] A. C. Hazelwood and A. C. Glauser, "Comparison of HMX Types B & C With Chemring HMX Products," techreport, AWE Plc., Mar. 2009.

[5] A. C. Hazelwood, "Comparison of Class 2 HMX Products," techreport, AWE Plc., Mar. 2013.

[6] "MIL-DTL-45444C - HMX Specification."

[7] "AWE Specification HR145 Issue 8 - HMX."

[8] G. R. Miller and A. N. Garroway, "A review of the crystal structures of common explosives part I: RDX, HMX, TNT, PETN and Tetryl," tech. rep., University of Maryland, College park; Naval Research Laboratory, United States Navy, 2001.

[9] "Material Safety Data Sheet - EDC40 - XTF/B/MSDS/005."

[10] J. L. Boyd-Livingston, "HE Data Manual Issue 4," resreport, AWE Plc., 1987.

[11] Wikipedia User Wolfmankurd, "Photoelectric effect." Public Domain, Jan. 2001. Accessed on 16th April 2019, https://commons.wikimedia.org/w/index.php?curid=2072934.

[12] K. S. Krane, *Introductory nuclear physics, ISBN: 9780471805533*. Wiley, 1987.

[13] Wikipedia User JabberWok, "Compton-scattering." Electronic, Dec. 2006. Accessed 6-April-2019, Licensed under Creative Commons Attribution-Share Alike 3.0 via Wikimedia Commons, http://commons.wikimedia.org/wiki/File:Compton-scattering.svg.

[14] "Pair-production," 2016. Accessed 6-April-2019, Free to share, copy and redistribute the material in any medium or format, under the Creative Commons Attribution-ShareAlike 3.0 License, http://electrons.wikidot.com/pair-production-and-annihilation.

[15] Nuclear power contributors, "Interaction of gamma radiation with matter-attenuation.png." Electronic, 2019. Accessed 06-April-2019, Redistribution or reproduction permitted for Educational (i.e. non-commercial), https://www.nuclear-power.net/wp-content/uploads/2015/03/attenuation.png.

[16] J. H. Hubbell, "Tables of X-Ray Mass Attenuation Coefficients and Mass Energy-Absorption Coefficients from 1 keV to 20 MeV for Elements Z = 1 to 92 and 48 Additional Substances of Dosimetric Interest," techreport, National Institute of Standards and Technology, July 2004.

[17] J. H. Hubbell and S. M. Seltzer, "X-Ray mass attenuation coefficients," tech. rep., NIST, 2004.

[18] A. F. Parsons, *An introduction to free radical chemistry, ISBN: 9780632052929*. Wiley, 2000.

[19] NME-AEC Panel, "Radiological Warfare Report TID-204," tech. rep., Oak Ridge National Laboratory and Picatinny Arsenal, 1948.

[20] H. Rosenwasser, "Effects of gamma radiation on explosives : Final and summary report on Army Ordnance Project TA3-5003R Stability and reactions of explosives," tech. rep., Oak Ridge, TN : Oak Ridge National Laboratory, 1955.

[21] J. V. R. Kaufman, "The effect of nuclear radiation on explosives," tech. rep., Picatinny Arsenal, 1958.

[22] E. Mapes, "Effects of gamma-ray irradiation on five plastic-bonded high explosive compositions," tech. rep., Brookhaven National Laboratory supported by Picatinny Arsenal, April 1962. Declassified from Secret to Unclassified 19th of October 1971.

[23] Larry G. Hill, Robert Mier, Matthew E. Briggs, "PBX 9404 Detonation Copper Cylinder Tests: A Comparison of New and Aged Material," tech. rep., Los Alamos National Laboratory, 2009.

[24] Thomas S. Costain, Rocco and V. Motto, "The sensitivity, performance and material properties of some high explosive formulations," tech. rep., Picatinny Arsenal, 1973.

[25] M. J. Urizar, E. D. Loughran and L. C. Smith, "A study on the effects of nuclear radiation on organic explosives," tech. rep., Los Alamos Scientific Laboratory, 1962.

[26] J. Velkinburgh, "Skid test evaluation of PBX 9407," tech. rep., Pantex Plant, 1976.

[27] J. A. Berberet, "The effects of nuclear radiation on explosive solids - technical report ATL-TDR-64-53," tech. rep., Air Force Systems Command, 1964.

[28] Thomas C. Castorina, Jerome Haberman and Andrew F. Smetana, "Radiation-enhanced surface activity of an organic explosive, gammma-HMX," *International Journal of Applied Radiation and Isotopes*, vol. 19, pp. 495–503, 1968.

[29] B. Lee, M. Lee, "Decomposition of 2,4,6,-trinitrotoluene (TNT) by gamma irradiation," *Environmental science and technology*, vol. 39, no. 23, pp. 9278–9285, 2005.

[30] Louis Avrami, et al, "Radiation induced changes in explosive materials," tech. rep., Picatinny Arsenal, 1973.

[31] Louis Avrami & Henry J. Jackson, "Effect of long term low-level gamma radiaiton on thermal sensitivity of RDX/HMX mixtures," tech. rep., Picatinny Arsenal, 1976.

[32] E. Piantanida & N. Piazzi, "Behavior of explosives under the action of gamma rays," tech. rep., Picatinny Arsenal, 1961.

[33] Unknown, "STANAG 4147 - chemical compatability of amunition components with explosives (Non-Nuclear Applications)." Electronic, June 2001.

[34] Louis Avrami, "Radiation effects on explosives, propellant and pyrotechnics," *Encyclopedia of explosives and related items*, vol. 9, p. 2700, 1980.

[35] J. J. Dick, "Plane shock initiation of detonation in gamma-irradiated pentaerythritol tetranitrate," *Journal of applied physics*, vol. 53, no. 9, pp. 6161–6167, 1982.

[36] M. H. Miles, K.L. DeVries, A.D. Britt and W.B. Moniz, "Generation of free radicals in RDX and HMX compositions," *Propellants, explosives, pyrotechnics*, vol. 7, pp. 100–106, 1982.

[37] M. H. Miles, K.L. DeVries, A.D. Britt and W.B. Moniz, "Impact sensitivity of gamma irradiated HMX," *Propellants, explosives, pyrotechnics*, vol. 8, pp. 49–52, 1983.

[38] M. H. Miles and K. L. DeVries, "Free radicals in gamma irradiated PETN," *Journal of materials science*, vol. 19, pp. 467–472, 1984.

[39] B. C. Beard, "The radiation sensitivity of NTO," *Journal of energetic materials*, vol. 7, pp. 181–198, September 1989.

[40] B. C. Beard, "X-Ray radiation decomposition of cyclo-1,3,4-trimethylene-2,4,6-trinitramine (RDX), at low temperature: initial reaction steps," *Propellants, explosives, pyrotechnics*, vol. 16, pp. 81–87, September 1991.

[41] V. S. Ivanov, *Radiation chemistry of polymers, ISBN: 9789067641371*. New concepts in polymer science, Taylor & Francis, 1992.

[42] C. Skidmore, D. Idar, G. Buntain, S. Son and R. Sander, "Ageing and PBX 9502," tech. rep., Los Alamos National Laboratory, 1998.

[43] S. C. Connors, *The Effects of Gamma Radiation on a PBX containing TATB and the fluoropolymer FK-800*. PhD thesis, Cranfield University, 2014.

[44] A. D. Britt, W. B. Moniz, G. C. Chingas, D. W. Moore, C. A. Heller and C. L. Ko, "Free radicals of TATB," *Propellants and explosives*, vol. 6, p. 94, 95 1981.

[45] D. W. Firsich and M. P. Guse, "On the photochemical phenomenon in tatb," *Journal of Energetic Materials*, vol. 2, no. 3, pp. 205–214, 1984.

[46] M. R. Manaa, R. D. Schmidt, G. E. Overturf, B. E. Watkins, L. E. Fried and J. R. Kolb, "Towards unraveling the photochemistry of TATB," *Thermochimica Acta*, vol. 3, no. 84, pp. 85–90, 2002.

[47] W. Reusch, "Visible and ultraviolet spectroscopy." Electronic, May 2013. Accessed 6-April-2019, `https://www2.chemistry.msu.edu/faculty/reusch/virttxtjml/spectrpy/uv-vis/spectrum.htm`.

[48] A. R. Leach, *Molecular modelling principles and applications, ISBN: 9781402092534*. Prentice Hall, 2001.

[49] J. Padfield, "Final report of feasability study," tech. rep., Cranfield University, 2008.

[50] C. Burgess, "Literature review of the lifetime of DOE materials: Aging of plastic bonded explosives and the explosives and polymers contained therein," techreport, Amarillo national resource center for plutonium, Sept. 1998.

[51] J. Padfield, "Private communications." Private communications sent via email and data exchange, Sept. 2014.

[52] Y. Xiong, J. Liu, F. Zhong, T. Xu and K. Cheng, "Identification of the free radical produced in the photolysis of 1,3,5-Triamino-2,4,6-trinitrobenzene (TATB)," *The Journal of Physical Chemistry*, vol. 118, no. 34, pp. 6858–6863, 2014.

[53] X. Tian, X. Wang, K. Yu, J. Sun and D. Xiao, "A new insight to the color change phenomenon of TATB: structural color," *Propellants, Explosives and Pyrotechnics*, vol. 42, no. 11, pp. 1247–1251, 2017.

[54] Zoe H. Barber, ed., *Introduction to Materials Modelling, ISBN: 9781902653761*. Maney - For the Institute of Materials, Minerals and Mining, 2005.

[55] Walley, S.M. and Field, J. and Greenaway, M., "Crystal sensitivities of energetic materials," *Materials Science and Technology*, vol. 22, pp. 402–413, Apr. 2006.

[56] Wikipedia contributors, "Ab initio quantum chemistry methods — Wikipedia, The Free Encyclopedia." Electronic, 2019. Accessed 6-April-2019, https://en.wikipedia.org/w/index.php?title=Ab_initio_quantum_chemistry_methods/&oldid=888805071.

[57] Wikipedia contributors, "Moller-Plesset perturbation theory — Wikipedia, The Free Encyclopedia." Electronic, 2019. Accessed 6-April-2019, https://en.wikipedia.org/w/index.php?title=M%C3%B8ller%E2%80%93Plesset_perturbation_theory&oldid=884774939.

[58] Wikipedia contributors, "Configuration interaction — Wikipedia, The Free Encyclopedia." Electronic, 2017. Accessed 6-April-2019, https://en.wikipedia.org/w/index.php?title=Configuration_interaction&oldid=800204115.

[59] D. C. Sherrill, "A brief review of elementary quantum chemistry," 2001. Accessed 12-May-2019, http://vergil.chemistry.gatech.edu/notes/quantrev/quantrev.pdf.

[60] Wikipedia contributors, "Density functional theory — Wikipedia, The Free Encyclopedia." Electronic, 2019. Accessed 6-April-2019, https://en.wikipedia.org/w/index.php?title=Density_functional_theory&oldid=890459412.

[61] Wikipedia contributors, "Hybrid functional — Wikipedia, the free encyclopedia." Electronic, 2019. Accessed 6-April-2019, https://en.wikipedia.org/w/index.php?title=Hybrid_functional&oldid=882561208.

[62] J. Moxnes, T. Jensenand, E. Unneberg, "Study of Thermal Instability of HMX Crystalline Polymorphs with and without Molecular Vacancies Using Reactive Force Field Molecular Dynamics," *Advanced Studies in Theoretical Physics*, vol. 10, no. 7, pp. 331–349, 2016.

[63] M. Svensson, S. Humbel, R. Froese, T. Matsubara, S. Sieber and K. Morokuma, "ONIOM: A multilayered integrated MO + MM method for geometry optimizations and single point energy predictions," *The journal of physical chemistry*, vol. 100, no. 50, pp. 19357–19363, 1996.

[64] Wikipedia contributors, "Implicit solvation — Wikipedia, the free encyclopedia," 2019. Accessed 6-April-2019, https://en.wikipedia.org/w/index.php?title=Implicit_solvation&oldid=883702156.

[65] Wikipedia User Tubas, "Cobalt-60m-decay," 2019. Accessed 6-April-2019, Licensed under Public domain via Wikimedia Commons, http://commons.wikimedia.org/wiki/File:Cobalt-60m-decay.svg.

[66] J. Akhavan and J. Padfield, "Final report: feasibility study on the effect of gamma radiation on polymer bonded explosives," tech. rep., Cranfield University, 2015.

[67] Wikipedia User J. Brown, "NMR Splitting," June 2010. This work has been released into the public domain by its author, JBancroftBrown at English Wikipedia, `https://commons.wikimedia.org/wiki/File:NMR_splitting.gif`.

[68] M. J. Frisch, G. W. Trucks, H. B. Schlegel, G. E. Scuseria, M. A. Robb, J. R. Cheeseman, G. Scalmani, V. Barone, G. A. Petersson, H. Nakatsuji, X. Li, M. Caricato, A. V. Marenich, J. Bloino, B. G. Janesko, R. Gomperts, B. Mennucci, H. P. Hratchian, J. V. Ortiz, A. F. Izmaylov, J. L. Sonnenberg, D. Williams-Young, F. Ding, F. Lipparini, F. Egidi, J. Goings, B. Peng, A. Petrone, T. Henderson, D. Ranasinghe, V. G. Zakrzewski, J. Gao, N. Rega, G. Zheng, W. Liang, M. Hada, M. Ehara, K. Toyota, R. Fukuda, J. Hasegawa, M. Ishida, T. Nakajima, Y. Honda, O. Kitao, H. Nakai, T. Vreven, K. Throssell, J. A. Montgomery, Jr., J. E. Peralta, F. Ogliaro, M. J. Bearpark, J. J. Heyd, E. N. Brothers, K. N. Kudin, V. N. Staroverov, T. A. Keith, R. Kobayashi, J. Normand, K. Raghavachari, A. P. Rendell, J. C. Burant, S. S. Iyengar, J. Tomasi, M. Cossi, J. M. Millam, M. Klene, C. Adamo, R. Cammi, J. W. Ochterski, R. L. Martin, K. Morokuma, O. Farkas, J. B. Foresman, and D. J. Fox, "Gaussian 16, Revision a.03," Dec. 2016.

[69] R. Dennington, T. A. Keith and J. M. Millam, "GaussView Version 6." Electronic, 2016. Semichem Inc. Shawnee Mission KS.

[70] J. Ochterski, "Thermochemistry in Gaussian," software, Gaussian, Inc., June 2000.

[71] D. Chong, V. Barone, A. Bencini and P. Fantucci, *Recent advances in density functional methods, ISBN: 9789810248253*. No. pt. 3 in Recent Advances in Density Functional Methods, World scientific, 1995.

[72] A.G. Biternas, G.T.P. Charnock and I. Kuprov, "A standard format and a graphical user interface for spin system specification," *Journal of Magnetic Resonance*, vol. 240, pp. 124 – 131, 2014.

[73] MATLAB, "MATLAB Version 2018b." Software, 2018. `https://uk.mathworks.com/products/matlab.html`.

[74] S. Stoll and A. Schweiger, "EasySpin, a comprehensive software package for spectralsimulation and analysis in EPR," *Journal of Magnetic Resonance*, vol. 178, pp. 42–55, Sept. 2005. Version 5.2.25.

[75] S. Hirata and M. Head-Gordon, "Time-dependent density functional theory for radicals: An improved description of excited states with substantial double excitation character," *Chemical Physics Letters*, vol. 302, pp. 375–382, Mar. 1999.

[76] Pyper, J. W., "The Measurement of Bound and Free Moisture in Organic Materials by Microwave Methods," techreport, Lawrence Livermore National Laboratory, A 1984.

[77] J. Byrnes, *Unexploded Ordnance Detection and Mitigation, ISBN: 9781402092510*. Spinger Science & Buissness Media, 2008.

[78] V. Golubev, "Effect of electronic excitation and ionization on decomposition mechanisms of 1,3,5-triamino-2,4,6-trinitrobenzene molecules," *New Trends in research of Energetic Materials - NTREM*, Apr. 2010.

[79] B. Nguyen Vana, E.V. Nikolaevab, A.G. Shamovb, G.M. Khrapkovskiia and R.V. Tsyshevsky, "Exploration of decomposition pathways of 2,4,6-trinitrotoluene (TNT) radical ions by means of density functional theory," *International Journal of Mass Spectrometry*, vol. 392, pp. 7–15, 2015.

[80] J. Padfied and N. Flood, "Results from irradiation," tech. rep., Cranfield University, 2016.

[81] Z. Yu and E. R. Bernstein, "Decompostion of pentaerythritol tetranitrate [C(CH2ONO2)4] following electronic excitation," *The Journal of Chemical Physics*, 2011.

[82] Wikipedia contributors, "Nuclear weapon — Wikipedia, The Free Encyclopedia," 2019. Accessed 6-April-2019, https://en.wikipedia.org/w/index.php?title=Nuclear_weapon&oldid=890157459.

[83] Wikipedia contributors, "Electron paramagnetic resonance — Wikipedia, The Free Encyclopedia." Electronic, 2019. Accessed 6-April-2019, https://en.wikipedia.org/w/index.php?title=Electron_paramagnetic_resonance&oldid=886620328.

[84] *A versitile synthesis of 1,3,5-Triamino-2,4,6-Trinitrobenzene (TATB)*, 37th International Institute of Chemical Technilogy (ICT) Conference Preceedings, 2006. A. R. Mitchell et al.

[85] Unknown, "Unidos PTW calibration certificate ," tech. rep., AWE Plc, 2014.

[86] Unknown, "ISO Standard 4037-2:1996." Electronic, 1996.

[87] P. Andreo, L. Rodrigues, L. Lindborg and T. Kraepelien, "On the calibration of plane-parallel ionization chambers for electron beam dosimetry," *Physics in medicine and biology*, vol. 37, pp. 1147–1165, may 1992.

[88] M. F. Foltz, D. L. Ornellas, P. F. Pagoria, A. R. Mitchell, "Recrystallization and solubility of 1,3,5-triamino-2,4,6-trinitrobenzene in dimethyl sulfoxide," *Jounal of materials science*, 1996.

[89] J. Akhavan, *The chemistry of explosives, ISBN:978-1-84973-330-4*. The Royal Society of Chemistry, 2011.

[90] C. Entwhistle, "Synthesis of Mono-Furazan Derivative of TATB - Unpublished Results," technical report, Atomic Weapons Establishment, Apr. 2019.

[91] J. C. Coles, S. N. Ahmed, H. U. Mehta and J. E. Kaufmann, "Role of free radical scavenger in protection of spinal cord during ischemia," *552 the annals of thoracic surgery*, vol. 41, no. 5, pp. 551–556, 1986.

[92] Wikidata, "Q211891 — Wikidata," 2019. Accessed 6-April-2019, https://www.wikidata.org/w/index.php?title=Q211891&oldid=896684746.